DESIGN AND DEVELOPMENT OF Ca-Mg-Fe-Ti-OXIDES BASED PEROVSKITE FOR HIGH SENSITIVE HUMIDITY SENSORS AND WOUND HEALING APPLICATIONS

ASHIS TRIPATHY

FACULTY OF ENGINEERING
UNIVERSITY OF MALAYA
KUALA LUMPUR

2017

DESIGN AND DEVELOPMENT OF Ca-Mg-Fe-Ti-OXIDES BASED PEROVSKITE FOR HIGH SENSITIVE HUMIDITY SENSORS AND WOUND HEALING APPLICATIONS

ASHIS TRIPATHY

THESIS SUBMITTED IN FULFILMENT OF THE REQUIREMENTS FOR THE DEGREE OF DOCTOR OF PHILOSOPHY

FACULTY OF ENGINEERING
UNIVERSITY OF MALAYA
KUALA LUMPUR

2017

UNIVERSITY OF MALAYA
ORIGINAL LITERARY WORK DECLARATION

Name of Candidate: ASHIS TRIPATHY

Matric No: KHA140009

Name of Degree: Doctor of Philosophy

Title of Project Paper/Research Report/Dissertation/Thesis ("this Work")::

Design and development of Ca-Mg-Fe-Ti-Oxides based perovskite for high sensitive humidity sensors and wound healing applications

Field of Study: Biomedical Engineering

I do solemnly and sincerely declare that:

(1)   I am the sole author/writer of this Work;
(2)   This Work is original;
(3)   Any use of any work in which copyright exists was done by way of fair dealing and for permitted purposes and any excerpt or extract from, or reference to or reproduction of any copyright work has been disclosed expressly and sufficiently and the title of the Work and its authorship have been acknowledged in this Work;
(4)   I do not have any actual knowledge nor do I ought reasonably to know that the making of this work constitutes an infringement of any copyright work;
(5)   I hereby assign all and every rights in the copyright to this Work to the University of Malaya ("UM"), who henceforth shall be owner of the copyright in this Work and that any reproduction or use in any form or by any means whatsoever is prohibited without the written consent of UM having been first had and obtained;
(6)   I am fully aware that if in the course of making this Work I have infringed any copyright whether intentionally or otherwise, I may be subject to legal action or any other action as may be determined by UM.

Candidate's Signature   Date:

Subscribed and solemnly declared before,

Witness's Signature   Date:

Name:

Designation:

ABSTRACT

Armalcolite, which is a rare ceramic mineral and normally found in the lunar earth, was synthesized by solid-state step-sintering. The *in situ* phase-changed novel ceramic nanocrystals of Ca-Mg-Fe-Ti based oxides (CMFTO), their chemical reactions, and bonding with polydimethylsiloxane (PDMS) were determined by x-ray diffraction, infrared spectroscopy, and microscopy. Water absorption of all the CMFTO was high. Different types of humidity sensors were developed using three distinct principles. The lower dielectric loss tangent value was obtained for the CMFTO ceramic sintered at 1050 °C (S1050) (0.155 at 1 MHz) and S1050/PDMS nanocomposite (0.002 at 1 MHz) film, which was made by spin coating at 3000 rpm. The excellent flexibility (Young's modulus≈0.27 MPa and elongation >90%), viscoelastic property (tanδ = E″/E′: 0.225) and glass transition temperature (T_g: -58.5 °C) were obtained for S1050/PDMS film. Humidity dependent capacitive, resistive, and dielectric response of S1050 electroceramic was studied successfully. The S1050 electroceramic based capacitive sensor showed excellent sensitivity of 3000% as well as fast response (14.5 s) and recovery (34.27 s) times, which are extremely lower than those of the other conventional capacitive humidity sensors. The impedance and dielectric sensors showed improved sensitivity of 0.23 MΩ/Δ%RH and ~2310%, respectively. The response and recovery times were 20 and 40 s, respectively for resistive sensor and for dielectric sensor, they were 18 and 35 s, respectively. All the three capacitive, resistive and dielectric humidity sensors showed extreamly low hysteresis and high stability. Therefore, best sensing performance of the flexible S1050/PDMS composite film (306%) based humidity sensor was found at 100 Hz, better than conventional materials.

In order to evaluate the biocompability of the S1050 and S1050/PDMS composite film based sensors with the direct contact to dermal surface, an *in vitro* study was employed using human dermis fibroblast cells. It showed that both the materials have

good biocompatibility and can thus be suitable for measuing the humidity at the skin and inner prosthetic surfaces.

To evaluate the drug carrying capacity of the present nanomaterials with the direct contact to dermal surface for wound healing applications, an *in vivo* assay was performed by aplying some hydrogels on rat's dorsal wounds. To investigate the histological and immunohistochemical effects of the curcumin drug loaded S1050 nanocomposite hydrogels disperred in poly(vinyl alcohol) solution, an *in vivo* cutaneous full-thickness excisional wound rat model was adopted using adult male sprague dawley (SD) rats. The normal and diabetic (created by injection of Streptozotocin (dosage: 55mg/kg)) rats were wounded of size 2 cm diameter at the posterior neck area. The rats were topically applied with 0.2 ml gels of curcumin, S1050, and curcumin loaded S1050 hydrogel separately for 14 days. Many interesting improved results were found for diabetic subjects using present hydrogels. Briefly, the *in vivo* results revealed improved wound contraction and tissue regeneration in diabetic rats applied with curcumin, S1050, and curcumin loaded S1050 hydrogels as compared with diabetic rats using normal hydrogel.

Moreover, beside sensors, the novel S1050 (i.e. armalcolite based nanocomposites) would be potential drug carrier for wound healing applications since their hydrogels showed as biocompatible, nontoxic, nonimmunogenic, and efficient drug carriers.

ABSTRAK

Armalcolite, yang merupakan mineral seramik yang hanya ditemui di kawasan lunar bumi, telah disintesis dalam melalui langkah-pensinteran keadaan pepejal. Fasa perubahan *in situ* nanokristal seramik novel bagi oksida-oksida berasaskan Ca-Mg-Fe-Ti (CMFTO), tindak balas kimia, dan ikatan polidimetilsiloksan (PDMS) ditentukan oleh pembelauan sinar x-ray, spektroskopi inframerah, dan mikroskopi. Penyerapan air pada semua CMFTO adalah tinggi. Pelbagai sensor kelembapan telah dibangunkan menggunakan tiga prinsip. Nilai tangent kehilangan dialetrik lebih rendah yang dicatat oleh seramik CMFTO adalah pada 1050 °C (S1050) (0.155 pada 1 MHz) dan filem nanokomposit S1050/PDMS (0.002 pada 1MHz), yang diperbuat menggunakan "spin coating" pada 3000 rpm. Fleksibiliti yang baik (modulus Young $\approx$ 0.27 MPa dan pemanjangan >90%), ciri-ciri viskoelastik (tanδ = E''/E': 0.225) dan suhu peralihan kaca (T_g: -58.5 °C) didapati pada filem S1050/PDMS. Tindak balas kapasitif, rintangan dan dielektrik bagi elektroseramik S1050 yang bergantung kepada kelembapan, telah berjaya dikaji. Sensor kapasitif elektroseramik S1050 menunjukkan sensitiviti yang sangat baik iaitu pada 3000%, serta tindak balas (14.5 s) dan masa pemulihan (34.27 s) yang cepat, yang amat rendah berbanding milai untuk sensor kelembapan kapasitif konvensional yang lain. Sensor impedans dan dielektrik menunjukkan sensitiviti yang lebih baik iaitu 0.23MΩ /Δ% RH dan ~ 2310%. Kadar tindak balas dan pemulihan ialah 20 dan 40 s untuk sensor rintangan dan untuk sensor dielektrik, masing-masing 18 dan 35 s. Sensor kelembapan kapasitif, resistif, dan dielektrik menunjukkan histerisis yang sangat rendah dan kestabilan yang tinggi. Oleh itu, prestasi sensor yang paling baik untuk sensor kelembapan berasasken filem komposit S1050 / PDMS fleksibel (306%) ditemui pada 100 Hz, lebih baik berbanding bahan-bahan konvensional. Dalam usaha untuk menilai biokeserasian sensor berasaskan filem komposit S1050 dan S1050 / PDMS dengan hubungan secara langsung ke permukaan kulit, kajian *in vitro* telah

dilakukan menggunakan sel-sel fibroblast dermis manusia. Ia menunjukkan bahawa kedua-dua bahan mempunyai biokeserasian yang baik dan sesuai untuk mengukur kelembapan pada kulit dan permukaan dalaman prostetik.

Di samping itu, dalam menilai keupayaan mengangkut dadah menggunakan nanobahan yang tersedia dan hubungan secara langsung dengan permukaan kulit untuk penyembuhan luka, "*in vivo* assay" telah dilakukan dengan meletakkan beberapa hidrogel pada permukaan luka tikus. Penyiasatan kesan histologi dan "immunohistochemical" bagi hidrogel nanokomposit S1050 dimuat dadah curcumin dalam poli(vinil alkohol), model tikus luka pemotongan ketebalan penuh kulit *in vivo* telah diadaptasi menggunakan tikus Sprague Dawley (SD) jantan dewasa. Tikus normal dan diabetik (yang dicipta melahui suntikan streptozotocin (dos: 55 mg/kg)) dicederakan di bahagian belakang leher ber ukuran diameter 2 cm. Tikus-tikus telah diletakkan 0.2 ml gel curcumin, S1050, dan hidrogel S1050 yang dimuatkan curcumin secara berasingan selama 14 hari. Keputusan yang memuaskan dilihat pada subjek diabetik menggunakan hidrogel. Secara ringkas, keputusan *in vivo* mendedahkan pengecutan luka dan pertumbuhan semula tisu yang lebih baik pada tikus diabetik yang diletakkan dengan curcumin, S1050, dan hidrogel S1050 yang dimuatkan curcumin berbanding dengan tikus diabetik yang menggunakan hidrogel normal.

Tambahan pula, selain sensor, S1050 (iaitu nanokomposit berasaskan armalkolit) yang novel akan menjadi pembawa dadah yang berpotensi untuk menyembuhan luka kerana hydrogel masing-masing ditunjukkan sebasni pembawa dadah bioserasi, nontoksik, nonimunogenik, dan cekap.

ACKNOWLEDGEMENTS

This thesis is dedicated to my beloved parents

Mr. Dillip Kumar Tripathy

Mrs. Ramamani Satapathy

for their endless love, support and encouragement

TABLE OF CONTENTS

LIST OF FIGURES

LIST OF TABLES

LIST OF SYMBOLS AND ABBREVIATIONS

CCTO	:	Calcium copper titanate oxide
IBLC	:	Internal barrier layer capacitance
PDMS	:	Polydimethylsiloxane
NPs	:	Nano particles
CMFTO	:	Ca,Mg,Fe,Ti-oxides
A.C	:	Alternating current
ε'	:	Dielectric constant
ε''	:	Dielectric loss
$\tan\delta$	:	Dielectric loss tangent
VP	:	Vapor pressure
SVP	:	Saturation vapor pressure
DP	:	Dew point
FP	:	Frost point
RH	:	Relative humidity
LiCl	:	Lithium chloride
QCM	:	Quartz crystal microbalance
ECM	:	Extracellular matrix
TGFs	:	Transforming growth factors
PDGFs	:	Platelet-derived growth factors
FGFs	:	Fibroblast growth factors
VEGFs	:	Vascular endothelium growth factors
EGFs	:	Epidermal growth factors
MSNs	:	Mesoporous silica nanoparticles
NO	:	Nitric oxide

MMT	:	Montmorillonite
PVA	:	Poly(vinyl alcohol)
XRD	:	X-ray diffraction
FESEM	:	Field emission scanning electron microscopy
PSD	:	Pore size distribution
TGA	:	Thermo gravimetric analysis
FTIR	:	Fourier transform infrared
WCA	:	Water contact angle
AFM	:	Atomic force microscope
DMA	:	Dynamic mechanical analysis
IS	:	Impedance spectroscopy
HDF	:	Human dermis fibroblast
PBS	:	Phosphate buffered saline
DMEM	:	Dulbecco's Modified Eagle Medium
DNA	:	Deoxyribonucleic Acid
STZ	:	Streptozotocin
NAD	:	Nicotinamide adenine dinucleotide
NC	:	Normal control
DC	:	Diabetic control
MW	:	Maxwell–Wagner
ANOVA	:	Analysis of Variance
S.E.M.	:	Standard Errors of the Mean

CHAPTER 1: INTRODUCTION

Nanotechnology involves various fields of research, including biology, chemistry, engineering, and physiology. In fact, it has shown great potential and impact in various technological and medical applications over the past few years. Materials of nano size, such as nanotubes, nanowires, nanoparticles, nanoceramics, and thin films, have offered successful platforms for the progress of numerous diagnostic applications in the biomedical fields. Nanomaterials are available in various forms, such as rods, crystals, or spheres with diameters between 1 to 100 nm. These nanomaterials function as a bridge between bulk and molecular or atomic level of materials. Due to the nano structure, these materials are widely used in various fields, such as magnetic recording media, computer memory chips, magnetically guided target specific drug delivery systems, cells, DNAs, radio frequency antennas, and many branches of telecommunication (Chen *et al.*, 2000; Ederer & Spaldin, 2004; Herzer *et al.*, 2005; Knobel *et al.*, 2003; Rozman & Drofenik, 1998; Taylor *et al.*, 1995; Zhao *et al.*, 2003). The shape and size also determine the unique and novel physical properties of the nanomaterials. The chemical composition, the morphology, the crystal lattice, the particle size and shape, as well as the interaction of the particles with the surrounding atoms, determine their magnetic, electrical, and biological properties. In recent years, ceramic nanomaterials and polymers individually, as well as their different composites, have demonstrated a special impact in the field of material science. A composite material consists of two or more distinct materials with significantly different physical or chemical properties, suitably arranged or distributed phases with an interfacial separation. When the two or more distinct materials are combined, they produce a composite material with characteristics that differ from the individual components (Chawla, 2012).

Due to the excellent and tailorable properties of ceramic-polymer composites, they have emerged as a great challenge to the world of science and technology. In fact, ceramic-polymer composites improve various mechanical properties, such as hardness, stiffness, density, flexibility, elasticity, and fracture strength, compared to their different monophasic materials for suitable applications. Recently, the fundamental idea of designing and developing flexible electronic devices has motivated many researchers to develop low loss factor, but high dielectric-based materials (Bai *et al.*, 2000; George & Sebastian, 2009). As such, researchers too have become passionate in developing electronic systems due to their multi-functional applications. In this context, polymer dielectric materials have drawn a great deal of attention owing to their easy and low temperature processing in capacitive-based systems. Furthermore, due to high technological demand, the electrical, mechanical, and thermal characteristics of the ceramic-polymer composites have been widely studied (Ahmad *et al.*, 2009; Bai *et al.*, 2000; Cheng *et al.*, 2007; George & Sebastian, 2009; Lam & Chan, 2005; Patel *et al.*, 2010; Petchsuk *et al.*, 2009; Tanase *et al.*, 2005; Thamjaree *et al.*, 2005; Wang *et al.*, 2004; Zhang *et al.*, 1994).

In the present work, ceramic-polymer composites for capacitor, humidity sensor, and medical applications were synthesized and characterized. Therefore, in chapter 2 a brief review about some effective ceramics and polymers systems for humidity sensor, capacitor, and biomedical applications are given.

1.1   Ceramics

Ceramics play important roles in the progress of material science and technology. The ceramics belong to the structural group are used generally in structural applications for their superior nuclear, chemical, thermal, and mechanical properties. Functional ceramics are another group of materials. Their electrical, optical, thermal, biological,

and magnetic properties are typically used as ferroelectric, piezoelectric, ceramic, thermo-sensitive, pressure-sensitive, and gas-sensitive ceramic materials in different device applications. The functional ceramics using electrical principles are also popularly known as electroceramics. The present research work has mainly focused on electroceramic and thus, it is briefly explored in this section. The electroceramics can be classified into three basic subclasses i.e., *piezoelectric*, *pyroelectrics*, and *ferroelectrics*. In the *piezoelectric* materials, when an external mechanical force is applied, it creates a change in electrical polarization. The piezoelectric electroceramics are normally used in radar, actuators, sensors, and other numerous applications (Park & Shrout, 1997; Wang *et al.*, 2004; Wolny, 2005). In the *pyroelectric* materials, electrical polarization changes occur due to external heat energy. The pyroelectric electroceramics are used in infrared (IR) detectors, pyro sensors, and other numerous devices (Chopra *et al.*, 2003; Kumar & Kumar, 2010). Contrastingly, in *ferroelectric* electroceramics, the electrical polarization changes take place after applying external electric fields and this material exhibits both piezoelectric and pyroelectric properties. The ferroelectric electroceramics are used in actuators and sensors. The dielectric ceramics and ferroelectric thin films are used for non-volatile memories and capacitive devices. Besides, the piezoelectric ceramic materials are similar to those of ceramic electro-optic for medical ultrasound imaging, data storage, and display applications (Bell, 2008; Guerrero *et al.*, 2001; Liu *et al.*, 2010; Mardare *et al.*, 2005; Minamikawa *et al.*, 2001; Noda *et al.*, 1999; Takezoe *et al.*, 2001).

1.1.1 Types of Ferroelectric Ceramics

Based on the chemical structure, the ferroelectric ceramics have been classified into three different types, such as ferroelectrics with hydrogen bonded radicals, ferroelectrics with perovskite structure, and ferroelectrics with tungsten bronze structure.

1.1.1.1 Ferroelectrics with Hydrogen Bonded Radicals

Before the discovery of barium titanate ($BaTiO_3$) polycrystalline ceramics, it was a misperception that ferroelectric properties cannot be observed without hydrogen bond inside the materials, such as potassium dihydrogen phosphate (KH_2PO_4), triglycine sulfate ($(NH_2CH_2COOH)_3.H_2SO_4$), and Rochelle salt ($NaKC_4H_4O_6.4H_2O$) (Safari *et al.*, 2011). Ferroelectric properties are also observed in numerous water-soluble single crystals with hydrogen bonded radicals. However, due to many drawbacks, such as deliquescence and weak ferroelectricity, low Curie temperature (T_C), and lower mechanical properties, single crystal salts, such as KH_2PO_4, $(NH_2CH_2COOH)_3.H_2SO_4$, and $NaKC_4H_4O_6.4H_2O$, are replaced by polycrystalline ferroelectric ceramics, including $BaTiO_3$.

1.1.1.2 Ferroelectrics with Perovskite Structure

The terminology 'perovskite' was nomenclatured by a Russian mineralogist, Count Lev Aleksevich von Perovski (1792-1856). The perovskite structured materials are frequently used in various fields of physics, chemistry, and materials science due to their fascinating functional properties for technological applications (Tejuca & Fierro, 2000). The perovskite is a large family of crystalline materials of crystal structure ABX_3, where, A-site and B-site are large and small size cations, respectively; while X-site is for anions, i.e., oxygen (O). 'A' has 12-fold cuboctahedral coordination with anions 'X', whereas 'B' is octahedrally coordinated by anions (O). Dipole moment of the perovskite crystals is created by the B-site atom present in the oxygen octahedron voids. Moreover, due to the presence of substantial space in this oxygen octahedron void, a wide range of substitutions are indeed possible. Furthermore, the perovskite structured materials have displayed various attractive properties, including spin

4

dependent transport, high thermo power, colossal magneto resistance, ferroelectricity, superconductivity, and so on. For such reasons, they are used in various fields of science and technology, such as catalytic electrodes in fuel cells, actuators, sensors, and many others (Safari *et al.*, 2011). The most well-known perovskite structured ferroelectric materials are calcium titanate ($CaTiO_3$), $BaTiO_3$, lead zirconate titanate (PZT), lead titanate ($PbTiO_3$), lanthanum zirconate titanate (PLZT), lead magnesium niobate (PMN), potassium tantalate niobate ($K(Ta_xNb_{1-x})O_3$), and lead potassium sodium niobate ($K_xNa_{1-x}NbO_3$/KNN). The unit cell of a perovskite structure is shown in Figure 1.1.
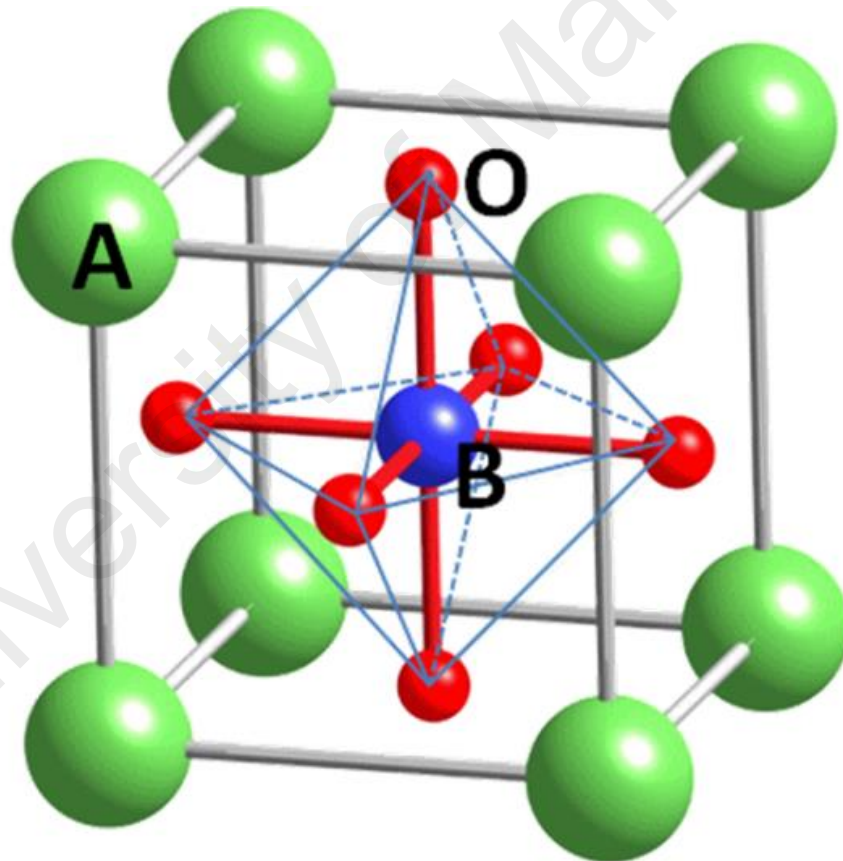
Figure 1.1: Unit cell of a perovskite structure (adapted with permission from (Fu & Itoh, 2011; Safari et al., 2011)).

5

1.1.1.3 Ferroelectrics with Tungsten Bronze Structure

The tungsten bronze type ferroelectric crystals share similar type of structure with potassium tungstate (K_xWO_3, x<1), which was first elucidated by Magneli et al. (Magnéli, 1949). Lead niobate ($PbNb_2O_6$) was one of the first crystals in the tungsten bronze type structure to demonstrate useful ferroelectric properties. This crystal structure has three types of open channels that are developed through the octahedrons (see Figure 1.2), which allows a wide range of ionic substitutions, either in the channels or within the octahedral void. The site occupancy formula for this type of structure is given by $(A1)_2(A2)_4(C)_4(B1)_2(B2)_8O_{30}$. Normally, this structure consists of three types of pseudo symmetric open channels with interconnected corner sharing octahedral oxygen (i.e. 3-fold, 4-fold, and 5-fold). A schematic projection of the tungsten bronze type structure on the (001) plane is illustrated in Figure 1.2. Besides, a wide range of cation and anion substitutions without any loss of ferroelectricity had been found to occur due to its open nature of the structure as compared to that of perovskite. Moreover, more than 100 numbers of oxide ferroelectrics exist in the tungsten bronze family.
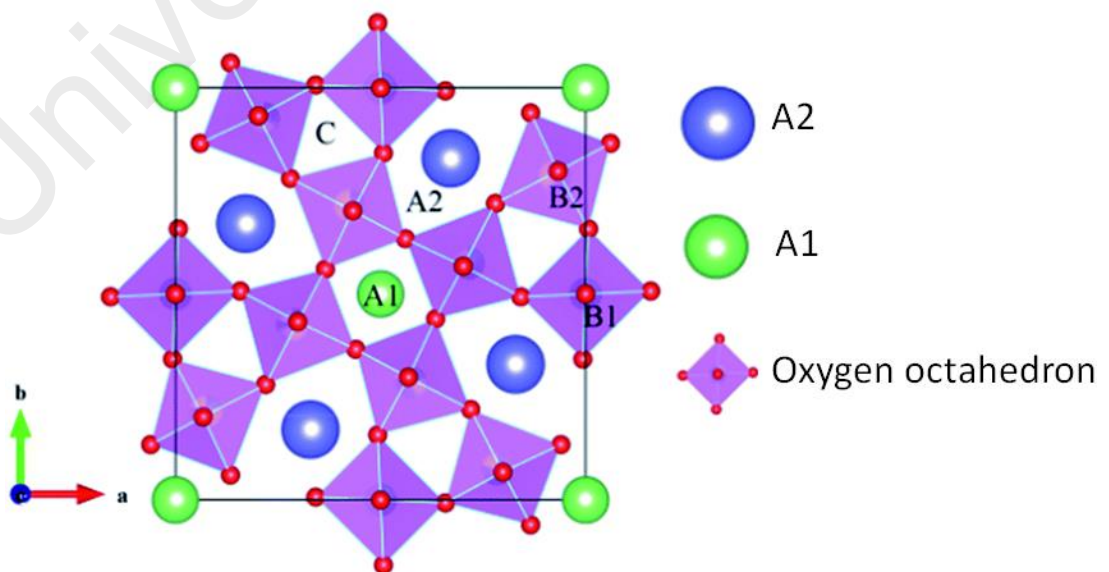
Figure 1.2: Schematic diagram of tungsten bronze structure (adapted with permission from (Castel et al., 2009; Ma et al., 2015)).

1.1.2 High Dielectric Constant Perovskite Structured Ceramics

Recently, high dielectric response has been observed in perovskite structured materials. The calcium-copper-titanium-oxides (CCTO) ceramic is one of the most frequently used perovskite structured high dielectric response materials, as first reported by M. A. Subramanian (Subramanian *et al.*, 2000). Neutron powder diffraction of CCTO indicates a cubic-perovskite structure with Im3 group symmetry and cubic lattice parameter a = 7.391 Å (Homes *et al.*, 2001). The structure of a CCTO (e.g., $CaCu_3Ti_4O_{12}$) is shown in Figure 1.3. The high dielectric constant (ε') in the CCTO is mainly due to the tilting of Ti^{4+} ion within the TiO_6 octahedron. Moreover, CCTO shows more constraint than ferroelectric materials. The octahedral tilt of TiO_6 in CCTO material develops a square planar arrangement around the Cu^{2+} ion. Furthermore, it had been found that under a tension, Ti-O bond influences the effect of polarization of the TiO_6 octahedral (Subramanian *et al.*, 2000). The CCTO compounds have shown high ε' (i.e., 10^3 to 10^5), which is independent of temperature in the range of 100–600 K and low loss tangent (tanδ: 10^{-1} to 10^3) (Subramanian *et al.*, 2000) in the frequency range of 10^2–10^6 Hz. The origin of the giant dielectric response in CCTO, nevertheless, has not been fully understood to date. In CCTO, neither a phase transition nor a crystal structure change has been detected in the temperature range of 35–1273 K (Subramanian *et al.*, 2000). It seems the high dielectric constant in CCTO is mainly extrinsic; not intrinsic. The high dielectric mechanism in CCTO can be explained by an internal barrier layer capacitance (IBLC) model. In this model, the high dielectric phenomenon of CCTO ceramics is attributed to the existence of a grain-boundary IBLC effect (Prakash *et al.*, 2008). The high dielectric response in CCTO-based material is attributed to Maxwell–Wagner (M–W) relaxation model, which insists semiconducting and insulating properties inside the grain and at the grain boundary (GB), respectively (Wu *et al.*, 2002). The processing routes affect the grain size and the density of the functional

ceramics, which alter the properties of the materials. Moreover, the variation in phase, density, and microstructure of the ceramics largely affect the electrical properties (Li *et al.*, 2010).
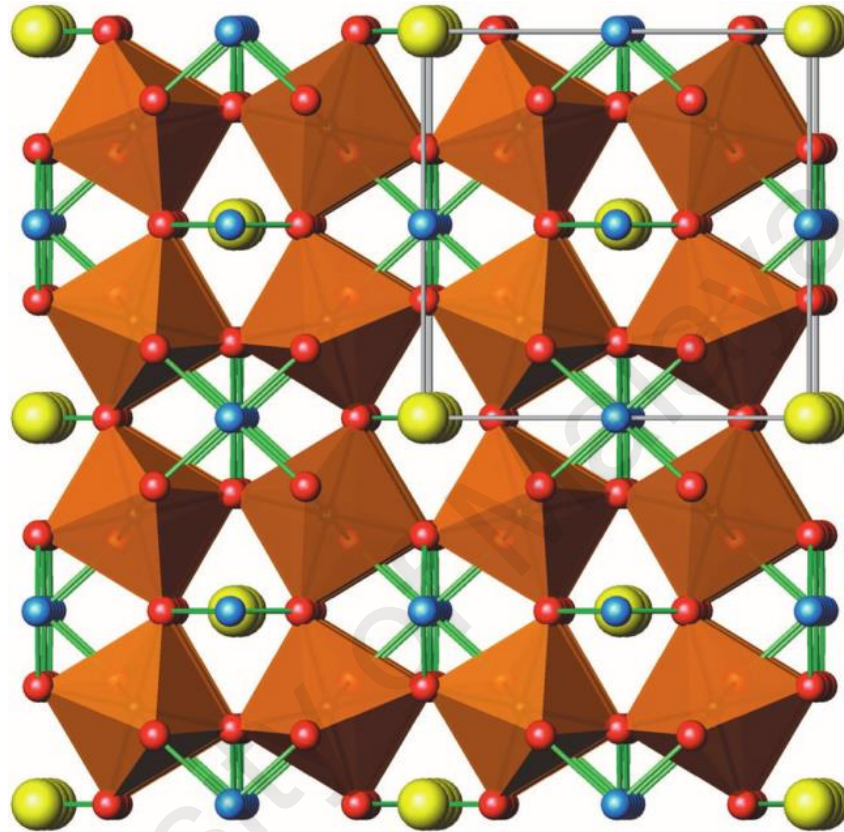
Figure 1.3: The structure of CCTO (Cu-blue, Oxygen-red, Ca-yellow) (adapted with permission from (Homes *et al.*, 2001)).

In addition, the dielectric layers of functional ceramics and inner electrodes are arranged layer by layer to form a multilayer structure to increase the volume efficiency of the material. From both intrinsic and extrinsic viewpoints, various proposed models to understand the high dielectric responses in the perovskite ceramics are still controversial (Prakash *et al.*, 2008; Subramanian *et al.*, 2000; Wang *et al.*, 2007; Wu *et al.*, 2002). Additionally, there are various possible reasons for high ε': (i) presence of defects inside the grains causes inhomogeneous conduction within the crystal, (ii)

different work functions of an electrode and a sample cause electrode polarization effects, (iii) the insulating grain boundaries surrounding semiconducting grains generate internal barrier layer capacitor (IBLC) effects, (iv) fluctuations of lattice-distortion induce dipoles in nano size domains, and (v) intra-grain insulating barrier effects ionic mobility (Subramanian *et al.*, 2000).

These models suggest that the giant dielectric response in the perovskite materials is mainly due to the charge dynamics inside the grain and at the GB. The aforementioned studies also hint that due to addition of various cation and anions in the CCTO material, one can alter its electrical and dielectric characteristics for various electronic applications.

Despite the discussed advantageous applications of electroceramics, they did show some drawbacks, which hinder them to be used as the best material in the field of electronics. Though electroceramics display high piezoelectric charge co-efficient, high acoustic impedance, and large dielectric constant, lack of flexibility and elasticity hinders their utilization in various electronic applications. Undesired morphological structures, inherent brittleness, insufficient porosity, and inhomogeneous distribution of pores significantly hinder water absorption by showing lower hydrophilicity in the ceramics, besides lower flexibility. Nonetheless, to improve its flexibility, suitable polymer materials can be incorporated with the ceramics.

1.2 Polymers

The elasticity, flexibility, low density, and high breakdown strength of the ceramics can be tailored by combining the ceramics with the polymer matrixes. Therefore, the selection of a suitable polymer matrix is also a most challenging job to overcome the problems of eletroceramics. Polymer is a large molecule of repeating structural units

9

connected by covalent σ-bonds. Hence, no free electron is available to participate in current conduction and thus, the solid saturated polymers exhibit electrical insulating characteristics. Due to this reason, the charge carriers generated by external electrostatic field are acquired in the polymers to retain them for a long time. Besides, low level current conduction occurs in insulating materials due to many distinct reasons. The impurities may provide very small amounts of charge carriers in the form of electrons or ions. At very high electric field, the current is conducted due to the injection of new charge carriers into the polymers. The salient features of polymer matrix are low in cost, ease of processability, low in specific gravity, and good chemical resistance. Nevertheless, the main drawbacks of polymer matrix are low thermal resistance and high coefficient of thermal expansion.

1.2.1 Ferroelectric Polymers

Ferroelectric polymers, which refer to a group of crystalline polar polymers, have permanent electric polarization. They control permanent electric polarization that can be switched or reversed in the direction of applied external electric fields. The piezoelectric effect can be observed in both natural and synthetic polymers. Wood and tendon are good examples of natural piezoelectric polymers. The substantial piezoelectric and pyroelectric effects in synthetic polymers under strong direct current (DC) electric field had been reported by Kawai et al. (Kawai, 1969). Most polymers, in fact, show excellent mechanical flexibility and have been used in various electronics and biomedical fields. Some widely used synthetic ferroelectric polymers are polyvinylidene fluoride (PVDF) and its copolymers with trifluoroethylene (TrFE) and tetrafluoroethylene (TFE), as well as vinylidene cyanide (VDCN).

1.2.2 Nonferroelectric Polymers

Nonferroelectric polymers are dimensionally more stable and relatively inexpensive than ferroelectric polymers. These amorphous polymers are mainly thermosets. Nonferroelectric polymers have high thermal stability, good electrical, excellent combination of mechanical, and corrosion resistance properties. Epoxy and phenolic thermosetting polymers are the most commonly used nonferroelectric polymers.

Though there are various ferroelectric and nonferroelectric polymers; among them, the polydimethylsiloxane (PDMS) ferroelectric polymer has been used as a potential polymer material in various electronics and medical applications due to its good optical transparency, viscoelastic, chemical and thermal stability, as well as high flexible properties.

1.2.3 Polydimethylsiloxane (PDMS)

PDMS is one of the cost effective flexible electronic materials that are used in various industries. Besides good physical and chemical stability, it has unique flexibility with shear elastic modulus of 250 kPa and the lowest glass transition (T_g) temperature that makes it a potential material for flexible electronics. PDMS also possesses low curing temperature, clean room processability, ability to functionalize easily, very low change in elasticity with temperature and time as well as high compressibility. The tunable properties of PDMS make it an ideal material to serve as a substrate for flexible electronics. In fact, numerous approaches have been taken to develop different flexible materials as substrates by various researchers in the past few decades (Cheng & Wu, 2010; DeJean *et al.*, 2005; Nikolaou *et al.*, 2006) for flexible sensor and flexible integrated circuits (IC). In these applications, various types of polymers (e.g., liquid crystal polymer (LCP), polyethylenimine (PEI), and polyethylene terephthalate (PET))

have been selected as the substrate for flexible electronic applications with suitable radio frequency (RF) characteristics, including low dielectric constant (ε) and low dissipation factor (tanδ) (DeJean *et al.*, 2005). In addition, the PDMS has shown great popularity and usability in fabrication of microwave microsystem in recent years (So *et al.*, 2009; Tiercelin *et al.*, 2006). Due to its excellent chemical stability and very low dielectric constant, PDMS has been used as the best microwave frequency electronics-substrate. Moreover, PDMS can be attached to other substrate materials easily after surface treatment by oxygen plasma. In fact, the PDMS-based photoresist for printed circuit board (PCB) applications was first developed by IBM company. Low dielectric constant and low tangent loss characteristics of PDMS also had been found to enhance its feasibility for wireless applications (Ghannam *et al.*, 2009; Mbairi & Hesselbom, 2005).

On top of that, PDMS is also compatible with biological tissues. It is impermeable to water, nontoxic to cells, and permeable to gases. Despite of the bioinertness of PDMS, the low hydrophilic characteristic is the main drawback of its application in humidity, as well as many biomedical fields. Therefore, in order to enhance the flexibility of ceramic material and to improve the hydrophilic property of PDMS, it is very essential to develop a PDMS-based ceramic-polymer composite.

1.3 Ceramic-Polymer Composites and Its Electronic Application

The high demand of low cost, good performance, small size, large surface area, flexibility, and lightweight properties of electronic devices has forced scientists to develop new material systems with improved characteristics (Ramajo *et al.*, 2007). Recently, numerous polymer-ceramic composites have been introduced in telecommunication, microelectronics, and also in medical applications (Taya, 2005). In the past few decades, various polymer matrices, such as polyethylene (PE),

12

polytetrafluoroethylene (PTFE), polybenzoxazole, epoxy, cyanate ester, polyimide (PI), and polystyrene (PS) with ceramic fillers, have been analyzed (Im *et al.*, 2012; Janardhanan *et al.*, 2012; Subodh *et al.*, 2009; Thomas *et al.*, 2009). For more than forty years, polymeric materials have been used in various forms, such as insulators, encapsulants, as well as electronics as resists and intermediate dielectrics (Goyal *et al.*, 2011). Besides, polymers have numerous advantages, such as flexibility, good dielectric properties, and low processing temperature. However, still they have many drawbacks, such as high coefficient of thermal expansion and low thermal conductivity, and restrict them to be used in various electronics, as well as biomedical applications. On the other hand, ceramics have desired dielectric properties, but their high processing temperature, undesired morphology, and inherent brittleness restrict their use in current IC technologies. Furthermore, the diverse and multifunctional features are the major requirement of modern electronic devices and systems, which cannot be fulfilled by using only single-phase materials (Batra *et al.*, 2008). Therefore, this problem can only be solved by integrating the properties of both polymer and ceramic materials (Sebastian & Jantunen, 2010). Hence, the composites of monolithic polymer and ceramic can replace the usual polymers or ceramics. In fact, numerous polymers are available, such as PS, PE, and PTFE, but their stretchability has failed in reaching up to the desired mark of many electronics and especially for medical applications. Therefore, PDMS-ceramic composites could solve those problems easily.

PDMS/ceramic composites have numerous applications in the electronic fields (Rao, Ogitani*, et al.*, 2000; Rao, Wong*, et al.*, 2000) such as acoustic emission sensors, microelectronic chips, integrated decoupling capacitors, and electronic packaging materials (Dias *et al.*, 2004; Ramajo *et al.*, 2010; Ramajo *et al.*, 2007). The electroceramics have very high dielectric constant, while flexible PDMS-based materials have high dielectric breakdown voltage and low processing temperature (Bai

et al., 2000). Therefore, the composite of PDMS-based electroceramic composites offer better performance compared to their corresponding single phase material. Hence, the PDMS/ceramic composite materials with high breakdown voltage and high dielectric constant can be used in energy storage capacitive applications (Hebestreit *et al.*, 2003; Murugendrappa & Prasad, 2006). The PDMS/ceramic composites also have various other advantages, such as good electromechanical properties, easy processing, and easy to give any typical shape through simple molding process. Moreover, the suitable stoichiometry of polymer and ceramic can provide the composite for multipurpose functions, such as electrical, electronic, and biomedical applications (Bhuvanesh & Gopalakrishnan, 1997).

In this research work, the design and the development of PDMS/ceramic composite with high flexibility, as well as improved mechanical, water adsorption, and dielectric properties, using spin coating technique to produce a low cost and flexible humidity sensor are presented.

1.4   Motivation for Material Selection

The piezoelectric ceramic composites are the current gold standard as multifunctional material for various advance electronic and sensor applications. Perovskite structure is one of the main structural properties of piezoelectric ceramic materials. The perovskite materials e.g., $CaCu_3Ti_4O_{12}$ (CCTO) have been explored much as electroceramics owing to their ''giant dielectric response'' (Hu *et al.*, 2012; Singh *et al.*, 2013; Thomas *et al.*, 2010). The high dielectric materials are generally suitable for capacitive type sensor device. The dielectric constant is proportionally related to the capacitance, which is increased significantly with relative humidity (Tripathy *et al.*, 2014). In other words, it can also be said that the lower dissipation factor (D) or dielectric loss tangent, $\tan\delta$ (i.e., ratio of energy loss per cycle, ε'' to energy storage per cycle, ε') would benefit to improve the quality factor (Q) for any

14

electronic device. The D is inversely proportional to the Q of an electronic device. The tanδ is directly proportional to the ε''. Therefore, evaluation of tanδ is an indirect measurement of dissipation of energy under an external electric field. It includes the effects of both dielectric loss and conductivity of a material. There are also some precision capacitive methods which have shown fast response and high temperature compensation (Matko & Donlagic, 1996). The capacitive method which uses open capacitor as a sensing element has fast dynamic response and also good electronic circuit with fast response (Matko, 2011). A new method developed by Matko et al., reduces offset, temperature characteristic of main sensing element, temperature drift, and noise by switching method and it showed fast dynamic response (Matko & Milanović, 2014). Nevertheless, at high precision measurement, it is important to reduce any disturbing noise with good noise compensation (Bonfig *et al.*, 1988). In this instance, deconvolution method using the pseudo-stochastic excitation signals can compensate all kind of noises and temperature drift. The titanates are most important group for many advanced piezoelectric ceramics. It is basically perovskite, $M^{2+}TiO_3$, in structure, which is face-centered cubic (FCC) (if M= Ca, Ba, and Sr) or trigonal (if M= Fe, Co, Ni, Mn, and Mg) depending on chemical composition (Neufuss & Rudajevová, 2002; Pramanik *et al.*, 2013). Lead (Pb) free perovskite materials have been investigated to be used in many energy storage applications (Shen *et al.*, 2015; Zhou *et al.*, 2015). The perovskite calcium titanate (orthorhombic or monoclinic $CaTiO_3$) and geikeilite magnesium titanate (rhombohedral $MgTiO_3$) are being used as attractive materials in many ceramic coating industries (Wei *et al.*, 2007; Zabicky *et al.*, 1997). It has been found that thermal diffusivity of these materials e.g., $MgTiO_3$–$CaTiO_3$, decreases with temperature but thermal conductivity increases with sintering temperature (Neufuss & Rudajevová, 2002). The iron oxide based composites have also been used as potential dielectric as well as humidity sensor materials (Ang *et al.*, 2014).

On the other hand, armalcolite ($Fe_2MgTi_3O_{10}$) is geochemically significant, might be used as indicators of oxygen fugacity and temperature, and can be used for producing refractory ceramics and ferromagnetic materials (Medvedev, 1996). The ilmenite ($FeTiO_3$) phase is thought to be transformed into armalcolite type ($(Mg,Fe^{2+})Ti_2O_5$) after a solid state reaction with magnesium silicate ($MgSiO_3$) at very high pressure (~1.4 GPa) that might have been occurred by cumulate overturn process (Khan *et al.*, 2013; Thacker *et al.*, 2009). The phase equilibria in the MgO-FeO-Fe_2O_3-TiO_2 system indicate the stability of armalcolite in the crust at 900–1200 °C (Hayob & Essene, 1995). Since ilmenite and armalcolite ceramics have been attempted in humidity and remote sensing missions (Chuang *et al.*, 2010; Yazawa *et al.*, 2012), their derivative materials could be used as potential materials for humidity sensor applications. However, the major limitations of ceramic materials are the undesired morphological structures beside the brittleness. Most of the ceramics have insufficient porosity and inhomogeneous distribution of pores. Specially, these two problems reduce the absorption of water or moisture and show lower hydrophilicity beside. It significantly hinders the electrical conductivity between the microelectrodes in the micro-/nano- sensors and further inhibits the sensing response to the humidity sensors. To improve the flexibility of the ceramic materials, composites with polymers or elastomers show as best (Ataollahi *et al.*, 2015; Kar & Pramanik, 2014; Nayak *et al.*, 2013; Su & Wang, 2008; Tripathy *et al.*, 2014). However, improving of hydrophilicity is a great challenge to the researchers for the flexible composite materials to date. Furthermore, flexibility of the composites was also not evaluated properly in other studies (Nayak *et al.*, 2013; Su & Wang, 2008) . In this context, polydimethylsiloxane (PDMS) elastomer has shown excellent flexible property in many advanced applications for humidity sensors (Ataollahi *et al.*, 2015; Lim *et al.*, 2014; Tiercelin *et al.*, 2006; Tripathy *et al.*, 2014).

Apart from the sensor applications, the ceramic nanocomposites are also considered as a potential material in biomedical applications. The nanoparticles of metals, ceramics and polymers, which can resist the human pathogens such as bacterium or virus and even cancer, are used in new age drug compounds. The importance of ceramic nanoparticles (NPs) having potent germicidal activity is inevitable because of their effect against resistant strains of pathogens. The large surface area to volume ratio of ceramic nanoparticles accelerates their chemical activities. In recent trend, ceramic NPs are considered as the most potential material among all the other NPs. In particular, ceramic oxide NPs are well known for their strong antimicrobial activity. However, titanium and iron based NPs are the most important ceramic oxide NPs compared to other ceramics. These ceramics have shown good mechanical properties, antibacterial effect against gram-positive (e.g., *S. Aureus* and *B. subtilis*) and gram-negative (e.g., *E. Coli*, *P. aeruginosa*) bacteria, cell growth and high corrosion resistance.

In this context, the armalcolite, rare earth mineral has not been properly synthesized in laboratory to date. So far, it has not been investigated as potential humidity sensing or energy storing and biomaterials, specifically for wound healing applications at all in the world. Hence, for the first time, the novel synthetic armalcolite ceramic would be used as potential multifunctional materials, including charge or energy storing, electro ceramic and humidity sensing materials. In addition, the crystalline phases, porosity, and morphology would be controlled by an *in situ* step-sintering technique without using any further expensive method. Due to high porous and nontoxic nature of the armalcolite nanocomposite, an attempt has also been taken to apply these ceramic NPs in the wound healing application on diabetic rat model in the present study.

1.5   Problem Statement

The most unique properties of ceramic materials are their relatively high thermal, chemical, and mechanical stability (Kulwicki, 1991; Traversa, 1995). These properties have made them the most suitable potential candidate in sensor applications. However, the major limitations of ceramic materials are the undesired morphological structures and the inherent brittleness. In addition, other disadvantages of most of the common ceramics are insufficient porosity and inhomogeneous distribution of pores. In specific, these two problems reduce the absorption of water or moisture, display lower hydrophilicity, and amplify the issue of brittleness. They significantly hinder the electrical conductivity between the microelectrodes in the micro- or nano- sensors and further inhibit the sensing response to the humidity sensors. Hence, in order to improve the flexibility of the ceramic materials, composites with polymers or elastomers have shown the best desired properties (Kar & Pramanik, 2014; Su & Wang, 2008; Tripathy *et al.*, 2014). However, controlling the aspect of hydrophilicity in such flexible composite materials is a great challenge to researchers to date. Furthermore, flexibility of the composites had not been evaluated extensively in other studies (Nayak *et al.*, 2013; Su & Wang, 2008). Moreover, as most of the ceramic materials are toxic in nature, they become a hindrance for biomedical applications.

1.6   Objectives

In this thesis, a novel armalcolite nanocomposite has been synthesized from few inexpensive ceramic oxide nanomaterials and its potential applications in humidity sensor and wound healing have been investigated. Specifically, the present investigation has been carried out based on five broad goals, as precisely mentioned below.

I.   To synthesize and characterize a novel submicroporous ceramic armalcolite, along with a perovskite phase from some metallic (Ca, Mg, Ti, and Fe) oxides with good dielectric (ε_r) and minimum dissipation of energy under an external electric field. This objective is described in Chapter 3 and Chapter 4.

II.   To design and develop a porous nanocomposite of armalcolite electroceramic with improved sensing properties via physisorption for capacitive, resistive, and dielectric humidity sensor applications, which is highlighted in Chapter 3 and Chapter 5.

III.   To prepare a flexible thin film of the armalcolite/perovskite and polydimethylsiloxane (PDMS) composite with improved flexibility and water absorption properties for flexible resistive humidity sensor application. This objective is clearly explained in Chapter 3 and Chapter 5.

IV.   To investigate the *in vitro* biocompatibility of armalcolite nanocomposite NPs as well as flexible film. It is clearly narrated in Chapter 3 and Chapter 4.

V.   To determine the *in vivo* effect of curcumin drug loaded armalcolite nanocarrier based hydrogel in wound healing applications using diabetic rat model. This objective is clearly explained in Chapter 3 and Chapter 5.

1.7 Thesis Layout

The present thesis is organized into six chapters. A brief summary of each chapter is concisely mentioned below.

Chapter 1 begins with the introduction about the fundamental idea and the properties of various ceramics, polymers, and their composites, as well as their motivation for the development of humidity sensor and usage in biomedical applications.

Chapter 2 starts with a literature survey on a number of humidity sensors that had been developed using various measurement techniques. This chapter describes the role of morphological structure, doping, and coating of different materials in sensing characteristics of humidity sensors. In addition, it narrates the basic idea of wound and the different process of wound healing. This section also surveys the effect of various nanocomposites and their hydrogels in wound healing application.

Chapter 3 focuses on the complete materials and methods. In this chapter, the syntheses of calium-magnesium-iron-titanium oxides based compound (CMFTO), S1050/PDMS (S1050: CMFTO ceramic sintered at 1050 ℃ sintering condition, composed of armalcolite ($Fe_2MgTi_3O_{10}$), perovskite ($CaTiO_3$), and ferrite (Fe_3O_4) structured ceramics) composite thin film, as well as the development and design of S1050 electroceramic-based capacitive, resistive, and dielectric humidity sensor, including S1050/PDMS-based flexible resistive humidity sensor, are explained explicitly. Apart from humidity sensor, it also describes all the experimental procedures of *in vitro* biocompatibility study and the experimental details of wound healing application.

Chapter 4 presents the results and discussions on physical, thermal, mechanical, and electrical properties of synthesized CMFTO composite, S1050/PDMS flexible film, and

polyvinyl alcohol (PVA)/armalcolite/drug composite hydrogel. The *in vitro* biocompatibility study of the armalcolite-based nanocomposite is also depicted here.

Chapter 5 contains the results and discussion of humidity sensor response and also describes the wound healing results. The first part of the chapter portrays the humidity-dependent capacitive, resistive, and dielectric responses of S1050 electroceramic-based sensor and also the responses of S1050/PDMS-based flexible resistive humidity sensor. Meanwhile, the second part describes the *in vivo* effect of curcumin drug loaded armalcolite nanocarrier based hydrogel in wound healing applications using diabetes rat model.

Chapter 6, finally, presents the conclusions of the whole study and offers some suggestions for future studies.

CHAPTER 2: LITERATURE REVIEW

2.1 Introduction

Nanobiotechnology is the combination of two different fields of science, such as nanotechnology and biotechnology to introduce a new technology. In recent years, the amalgamation of biology, chemistry, physics, material science, and medicine has been incarnated as nanotechnology (Shanmugasundaram *et al.*, 2013). Different nanoparticles (NPs) have also been widely studied owing to their unique properties and versatile applications in the field of science and technology (Ingle *et al.*, 2009). Nowadays, the ceramic-based nanocomposite is considered as a potential material in the advance electronics, sensor, and biomedical applications. The most unique properties of ceramics, including relatively high thermal, chemical, and mechanical stability (Kulwicki, 1991; Traversa, 1995), make them the most suitable potential candidate in sensor applications. The excellent water adsorbing and removing property of metal oxide ceramics, such as titania (TiO_2) (Faia *et al.*, 2004), zinc oxide (ZnO) (Zhang, Yu, Ouyang*, et al.*, 2005), ferrites (Shah *et al.*, 2007), alumina (Al_2O_3) (Cheng *et al.*, 2011; Sberveglieri *et al.*, 1994), and barium strontium titanate (BST, $(Ba,Sr)TiO_3$) (Agarwal & Sharma, 2002; Yuk & Troczynski, 2003) have been extensively utilized as humidity sensors. In particular, the porous ceramic-based capacitive sensors can remain stable at high humidity condition even at elevated temperatures by showing high sensitivity (Chang & Tseng, 1990; Wang *et al.*, 2012).

Moreover, nanomaterials have already proven their significant impact and versatile applications in various fields of sciences. This is especially when nanomaterials exhibit their excellent efficiency in the biomedical field, including bio-molecular sensing, biological imaging, drug delivery vehicles, and wound healing in the form of micelles and vesicles, disease therapy, as well as scaffolds in tissue engineering applications.

Since nanocomposite has versatile application in different fields, it is indeed essential to carry out an extensive study pertaining to the various ceramic nanocomposites in the field of humidity sensors, as well as wound healing applications.

2.2 Ceramic Nanocomposite as Humidity Sensor

Humidity plays an important role in many sectors, including engineering, medical, and various industrial sectors. Therefore, it is very important to select a suitable humidity sensing material to obtain good reliability, best linearity, long-term stability, rapid response and recovery, and small hysteresis. In this section, neumerous carbon, ceramic oxide, and polymer based humidity sensors have been surveyed.

2.2.1 Introduction

Humidity is evaluated by different functions such as *vapor pressure* (*VP*), *saturation vapor pressure* (*SVP*), *dew point* (*DP*) temperature, *frost point* (*FP*) temperature, and *relative humidity* (*RH*) (Chen & Lu, 2005). *VP* (hPa) is a partial pressure of water vapor in the air. *SVP* is measured on a surface of water or ice at thermodynamic equilibrium condition. *DP* is a temperature, above 0 °C, at which the air will be cooled down to reach saturation at constant pressure and it is generally equal to or lower than the actual air temperature. *FP* is a temperature, below 0 °C, at which moist air saturates with respect to ice. *RH* (%) is a ratio of the VP of moist air to its SVP at a given temperature, which is expressed by Equation 2.1.

$$\text{RH} = \frac{VP}{SVP} \times 100 \text{ \%} \tag{2.1}$$

Humidity can also be expressed as *absolute humidity* (g/m^3) which is defined as the amount of water vapor contain in unit volume of dry air i.e., mixing ratio m_r (parts per

million by volume, ppmv) and the ratio with respect to saturation is defined as saturation deficit p_{sd} (mbar).

In 1450, Nicolas Cryfts invented a hygrometer which is the first humidity measurement instrument on record. This hygrometer used wool to determine the changes of humidity in air (Aezinia *et al.*, 2012). Over the past 550 years, many kinds of hygrometer have been invented. In 1550, the device was first improved by substituting the wool with a sponge and various versions of the hygrometer. Subsequently, the sponge was replaced by paper, hair, nylon, and acetate. During the 17th and 18th centuries, there were several opinions about the mechanisms of water dissolution in air. At that time, it was also established that there is a relationship between humidity and frequency or temperature. Currently, miniaturized humidity sensors have shown many advantages, including integration, small size, low power consumption, high performance, low cost, and ease of mass fabrication compared to the classical measurement used in different hygrometers such as lithium chloride (LiCl) dew point and chilled mirror type sensors (Wiederhold, 1997). Different types of humidity sensors are classified according to the working technology and sensing principle and illustrated in the Figures 2.1(a) and 2.1(b), respectively.

(a) Humidity sensor based on method & miniaturization

Synthesis method

- Sol – gel (e.g., Li-doped mesoporous silica SBA-15)
- Screen printing (e.g., KCl-doped SnO_2 nanofiber)
- Metal-organic decomposition (e.g., $Bi_{0.5}(Na_{0.85}K_{0.15})_{0.5}Ti_{0.97}Zr_{0.03}O_3$(BNKTZ))
- Hydrothermal (e.g., $NaTaO_3$ nanocrystalline)
- One-pot method (e.g., ZnO–SiO_2 composite)
- Vapor decomposition e.g., Zn_2SiO_4/Si nanoporous pillar array (Si-NPA))
- Nano-casting route (e.g., Mesoporous $LaFeO_3$)
- Radical copolymerization (e.g., silicone-containing polyelectrolyte (Si-PE))
- In situ photo-polymerization (e.g., TiO_2 nanoparticles/polypyrrole)
- Dip-coating (e.g., $TiO_2$and polystyrene sulfonic sodium (NaPSS))
- Thermal dispersion (e.g., K_2CO_3-SBA-15 composites)
- Wire electrical explosion (WEE) (e.g., KCl-doped Cu–Zn/CuO–ZnO nanoparticles)
- Liquid-phase method (LPD) (e.g., Li-doped iron oxide thin films)
- Thermal decomposition (e.g., TiO_2 Nanofibers)
- Chemical polymerization (e.g., polypyrrole composite film quaternized with 1,4 bromobutane)
- Liquid-state doping (e.g., $LiZnVO_4$-doped SnO_2)
- Chemical solution (e.g., $Bi_{0.5}K_{0.5}TiO_3$(BKT))
- Electro-spinning and calcination (e.g., KCl-doped ZnO nanofibers)
- Doctor Blade (e.g., Bi_2MO_6(M=W, Mo) oxide)
- Energy activation (e.g., Nanocrystalline WO_3/TiO_2-based powder)
- Polymeric precursor (e.g., WO_3/TiO_2 nanopowder)
- Radio-frequency sputtering (e.g., ZnO and In_2O_3 thin films on SiO_2/Si substrates)
- Co-precipitation approach (e.g., Porous $ZnAl_2O_4$ spinel nanorods)

Miniaturization

- Capacitive
  1. Gold–polyvinyl alcohol core–shell nanocomposites
  2. ZnO nanorods humidity sensor
  3. ZnO/Si nanoporous pillar array (Si-NPA)
- Resistive
  1. CA-NH_4BF_4-PEG600 based sensor
  2. Multiwall carbon nanotube/ polyimide films
- Gravimetric
  1. Polyvinyl-difluorene (PVDF)
- Hygrometric
  1. Silicon/polysilicon and polymide
- Optical
  1. porous silica xerogel film
  2. Polyvinyl alcohol coated photonic crystal optical fiber
  3. Mercaptopropionic acid capped CdTe nanocrystals on porous silicon

(b) Humidity sensor based on materials & principles

Materials

- Carbon (e.g., Amorphous carbon film/n-Si)
- Vanadium (e.g., NH_4VO_3 + oxalic acid)
- Iron (e.g., Li doped γ-Fe_2O_3)
- Silicon (e.g., Li/Fe/K^+-doped mesoporous silica SBA-15)
- Polymer (e.g., Silicone + polyelectrolyte (Si-PE))
- Tin (e.g., KCl-doped SnO_2nanofibers)
- Titanium (e.g., KCl-doped TiO_2 nano fibers)
- Zinc (e.g., LiCl-doped ZnO)
- Sodium (e.g., $NaTaO_3$ nanocrystalline)
- Zirconia (e.g., Y^{3+} -doped and Mg^{2+}-doped zirconia)

Principles

- Resistance variation with temperature/frequency (e.g., K_2CO_3 doped $LaCo_{0.3}Fe_{0.7}O_3$)
- Resistance variation with Relative humidity (e.g., Li^+/K^+/Mg^{2+}-doped iron oxide)
- Capacitance variation with frequency/ temperature (e.g., $BaTiO_3$nanofiber)
- Evanescent wave monitoring (e.g., $CoCl_2$doped Polyvinyl alcohol (PVA) filM)
- Absorption measurements (e.g., Polyvinyl alcohol (PVA)/SiO_2/$CoCl_2$)
- Interferometric approach (e.g., SiO_2–[PDDA + /poly silicon(PS)-119]-air cavity)
- Intensity variation with refractive index (e.g., Polyvinyl alcohol (PVA) film)
- Strain induced Bragg wavelength measurement (e.g., Polyimide(PI) based)
- LPG (Long Period Gratings) resonance band wavelength shift measurement (e.g., SiO_2nano-sphere film)

Figure 2.1: Humidity sensors based on (a) synthesis method and miniaturization, (b) Humidity sensors based on materials and principle.

2.2.2 Miniaturized Humidity Sensor

For many sophisticated applications, the size of the sensors has keenly been tried to reduce using most advanced technologies called miniaturization. Miniaturized humidity

25

sensors depend on mainly five different transduction principles such as hygrometric, capacitive, resistive, gravimetric, optical, and mechano-optoelectronic.

2.2.2.1 Hygrometric Sensor

Hygrometric sensor that has been using in old device since many decades for the measurements of humidity of air is converted into devices to develop mechanical energy (Gerlach & Sager, 1994; Sager *et al.*, 1994), and it is classified into four basic types such as (a) mechanical, (b) dry bulb - wet bulb, (c) chilled mirror, and (d) lithium chloride (LiCl) dew point.

Generally, hygrometric sensor consists of two different materials, such as polysilicon membrane and hygroscopic material, e.g., polyimide with different thermal expansions coefficients. The polyimide as a hygroscopic coating expands owing to the absorption of water. Due to the unequal expansion occurred between the polyimide and polysilicon, a change in bending structure of the membranes is observed. The change in bending is converted into electrical signal via piezoresistor.

2.2.2.2 Gravimetric Sensor

The quartz crystal microbalance (QCM) (Pascal-Delannoy *et al.*, 2000) is the main source of inspiration for gravimetric sensor. This sensor consists of a piezoelectric quartz plate, which is coated with hygroscopic material having resonance frequency in the range of MHz, and it measures humidity due to the change of frequency. The change in frequency (Δf) can be calculated by Sauerbrey Equation 2.2 (Pramanik *et al.*, 2013)

$$\Delta f = -2\frac{1}{A}\frac{f_0^2}{\sqrt{\mu\rho}}\Delta m \tag{2.2}$$

where, *A* represents the area of surface, μ is the shear modulus, f_o is the nominal frequency, ρ is the density, and Δm is the mass change due to absorption of moisture.

2.2.2.3 Resistive Sensor

The most common resistive sensors are based on electrical resistance. The electrical resistance of a material resists the mobility of electric current through it. Since the humidity can change the electrical resistance or impedance of a material noticeably, the resistive humidity sensors have been developed using the principle of change in electrical resistance or impedance. Generally, the all resistive sensors have mainly four layers such as (a) substrate, (b) interdigital electrode, (c) humidity sensitive film and (d) protective layer. In resistive or impedance humidity sensors, humidity in air changes with the variation of resistance and follows the Equation 2.3 (Rittersma, 2002).

$$\log\left(\frac{R(r_h)}{R_0}\right) = \frac{\log a - \log r_h^n}{1 + b/r_h^n} \tag{2.3}$$

where, $R(r_h)$ represents the resistance at relative humidity (RH) at a specific humid condition r_h, R_0 is the resistance at zero humidity, and *a* and *b* are the constants.

The sensing response (S_R) can be measured using an expression given in Equation 2.4 (Chu *et al.*, 2013).

$$S_R = \frac{R_h - R_0}{R_0} \times 100 \ \% \tag{2.4}$$

where, R_h refers to the resistance at certain RH and R_0 represents the original resistance of the sensors at air of 3 %RH.

2.2.2.4 Capacitive Sensor

Capacitance of a sensor indicates its ability to store an electrical charge. Capacitance value can be altered significantly with the variation of humidity. Using this principle,

the capacitive type humidity sensors have been developed. Fundamentally, the capacitive type humidity sensors are function of dielectric changes of thin films due to the absorption of water vapor. Its characteristics mainly depend on hygroscopic nature of the material and the geometry of the electrode. In this regards, capacitance (C) of all the parallel plate capacitive sensors follow a relation given in the Equation 2.5.

$$C = \frac{\varepsilon A}{d} \tag{2.5}$$

Where, ε is the dielectric permittivity, A is the overlapping area, and d is the distance between two parallel plates. The sensitivity (S_c) of this capacitive humidity sensor is evaluated using the Equation 2.6 with a certain range of humidity.

$$S_c = \frac{maximum\ capacitance}{minimum\ capacitance} - 1 \tag{2.6}$$

There are some other types of sensors have also been investigating with the principle of optical (Estella *et al.*, 2010) and mechano-optical (Hassan *et al.*, 2000) properties of the materials, as reported in the previous study (Tripathy *et al.*, 2014).

2.2.3   Different Key Sensing Characteristics of Humidity Sensor Materials

Plenty of sensing materials have been developed in last five decades for different types of humidity sensor in the wide fields of applications. The most common commercial sensors are mostly based on metal oxides, porous silicon and polymers (Chu *et al.*, 2013). In a humidity sensor, fundamentally, the humidity signals obtained via two-electrode techniques are affected by polarization effect. This is happened owing to the migration of electrons from the metal probe into the conductive specimen. Polarization effect may be caused by the migration of the H^+ ions into the metallic probe as the H^+ ions are found in the physisorbed absorbed water (Chu *et al.*, 2013; Pokhrel & Nagaraja, 2003). Thus, positive charges in the specimen migrate towards the

28

metallic probe and create a cation layer between the metallic probe and the specimen. In this context, plenty of structures of electrodes have been proposed for various sensing systems. Hence, this literature study has mainly focused on the key sensing materials and their typical characteristic properties for the humidity sensor applications.

Due to addition of different coatings or dopants in a base material, its physical, chemical, electrical as well as structural characteristics are changed and these characteristics are also changed with different base materials. In this section, different electrical characteristics (i.e., impedance or resistance, capacitance, response and recovery time, hysteresis, and stability with the variation of relative humidity, frequency, and temperature) of various sensor materials based on carbon, vanadium, iron, silicon, polymer, tin, titanium, zinc, zirconia and sodium are compared. Both similarity and dissimilarity in the electrical characteristics for different sensor materials are observed. They strongly vary with doping concentration of different materials, film thickness of the substrate and the morphological changes. Some important methods and humidity dependent electrical response (response time, recovery time, and hysteresis) of various materials are illustrated in Tables 2.1-2.4.

Table 2.1: Response time, recovery time, and hysteresis of different silicon based humidity sensor materials.

Materials	Condition/Doping Concentration	Response Time (s)	Recovery Time (s)	Hysteresis (%RH)	Ref.
Silica aerogel	coating viscosity of 15 cp	41	55	3.3	(Wang C.-T. *et al.*, 2005)
Li-SBA-15 (0.1Li$^+$)	weight ratio of LiCl to SBA-15 = 0.10	21	51	6	(Geng *et al.*, 2007)
SBA-16/Li$^+$	10 wt% Li	25	120	4	(Tu *et al.*, 2009)
K$_2$CO$_3$-SBA-15	weight ratio of K$_2$CO$_3$ to SBA-15 = 0.8	15	50	-	(Yuan *et al.*, 2009)
K-SBA-15	weight ratio of KCl to SBA-15 =0.5	10	<25	3	(Zhang *et al.*, 2012)
ZnO–SiO$_2$	molar ratio of ZnO to SiO$_2$ =1	50	100	2	(Yuan *et al.*, 2010)
nw-SiC/Si-NPA	-	105	85	4.5	(Wang *et al.*, 2012)
Zn$_2$SiO$_4$/Si-NPA	-	25	15	1.99	(Wang W. C. *et al.*, 2013)
Li-SBA-15 (0.15Li$^+$)	weight ratio of LiCl to SBA-15 = 0.15	60	180	3	(Zhang, Wang, *et al.*, 2008)
Fe-SBA-15	weight ratio of Fe(NO$_3$)$_3$ to SBA-15 = 0.5	20	50	-	(Qi, Zhang, Zheng, *et al.*, 2008)

Table 2.2: Different types of tin oxide based humidity sensors and their synthesis methods.

Sensor Material	Method	Response Time (s)	Recovery Time (s)	Ref.
KNO$_3$-doped SnO$_2$–LiZnVO$_4$	Wet chemical and calcination	<80	100	(Hu *et al.*, 2008)
SnO$_2$–LiZnVO$_4$ ceramic	Liquid state	60	100	(Hu & Fu, 2010)
La^{3+}and K$^+$ co-doped Ti$_{0.9}$Sn$_{0.1}$O$_2$ thin films on alumina substrates	Sol-gel	-	-	(Anbia & Fard, 2011)
SnO$_2$ nanoparticles	Microwave irradiation	-	-	(Parthibavarman *et al.*, 2011)
KCl-doped nanoporous Ti$_{0.9}$Sn$_{0.1}$O$_2$ thin films	Sol–gel	11	14	(Anbia & Fard, 2012)
ZnSnO$_3$ cubic crystallites	Hydrothermal	7	6	(Bauskar *et al.*, 2012)

Table 2.3: Different types of titanium oxide based humidity sensors and their synthesis methods.

Sensor Material	Method	Respone Time (s)	Recovey Time (s)	Hysteresis (%)	Ref.
$CdTiO_3$ nanofibers	Electrospinning	4	6	≈ 7	(Imran *et al.*, 2013)
$Bi_{0.5}(Na_{0.85}K_{0.15})_{0.5}Ti_{0.97}Zr_{0.03}O_3$ (BNKTZ)	Metal–organic decomposition	18	60	4	(Wang *et al.*, 2014)
$Bi_{0.5}K_{0.5}TiO_3$ (BKT) powder	Chemical solution method	12	25	3	(Zhang *et al.*, 2010)
Barium titanate ($BaTiO_3$) nanofiber	Electro-spinning and calcination	<5	<4	5	(He *et al.*, 2010)
$Bi_{0.5}Na_{0.5}TiO_3$–$Bi_{0.5}K_{0.5}TiO_3$ (BNT–BKT) powder	Metal-organic decomposition	20	60	4	(Zhang *et al.*, 2011)

Table 2.4: Different types of zinc oxide based humidity sensors and their synthesis methods.
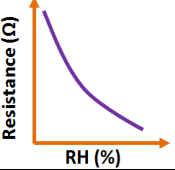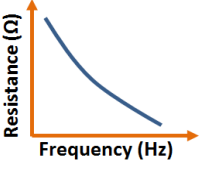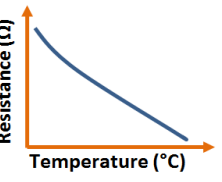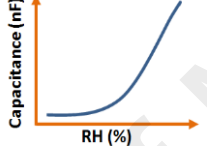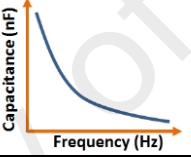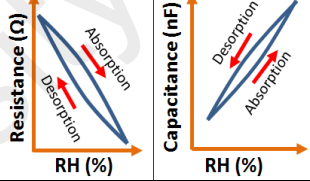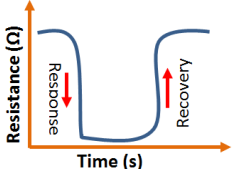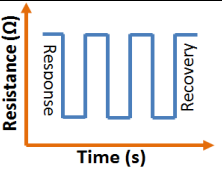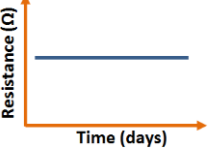
Sensor Material	Method	Response Time (s)	Recovery Time (s)	Hysteresis (%)	Ref.
KCl-doped ZnO nanofibers	Electrospinning	2	1	-	(Qi, Zhang, Wang, *et al.*, 2009)
Nanocrystalline zinc tungstate ($ZnWO_4$) (nanoparticles, nanorods)	Precipitation or hydrothermal	3	50	5.5	(You *et al.*, 2012)
KCl-doped Cu–Zn/CuO–ZnO(KCZ/CZN) nanoparticles	Wire electrical explosion (WEE)	40	50	4	(Qi, Zhang, Zeng, *et al.*, 2009)
High pure ZnO colloidal nanocrystal clusters (CNCs)	Modified hydrolyzation	110	80	-	(Si *et al.*, 2010)
Mn-doped ZnO nanopowders	Sol-gel	6	20	4.36 (for 6 At %Mn doping)	(Peng *et al.*, 2012)

2.2.4   Concluding Remarks

Humidity sensors based on various materials for relative humidity have been reviewed extensively, on different types of materials, including carbon, vanadium, iron, silicon, polymer, tin, titanium, zinc, zirconia, and sodium. The electrical properties of humidity sensors such as resistance, capacitance, effects of temperature, frequency and relative humidity, sensitivity, response time, hysteresis and stability have been compared in details for various materials. For different sensor materials, the electrical properties are significantly changed with doping concentration of different materials, film thickness of the substrate and the morphological changes. Basic principle of six different type humidity sensors and their typical advantages as well as disadvantages are discussed in the miniaturization section. Based on the overall review, the general electrical responses such as resistance, capacitance, hysteresis, response and recovery times, stability and their best characteristics feature for different materials with respect to relative humidity, frequency and temperature are depicted in Table 2.5. From the above analysis, it has been observed that the different doping materials of humidity sensor such as carbon, vanadium, iron, silicon, polymer, tin, titanium, zinc, zirconia and sodium shows their best linearity at the optimized frequency of 1 kHz, 100 Hz, 100 Hz, 100 Hz, 1 kHz, 100 Hz, 100 Hz, 100 Hz,100 Hz, and 1 kHz, respectively.

Hysteresis is one of the most important parameter for all sensors. For practical application, a sensor must have minimum hysteresis value. In this review article, the best hysteresis value for different doping materials of humidity sensor such as carbon, vanadium, iron, silicon, polymer, tin, titanium, zinc, zirconia, and sodium is 3.57, < 3, 4, 1.99, 1, 3, 3, 1.9, 3, and 1%, respectively. The hysteresis for vanadium oxide based sensors also show lower compared to carbon based materials. The response and recovery times are also an important parameter for all humidity sensors.

Table 2.5: The general electrical response and their best characteristics remark for different materials.

Parameter	Characteristic	Remark for Best Response
Resistance, Relative humidity(RH)		Resistance should decrease with RH
Resistance, Frequency		For best response resistance should decreases with frequency
Resistance, Temperature		For best response resistance should decreases with temperature
Capacitance, Relative humidity(RH)		For best response capacitance should increases with RH
Capacitance, Frequency		For best response capacitance should decreases with frequency
Hysteresis		For best response hysteresis loop should be as narrow as possible.
Response and recovery time		For best response recovery and response time should be as minimum as possible, so that the sensor will give fast response
Repeatability		For best response the same response should repeat with time
Stability		For best stability resistance fluctuation should be minimum with time

The response and recovery times of different doped humidity sensors have been critically reviewed in this present section. The best response time of carbon, vanadium, iron, silicon, polymer, tin, titanium, zinc, zirconia and sodium doped sensor materials is 16, 13, 32, 10, < 2, 5, 3, 2, 5 and 3 s, respectively and best recovery time of these sensor materials is 8, 5, 36, 15, 20, 6, 3, 1, 5 and 32 s, respectively.

2.3 Nanomaterials and Hydrogel for Infection Control and Healing of Acute and Chronic Wounds

Wound healing is one of the complex biological processes. It needs proper care to prevent the chronic wounds. Several ceramic nanocomposite based hydrogels have been tried to get a satisfactory wound healing performance, however, selection of material is still a big challenge to the researchers in order to develop a suitable nanocomposite based hydrogels for wound healing applications. Therefore, in this section, the basic idea of wound healing process and various types of nanocomposite based hydrogels have been reviewed.

2.3.1 Introduction

Wound is defined as a physical damage in the integrity and functional structure of skin. The skin provides a primary defense barrier against any external agent. When wound destroys the skin, the dynamic functionality reduces, disability increases, and finally, the patient dies (Kumar *et al.*, 2007). Wounds normally go through various processes, such as bleeding, vessels shrinkage, coagulation, complement system activation, and inflammation (Robson *et al.*, 2001).

Chronic wound refers to a wound that does not heal in a predictable amount of time, which includes diabetic ulcers, pressure ulcers, and vascular ulcers. There are several risk factors of chronic wounds, such as peripheral arterial diseases, peripheral

34

neuropathy, age, diabetes, and immunocompromised status. Diabetic wound is also one of the major risk indicators for chronic patients (Singh *et al.*, 2005). The severe unhealed diabetic foot ulcer may cause limb amputation due to infection. In fact, it had been found that 2.1−13.7 per 1000 diabetic patients suffered from limb amputation (Singh *et al.*, 2005) and this rate increased to 80% in the last five years (Rayber, 2001). Therefore, many researchers have attempted to develop better and more efficient therapeutic techniques to control the infection and also to achieve faster healing of chronic wounds.

Furthermore, recent researches have shown that nanomaterials do play an important role in controlling wound infection and help to heal faster (Ghobril & Grinstaff, 2015). Besides, nanomaterials, specifically polymers (both synthetic and natural polymers), can function as therapeutic agents for faster regeneration of damaged epidermal and dermal tissues. All the polymeric biomaterials have numerous advantages, such as high water content, biocompatibility, and biodegradable nature. All these salient features of polymers help them to mimic a few physiological characteristics of native tissues. Some of the most popular, natural, and synthetic polymers used in wound healing are illustrated in Figure 2.2.

```
                              Polymers

              Natural              ↓         Synthetic


    Polysaccharides (chitosan,          poly(glycolic acid) (PGA),
    chitin, dextran, alginates,      poly-D,Llactide-co-glycolide (PLGA),
   chondroitin, and heparin),           poly(vinyl alcohol) (PVA),
         proteoglycans,                  poly(lactic acid) (PLA),
   proteins (collagen, gelatin,          poly(acrylic acid) (PAA),
    fibrin, silk fibroin, and           poly(εcaprolactone) (PCL),
            keratin)                 poly(ethylene glycol) (PEG), and
                                     poly(vinylpyrrolidone) (PVP)
```

Figure 2.2: Classification of natural and synthetic polymers (Chattopadhyay & Raines, 2014; Hu M. S. et al., 2014; Jayakumar et al., 2011; Moura et al., 2013).

Though these biopolymers have been used prominently in various wound healing applications, they have yet to achieve the highest priority due to lack of bioactivity and the ability to accelerate the wound healing process. Hence, it is essential to incorporate several nanomaterials within the polymeric matrix. Nanomaterials are really very useful to accelerate the healing process due to their sustained and controlled release of therapeutics actions.

In addition, there are various types of nanomaterials, including polymeric, metallic, and ceramic materials, which have been looked into for wound healing applications (Kalashnikova *et al.*, 2015; Rieger *et al.*, 2013). These nanomaterials are available in various forms, such as nanoparticles, nanofibers, nanocomposites, and nano-hydrogels (Whitmire *et al.*, 2012). These nanomaterials are used for various purposes, such as tissue adhesives, hemostats, antimicrobial agents, and drug, therapeutics or cell delivery agents. Normally, most of the nanomaterials are used externally to minimize the perceived risks associated with internal use (Steed *et al.*, 2006). Moreover, the exposure

of NPs is more localized and controlled in external wounds in comparison to systemic administration (Jain *et al.*, 2009). Due to the easy accessibility of the target area, any undesirable effects of nanomaterials can be easily detected and controlled. Since the whole system is done externally, it allows applying proper treatments for faster wound healing and aesthetic remodeling.

2.3.2 Acute and Chronic Wound Healing Processes

Wound healing is a complex and systematic process that starts just after injury. During the healing process, various growth factors and cytokines are released by sequential phases: (a) hemostasis and tissue inflammation, (b) cellular proliferation and new tissue formation, and (c) tissue remodeling to coordinate and to accelerate wound healing process (Figure 2.3). Although the wound healing is a continuous process, each phase of wound healing is distinct and also overlaps the next.
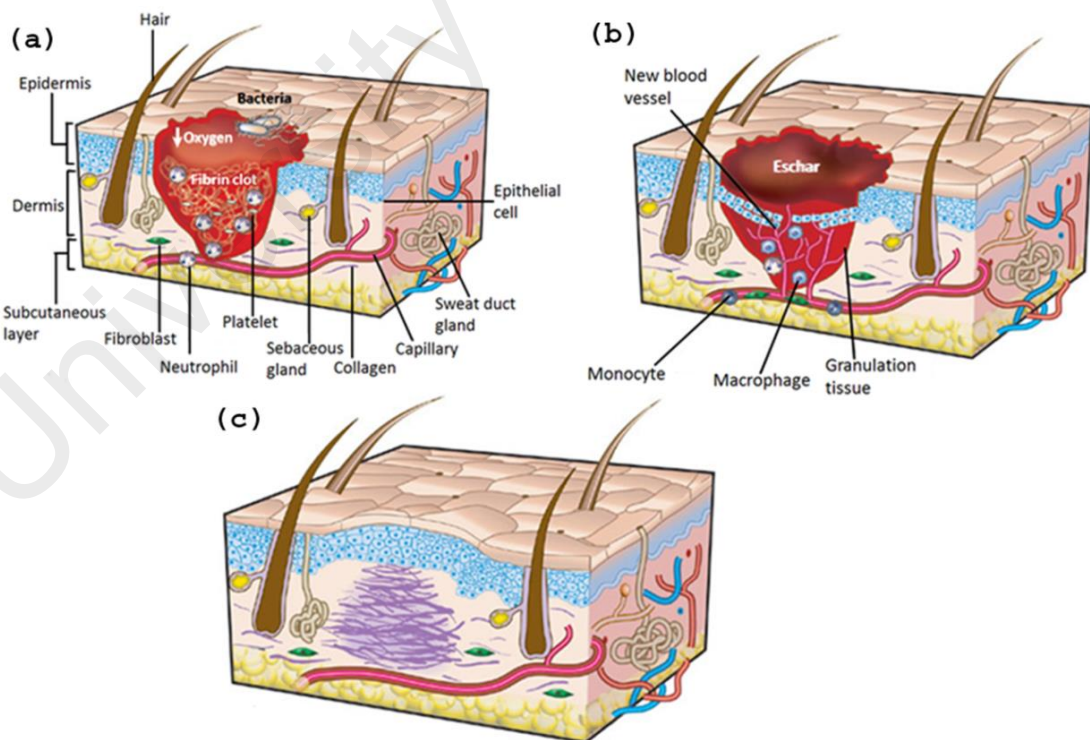
Figure 2.3: Various stages of wound repair (adapted with permission from (Gurtner *et al.*, 2008)).

During injury, blood vessels are damaged and result in bleeding. Just after bleeding, the first protective step is hemostasis. The hemostat is achieved though vascular constriction, platelet aggregation, and coagulation. In this process, the fibrin clots to perform the following three major tasks involved in wound healing: (a) plug the broken blood capillaries to stop bleeding, (b) limit pathogen entry into the bloodstream, and (c) act as a provisional extracellular matrix (ECM) for migration and proliferation of the cells. In the meantime, the platelets off-load growth factors, such as transforming growth factors (TGFs), platelet-derived growth factors (PDGFs), fibroblast growth factors (FGFs), vascular endothelium growth factors (VEGFs), and epidermal growth factors (EGFs), are activated. The abovementioned growth factors initiate the process of inflammations by attracting pro-inflammatory neutrophils, monocytes, and lymphocyte (Singer & Dagum, 2008). This inflammation stage lasts until about 48 h after injury. Besides, the first cleanup step of the wound bed is done by neutrophils by isolating invading microbes and dead cells of the host tissues (Simpson & Ross, 1972). Monocytes help to secrete cytokines, which mount strong secondary inflammatory responses by introducing extra pro-inflammatory cells. Ultimately, the induction of apoptosis of inflammatory cells and the cleaning up of the dead cells by the macrophages help to reduce inflammation and finally, initiate cell proliferation.

After the inflammatory stage, the proliferation phase starts. This stage occurs about 2–10 days after injury. In this phase, new tissues are formed and the type III collagens are secreted by the fibroblasts to replace the damaged ECM. The secretion of type III collagen also helps the proliferation of endothelial cells on the ECM. Due to the proliferation of endothelial cells, new blood vessels (angiogenesis) are formed, which help to supply of oxygen, nutrients, and growth factors to accelerate tissue-growth. As a result, the damage tissues of the wound are filled with granulation tissue by forming a new connective tissue layer and blood vessels. At the final stage of proliferation, the

fibroblasts generate traction forces that help to reduce the wound area gradually (Ehrlich & Rajaratnam, 1990).

Remodeling is the final and the longest phase in wound healing process. This stage lasts for a year or longer. In this phase, the TGF-β and cytokines are released from the platelets and the activated macrophages induce the fibroblasts to differentiate the contracting myofibroblasts. Extensive remodeling is not needed for minor superficial injuries. In minor injuries, the wound can be healed by producing a minimum amount of ECM and without scarring by keratinocyte regeneration. However, extensive remodeling is needed for major injuries and it undergoes over a long period. In the extensive remodeling, the wound contraction rate is approximately 10−20 μm/day and during this time, the production of ECM is too high (Tomasek *et al.*, 2002). The granulation tissue cells go through apoptosis process and due to the formation of scar tissue, the cell-rich granulation tissue is generated (Desmouliere *et al.*, 1995). In this stage, striated scar tissues that consist of collagen fibers and myofibroblasts are formed. As a result, the density of the blood vessels in the granulation tissue is reduced and due to the reduction of blood flow, the wound becomes pale in color (Mehendale & Martin, 2001). At the end of this stage, a skin is developed over the scar tissue and the strength of this skin increases gradually up to a maximum of 80% of strength of the native tissue (Witte & Barbul, 1997).

Since the chronic wound healing is a process that takes up a long time, an excessive amount of neutrophil, pro-inflammatory cytokines, reactive oxygen species, and wound proteases are gathered at the inflammation phase within this time span. Excessive gathering of wound proteases creates obstacle for the formation of ECM proteins (Wlaschek *et al.*, 1997). In chronic wounds, nonetheless, the survival and proliferation of progenitor cells are also often affected (Albiero *et al.*, 2011).

Hence, in order to improve the healing of chronic wounds among diabetic patients, the topical application was first time approved by FDA in 1998 (Wieman, 1998). A huge number of wound managements have been introduced for chronic wounds so far. However, only 59% of diabetic human foot ulcers were healed without amputation. Therefore, still it is a challenging job for fellow researchers to develop a more practical, safe, and effective technique for non-healing chronic wounds.

2.3.3 Ceramic-Based Nanomaterials Used in Wound Healing

In this section, various types of ceramic NPs are highlighted for infection control and wound healing. The high surface area-to-volume ratio and the charged surfaces of ceramic NPs make them more popular in the controlled delivery of wound healing applications. Some ceramic nanomaterials, including silica, silicate clays, bioglass, zinc oxide, and titanium oxide NPs, are semicrystalline in nature. Hence, the ionic dissolution products of all these nanomaterials also has shown a positive influence on angiogenesis and wound healing.

2.3.3.1 Silica Nanoparticles

Silica (SiO_2) NPs are mesoporous in nature. Due to this structure, it accelerates growth factors (e.g., bFGF) to the wound healing process. In this context, Zhang et al., (2009) used an *in situ* water-in-oil microemulsion method using mesoporous silica nanoparticles (MSNs) to encapsulate the bFGF via *in situ* process (Zhang *et al.*, 2009). The loading efficiency of bFGF in MSNs was 72%, and the release kinetics was 50% up to 8 days and approximately 75% on day 15. The *in situ* encapsulated bFGF-loaded MSNs nanoparticles entered into the endothelial cells of the human umbilical vein and

remained in the cytoplasm. The bFGF-loaded MSNs NPs interacted with the cells and accelerated the cell proliferation, indicating that NPs are indeed a potential for wound healing applications (Zhang *et al.*, 2009). In another study, the SiO_2 NPs were used to release nitric oxide (NO) for accelerating the wound healing process. Sol-gel technique was used to synthesize the SiO_2 NPs with a secondary amine functional group from tetraethoxysilane or tetramethoxysilane (Shin *et al.*, 2007). By exposing SiO_2 NPs of secondary amino groups at the elevated pressures of NO gas for 3 days, it was converted into NO-releasing N-diazeniumdiolate groups. These SiO_2 NPs were able to release NO at the contact with water. The variation of the structure, the concentration of silane precursors, and the reaction parameters helped to obtain the NPs, which controlled the quantity and the duration of NO release. The incorporation of NO-releasing silicate NPs with electrospun polyurethane fibers was also found to control the release of NO (Koh *et al.*, 2013). In a further study, NO-releasing nanocomposites were also obtained by using poly(ethylene glycol) (PEG) and chitosan using the sol−gel technique (Friedman *et al.*, 2008). The NO-releasing SiO_2 NPs were also obtained by heating the PEG-chitosan nanocomposites. When the PEG-chitosan nanocomposites came in contact with water molecule, the trapped NO was released. NO-releasing SiO_2 NPs are the most suitable material in wound healing due to their tendency to increase the fibroblast proliferation and migration *in vitro* by accelerating the collagen deposition and angiogenesis in the wound area. Besides, it was observed that when the wounds were treated with NO-releasing SiO_2 NPs, the wound healing was completed within 12 days.

2.3.3.2   Synthetic Silicate Clay

Synthetic silicate clays are ultrafine NPs with ingredients of silicates, sodium, magnesium, and lithium (Carrow & Gaharwar, 2015;Chimene *et al.*, 2015; Kerativitayanan *et al.*, 2015). These clays are considered as a potential biomaterial in

41

numerous fields of biomedical applications, including bone tissue engineering, wound healing, regenerative medicine, and therapeutic delivery. Aluminosilicate clay, such as montmorillonite (MMT), has excellent blood-clotting ability. Due to this feature of MMT, the MMT-Epidermal growth factor (EGF) nanocomposite was evaluated for epithelial wound healing applications (Vaiana *et al.*, 2011). In the MMT-EGF nanocomposite, the EGF played a vital role in cell proliferation and migration during the wound healing process. Moreover, an addition of 0.3% of EGF in MMT generated sufficient amount of Na^+ ions to carry out the cationic activation required for blood-clotting. The MMT-EGF nanocomposite was implemented on the human skin. The result showed that the keratinocyte cell line (HaCaT) spontaneously transformed with MMT-EGF nanocomposite to activate the Epidermal growth factor receptor (EGFR) at the cell membrane, which accelerated cell growth and migration. On the other hand, in the gene expression study of VEGF and thrombospondin, the normal proliferation was found to be activated by MMT-EGF and migrating signals in HaCaT cells. Meanwhile, from the *in vitro* study of wound scratch assays, cell migration was found to be accelerated by the MMT-EGF treatment and the wound area was healed completely (Vaiana *et al.*, 2011).

2.3.3.3 Bioglass Nanoparticles

Bioglass NPs have been used in biomedical fields, tissue engineering, angiogenesis, and wound healing applications (Colilla *et al.*, 2014;Erol-Taygun *et al.*, 2013; Izquierdo-Barba *et al.*, 2016). Ionic dissolution products of bioglass are mainly responsible to accelerate cell proliferation, angiogenesis, and wound healing. The interaction mechanism between the dissolved ion and human cells, nevertheless, has yet to be confirmed. Recent literature review predicts that the bioactive glass NPs can be bound to soft tissue through apatite layers that may form on their surface upon contact

42

with cells (Day, 2005; Leu & Leach, 2008). The bioactive glass NPs accelerated the secretion of angiogenic growth factors from human stromal cells and facilitated angiogenesis (Day, 2005). Furthermore, the 45S5 bioglass (45% SiO_2, 24.5% Na_2O, 24.5% CaO, and 6% P_2O_5) particles had been proven as a potential material to stimulate angiogenesis *in vitro* and *in vivo* through their dissolution products (Day, 2005; Leu & Leach, 2008). Moreover, better bioactivity and biocompatibility property had been observed in sol−gel derived bioactive glass particles than the melt-derived bioglass particles (Chen X. *et al.*, 2009). On top of that, due to the potentiality for stimulating the angiogenic growth in cultured human umbilical vein endothelial cells (HUVECs), bioglass NPs had displayed a great impact in the modern research (Chen X. *et al.*, 2009). Increased expression of pro-angiogenic genes was also observed due to the interaction of HUVECs and bioglass nanoparticles. The bioglass NPs accelerated noticeably cell proliferation, angiogenic tube formation, and wound healing process (Chen X. *et al.*, 2009).

2.3.3.4 Zinc Oxide Nanoparticles

The zinc oxide (ZnO) NPs also exhibited good antimicrobial activities. Nevertheless, the efficiency of ZnO NP significantly depended on the particle size and the release of free Zn^{2+} ions from colloidal solution of ZnO (Raghupathi *et al.*, 2011). The wound healing and angiogenesis assays showed that the ZnO acted very effectively in wound healing by inducing angiogenesis and chemotaxis of cells (Barui *et al.*, 2012). Besides, ZnO/chitosan/chitin-based wound dressing bandages showed better blood clotting ability, better wound healing, and antibacterial characteristics than the chitosan or chitin-based wound dressing bandages (Sudheesh Kumar *et al.*, 2012). The ZnO NPs also enhanced fibroblast cell proliferation, which had been confirmed by its wound healing ability (Augustine *et al.*, 2014).

2.3.3.5 Titanium Oxide Nanoparticles

The recent development in nanotechnology has motivated many researchers to develop highly antibacterial nanomaterials, such as TiO_2, ZnO, and Ag (Allahverdiyev et al., 2011; Huang et al., 2008). Among the various nanomaterials, TiO_2 has occupied a unique place due to its photocatalytic, biocompatible, and nontoxic properties. Due to its photo catalytic property, it is capable enough to kill cancer cells, bacteria, and viruses under mild ultraviolet (UV) illumination (Yu et al., 2011). Nowadays, TiO_2 nanomaterials have become more popular in the field of wound healing. For instance, Wu et al., developed a TiO_2/poly(lactic-co-glycolic acid) (TiO_2/PLGA) biocompatible composite for wound dressing applications (Wu et al., 2014). To analyze its *in vitro* wound healing ability, the fibroblasts (L929s), the bovine carotid artery endothelial cells (BECs), and the human keratinocytes (HaCaTs) were seeded on the TiO_2/PLGA composite biofilms. Moreover, in order to analyze the biocompatibility of the biofilm *in vivo*, a histological study on rat was performed. They discovered that 10% TiO_2 in TiO_2/PLGA composite biofilm had effective antibacterial property. In further study, TiO_2 NPs-based *Moringa oleifera* leaves composite was synthesized for wound healing activity.

2.3.4 Hydrogel

Hydrogel is a three-dimensional (3D) hydrophilic polymeric network-structured material. It can absorb large amounts of water or biological fluid without dissolution due to the presence of chemical crosslinks or physical crosslinks (Peppas & Merrill, 1976; Risbud et al., 2000). In addition, hydrogel can absorb excess wound exudates to protect the wound from secondary infection and to promote effectively the healing

process by providing a moisturized wound healing environment (Winter, 1962). Moreover, hydrogels are often used as drug delivery systems because of their ability to swell and to release the trapped particles into the surrounding medium (Qiu & Park, 2001). An ideal wound dressing should absorb body fluids effectively, and should have painless removal, high elasticity, good adhesion, and easy replacement, besides forming a barrier against bacteria (Ajji *et al.*, 2005; Rosiak, 1994). In fact, many commercially available synthetic polymers, such as polyvinyl alcohol (PVA), have shown good physicochemical and mechanical properties compared to biological tissues (Hassan *et al.*, 2000; Li *et al.*, 2004; Seabra & de Oliveira, 2004). These PVA-based hydrogels have received great attention in both biomedical and biochemical applications due to their permeability, biocompatibility, and biodegradability (Matsuyama *et al.*, 1997; Mühlebach *et al.*, 1997). Therefore, PVA hydrogels have been developed to repair wounds and for promotion of wound healing (Burczak *et al.*, 1994). Glycerin is a type of sweet, colorless, transparent, and odorless syrupy liquid. It is a humectant, i.e., "draws moisture". It is used in creams, lotions, facial treatments, masks, and other body care products. However, most hydrogels are fragile and rigid in nature. These are the main drawbacks for most of the existing polymeric hydrogels.

2.3.5   Wound Dressings based on PVA/Composite Polymers

Due to the fragileness and rigidness of polymeric hydrogels, they are not suitable to be transformed into non-spherical polymer forms, such as filamentous via gel state, films, and membranes. Nonetheless, various techniques have been tested to solve the abovementioned problems so far. This problem would potentially be overcome with PVA-based hydrogel blended with high strength compatible ceramics or with flexible

45

composites e.g., certain synthetic polymers or nano-fillers (e.g. clays, minerals or calcium phosphate nanoparticles).

2.3.5.1   PVA/Cellulose Acetate/Gelatin/Ag Composite Hydrogels

In a study, El-Mohdy et al., had synthesized PVA/cellulose acetate/gelatin and silver (Ag) NPs-based composite hydrogels using gamma radiation to get better crosslinking via novel *in situ* technique for wound dressing application (El-Mohdy, 2013). They observed that Ag NPs obstructed the degree of crystallization in PVA-based gel and provided antimicrobial activity against various bacteria and fungi after using PVA/cellulose acetate/gelatin hydrogels. Their results suggested that the antimicrobial activity was significantly enhanced by increasing the amount of $AgNO_3$ NPs in the composite hydrogel. In another study, the electrospun PVA/chitosan/Ag NPs based fibrous mats had been used for wound healing applications (Li *et al.*, 2013).

2.3.5.2   PVA/Sodium-Montmorillonite (Na-MMT) Nanocomposite Hydrogel

Nanoclays and nanominerals (e.g., sodium-montmorillonite, Na-MMT) based polymer (e.g., PVA) hydrogels have shown excellent and improved properties, such as increased mechanical strength and thermal resistance, as well as decreased gas permeability and flammability, in comparison to their individuals (Kokabi *et al.*, 2007). By using repeated freeze–thawing cycles, the crosslinking was done in PVA/Na-MMT nanocomposite hydrogel. Besides, the PVA/Na-MMT clay nanocomposite hydrogels fulfilled the desired features, such as excellent mechanical, physical, and morphological properties, for ideal wound dressing materials (Kokabi *et al.*, 2007).

2.3.5.3   PVA/Bentonite/Clove Extract/Cellulose/Ag Nanoparticles Hydrogel

On the other hand, Gonzalez et al., adopted the freeze–thawing method to synthesize PVA/Ag nanoparticles, PVA/bentonite, PVA/clove extract, and PVA/cellulose nanocomposite hydrogels. They found that the PVA/clove hydrogels did not exhibit any homogenous aspect, whereas PVA/Ag and PVA/bentonite nanocomposites hydrogels showed very good antimicrobial activity against the growth of *E. Coli*. Due to the addition of clay and Ag NPs as filler in the PVA hydrogel, water vapor transmission rate and water absorbing capacity were enhanced (Gonzalez *et al.*, 2011).

2.3.5.4   PVA/Chitosan/ZnO Nanocomposite Hydrogels

Meanwhile, Vicentini et al. prepared PVA/chitosan/ZnO nanocomposite hydrogels crosslinked by physical blending using PVA and chitosan portions with glycerin and tween-80 (T80) as plasticizers. They concluded that the properties, such as good thermal stability and decreased tensile strength elongation to break the PVA/chitosan film, could be varied by changing the concentration of ZnO nanoparticles and plasticizers (glycerin and T80). Moreover, the porous structure of the PVA/chitosan hydrogel was formed due to the increased concentration of T80. The PVA/chitosan/ZnO nanocomposite hydrogel, nevertheless, exhibited better antibacterial activity against the growth of *S. aureus* than the PVA/chitosan neat hydrogel (Vicentini *et al.*, 2010).

2.3.5.5   PVA/Sodium Alginate (SA) Hydrogel

In addition, Shalumon et al., incorporated ZnO NPs in PVA/sodium alginate (PVA/SA) hydrogel nanofibers via electrospinning technique. Their results suggested that the properties of PVA/SA hydrogel nanofiber could be changed by adding ZnO. They also observed that the low concentration of ZnO in the hydrogel made it nontoxic,

but the high ZnO concentration increased the toxicity property. Furthermore, due to the presence of ZnO NPs in the mat components, the PVA/SA/ZnO hydrogel showed excellent antibacterial activity and formed an inhibition zone against the growth of *E. coli* and *S. aureus* (Shalumon *et al.*, 2011).

Therefore, the toxicity of the composite hydrogels could be optimized by varying or by using optimized ceramic NPs concentration to be used as potential wound dressing applications.

2.4   Summary

This section summarizes the use of various nanocomposites in humidity sensor and wound healing applications. The basic theories and introductory ideas of humidity sensor, type, advantages, and disadvantages have been focused in the sections 2.1 and 2.2. It also covered different types of nanocomposite for humidity sensor application and their humidity sensor responses such as linearity, response and recovery time, hysteresis, and stability. Section 2.3 reviews the nanomaterials and hydrogels for infection control and wound healing applications. More specifically, the section 2.3.2 gives a basic idea of acute and chronic wound healing processes, section 2.3.2 describes numerous ceramic-based nanomaterials for wound healing study, and section 2.3.4 highlights various ceramic nanocomposites and PVA based hydrogels for wound healing applications.

CHAPTER 3: MATERIALS AND METHODS

3.1   Introduction

Currently, the synthesis of ceramic powders has attracted much attention to fulfil the huge demand for the miniaturization of low cost and reduced size modern microelectronic elements, sensors, and energy storage devices with high energy density. Moreover, in the last few decades, most researchers were fascinated about the development of suitable synthesis technique to meet the modern industrial demands. These different fabrication techniques produced different particle morphology, compositional homogeneity, and crystallite sizes; in which as a result, the dielectric and electrical properties of the ceramic composites have been affected greatly. Therefore, a suitable synthesis technique still happens to be an intense area of research for the fabrication of nanocrystalline ceramic composites with suitable features for the miniaturization of electronic devices. These synthesis techniques are mainly classified into two types: mechanical (e.g., solid-state reaction, high-energy ball milling, screening, and elutriation) and chemical (e.g., co-precipitation, sol-gel, hydrothermal, and spray pyrolysis). In the recent researches, both mechanical and chemical routes have been used. Mechanical solid-state reaction, which is also known as mixed oxide method, was only used for cost effective applications, whereas chemical methods were used for more stringent applications. The mixed-oxide method, on the other hand, was used in various large-scale productions of bulk ceramic powders due to its cost effective and flexible nature. However, in the production of fine and pure ceramics, this technique has some drawbacks, for instance, in the mixed-oxide method, normally high temperature was used for chemical processing as excessively high temperature made the particles coarser, and also, high energy was required to turn it into fine powder (Aruna *et al.*, 1998; Johnson *et al.*, 1985). Besides, the solid-state reaction technique was also

used by many researchers (Chandratreya *et al.*, 1981; Haertling & LAND, 1971; Matsuo & Sasaki, 1965). The proper chemical reaction and the product uniformity depended on the geometry of the particle, the homogeneity of the mixture, the sintering steps, and the calcination atmosphere. Moreover, many other non-conventional chemical methods had been implemented to desired purity, homogeneity, particle size, and morphology (Veale, 1972). All the above discussed routes have their own advantages. Due to the numerous advantages of solid-state technique, such as improved porosity, homogeneous mixing, low density, proper grain distribution, and desired morphology; this route had been selected to synthesize the material in the present study.

3.2   Solid-State Reaction Method

The solid-state reaction technique was used for the synthesis of polycrystalline samples of the compounds. In this method, both carbonates and oxides were used. The solid-state reaction adhered to some sequent processes, such as selection of raw material, weighing and mixing, calcination, grinding and pelletization, sintering, as well as electroding, as depicted in Figure 3.1.
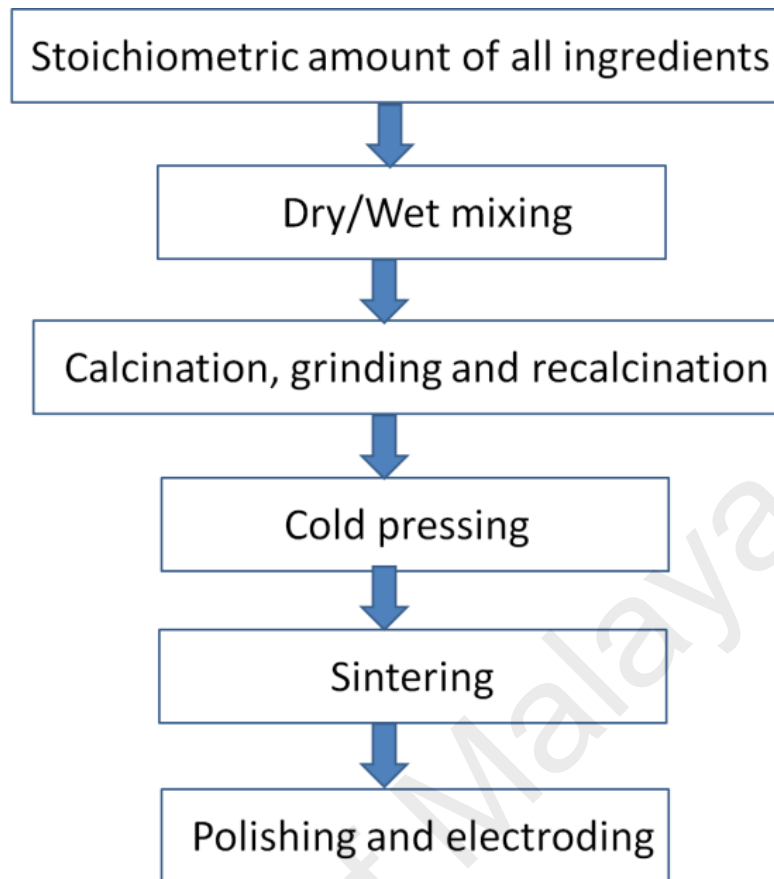
Figure 3.1: A flow charts of ceramic sample preparation using solid-state reaction technique.

3.3   Raw Material used for the Synthesis

The starting raw materials used for the synthesis of Ca-Mg-Ti-Fi-Oxide (CMTFO) based nanocomposite and (CMTFO)/Polydimethylsiloxane (PDMS) nanocomposite based flexible thin film are described in sections 3.3.1-3.3.2.

3.3.1   Raw Material used for CMTFO Electroceramic

All the raw materials used to synthesis of Ca-Mg-Ti-Fi-Oxide (CMTFO) based electroceramic nanocomposites in this study are listed in Table 3.1. All the used chemicals were analytical grade (99.9% pure supplied by Fisher Scientific, Selangor, Malaysia) and used without any further purification.

Table 3.1: Starting chemicals and their manufacturer's name for synthesis of CMTFO electro ceramic.

Material	Manufacturer's Name
Calcium oxide (CaO)	Fisher Scientific Ltd.
Magnesium carbonate ($MgCO_3$)	-do-
Iron oxide (Fe_2O_3)	-do-
Titanium oxide (TiO_2)	-do-
70% absolute alcohol (C_2H_5OH)	-do-

3.3.2   Raw Material used for CMTFO/PDMS Composite Thin Film

All the raw materials used to synthesis of (CMTFO)/Polydimethylsiloxane (PDMS) based nanocomposite thin film in this study are listed in Table 3.2. All the used chemicals were analytical grade (99.9% pure supplied by Fisher Scientific, Selangor, Malaysia) and used without any further purification.

Table 3.2: List of raw materials and the company of the used raw materials.

Material	Manufacturer
CaO	Fisher Scientific Ltd.
$MgCO_3$	-do-
Fe_2O_3	-do-
TiO_2	-do-
70% alcohol	-do-
Polydimethylsiloxane (PDMS)	-do-
Curing agent	-do-

3.4   Synthesis Technique

The synthesis techniques used for the preparation of armalcolite structured CMFTO based perovskite electroceramic nanocomposite as well as flexible thin films of armalcolite, perovskite, and ferrite based electroceramic/PDMS polymer nanocomposite are elaborated in the following sections.

3.4.1 Preparation of CMFTO Electroceramic

The raw ceramic powders such as CaO, MgCO$_3$, Fe$_2$O$_3$ and TiO$_2$ were used to synthesize the electroceramic materials without any further purification. The commercial CaO, MgCO$_3$, Fe$_2$O$_3$ and TiO$_2$ powders with optimized concentration of 11.59, 17.4, 21.9, and 49.11 wt%, respectively were mixed in 75 ml of 70 vol% absolute ethanol. Then Ca-Mg-Fe-Ti-based oxides (CMFTO) mixed solution was mechanically wet-milled by planetary ball-mill (PM200, Retsch) at room temperature for 36 h at a constant speed of 300 rpm speed using alumina ball (diameter: Φ10 mm). The solid sample to balls ratio was 1:200 (w/w). The milled CMTFO powder was dried at 105 °C in a convection oven (OF-11E, Lab Companion) for 6 h. It was then used to make pellets (Φ10 mm × 2.75 mm, diameter × thickness) by cold compaction pressure at 450 MPa for 2-5 min using uniaxial hydraulic press (GS15011, Graseby Specac). The pellets were sintered by solid-state step-sintering at proper selected temperatures such as 450, 650, 850, and 1050 °C for suitable soaking times, as illustrated in Table 3.3, and they are denoted by S450, S650, S850, and S1050, respectively. The material without any heat treatment is denoted by unsintered sample. The flow chart for the sample preparation is depicted in Figure 3.2. The *in situ* solid-state step-sintering was used to control the particle size, pore size, as well as porosity up to a desired range. The probable chemical reactions during mixing at 25 °C and sintering above 450 °C or 850 °C are depicted in Reactions (3.1) and (3.2) or (3.3), respectively. It indicates that during mixing at 25 °C, there was a plausible chance to produce armalcolite (Fe$_2$MgTi$_3$O$_{10}$) and CaCO$_3$ (see Reaction (3.1)). After calcining over 450 °C, the produced CaCO$_3$ reacted with remained TiO$_2$ and produced solid CaTiO$_3$ (see Reaction (3.2)) and carbon dioxide (CO$_2$) as gas. After sintering over 850 °C, the remained Fe$_2$O$_3$ reacted with atmospheric oxide and converted into solid Fe$_3$O$_4$ and oxygen (O$_2$) gas (see

Reaction (3.3)). Therefore, the net chemical reaction after sintering at 1050 °C is depicted in the Reaction (3.4).

$$CaO + MgCO_3 + 2Fe_2O_3 + 4TiO_2 \rightarrow Fe_2MgTi_3O_{10} + CaCO_3 + Fe_2O_3 + TiO_2 \quad (3.1)$$

$$CaCO_3 + TiO_2 \rightarrow CaTiO_3 + CO_2 \uparrow \quad (3.2)$$

$$3Fe_2O_3 + 0.5O_2 \uparrow \rightarrow 2Fe_3O_4 + O_2 \uparrow \quad (3.3)$$

$$CaO + MgCO_3 + 4Fe_2O_3 + 4TiO_2 + 0.5O_2 \uparrow \rightarrow Fe_2MgTi_3O_{10} + CaTiO_3 + 2Fe_3O_4 + O_2 \uparrow + CO_2 \uparrow \quad (3.4)$$
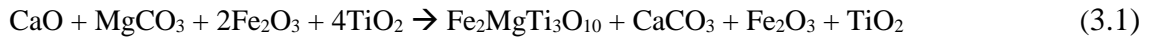
Table 3.3: Schematic sintering steps of the samples S450, S650, S850, and S1050.

Steps	Parameters	Sample Details			
		450 °C	650 °C	850 °C	1050 °C
Step-I	Temperature (°C)	450	250	350	350
	Time (h)	3.5	1	1	1
	Ramp rate (°C/min)	5	5	5	5
Step-II	Temperature (°C)	-	650	550	550
	Time (h)	-	3.5	3.5	3.5
	Ramp rate (°C/min)	-	10	10	10
Step-III	Temperature (°C)	-	-	850	1050
	Time (h)	-	-	1.3	1.3
	Ramp rate (°C/min)	-	-	15	15
Step-IV	Temperature (°C)	-	-	750	750
	Time (h)	-	-	3	3
	Ramp rate (°C/min)	-	-	20	20
Symbols		S450	S650	S850	S1050
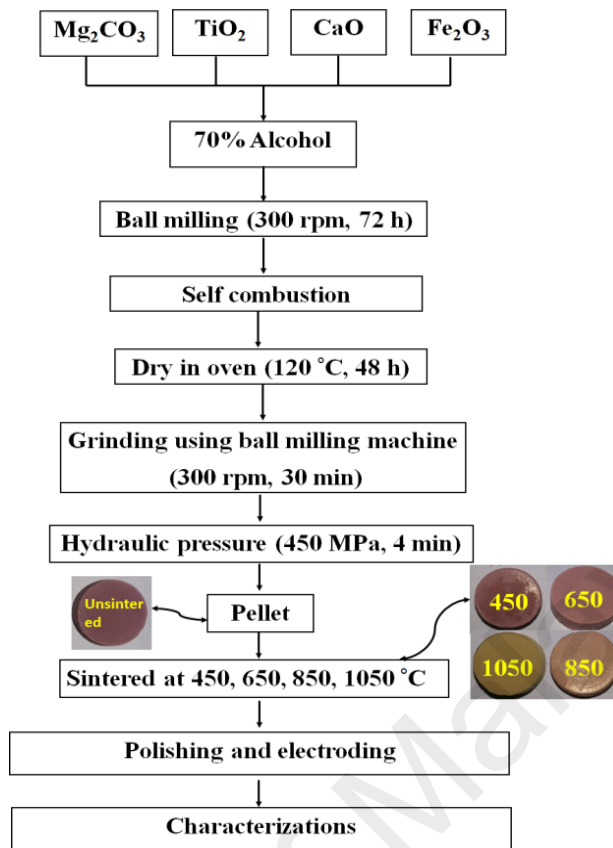
Figure 3.2: A flow chart of ceramic sample preparation by using solid-state reaction technique followed by characterizations.

3.4.2 Preparation of S1050/PDMS Based Composite Flexible Film

To prepare the S1050/PDMS composite film, at first, the pellets of S1050 compound, which were sintered at 1050 °C, were re-crushed and dry ball-milled for 16 h at 300 rpm with sample to ball ratio of 1:100 (w/w). Then, the re-crushed powder of S1050 ceramic was used to make composite with PDMS matrix. S1050 (sintered at 1050 °C) was selected as a second phase ceramic material to make composite with PDMS matrix owing to comprising of confirmed desired three different phases of the ceramics. The flexible S1050/PDMS composite film was explicated using same method as described in a previous study (Ataollahi *et al.*, 2015). Briefly, the S1050/PDMS composite was first, prepared by homogeneous mixing of PDMS-gel (Sylgrade184 Silicon Elastomer Base, Dow Corning) matrix with an optimized concentration (20 wt%) of re-crushed

sintered S1050 compound powder in the ball-mill (PM200, Retsch) for 4 h at 300 rpm with sample to ball ratio of 1:100 (w/w). Thereafter, a referred curing agent (Dow Corning, curing agent: PDMS of 3:25 (w/w)) was added to the S1050/PDMS mixture to render more cross-links in PDMS chains. Again, ball-milling was extended to another 8 min at 300 rpm. The uncured mixture was then spin coated on a glass petri-dish at optimised 3000 rpm for 20 s under vacuum using spin coater (650 M, Laurell Technologies) to make a film around 0.7 mm thick. The film was then kept under self-drying vacuum pump (PM200, Memmert) at 500 mbar for 10 min to minimize the micro-bubbles. Finally, it was properly cured in oven (OF-11E, Lab Companion) at 60 °C for 5 h to get the flexible S1050/PDMS composite film. A flow chart of the thin film preparation is depicted in Figure 3.3.
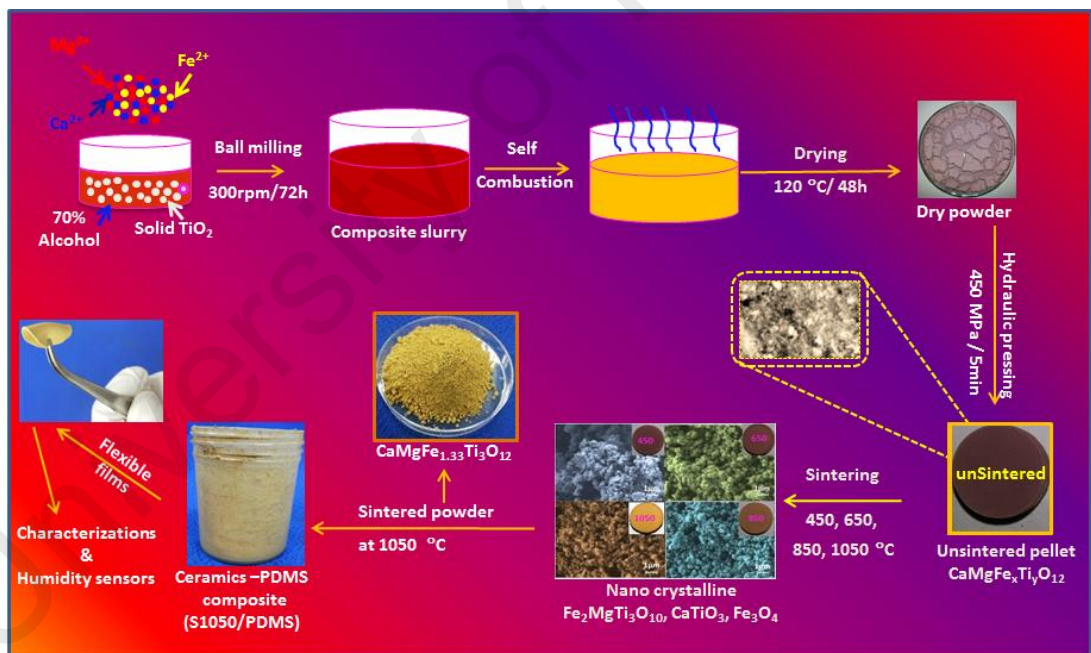
Figure 3.3: A complete flow chart for the preparation of flexible S1050/PDMS composite film.

3.5 Design and Development of S1050 Electroceramic Based Humidity Sensor for Capacitive, Resistive and Dielectric Response Study

In case of capacitive, resistive, and dielectric -type humidity sensors of the electroceramics, the sintered pellets were properly coated with silver paste to make a conducting surface in order to avoid the stray capacitance formation between the material and electrode. Then the silver coated pellet was dried at 250 °C for 1 h. Then, copper (Cu) wire was connected to silver (Ag)-electrode as conduct wire. Finally, the sensor was aged at 150 °C in air for 60 min (see Figure 3.4). Finally, the humidity sensors were obtained after aging at 95 % RH with a voltage of 1 V, 100 Hz for 24 h for better stability and durability.
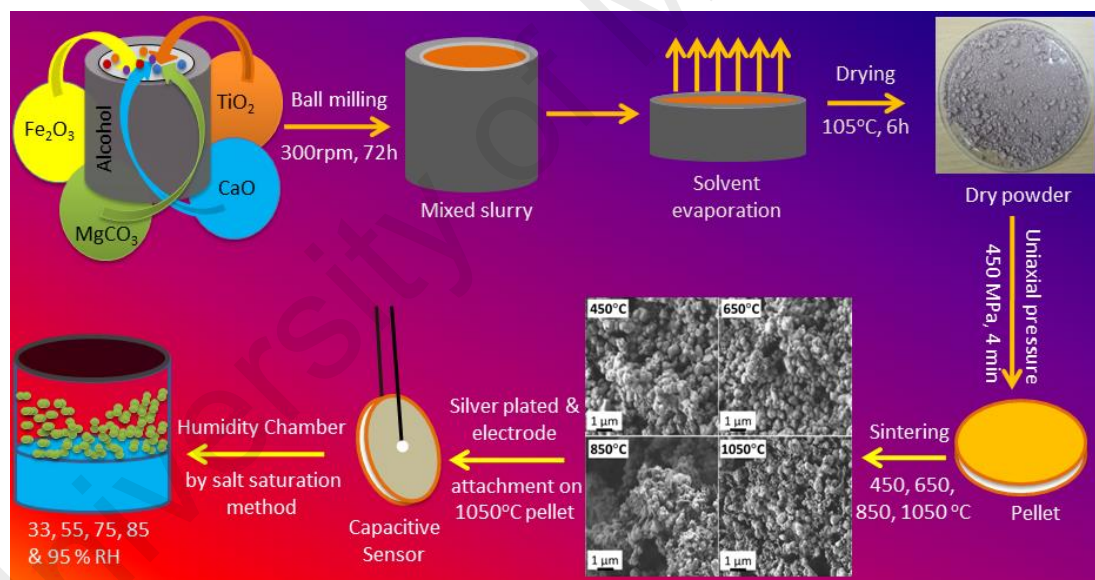
Figure 3.4: A flow chart for the sensor fabrication with the morphology at different sintering temperature.

3.6 Design and Development of S1050/PDMS Composite Based Flexible Resistive Humidity Sensor

Flexible resistive-type humidity sensors were obtained using an innovating thin film technique (TFT) for coating. The mixture gel of S1050/PDMS was deposited as a film

57

by spin coating on custom designed interdigitated gold (Au) electrodes (800 μm in width with 200 μm spacing) of a polyimide (PI) substrate (Hansaem Digitec Co. Ltd.) followed by heating at 90 °C for 1 h in a vacuum oven and the film thickness obtained was about 0.7 mm (see Figure 3.5). Finally, the humidity sensors were obtained after aging at 95 % RH with a voltage of 1 V, 100 Hz for 24 h to improve stability and durability.
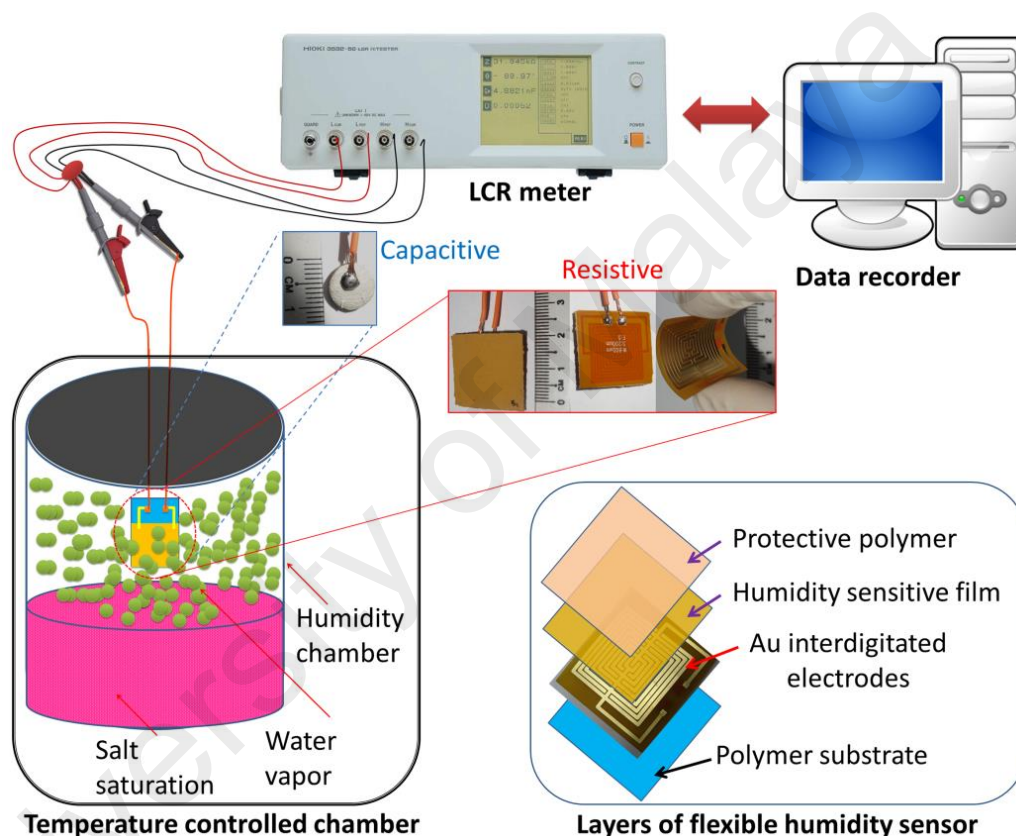
Figure 3.5: Schematic representation of capacitive- or resistive- type humidity sensors and measurement technique.

3.7   Materials Characterization Techniques

The material characterization techniques used for the structural, morphological, thermal, physical, mechanical, and electrical characteristics of the various sintered CMFTO nanocomposite and CMTFO/PDMS based flexible thin film have been described in the following sections.

3.7.1   X-ray Structural Studies

X-ray diffraction (XRD) technique is a powerful tool for detailed structural characterization of materials. Some important applications of XRD technique are phase identification, determination of accurate unit cell parameter, particle size measurement, quantitative phase analysis, determination of crystal structure. In this study, the XRD patterns were obtained by using X-ray diffractometer (Empyrean, PAN analytical) with Cu-Kα radiation (λ = 1.54056 Å). The crystallite size (t) of the sintered material was calculated using modified Debye Scherer formula in Equation 3.1 (Pramanik *et al.*, 2012)

$$t = \frac{\kappa\lambda}{\Delta\theta_{FWHM}.cos\theta - 4\epsilon.sin\theta} \qquad (3.1)$$

Where, $\Delta\theta_{FWHM}$ is the full width at half maxima of the XRD peak in radian, κ is a constant (e.g., 0.9) depends on the particle morphology, λ is the x-ray wave length (1.540546Å), crystal strain or elastic residual strain (ϵ), and θ is the Braggs' diffraction angle. All the data were recorded in a range of Braggs' angle (2θ) from 20 ° to 50 ° at room temperature. In order to determine the phase concentration from XRD, a quantitative analysis was done using Equation 3.2.

$$P\ (\%) = \frac{A_i}{\sum_{i=1}^{n} A_i} \qquad (3.2)$$

where P is phase concentration (%), A_i is area of peak of particular phase, i, and $\sum_{i=1}^{n} A_i$ is total area of peaks of all phases and n is the integer number, depends on the number of different phases.

The lattice parameter of the orthorhombic ceramics and cubic perovskite structure materials is calculated by the Equations 3.3 and 3.4, respectively;

$$\left[\frac{1}{d_{hkl}^2}\right]_{orthorhombic} = \frac{h^2}{a^2} + \frac{k^2}{b^2} + \frac{l^2}{c^2} \qquad (3.3)$$

$$\left[\frac{1}{d_{hkl}^2}\right]_{cubic} = \frac{h^2 + k^2 + l^2}{a^2} \qquad (3.4)$$

Where, d_{hkl} is the inter-planer distance between the planes (Abd-El-Aleem *et al.*, 2000); and *a*, *b,* and *c* are unit cell parameters.

3.7.2   Scanning Electron Microscopy (SEM)

The scanning electron microscopy (SEM) is a unique technique to understand the particle morphologies and their structures. The morphology of all the developed nanoceramic composites and the thin film had been studied by using field emission scanning electron microscope (FESEM) (AURIGA, Carl Zeiss) at an acceleration potential of 8 kV. The pore size distribution (PSD) of all the materials was analyzed from the Inverted images of their corresponding FESEM micrographs using ImageJ (version 1.46r) since this technique has been acknowledged as the best method over other techniques to study the porosity of ceramic-polymer composites. (Pramanik *et al.*, 2015).

3.7.3   Thermogravimetric Analysis (TGA)

Thermogravimetric analysis (TGA) is a useful tool to determine the thermal stability of the materials and also the volatility of the components by observing the weight change during the application of heat on the material. The analysis is usually carried out in air or in an inert atmosphere, such as nitrogen (N_2), helium (He) or argon (Ar). The weight changes are recorded as a function of increasing applied temperature. The decomposition points, the degradation temperatures, the absorbed moisture content of materials, the level of inorganic and organic components in materials, and the solvent

residues can be determined from TGA analysis. In this study, TGA of the unsintered ball-milled ceramic compound powder was employed by a thermogravimetric analyzer (Q500, TA Instrument, New Castle, USA) in nitrogen atmosphere at a heating rate of 10 ℃/min.

3.7.4 Fourier Transform Infrared (FTIR) Spectroscopy

FTIR spectroscopy analysis is based on the interaction of electromagnetic radiation with the material to determine the structure, the chemical compounds, and the changes that occur at the time of chemical reaction. In the FTIR spectroscopy, an infrared (IR) radiation is applied to the molecules to change their dipole moments. The frequency of vibration can be obtained by using Hooke's law, as shown in Equation 3.5:

$$\nu = \frac{1}{2\pi c} \sqrt{\frac{K}{\mu}} \tag{3.5}$$

where, ν is the vibrational frequency, c is the velocity of light, K is the force constant, and μ is reduced mass. Therefore, from the characteristic bands of certain vibrational frequencies in the FTIR spectra, one can retrieve the structural information about the molecules. In the present work, FTIR spectroscopy of the samples such as ceramic powder sintered at 1050 ℃ (S1050), pristine polydimethylsiloxane (PDMS) film, and S1050/PDMS composite film was performed using attenuated total reflectance-FTIR (ATR-FTIR) spectroscope (400, Perkin Elmer,Waltham, UK) to confirm the present bonds or development of any new bonds formed between the S1050 ceramics and PDMS polymers. The analysis was carried out in the wave region ranging between 4000 cm^{-1} and 600 cm^{-1} with the resolution of 4 cm^{-1}.

3.7.5   Density, Porosity, Water Absorption, Water Contact Angle (WCA) Measurements

Density (ρ, g/cc), open porosity (%), and absorbed water or water absoption (%) present in the porous materials were measured in water following Equations 3.6 to 3.8, respectively using modified Archimedes' principle (Pramanik *et al.*, 2013; Pramanik *et al.*, 2014). The resolution of the weighing machine was ±0.0005 g.

$$\rho(g/cc) = \frac{M_1}{M_3 - M_2} \times \rho_{water}^{25^{\circ}C} \tag{3.6}$$

$$P_{open}(\%) = \frac{M_3 - M_1}{M_3 - M_2} \times 100 \tag{3.7}$$

$$\text{Absorbed water } (\%) = \frac{M_3 - M_1}{M_1} \times 100 \tag{3.8}$$

where, M_1 is the initial dry mass of the samples in air, M_2 is the mass of the specimen in distilled water, and M_3 is the mass of the wet specimen after taking out from the water. At least five identical specimens were to evaluate the standard deviation (SD) for each sintered sample, where $\rho_{water}^{25^{\circ}C}$ was water density at tested temperature 25 °C. Water contact angle (WCA) of the materials were measured using sessile contact angle meter (OCA15E, Data Physics Instruments GmbH, Filderstadt, Germany) at room temperature (droplet size: 3 µl, dosing rate: 0.5 µl/s). The WCA was captured after 20 s for the flexible films at stable condition of the droplet, whereas WCA had to be captured instantly for the all ceramic pellets since they showed super surface-hydrophilicity.

3.7.6   Mechanical Study

Three main mechanical characterizations, such as static tensile stress, atomic force microscopy, and dynamic mechanical properties of the CMFTO/PDMS based flexible film are explained in the following sections.

3.7.6.1   Static Tensile Properties

Flexibility of the PDMS and S1050/PDMS composite films was tested by measuring the static tensile modulus using universal testing machine (5848, Instron Micro Tester). At least three identical tensile specimens following the ASTM D 412 standard with dog-bone shaped of 6.6 mm × 1.1 mm × 0.7 mm (gauge length × gauge width × thickness) were tested with a constant crosshead speed of 1 mm/min (Ataollahi *et al.*, 2015; Liu *et al.*, 2009).

3.7.6.2   Force Spectroscopy using Atomic Force Microscope (AFM)

Force spectroscopy in tapping mode study was employed using atomic force microscope (AFM) (Nanowizard BioScience AFM, JPK Instruments, Berlin, Germany) to confirm the more precise Young's modulus of PDMS and S1050/PDMS composite films and their corresponding topography morphology. At least five positions were selected to take more than ten times indention at each potion.

3.7.6.3   Dynamic Mechanical Analysis (DMA)

Dynamic mechanical analysis (DMA) of the PDMS and S1050/PDMS composite film (size: 0.4 mm × 10 mm × 40 mm) was carried out by dynamic mechanical analyser (RSA-G2, TA Instruments, New Castle, USA) in tensile mode at a heating rate of 10

°C/min in liquid nitrogen atmosphere in the range from -110 to -35 °C at a constant frequency of 1 Hz.

3.7.7 Dielectric and Complex Impedance Study

The dielectric and complex impedance analyses were employed by impedance spectroscopy (IS) (3532-50 LCR Hi tester, Hioki, Ueda, Japan) over the frequency (f) range of 100 Hz – 1 MHz at 25 °C. For these analyses, both sides of the ceramics pellet samples were polished and coated with conductive silver paste followed by drying at 110 °C for 2 h to get good electrical contact with the external applied electrodes. The frequency dependence of electrical properties of a material is often represented in terms of complex permittivity (ε^*), complex impedance (Z^*), complex electric modulus (M^*) and dielectric loss tangent (tanδ). The mathematical relations among these characteristics are expressed in the Equation 3.9–3.11 (Khatri *et al.*, 2009; Sinclair & West, 1989).

$$Z^* = Z' - jZ'' = R_s - \frac{1}{j\omega C_s} \tag{3.9}$$

$$M^* = \frac{1}{\varepsilon^*(\omega)} = M' + jM'' = j\omega C_0 Z^* \tag{3.10}$$

$$\tan\delta = \frac{\varepsilon''}{\varepsilon'} = \frac{M''}{M'} = -Z'/Z'' \tag{3.11}$$

Where, Z', M', and ε' indicate the real components of impedance, modulus and dielectric constant or permittivity, respectively; Z'', M'', and ε'' are the imaginary components of impedance, modulus and dielectric constant or permittivity, respectively; $\varepsilon^* = \varepsilon' - j\varepsilon''$, $j=\sqrt{(-1)}$ is imaginary number, ω is the angular frequency in rad/sec (i.e., $\omega=2\pi f$, where f is applied alternating frequency in Hz), C_o is capacitance of vacuum ($C_o=\varepsilon_o A/t$, where ε_0 is called free space permittivity = 8.854×10^{-12} $C^2N^{-1}m^{-2}$ or Fm^{-1}, and

t and A are the thickness and the cross-sectional area of the pellet, respectively), C_s is the capacitance and R_s is the resistance for series combinations of circuit elements. The dielectric constant components, ε' and ε'' were calculated by the Equation 3.12 and 3.13, respectively (Prasad *et al.*, 2010).

$$\varepsilon'(\omega) = \frac{Z''}{\omega C_0\left(Z'^2 + Z''^2\right)} \tag{3.12}$$

$$\varepsilon''(\omega) = \frac{Z'}{\omega C_0\left(Z'^2 + Z''^2\right)} \tag{3.13}$$

3.7.8   A.C. Conductivity Study

The AC conductivity (σ_{ac}) and activation energy (E_a) of the compounds at high temperatures (i.e., in paraelectric phase) were calculated from the measured dielectric data using the Equation 3.14.

$$\sigma_{ac} = \omega \varepsilon_r \varepsilon_0 tan\delta = \sigma_0 \exp(-{E_a}/{kT}) \tag{3.14}$$

Where, ε_r is relative permittivity also termed as ε', σ_0 is free space conductivity, E_a is activation energy, T is temperature and k is Boltzmann constant, and all the other parameters already defined before. The σ_{ac} can also be represented as a function of temperature (T) and angular frequency (ω) by using power law as mentioned in Equation 3.15 (Jonscher, 1977).

$$\sigma_{ac}(\omega, T) = B\omega^s \tag{3.15}$$

where, B is a constant and S is an exponent.

3.8   Humidity Sensing Characterizations

Mainly three types of humidity sensors such as capacitive, impedance, and dielectric were designed in this study using the materials sintered at 1050 °C (S1050). The flexible nanocomposite (S1050/PDMS) comprising S1050 electroceramic composite and PDMS was studied for capacitive as well as resistive type sensors. The characteristics of humidity sensors were evaluated by the LCR meter. The frequency was varied from 10^2 to 10^6 Hz and 1 V AC voltage was applied for this test. The measurement was performed at 25 °C in a temperature controlled chamber (Memmet, Naluri Scientific, Schwabach, Germany) with a resolution of ±5 °C, as depicted in Figure 3.6. The atmospheres of different RH were produced by different saturated aqueous salt solutions in several chambers. The equilibrium states of humid atmospheres for magnesium chloride ($MgCl_2$), magnesium nitrate ($Mg(NO_3)_2$), sodium chloride ($NaCl$), potassium chloride (KCl) and potassium nitrate (KNO_3) salt solutions are 33 %RH, 54 %RH, 75 % RH, 85 %RH and 95 %RH, respectively with a resolution of about ±1 %RH at 25 °C (Greenspan, 1977). The response and recovery characteristic was evaluated from the time taken by the sensor to achieve ~ 90% of the total capacitance change in case of adsorption (humidification) and desorption (desiccation), respectively of the water vapours.
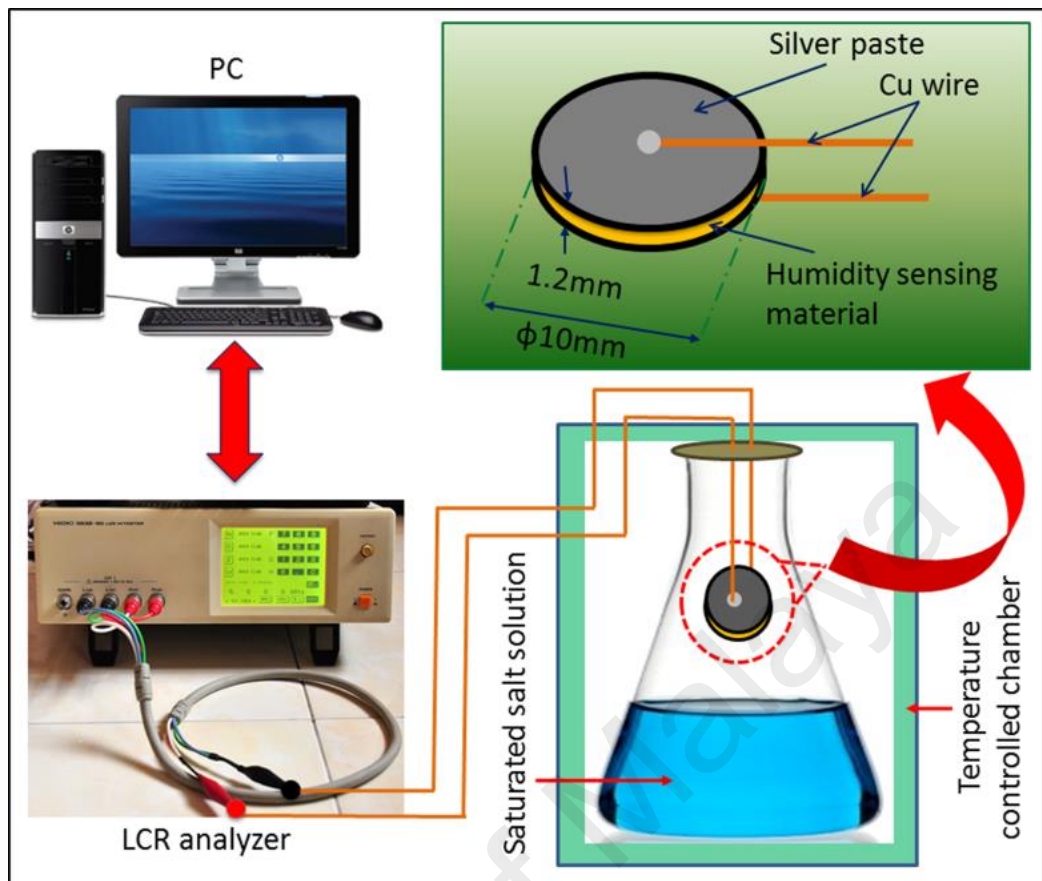
Figure 3.6: Experimental setup for the measurement of capacitive humidity response of electroceramic based sensor.

3.9 *In Vitro* **Biocompatibility Study**

In vitro biocompatibility property of the newly developed armalcolite based NPs and its thin film nanocomposites had been employed on the human dermis fibroblast (HDF) cells.

3.9.1 Cell Culture Methodology

Preparation of primary culture medium, cell seeding, and incubation period are described in the following sections.

3.9.1.1   Preparation of Primary Culture Medium

For the culture of bone marrow stromal cells, Dulbecco's Modified Eagle Medium (DMEM) containing 10% foetal calf serum (FCS), 100 unit/ml penicillin, and 100 unit/ml streptomycin had been used. All ingredients used in the whole cell culture study were obtained from Sigma Aldrich, except those mentioned specifically.

3.9.1.2   Cell Seeding and Incubation Period

A cell culture study was carried out by using human dermis fibroblast (HDF) cells. Pellets (size: ϕ10 mm $\times$ 1.2 mm, diameter $\times$ length) of S1050 were immersed in 70% ethanol overnight to free from contamination prior to fibroblast cell seeding. The fibroblast cells (initial concentration: 4×10^6 cells/ml) were isolated via outgrowth method from the harvested unused dermal tissue of extrinsic epidermal layer of human skin after cosmetic-plastic surgery was made in the Medical Hospital, University of Malaya (Manna *et al.*, 2016; Moradi *et al.*, 2016; Pramanik *et al.*, 2015). The collected cell suspension was centrifuged to collect the HDF cells and it was converted to a selected concentration of 2×10^4 cells/ml. Then, the pellets were washed with phosphate buffered saline (PBS), pH 7.4 to ensure the complete removal of 70% ethanol. Thereafter, sterilization of the nanocomposites pellets was conducted by placing the pellets in an autoclave (Omega 121/134, Prestige Medical) for around 20 min. Then, the pellets were rapidly soaked in 80 µl of freshly prepared DMEM chondrogenic medium in 24-well plate and placed in a humidified incubator maintained at 37 ºC, 5% CO_2, and 95% relative humidity (RH) environment for 24 h before seeding. Here, thermanox was used as positive control (thermanox with cell) and one pellet scaffold of each sample was used as blank or negative control (scaffold without cell). These HDF cells were re-suspended in freshly prepared culture medium, consisting of DMEM, 1X (High

glucose) supplemented with 10% (v/v) FBS, 1% HEPES, 1% Penicillin Streptomycin (PS), 1% non-essential amino acids, 50 µg/ml L-ascorbic acid, 40 µg/ml L-proline, and the volume of cell suspension was increased up to 4 ml. The 20 µl fibroblast cells of the prepared suspension with seeding density of 2×10^4 cells/ml was consecutively seeded on the pre-wetted upper surface of pellets of S1050 present inside the 24 well-plate. The whole procedure was performed inside biosafety cabinet. Thereafter, 200 µl freshly prepared DMEM chondrogenic medium was added to the 24 well-plate over seeded pellets and allowed to incubate in the incubator for 3 h to collect the cells gently on the surface of the pellets. All the samples were seeded and allowed to proliferate in the incubator for 7 days to assess the cellular activity on the seeded pellets on variations of day-1, day-3, and day-7. The cultured medium was changed at every even day. The biochemical assays were conducted on each time point.

3.9.2 *In Vitro* Cell Culture Assays on HDF Cells

In vitro cell culture study was focused on two assays, such as cell proliferation and viability study by deoxyribonucleic acid (DNA) Assay and live-dead cell assay.

3.9.2.1 Cell Proliferation and Viability Study by Deoxyribonucleic Acid (DNA) Assay

This is a quantitative study. This assay measures the amount of total DNA present in the cells and thus, gives a general idea of the number of cells (both live and dead). This assay was employed to determine the cell proliferation using DNA-assay at three time points, such as Day-1, Day-3, and Day-7. At least five identical scaffolds were subjected to papain digestion for DNA-assay for each material. Cells of each specimen (size: $\phi 10$ mm $\times$ 1.2 mm, diameter $\times$ length) were digested in 1 ml of papain digest buffer (contained 0.01 M L-cysteine, 0.01 M Na_2EDTA, and 0.125 mg/mL papain in 0.1 M sodium phosphate

buffer) and incubated overnight at 65 °C with intermittent agitations. The DNA measurement was done by adding 2 mg Hoescht 33258, which was added into each ml of H$_2$O to prepare the Hoescht stock solution, and stored in 4 °C in a dark bottle. Then, only the digested solution part was analyzed for DNA using Hoescht dye (0.1 µl/ml in Tris/EDTA/NaCl (TEN) buffer (a mixture of 10 mM Tris, 1 mM EDTA, and 0.2 M NaCl in PBS)) with calf thymus DNA as the standard. Serial dilutions were made of the DNA standard at 25, 12.5, 6.25, 3.125, 1.5625, and 0.78125 µg/ml. The original concentration was 50 µg/ml in 100 µl diluted in phosphate buffer solution with EDTA (PBE) (100 mM sodium phosphate buffer/10 mM Na$_2$EDTA). Meanwhile, in a 96-well plate, 10 µl PBE was added as a blank and a triplicate was made of this. The samples were added in the remaining wells. 200 µl of working solution was then added to each well prior to reading. Plate reading was performed at a particular excitation (~ 355 nm)/emission (~ 460 nm) wavelength in a microplate reader (FLUOstar Optima, BMG Labtech).

3.9.2.2 Live-Dead Cell Assay

This assay was carried out to demonstrate the cell viability status of the nanocomposites. It helps to identify the presence of live and dead cells. A qualitative analysis was carried out to determine the cell viability of the S1050 and S1050/PDMS thin films with live-dead cell assay using a confocal laser scanning microscope (CLSM) (Leica TCS SP5 II). LIVE/DEAD® Viability/Cytotoxicity Kit obtained from Invitrogen, UK comprised of calcein-AM (4 mM in anhydrous dimethyl sulfoxide (DMSO)) and ethidium homodimer-1 (2 mM DMSO/H$_2$O of 1:4 (v/v)). Two dyes, such as calcein AM (live strain, 1 µl) and ethidium homodimer-1 (dead strain, 2.5 µl), were mixed with 1 ml of preheated PBS (at 38 ºC for 16 h). The presence of live cells was distinguished in CLSM through green fluorescence due to staining of cytoplasm of live cells with calcein-AM, which possessed intracellular esterase activity. The existence of

dead cells was discriminated by bright red fluorescence because of the nucleic acids of the dead cells stained by EthD-1 followed through by defining the damaged cell membrane. The cell seeded pellets were immersed briefly into 1 ml of dye solution, diluted with calcein-AM and ethidium homodimer-1 strains, and were incubated for 45 min the incubator. Finally, the stained samples were subjected to acquire CLSM.

3.9.3　Statistical Analysis

A significance test for the difference in the results between the groups of samples was done to determine the normal distribution of each sample group. One-way analysis of variance (ANOVA) was used to compare the groups. The 95 % confidence of the one-way ANOVA indicated the insignificance for the variance $p > 0.05$ and significance for $p \leq 0.05$.

3.9.4　*In Vitro* Drug Release of Hydrogels

Before the *in vivo* study of the drug loaded hydrogels had been carried out, an *in vitro* drug release study of curcumin drug loaded S1050 NPs based hydrogels was conducted to investigate their drug releasing behavior at physiological conditions. First, the known concentrations of raw curcumin drug solution in PBS were measured from the UV-Vis absorption peak at a wavelength (λ) of 422 nm to get a standard absorption rate of the raw drug based on the previous report (Manna *et al.*, 2016). Then, the concentrations of the curcumin loaded hydrogel and curcumin loaded S1050 NPs based hydrogel were calculated from standard UV-Vis absorption curve nm to determine the concentration of curcumin drug released from tested hydrogels at different times.

3.10   *In Vivo* study: Wound Healing using Diabetes Rat Model

The drug loading and biological properties of the newly developed armalcolite based composite NPs had been studied by using the *in vivo* study on the diabetes rat model on the dermal tissues of sprague dawley (SD) rats.

3.10.1   Raw Material used for Wound Hydrogel

In this study, four different types of hydrogels, such as pure hydrogel, nanocarrier (S1050) based hydrogel, curcumin drug based hydrogel, and curcumin drug loaded composite nanocarrier hydrogel, were prepared. The raw materials used for all the above mentioned hydrogels preparation are listed in Table 3.4.

Table 3.4: List of raw materials used for the hydrogel preparation.

Material	Quantity (wt%)	Manufacturer
PVA	8.33	Fisher Scientific Ltd.
Glycerin (Gly)	15	-do-
Distilled water	76.66	Laboratory made
S1050 as nanocarrier	2.58	Synthesized in present study
Curcumin drug	0.64	Sigma Aldrich

3.10.2   Preparation of Wound Hydrogel

Preparation of armalcolite nanocomposite and curcumin drug with PVA based hydrogel has been described in the following sections.

3.10.2.1 Preparation of PVA Hydrogel

2.5 g PVA and 4.5 g glycerin were dissolved in 23 g distilled water at 120 °C and then, mixed using a magnetic stirrer for 60 min. Besides, in order to remove bubbles and prevent the hardening of the homogeneous solutions, the solution was placed in a water bath at 70 °C for 30 min. This solution was then poured into petri dishes and the gel was exposed to UV- radiation to increase the crosslinking.

3.10.2.2 Preparation of PVA/Nanocarrier Hydrogel

The S1050 ceramic nanocomposite was ground to prepare fine NPs powder. Then, 0.8 g fine powder was mixed with 30 g pure PVA hydrogel by using a magnetic stirrer for 6 h, and followed by ultrasonication for 30 min to prepare PVA/carrier hydrogel.

3.10.2.3 Preparation of PVA/Drug Hydrogel

PVA/drug hydrogel was prepared by employing a simple mixing method. Briefly, 0.2 g curcumin nanopowder was mixed with 30 g pure PVA hydrogel for 6 h, and followed by ultrasonication for 30 min. After the preparation of hydrogel, it was stored at 4 °C for further use.

3.10.2.4 Preparation of PVA/Nanocarrier/Drug Hydrogel

The curcumin drug and S1050 nanopowder was mixed in chloroform ($CHCl_3$, Sigma Aldrich). Briefly, 0.8 g of S1050 nanocarrier and 0.2 g curcumin drug nanopowder was mixed in 20 ml chloroform and the mixture was stirred for 60 min in a shaker, followed by ultrasonication in a closed bottle for 30 min to obtain a homogenous composite. Then, the mixture was kept at open atmosphere to evaporate the chloroform. 1 g of prepared drug loaded carrier nanocomposite was mixed in 30 g pure PVA hydrogel to prepare the drug/carrier nanocomposite hydrogel. After preparation, the hydrogel was preserved at 4 °C for further study.

3.10.3 Animals

In this study, 30 adult male Sprague Dawley rats of weight range between 200 and 250 g were purchased from the Animal house, Faculty of Science, University Putra Malaysia. The rats were kept in a clean and well-ventilated animal room with

standardized condition (12 h light/darkness: room temperature 25 ± 2 °C; with 2-3 animals per cage and 50% – 60% humidity) in order to maintain normal circadian rhythm in the animal room. The rats were fed commercial rodent food pellets with tap water *ad libitum*, which was given through special dropper-tipped bottles placed in the cages. The rats were allowed to acclimatize to the new environmental conditions for 7 days prior the experiment. The handling of animals was accordance to the experimental protocols, which were approved by the Ethical Committee for the Supervision of Animal Experimentation, Animal care, and Use Committee (ACUC), UM with Ethics 2015-180610/BENG/R/NAAO, Faculty of Medicine, University of Malaya.

3.10.4   Chemicals, Consumables, and Sterilization for Wound Healing Study

A list of all the chemicals with 99% purity used in the entire experiment is illustrated in the Table 3.5. All the chemicals were used without further purification.

Table 3.5: List of Chemicals and consumables that were used in this study.

Serial No	Chemicals	Source
1	Tetramethylenediamine (TEMED)	Sigma-Aldrich, St. Louis
2	Membrane (PVDF) Poly Vinylidene fluoride	Bio Rad, CA, USA
3	Bovine Serum Albumin (BSA)	Innovative, Peary Court Novy, Michigun, USA
4	Paraffin wax	Tyco Healthcare Group MA, USA
5	Micro BCA protein assay Kit	Thermo Scientific
6	Curcumin	Sigma-Aldrich, St. Louis
	Paraformaldehyde, Ethanol, Methanol, and Xylene	-do-
7	Multicolor broad range Ladder	Fermentas, USA
8	ABC staining Kit	Santa Cruz, CA, USA
9	Micro 96 well plate and cover	Applied Biosystem, USA
10	RNA extraction Kit	Qiagen, Germany
11	RNAs free water, RNA Later	Ambion, Foster city, USA
12	cDNA Conversion Kit, Taq man Fast advanced Master Mix	Applied Biosystem, USA
13	NaCl, NaHCO₃, NaHPO₄, KCl, MgSO₄, CaCl, Glucose-D, HEPES, Trinatrium Citrate, and HCl	Merck KGaA, Darmstadt, Germany
14	Pro-Prep protein extraction solution	Intron Biotechnology, Korea

Serial No	Chemicals	Source
15	4CN optic substrate Kit	Bio Rad, CA, USA
16		
17	Ultra-Cruz Mounting media	Santa Cruz, CA, USA
18	Ketamine and Xylazine	Sigma Chemical Co., St. Louis, MO, USA

Sterilization: All equipment, such as plastic tips, disposable glass, collection tubes, forceps, and scissors, were sterilized by autoclaving them for 20 min at 1.05 kg/cm² on liquid cycle using vertical stainless steel pressure steam sterilizer (75L APEX-LJ448, Shandong, China).

3.10.5 Induction of Diabetes in SD Rats

Induction of diabetes was done by injecting a combination of streptozotocin (STZ) and nicotinamide adenine dinucleotide (NAD) according to the dosage reported in previous studies (Pauzi *et al.*, 2013; Pimple *et al.*, 2012). Briefly, fasting animals for 12 h were rendered diabetes by injecting freshly prepared STZ at 55 mg/kg body weight (bw) dissolved in 0.1 M citrate buffer (pH 4.5). Nicotinamide (100 mg/kg bw) was given to them 15 min prior to STZ injection to minimize the destruction to the pancreas and to create type-2 diabetes (Adam *et al.*, 2016). STZ-nicotinamide injected animals were given 5% glucose for 24 h to prevent mortality caused by drug-induced hypoglycemia. Blood was drawn from the tail after 72 h to ensure successful induction of hyperglycemia. Rats with elevated blood glucose level ($\geq$ 10 mmol/L) were considered diabetic (Masiello *et al.*, 1998).

3.10.6   Excision Wound Creation

The acute wound healing activity of armalcolite (S1050) ceramic nanocarrier and curcumin loaded nanocarrier on excisional wound model of 4 cm^2 wound area (see Figure 3.7), as described by Gottrup, 2001, had been chosen as the cutaneous wound model in this study. The wound was made under general anesthesia by using intraperitoneal injection of ketamine (80 mg/Kg) combined with a sedative xylazine (8 mg/Kg). The weight of each rat was measured prior to anesthesia. The anesthetic animals were then placed immediately on a heat pad to avoid any fall in body temperature. The skin was shaved using an electric clipper at the dorsal neck region. It was then disinfected with 70% (v/v) alcohol, and 0.5 ml of lignocaine HCl (2%, 20 mg/ml) was injected as a local anesthetic agent.
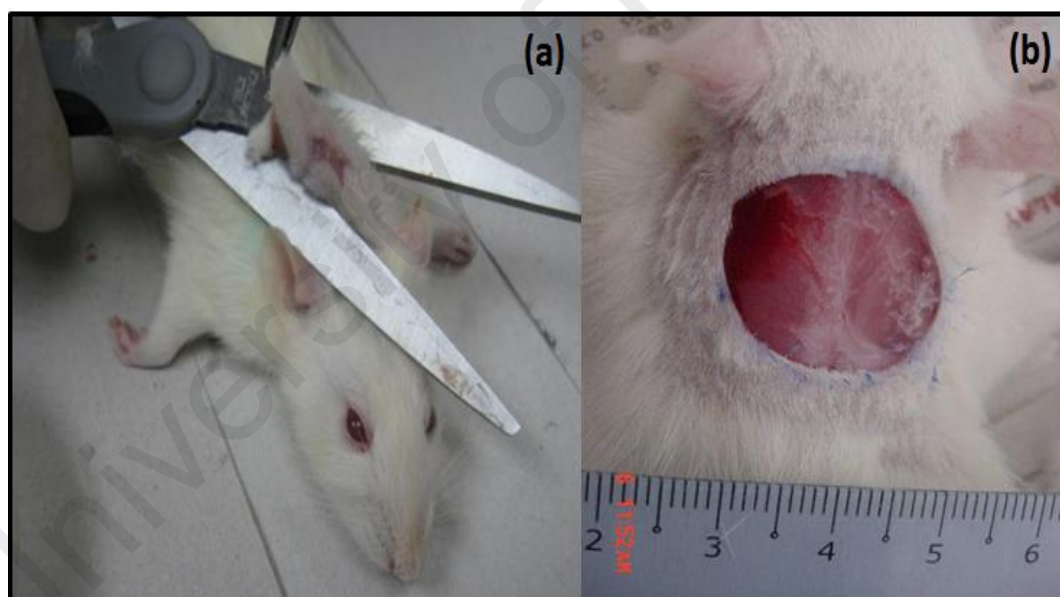
Figure 3.7: Full thickness skin excision (a) initial wound creation, (b) 2 cm wound (Gottrup, 2001).

After marking an oval wound on the shaved necks of the rats, a full thickness of the excision wound (approximately 2.00 cm) with 2 mm depth was created without any damage to the muscle layer using a sterile surgical blade and disinfected scissors (see

Figure 3.7a, b). The entire wound was left opened and air exposed to environment. The neck area of wound was chosen to avoid any unwanted biting and stretching from the rats. Any damage to the muscle layer was carefully avoided and all the procedures were performed with the constant tension of the skin. The forceps and scissors were cleansed with alcohol (70 %) after each use. The day of wound creation was labeled as Day 1 of treatment.

3.10.7   Grouping, Topical Treatment and Sampling

The prepared hydrogels with various healing compositions were applied topically to treated SD rats daily for 14 days. The rats were divided into five groups, viz. Group-1: normal control (NC), Group-2: diabetic control (DC), Group-3: diabetic control and curcumin drug (DC+C), Group-4: diabetic control and S1050 (DC+S1050), and Group-5: diabetic control, S1050, and curcumin drug (DC+S1050+C). Each group consisted of six rats (total rat 30 rats = 6 × 5), and treatments were started immediately after the wounding procedure. The rats were treated with different types of treatments successively. The grouping of the animals is illustrated in Table 3.6. Wounds of the Group-1 (NC) animals were topically treated with 0.2 ml pure hydrogel, once in a day as placebo control group for 14 days. Wounds of the Group-2 (DC) rats were also topically treated with 0.2 ml of pure hydrogel once in a day as diabetic control group for 14 days. Moreover, 0.2 ml of curcumin drug contained hydrogel was applied topically to Group-3 (DC+C) once in a day as diabetic control group for 14 days. The Group-4 (DC+S1050) animals were treated with 0.2 ml of armalcolite nanocarrier contained hydrogel once in a day as diabetic control group for 14 days. Finally, 0.2 ml of curcumin drug loaded armalcolite NPs hydrogel as a vehicle was applied topically to Group-5 (DC+S1050+C) once in a day as diabetic control group for 14 days. The

wounds were air exposed and treatments were applied topically once a day until they were euthanized.

Table 3.6: Grouping and treatment of diabetes induced wounded SD rats.

Groups	Number of SD Rats (n)	Metabolic Disorders	Treatment (Vehicle)	Healing Substance	Application	Healing Period (Day)
NC	6	-	Pure hydrogel	Hydrogel	Dermal wound	14
DC	6	Diabetes	Pure hydrogel	Hydrogel	Dermal wound	14
DC+C	6	Diabetes	Curcumin (C) loaded hydrogel	Drug (C)	Dermal wound	14
DC+S1050	6	Diabetes	Armalcolite loaded (S1050) hydrogel	Nanocarrier (S1050)	Dermal wound	14
DC+S1050+C	6	Diabetes	Curcumin (C) loaded armalcolite loaded (S1050) hydrogel	Drug (C) loaded nanocarrier (S1050)	Dermal wound	14

NC=Normal control; DC=Diabetic control; DC+C=Diabetic control+Curcumin; DC+S1050=Diabetic control+armalcolite; DC+S1050+C=Diabetic control+Armalcolite+Curcumin

3.10.8   Determination of Food, Water and Fasting Blood Glucose (FBG) Levels

The initial and final body weights, as well as daily food and water intakes, were determined by precise weight measurement. For determination of FBG, blood was collected by pricking the tail vein. FBG levels were measured at day 1, as well as 7th and 14th of the experimental period, by using a digital glucometer (Accu-Chek1, Roche, Mannheim, Germany).

3.10.9   Collection and Measurement of Blood Serum Hormone Level

Blood samples were collected through cardiac puncture by using 1 ml syringe 22G needles. The collected blood was transferred to a new clean tube and kept at room temperature for 15 min to allow clotting. The collected clotted blood was centrifuged for 15 min at 5000 rpm to separate clear fluid (serum) from blood. Clear serum was gently separated and collected into a new labeled autoclaved sterilized tube via careful pipetting in order to prevent mixing with red blood corpuscles (RBCs). The samples were kept and stored at -20ºC. Levels of steroid hormones i.e., insulin, was measured by using enzyme-linked immunosorbent assay (ELISA).

3.10.10   Determination of HbA1c and Insulin Levels

HbAa1c in whole blood was estimated by using a commercially available kit (BioSystems S.A. Costa Brava 30, Barcelona, Spain) and serum insulin level was measured by using enzyme-linked immunosorbent assay (ELISA) kit (EIA-2048, 96 wells, DRG Instruments GmbH, Marburg, Germany) according to the guideline provided by the manufacturer. Briefly, during incubation, insulin in the sample reacted with peroxidase-conjugated anti-insulin antibodies bound to micro-titer wells. Washing steps removed the unbound enzyme-labeled antibody. The bound conjugate was detected by the reaction with 3,30,5,50-tetramethylbenzidine. The reaction was stopped by adding acid to give a colorimetric end-point, while optical density was measured by using a microplate autoreader (iMarkTM; Bio-Rad, Hercules, CA, USA) at a wavelength of 450 nm.

3.10.11   Wound Contraction Measurement (Wound Closure)

Each rat was closely observed and inspected for general morphological changes of the wound healing process. The wounds were photographed with a digital camera on days 1, 3, 7 and 14 to assess the progress of wound closure. Wound size (surface area of the wound) and wound closure rates were measured by tracing the wound on days 1, 3, 7 and 14 via post-wounding surgery using a transparent paper, graph paper (Ponrasu & Suguna, 2012) and permanent marker under general anesthesia (a mixture of ketamine and xylazine), as described by (Nayak & Pereira, 2006). The wound areas recorded were measured using a graph paper. The percentage of wound contraction (%) was also determined by using Equation 3.16 (Teoh *et al.*, 2009):

$$\text{Wound contraction } = \frac{\text{Initial wound size} - \text{Wound size at specific day}}{\text{Initial wound size}} \times 100 \text{ \%} \qquad (3.16)$$

3.10.12   Tissue Collection and Sampling

The process of wound healing was determined by using two different approaches such as: microscopic and macroscopic technique. The dermal wound tissues were preserved using formalin solution at 4 °C for the period of 4 h followed after the sacrificing of SD rats. All samples were properly labeled before storage. The measurements were done systematically depending only on labels. This method was used to avoid experimental bias.

3.10.13   Tissue Homogenization

The removed wounded skin of each rat was weighed separately and placed in PBS (specimen weight $\times$ 10 = PBS volume), and the tissue homogenate was prepared with the aid of a homogenizer machine (Wisemax, HG-15A). The suspension was then

centrifuged at 4 °C, 3500 rpm, 20 mins, and the supernatant was removed and kept in Eppendorf tubes at -80 °C for later use.

3.10.14   Pre-histological Assessment

Pre-histological assessment was followed in different steps, such as preparation of tissue sample, tissue processing, tissue embedding, and sectioning.

3.10.14.1 Preparation of Tissue Sample and Tissue Processing

Each wound specimen was cut vertically through the skin up to the adipose tissue located underneath the skin. The wound tissue specimen was then trimmed and placed in the specimen cassette. This step was done to prevent the tissues from curling. The tissue specimens were then placed into the automated tissue processing machine for histological studies. In the dehydration step, the tissue samples were passed through a series of alcohol solution with increasing concentration for 2 h each to remove water from the tissue specimens. Each specimen was immersed in 80% alcohol solution, 95% alcohol (I) solution, 95% alcohol (II) solution, absolute alcohol (I) solution, absolute alcohol (II) solution, and 70% alcohol solution, successively. This process was needed because complete paraffin infiltration and embedding processes could only be done without the presence of water, since paraffin is immiscible with water. Besides, tissue processing is very necessary for dehydration steps. The specimens were cleaned thrice in the xylene solutions. This step was carried out to remove the remaining alcohol present inside the tissue specimens. Then, the tissue specimens were transferred sequentially to two changes of pure paraffin for 2 h each. This process was done to ensure that the paraffin had completely infiltrated into the tissue specimens.

3.10.14.2 Tissue Embedding and Sectioning

After the infiltration process had been completed, the tissue specimens were embedded carefully in the paraffin mold. To embed the tissue, the specimens were placed into molds prefilled with melted wax and cooled immediately at -60 °C to harden the wax. The epidermal surface of each tissue specimen was identified and the specimen was placed to stand at 90° in the mold. The blocks were then left to cool on the cold plate until it was ready for use. The paraffin block, which was ready for use, had been placed on ice prior to the sectioning process. After cooling and hardening, each paraffin block was placed into a microtome and was cut into a long ribbon of sections with the thickness of 5 µm.

The ribbons were then placed into water bath at 42 °C. A few sections were chosen from the long ribbon and fished onto the cleaned slides. This step was done to prevent wrinkles and folding of the sections. After completing the formation of tissue ribbon, the slides were heated in an oven at 50 °C.

3.10.15 Histological Analysis

In the histological analysis, two important cell morphological studies, such as hematoxylin-eosin staining and immunohistochemistry study were done.

3.10.15.1 Hematoxylin and Eosin Staining

The slides were then stained with hematoxylin and eosin (H&E), visualized under a light microscope under magnifications of 4×, 20×, and 40×. The circumferences and the thickness of dermal and epidermal layers were measured by using NIS-Elements AR program. All images were captured by using a Nikon Eclipse 80i that was attached to a light microscope (Olympus, Japan). All the experimental steps of H&E are illustrated in Table 3.7.

82

Table 3.7: Hematoxylin and eosin (H&E) staining procedure.

Process Steps	Procedure
Deparaffination	3 changes in Xylene for 3 min interval.
Rehydration	Tissues rehydration with decreasing ethanol grades 100%, 95% and 80% twice each for 3 min interval.
Hematoxylin staining	Sections were stained with hematoxylin for up to 50 s
Washing	Rinse 2 times in tap water for 1 min interval
Eosin staining	Sections were stained with eosin for up to 20 s.
Dehydration	Sections were dehydrated with increasing grades of 95% and 100% ethanol twice each for 5 min interval.
Mounting	1-2 drops of permanent mounting media was applied and covered with glass cover slips.

3.10.15.2 Immunohistochemistry

The tissue that was used in formalin-fixing and paraffin-embedding was sectioned at 5 μm thickness. Before the slides were stained, hydration was carried out by decreasing the grades of ethanol. After antigen retrieval, the slides were immersed in hydrogen peroxide (H_2O_2) solution for endogenous peroxidase activity.

The sections were then incubated with primary antibody with 1.5% blocking serum for 1 h at room temperature. The sections were then incubated with biotinylated secondary antibody of 1 μg/ml for 30 min. Then, after washing with PBS, the slides were incubated with AB enzymes for 30 min. The sites of antibody binding were visualized by DAB (Diaminobezidine) (Santa Cruz, US) staining, which gave dark brown stains. The stained sections were washed in de-ionized water for 5 min and were counter-stained with haematoxylin for 5-10 s. After staining, each paraffin-embedded section was dehydrated with decreasing grades of ethanol 10 s. The stained slides were then mounted with 1-2 drops of DPX (a mixture of distyrene (a polystyrene), a plasticizer (tricresyl phosphate), and xylene mounting media with a glass cover slip. All the steps of immunohistochemical procedures are portrayed in Table 3.8.

Table 3.8: Immunohistochemistry staining procedure.

Process Steps	Procedure
Deparaffination	3 changes in Xylene for 5 min each.
Rehydration	Tissues rehydration with decreasing ethanol grades 100% and 95% twice each for 10 min.
Antigen retrieval	Slides immersed in sodium citrate buffer and heated for 10 minutes at 50 °C.
Blocking of Endogenous peroxidase	Sections were incubated with 0.1% hydrogen peroxide Diluted in PBS for 30 min.
Blocking serum	Sections were incubated in 1% blocking serum in PBS for 1 h.
Primary Antibody	Sections were incubated with primary antibody of interest diluted in 1.5% blocking serum overnight.
Secondary Antibody	After washing with PBS, Sections were incubated with biotinylated secondary antibody for 1 h 30 min.
AB enzyme reagent	After washing, sections were incubated with AB enzyme reagent for 30 min.
Peroxidase substrate staining	Sections were incubated with 1-3 drops of peroxidase substrate until suitable substrate developed.
Counter staining	Sections were counter stained with haematoxylin for 20 s.
Dehydration	Sections were dehydrated with increasing grades of 95% and 100% ethanol twice each for 10 s.
Mounting	1-2 drops of permanent mounting media was applied and covered with glass cover slips.

3.10.16   Methodology of Antioxidant Measurement in Granulation Tissue

Antioxidant study in granular tissue determined the level of lipid peroxidation, superoxide dismutase (SOD) activity, catalase activity (CAT) and glutathione peroxidase (GPx) activity.

3.10.16.1 Determination of Dermal Tissue Lipid Peroxidation

The level of lipid peroxidation in dermal tissue was measured in terms of malondialdehyde (MDA, a product of lipid peroxidation) content and had been determined by using thiobarbituric acid (TBA) reagent. The reactivity of TBA was determined based on the method reported in (Buege & Aust, 1978). Briefly, the stock solution containing equal volume of 15% (w/v) TBA in 0.25 N HCl and 2-TBA 0.37%

84

(w/v) in 0.25 N HCl was prepared. A solution of 1:2 (v/v) sample to stock solution was prepared by mixing in a screw-capped centrifuge tube, vortexed, and heated for 15 min in a boiling water bath. After cooling in ice, the precipitate was removed by centrifugation at $1,000 \times$ g for 15 min. The absorbance wavelength of the supernatant was measured at 532 nm against a blank containing all reagents, except the test sample. The value was expressed as micromole (μmol) of MDA formed/g protein.

3.10.16.2 Measurement of Superoxide Dismutase (SOD) Activity

SOD activity was determined by using epinephrine assay, according to a method described by Misra et al. (Misra & Fridovich, 1972). The 2.0 ml reaction mixture was prepared by using 0.05 M carbonate buffer (pH 10.2), 30 mM epinephrine (freshly prepared), and clear supernatant. Change in absorbance was recorded at 480 nm, and measured at 10 s intervals for 1 min in a spectrophotometer (Hitachi model, u-2001). The activity of the enzymes was expressed as units per mg protein per min (/mg/min).

3.10.16.3 Measurement of Catalase Activity (CAT)

Dermal tissue catalase activity was assayed by adhering to the method proposed by Maehly et al. (Maehly & Chance, 1954). The reaction mixture was prepared in a final volume of 2.5 ml containing 0.05 M phosphate buffer (pH 7.0) and appropriate amount of supernatant. The reaction was initiated through the addition of 19 mM hydrogen peroxide (H_2O_2). The decomposition of H_2O_2 was followed directly by measuring the decrease in absorbance at 240 nm, at 10 s intervals for 1 min in a spectrophotometer (Hitachi model, U-2001). Catalase activity was expressed as μmol of hydrogen peroxide (H_2O_2) metabolized/mg protein/min.

3.10.16.4 Measurement of Glutathione Peroxidase (GPx) Activity

Glutathione peroxidase activity was measured according to the method described by Rotruck *et al.* (1973) (Rotruck *et al.*, 1973). A reaction mixture containing 2.0 ml of 0.4M Tris- HCl buffer, pH 7.0, 0.01 ml of 10mM sodium azide, 0.2 ml supernatant, 0.2 ml of 10 mM glutathione, and 0.5 ml of 0.2 mM H_2O_2 was prepared. The mixture was incubated at 37ºC for 10 min, and followed by termination of the reaction with the addition of 0.4 ml 10% (v/v) trichloroacetic acid (TCA). The samples were then centrifuged at 5000 rpm for 5 min. The absorbance of the product was recorded at 430 nm and expressed as µmol of glutathione (GSH) consumed/mg protein/min.

3.10.17   Statistical Analysis

The results are expressed as mean ± standard errors of the mean (S.E.M). Statistical analyses were performed using SPSS software version 18. The differences between groups were evaluated with one way ANOVA, and followed by Tukey post hoc test. *P* value <0.05 was deemed as significant (Park, 2003). Besides, the mean value for each group was obtained from six different rats.

CHAPTER 4: RESULTS AND DISCUSSIONS

Results of the whole materials characterizations of the CMFTO electroceramic and S1050/PDMS composite film are discussed in this chapter. All the structural, morphological, thermal, physical, and electrical characterizations of CMTFO and S1050/PDMS composite film are narrated in the first and second half of the current chapter, respectively. Later, drug carrying ability as well as *in vitro* biocompatibility results of CMTFO nanocomposite sintered at 1050 °C is discussed.

4.1   Characterizations of CMFTO Electroceramic

The main focus of this section is to describe the structural, morphological, physical, electrical, and dielectric characteristics of the CMFTO electroceramic sintered at different temperatures.

4.1.1   Structural Characterizations of CMFTO Electroceramic

In this section, the structural characteristic results, such as thermal analysis, XRD, SEM and pore size distribution of CMFTO electroceramic have mainly been discussed.

4.1.1.1   Thermal Analysis

After a small weight-loss (1.5 wt%) owing to removal of adsorbed water or moisture up to 120 °C, three important transitions have been found for the unsintered ceramic pellet in TGA (see Figure 4.1). According to TGA, the sintering temperatures were determined in order to get the different phases of the sintered materials. A larger weight change at 316.91–371.39 °C occurs due to removal of organic content such as absolute alcohol used during synthesis.
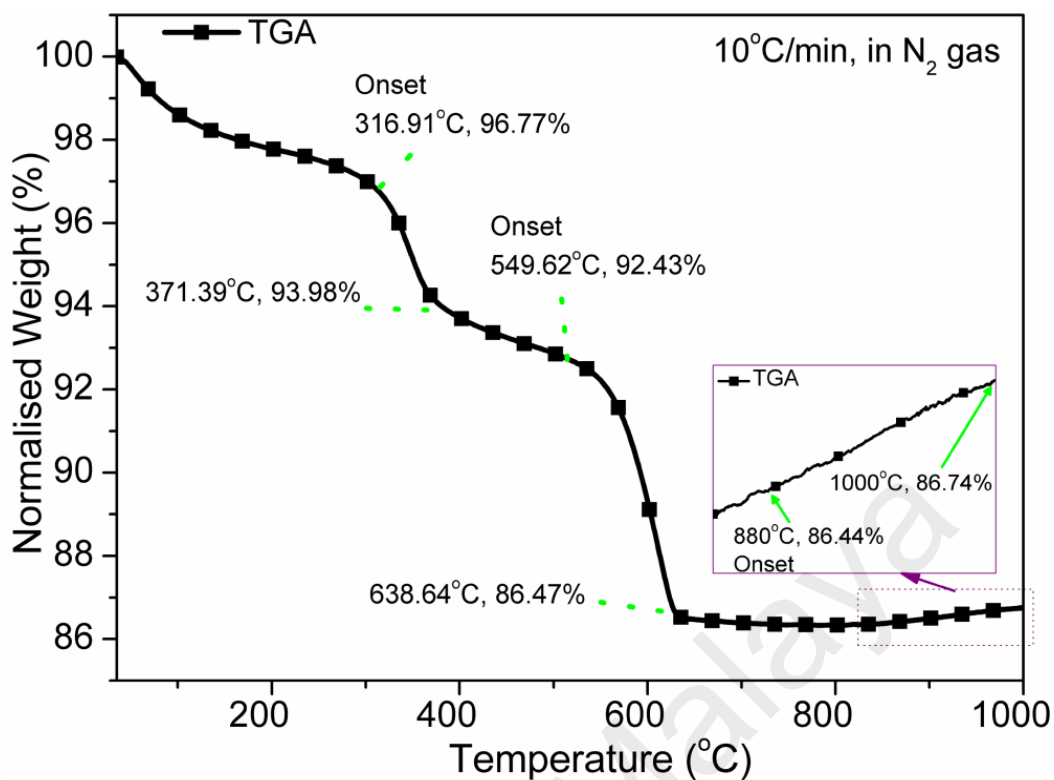
Figure 4.1: TGA of unsintered powder from 35 to 1000 °C (ramp: 10 °C/min, atmosphere: nitrogen gas).

The next largest weight change at 549.62–638.4 °C occurs due to decomposition of carbonate and formation of a new phase of CaTiO$_3$. This result is quite similar to the CCTO materials up to this stage (Zhu *et al.*, 2009). Further, the phase transformation would be confirmed by XRD and microscopy studies. Interestingly, the weight-change of the material goes upwards after 800 °C and indicates the diffusion in of more other elements because of transformation Fe$_3$O$_4$ from Fe$_2$O$_3$ at high temperature. It implies that a Fe^{3+} vacancy is created at higher temperature at above 800 °C which may further influence the dielectric properties of the ceramics (Pramanik *et al.*, 2013; Said *et al.*, 2015).

4.1.1.2 XRD Analysis

XRD patterns of unsitered and sintered at 1050 °C ceramic materials are depicted in Figure 4.2a–b. Presence of almost all the used raw materials was observed in XRD-pattern of unsitered ceramic mixture. The major crystalline peaks shown by anatase-TiO_2 (PDF:98-015-4609) along with few Fe_2O_3 (PDF:01-084-0308) are indicated in Figure 4.2a. The other small peaks of CaO and $MgCO_3$ have also been detected. A new peak of calcium carbonate ($CaCO_3$, PDF: 01-072-1650) at $2\theta = 29.59°$ indicates that the CaO and $MgCO_3$ had reacted during mechanochemical mixing. After sintering at 450 °C, the armalcolite phase has been found (Figure 4.2b) and it increases as sintering temperature increases up to 1050 °C (see Figure 4.2b-e). Above 650 °C, a few peaks of a new perovskite $CaTiO_3$ were prominently observed (Figure 4.2b) and intensity as well as number of $CaTiO_3$-peaks was found to be increased at 1050 °C (see Figure 4.2d-e). At sintering condition 1050 °C, the three new phases, which were resembled with the standard XRD patterns of armalcolite ($Fe_2MgTi_3O_{10}$, PDF:00-013-0353), perovskite ($CaTiO_3$, as PDF:00-008-0092), and Fe_3O_4 (PDF No. 01-088-0315), are depicted with different symbols in Figure 4.2e.

The two different crystallite sizes of the sintered materials at $2\theta = 25.70°$ for (101) plane of $Fe_2MgTi_3O_{10}$ and $2\theta = 33.32°$ for (440) plane of $CaTiO_3$ are 20.7 nm and 5.9 nm, respectively. This result clearly indicates that the material sintered at 1050 °C contained mainly two phases, which is also observed in the scanning electron micrograph (see Figure 4.3e). Interestingly, at $2\theta = 35.72°$, another new peak of Fe_3O_4 for (311) plane clearly indicates the transformation of Fe^{3+} into Fe^{2+} from Fe_2O_3 after sintering at 1050 °C. According to the peak areas of the corresponding peaks, the amounts of $Fe_2MgTi_3O_{10}$, $CaTiO_3$ and Fe_3O_4 present in the material sintered at 1050 °C are 85.80%, 12.16% and 2.04%, respectively (see Table 4.1) with respect to the total area of peak. The crystallite size of the individual phases for the different sintering

89

temperatures is also illustrated in Table 4.1. It indicates that these three phases increase with increasing of sintering temperature. The concentration of $CaTiO_3$ and Fe_3O_4 phases could not be detected since they were less than 1% in together up to 650 °C and overlapping of the peaks with the raw materials. However, phase concentration (PC) of Fe_3O_4, which might be formed at around 800 °C, were degraded from 7.36% to 2.03% due to increasing of temperature from 850 to 1050 °C (see Figures 4.2d and 4.2e).

On the other hand, PC of $Fe_2MgTi_3O_{10}$, which might be nucleated at around 400 °C, and $CaTiO_3$ phase, which might be developed at around 600 °C, were increased from 82.96% (at 850 °C) to 87.81% (at 1050 °C) and from 9.68% (at 850 °C) to 12.16% (at 1050 °C), respectively due to increasing of sintering temperature (see Figure 4.4). This is an extremely advantageous *in situ* type step-sintering technique for controlling the second phase materials in a nanocomposite according to desired properties.

Lattice parameters of the orthorhombic armalcolite ($Fe_2MgTi_3O_{10}$) and cubic perovskite ($CaTiO_3$) were calculated by the Equations 4.1 and 4.2, respectively; and the values are illustrated in Table 4.2.

$$\left[\frac{1}{d_{hkl}^2}\right]_{orthorhombic} = \frac{h^2}{a^2} + \frac{k^2}{b^2} + \frac{l^2}{c^2} \tag{4.1}$$

$$\left[\frac{1}{d_{hkl}^2}\right]_{cubic} = \frac{h^2 + k^2 + l^2}{a^2} \tag{4.2}$$

where, d_{hkl} is the inter-planer distance between the planes (h k l); and *a*, *b* and *c* are unit cell parameters.

It can be noticed that unit cell volume of both crystals lowers than that of standard unit cells of the corresponding crystals except the material sintered at 450 °C. This volume expansion is an indication of presence of raw materials along with the developed armalcolite crystals at 450 °C sintering condition. All the other volume shrinkage indicates normal sintering effect on the unit cell volume of the new phases.

An interesting result observed by the XRD is that the unit cell volume as well as crystallite sizes of the $CaTiO_3$, $Fe_2MgTi_3O_{10}$ and Fe_3O_4 increased significantly with the sintering from 850 to 1050 °C. Hence, this result implies that the particles of $CaTiO_3$ obtained at the 850 °C sintering condition were not grown completely. This result is also supported by the crystallite size results.
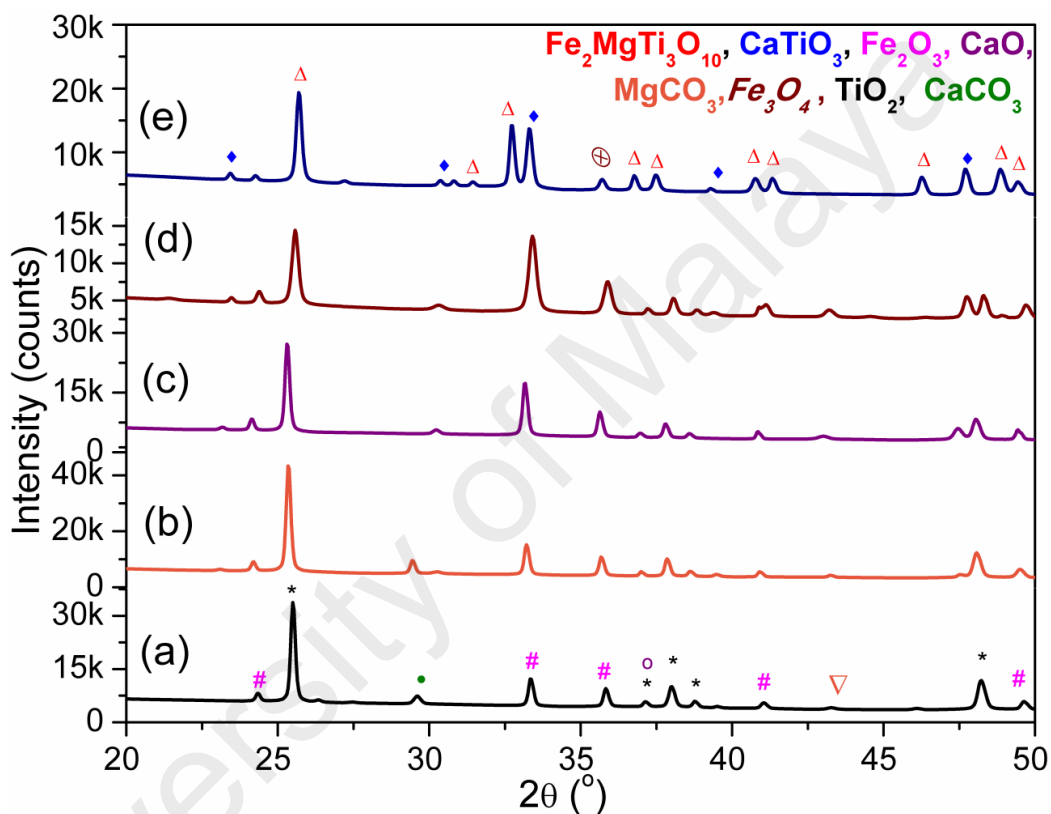
Figure 4.2: X-ray diffraction study of (a) unsintered and sintered at (b) 450 °C, (c) 650 °C, (d) 850 °C, and (e) 1050 °C samples.

Table 4.1: Concentration of crystalline phases present the sintered nanocomposites evaluated from XRD.

Crystalline Phase	450 °C		650 °C		850 °C		1050 °C	
	t	PC	t	PC	t	PC	t	PC
	nm	(%)	nm	(%)	nm	(%)	Nm	(%)
$Fe_2MgTi_3O_{10}$	17.5	-	18.1	-	19.3	82.96	20.7	85.80
$CaTiO_3$	-	-	4.9	<1%	5.2	9.68	5.9	12.16
Fe_3O_4	-	-	-	-	10.5	7.36	20.5	2.04

t = Crystallite size; PC= Phase concentration

91

Table 4.2: Comparison of lattice parameters of the two phases of sintered nanocomposites with the standard crystals.

Materials	Lattice Parameters (Å)			Lattice Volume	Unit Cell Volume Strain	Crystal System
	A	b	c	Å^3	%	
Unsintered CMTFO	-	-	-	-	-	-
CMTFO450						
$FeMg_{0.5}Ti_{1.5}O_5$	10.13	10.19	3.74	386.84	+6.69	Orthorhombic
CMTFO650						
$FeMg_{0.5}Ti_{1.5}O_5$	11.72	10	2.96	347.23	-4.24	Orthorhombic
$CaTiO_3$	-	-	-	2785.42	-21.46	Cubic
CMTFO850						
$FeMg_{0.5}Ti_{1.5}O_5$	9.59	8.15	3.73	292.07	-19.45	Orthorhombic
$CaTiO_3$	15.16	-	-	3482.53	-1.81	Cubic
Fe_3O_4	8.29	-	-	571.15	-2.77	Cubic
CMTFO1050						
$FeMg_{0.5}Ti_{1.5}O_5$	9.66	10.05	3.73	362.12	-0.13	Orthorhombic[*]
$CaTiO_3$	15.18	-	-	3498.74	-1.35	Cubic[*]
Fe_3O_4	8.33	-	-	579.57	-1.34	Cubic[*]
JCPDS Standard						
$FeMg_{0.5}Ti_{1.5}O_5$PDF: 00-013-0353	*9.77*	*9.95*	*3.73*	*362.59*	-	*Orthorhombic*
$CaTiO_3$PDF: 00-008-0092	*15.25*	-	-	*3546.58*		*Cubic*
Fe_3O_4PDF: 01-088-0315	*8.375*	-	-	*587.43*		*Cubic*

4.1.1.3   SEM Analysis

A uniform submicro-porous structure of the ceramic nanomaterials is revealed in the FESEM-images of Figure 4.3. Average particle size of the unsintered ceramic (~200 nm, see Figure 4.3a) was found to increase at sintering temperatures 450 °C (~350 nm, see Figure 4.3b) and 650 °C (~750 nm, see Figure 4.3c).
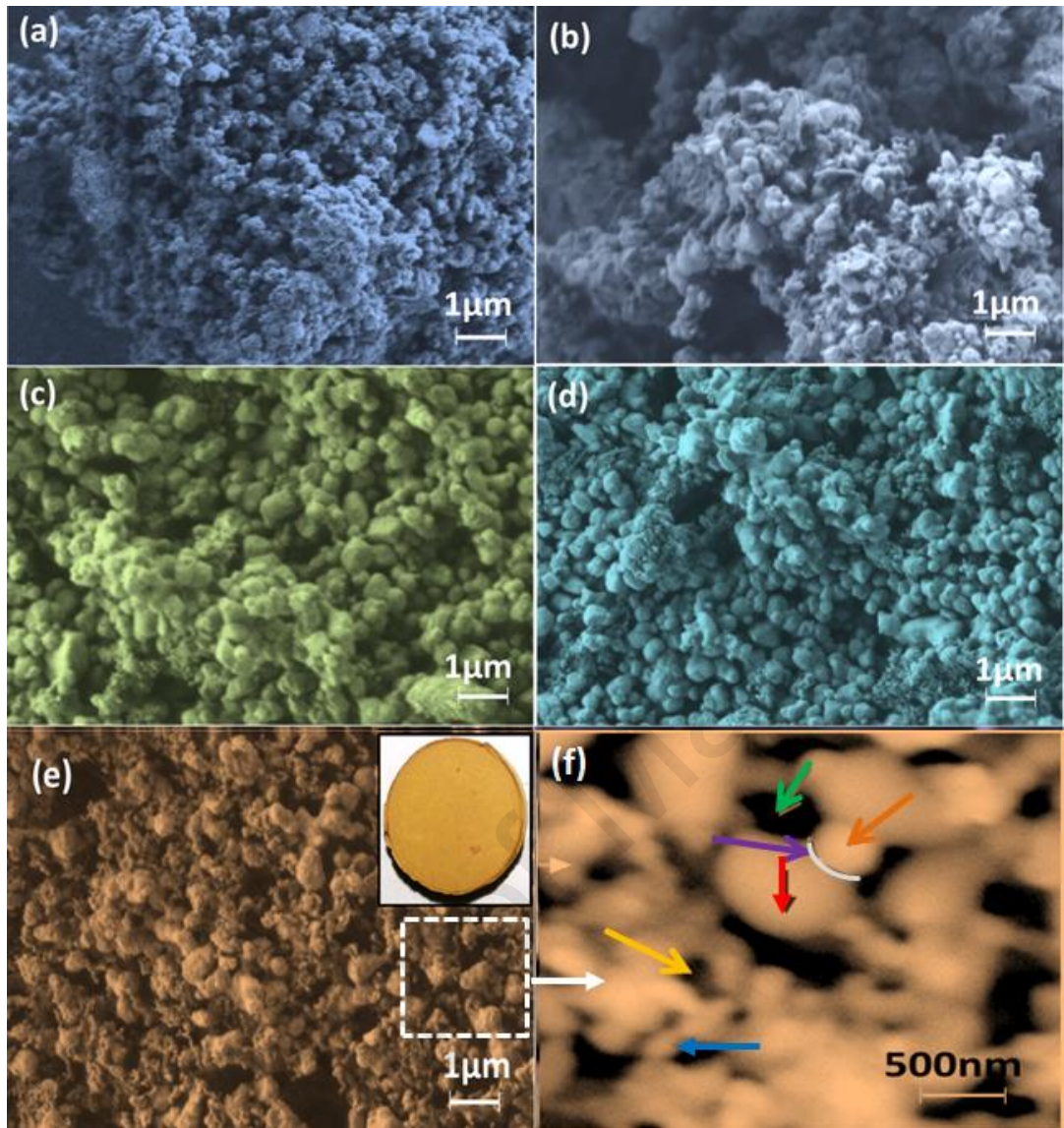
Figure 4.3: FESEM images of the (a) unsintered, (b) S450, (c) S650, (d) S850, (e) S1050 and (f) S1050 at higher magnifications ceramics samples.

However, growth rate was controlled by changing sintering steps for 850 and 1050 °C without much change in total pore distribution, where average pore sizes are 500 and 850 nm, respectively. The average particle sizes in the S850 and S1050 samples are 780 and 670 nm, respectively (see Figure 4.3d and 4.3e). A smaller size (typically <100 nm) of new phase of $CaTiO_3$ particles has been noticed in Figure 4.3e. The green and yellow arrows indicate pores and particles; and vertical red and horizontal blue arrows indicate the armalcolite (average size: 708 nm) and perovskite (<100 nm) structure phases,

respectively. The grain boundaries and grains are clearly revealed in the sintered materials at 1050 °C at higher magnifications as indicated by purple and orange colored arrows in Figure 4.3f.

4.1.1.4 Pore Size Distribution Analysis

Figure 4.4 depicts the pore size distribution (PSD) of unsintered and all the sintered (at 450, 650, 850, and 1050 °C) materials measuring from the Inverted SEM images using ImageJ software. The materials sintered up to 650 °C (see Figures 4.4a–4.4c) showed almost bimodal or single modal pore distribution with a PSD less than1.5 μm.
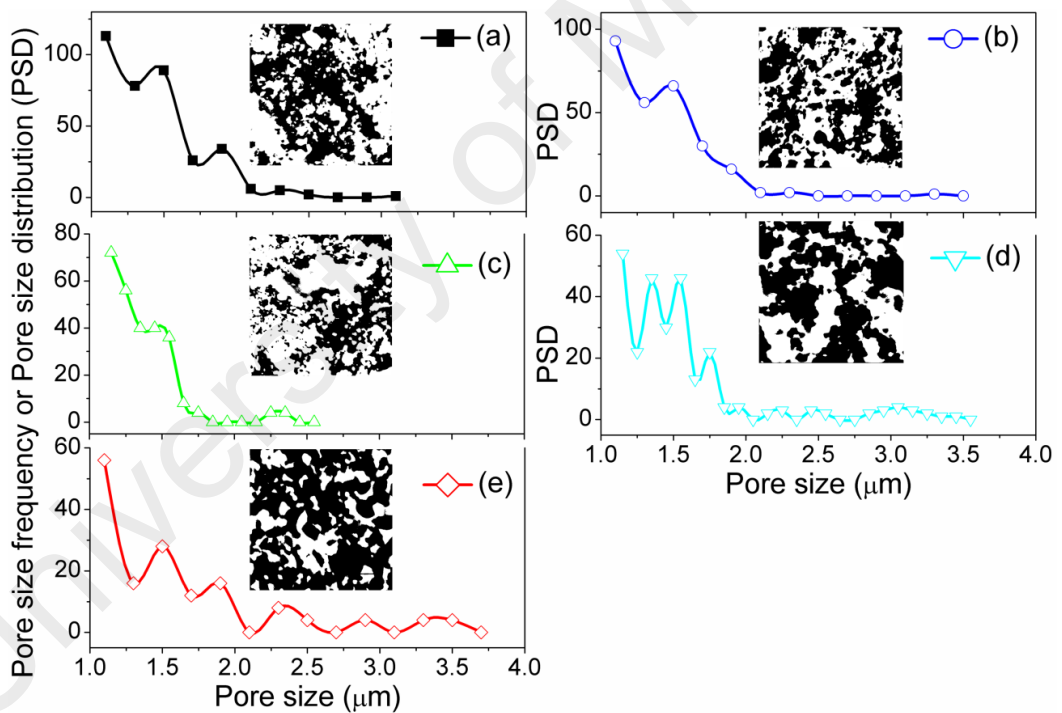
Figure 4.4: Pore size distribution (PSD) of (a) unsintered and sintered at (b) 450 °C, (c) 650 °C, (d) 850 °C and (e)1050 °C materials.

However, at higher sintering conditions such as 850 and 1050 °C (see Figures 4.4d–e), the maximum pore size was also found to be more than 3.5 µm. This result suggests that larger size open pores have been developed at higher sintering temperatures. The multimodal PSD at 850 and 1050 °C indicates that three different types of cluster have been developed by three different structural phases such as armalcolite, perovskite and ferrite, which will be confirmed by XRD study (see Figure 4.2), are inter connected. Hence, the multimodal PSD present in the sintered materials with higher pore size would be responsible to possess higher dielectric constant.

4.1.1.5   Physical Characterizations of CMTFO Electroceramic

The bulk density, open porosity, water absoption and WCA of all the pellet samples are depicted in Figure 4.5. Lower WCA in all the sintered pellets are significantly lower than that of unsintered pellet. The open porosity of all these materials was found to have lower than their close porosity. Open porosity present in the materials was calculated using their bulk density. The open porosity of unsintered and sintered at 1050 °C were measured to be 73.84±1.24 and 40.26±1.33%, respectively. On the other hand, density of unsintered material was strictly controlled (almost half) from 1.989±0.091 g/cc to 0.941±0.035 g/cc after sintering at 1050 °C. It is possible due to lattice diffusion phenomenon during sintering with keeping substantial porosity (Pramanik *et al.*, 2014). Lower density values of these pelletes compared to its comprised commercial ingredients indicates the presence of higher amount of porosity. This study also confirms that a new phase, CaTiO$_3$ (see Figure 4.2) occurred by lattice diffusion mechanism (Tripathy *et al.*, 2016). Total porosity present in the materials was evaluated from water absorption (see Figure 4.5). The higher amount of water absorption (nearly 67%) in the material sintered at 1050 °C confirms the uniform porosity that was revealed in the FESEM image (see Figure 4.3e). This material also showed lowest

density and larger porosity (compared to the sintering condition at 850 °C) with a wide pore size distribution. A larger pore size (see Figure 4.4) and high open porosity (see Figure 4.5) imply a much more active surface towards water vapor and thus the sensitivity of the capacitance to humidity will be increased. The large pores are necessary for a rapid response to exhibit easily adsorption and desorption or condensation of water vapor (Nitta *et al.*, 1980). Since the sample sintered at 1050 °C showed higher amount of water absorption (~ 67%) and higher porosity with lower density compared to the unsitered or sintered at or below 850 °C, the material sintered at 1050 °C would only considered as a most favorable candidate for humidity sensors analysis in further studies of this present work (Ataollahi *et al.*, 2015; Chuang *et al.*, 2010; Tripathy *et al.*, 2014; Yazawa *et al.*, 2012).
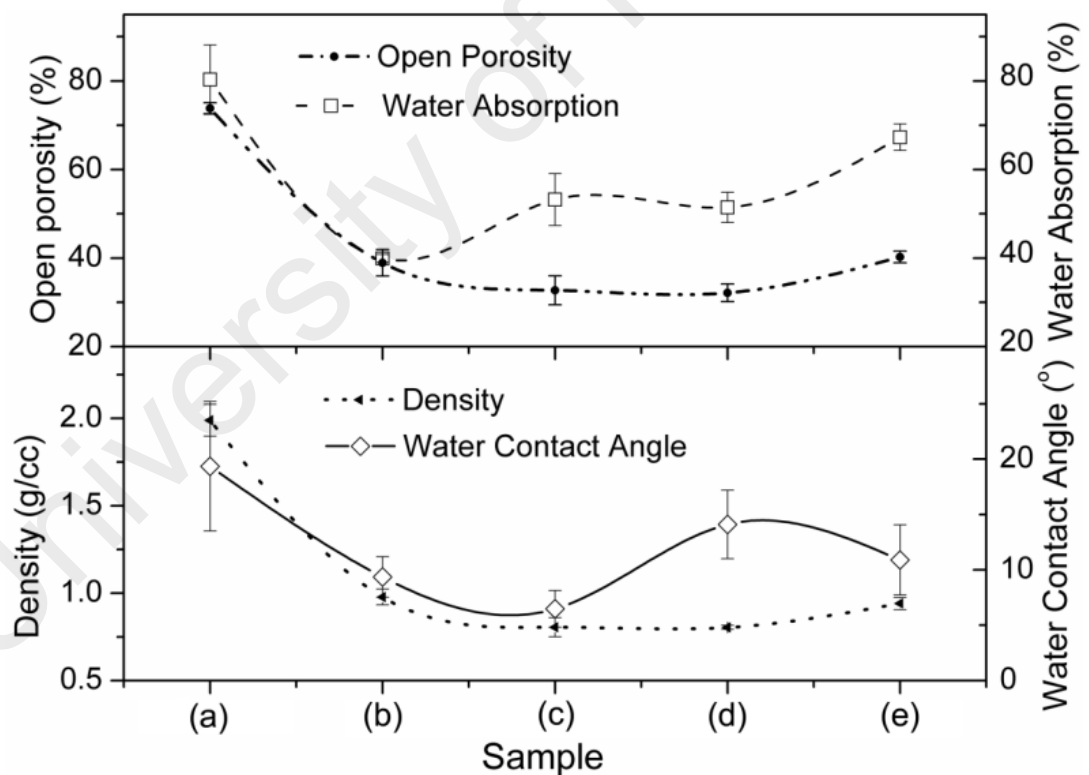
Figure 4.5: Density, open-porosity, water absorption and water contact angle (WCA) of (a) unsintered and sintered at (b) 450 °C, (c) 650 °C, (d) 850 °C and (e) 1050 °C ceramic samples.

4.1.2   Electrical and Dielectric Characterizations of CMFTO Electroceramic

From the above narrated SEM analysis of sintered and unsintered materials, it has been confirmed that the material sintered at 1050 °C forms grain boundary and exhibits three different phases, which were also confirmed in the XRD analysis (see Figure 4.2 and Tables 4.1 – 4.2). The multimodal PSD in the sintered material with higher pore size had been observed, which might alter the electrical characteristics of the developed nanocomposite. The confirmation of the formation of grain and grain boundary from the structural and morphological analyses claims the possibility of formation of the interfacial polarization and barrier layer formation at grain–grain boundary interfaces, which might alter the electrical or dielectric response of the developed perovskite structured complex ferrite material (Rai *et al.*, 2010).

In the present study, it was also expected that the higher cooling rate at 20 °C/min between 750 and 1050 °C might cause re-oxidation only at the surface layer of nanocrystals and grain boundaries due to their more disorderness and high energetic instability. As a result, insulating barrier layers might be generated at the grain boundaries and surface layers. Due to the very small particle size < 100 nm sintered at 1050 °C (see Figure 4.3e), more re-oxidation might occur at the perovskite structured part of the composite. In fact, more semiconducting characteristics might be developed at the perovskite structured domain of the composite due to the formation of insulating oxide layers (Dixit *et al.*, 2007; Raevski *et al.*, 2003). As a result, it may enhance the dielectric characteristics of the ceramic nanocomposite. Therefore, it is very important to carry out a thorough analysis of electrical, as well as dielectric characteristics of the present newly developed perovskite structured based armalcolite nanocomposite for its potential capacitive and memory storage applications.

4.1.2.1 Dielectric Study

The changes in dielectric constant (ε') and loss factor or dielectric loss tangent (tanδ) for unsintered and all the sintered samples are depicted in Figure 4.6 as a function of frequency in logarithm scale (in log-scale) at 25 °C. The dielectric constants were found to be decreased exponentially with increasing frequency. The ε' of sintered nanocomposites was higher than the unsintered compound. Besides, Figure 4.6 depicts that as the frequency increased, the ε' decreased. This trend also resembled the CCTO materials developed by different processes in previous studies (Rai *et al.*, 2009). The ε' was found to increase with the increasing sintering temperature. Meanwhile, for nanocomposite sintered at 1050 ºC ($Fe_2MgTi_3O_{10}/CaTiO_3/Fe_3O_4$), the ε' was the highest ($\varepsilon' = 8000$) and significantly higher than the unsintered compound ($CaMgFe_{1.33}Ti_3O_{12}$) ($\varepsilon' = 226$) at 100Hz frequency. This was possibly due to the interfacial polarization; because the major charge carriers might be blocked at the electrode interface under the influence of an electric field. This result indicates that the newly developed ceramics consist of insulating grain boundaries and semiconducting grains (Thostenson & Chou, 1999), and it was found to be more prominent in the microstructure of the materials after sintering (see Figure 4.3f). Therefore, the charge carriers are accumulated at the interface between these grains or at grain-boundaries that influences the dielectric constants, according to the Maxwell–Wagner effect (Babu & Govindan, 2014). In addition, Lunkenheimer et al., had also suggested that the grain-boundary effect and sintering conditions, which might change the oxygen partial pressure during sintering, could be a possible reason for this charge accumulation at the sample surface (Lunkenheimer *et al.*, 2004). The dielectric constant of the present material sintered at temperature 1050 °C is extremely high in comparison to the differently doped CCTO materials (ε' of Mg-doped CCTO ~7621.5, ZrO_2-doped CCTO ~ 5120, La-doped CCTO ~ 2700, Fe-doped CCTO ~ 6000, and so on, at 100 Hz), as reported in (Boonlakhorn &

Thongbai, 2015; Kwon *et al.*, 2008; Patterson *et al.*, 2005; Prakash & Varma, 2006; Rai *et al.*, 2011; Vangchangyia *et al.*, 2013).   Furthermore, the ε′ value for all the samples decreased abruptly at lower frequency up to 10^3 Hz and after that, the rate of change with frequency became very sluggish. The decreased trend in dielectric constant with increasing frequency indicates that this relaxation is owing to the Maxwell–Wagner polarization. This trend was also found in other studies on CCTO-based materials (Babu & Govindan, 2014; Devan & Chougule, 2007; Ibrahim *et al.*, 2012; Rai *et al.*, 2012; Rai *et al.*, 2011; Sivakumar *et al.*, 2010). On the other hand, the ε′ had been related to the dipole polarizability (an atomic property) of a material, which might arise from the structures with a permanent electric dipole that could change the orientation in an applied electric field (Homes *et al.*, 2001). Besides, Lunkenheimer et al., had also suggested that the drastic change in ε′ after 10^3 Hz and increasing trend in ε′ values at higher temperature were non-intrinsic and had been connected to the occurrence of grain boundaries in the polycrystalline samples (Lunkenheimer *et al.*, 2004). They stated that the contributions might arise from the charge carriers accumulated at the interface between grains or at grain boundaries and electrode polarization effect. The present investigated nanocomposites comprised of orthorhombic armalcolite ($Fe_2MgTi_3O_{10}$) with cubic perovskite ($CaTiO_3$) and cubic inverse spinel (Fe_3O_4) heterogeneous structural materials, according to the results obtained from the XRD analysis. Moreover, according to the Maxwell–Wagner principle, a heterogeneous structured material experiences interfacial polarization due to the trapping of charge carriers movement at the interfacial region at low frequency (Maxwell, 1973; Wagner, 1973). At high frequency, the frequency of hopping between ions could not follow the frequency of applied electric field and as a result, the dielectric constant decreased (Adams *et al.*, 2002). In addition, another phenomenon that might work for obtaining the high dielectric constant at lower frequency owed to the effect of titanium-based

99

ferro-oxide materials. It was reported that the perovskite-structured titanates such as $ATiO_3$ (where A = Ca, Sr, and Ba), at high sintering temperature, lost oxygen and re-oxidation took place at the time of cooling (Pullar *et al.*, 2009). In the present study, the re-oxidation may occur only at the surface layer of crystals and grain boundaries owing to the higher cooling rate at 20 °C/min between 1050 and 750 °C. This happened because the surfaces of crystals and grain boundaries had been more disordered and due to the presence of highly energetic unstable parts of a particle. As a result, the insulating layers were formed at the surface layers and grain boundaries. The perovskite-structured part of the material was more prone to be re-oxidized since its particle size was very small, < 100 nm (see Figure 4.3e). Due to the formation of insulating oxide layers, the perovskite-structured part became more semiconducting (Dixit *et al.*, 2007; Raevski *et al.*, 2003) and resulted in high dielectric constant compared to other ceramic materials (Brize *et al.*, 2006). Therefore, the present newly developed non-intrinsic giant dielectric ceramic nanocomposites would be a potential candidate for commercial applications as internal barrier-layer capacitor (IBLC).

Figure 4.6 also depicts the tanδ characteristics for all the sintered and unsintered ceramics. The tanδ value was higher at low frequencies range up to 10^3 Hz and it decreased exponentially up to 10^5 Hz, and followed by a small change until 10^6 Hz. The decrease in tanδ value with frequency was observed probably due to the electron hopping between Fe^{2+} and Fe^{3+} in octahedral sites even at 25 °C (Verwey, 1939) and also due to ionic interactions between Ti^{2+}, Ca^{2+}, Mg^{2+}, and Fe^{3+} ions (Ali *et al.*, 2014; Bamzai *et al.*, 2014; Radwan *et al.*, 2003). It also indicates that the tanδ peak for the sintered ceramic is due to dielectric relaxation at the low frequency region by space charge polarization, which was developed at the interfaces between the two-phased grains and grain-boundaries with different electrical conductivities (Bueno *et al.*, 2007). In the present study, the obtained tanδ values for both unsintered and sintered at 1050

°C samples are 0.023 (lowest) and 0.114 (highest), respectively, which have been extremely lower than the previously published different giant dielectric CCTO-based ceramic materials (e.g., Fe-doped CCTO ~ 0.89, Co-doped CCTO ~ 0.7, P_2O_5-doped CCTO ~ 3.5, Zr-doped CCTO ~ 0.4, and so on at 1 MHz) (Ardakani *et al.*, 2012; Goswami & Sen, 2010; Mu *et al.*, 2010; Patterson *et al.*, 2005; Rai *et al.*, 2010; Vangchangyia *et al.*, 2013). Therefore, the present ceramic nanocomposite could be a potential candidate for fabricating the capacitive devices and sensors applications.
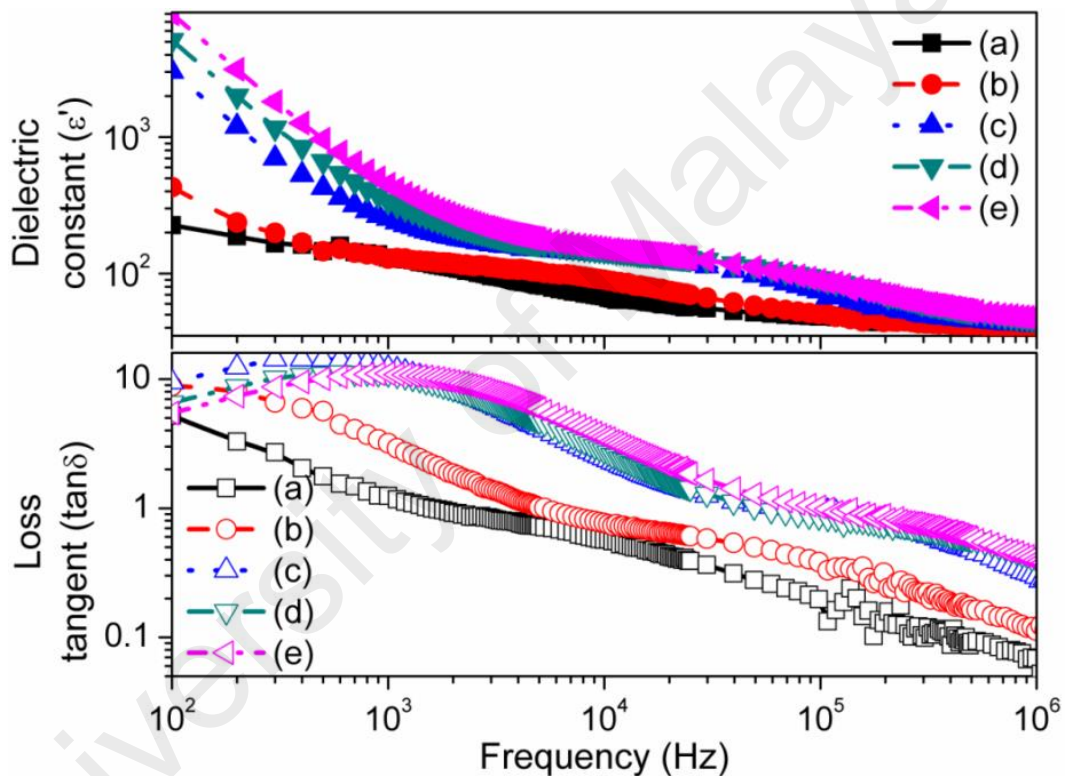
Figure 4.6: The variations of dielectric constant (ε′) (closed symbols) and dielectric tangent loss (tanδ) (opened symbols) for both unsintered and sintered materials at 25 °C with frequency in logarithmic scale (i.e., log(*f*)): (a) unsintered and sintered at (b) 450 °C, (c) 650 °C, (d) 850 °C, and (e) 1050 °C samples.

4.1.2.2   Impedance Analysis

Interfacial polarization and barrier layer formation at grain–grain boundary interfaces are the main common reasons for getting higher ε′ in a perovskite-structured complex

ferrite material (Rai *et al.*, 2010). The resistance and capacitance associated with an electrically active grain and the grain boundary regions in the complex ferrite material have been evaluated using impedance spectroscopy. The resistance and capacitance values generated at the grain and grain boundary are modelled by using a series-connected two parallel RC (resistor-capacitor) elements. In the series connected with two RC parallel networks; one represents the effect of grain, while the other represents the response of grain boundary. In order to understand the effects of grain and grain boundaries resistance on the dielectric properties, the complex impedance Cole–Cole plots at 25 °C of all the unsintered and sintered ceramic samples are depicted in Figure 4.7. In unsintered or low temperature sintered (450 °C) samples, a single semicircular arc was observed in the complex impedance (Z^*) plane of Cole-Cole plot. This high-frequency semicircular arc confirms the dipole relaxation process inside the material. The resistance of the material was calculated from the intersection of the semicircular arc in the Z'-axis. The non-zero intercept of the arc passing through the origin on the Z' axis in a high frequency range (i.e., lower Z'-value range) was probably due to the resistance of grain (R_g), while the second arc in the lower frequency range (i.e., higher Z'-value range) was obtained due to the resistance of the grain boundary (R_{gb}). The values of bulk resistance (R_b) and bulk capacitance (C_b) were obtained from the intercept of the semicircular arcs on real axis. The semicircular arc due to the grains at high-frequency had been suppressed by the high resistance of the grain boundary (R_{gb}), which was observed in IBLC (Raistrick *et al.*, 1987). The IBLC refers to an effect of interfacial polarization (also known as Maxwell–Wagner polarization) at grain boundaries. The presence of a semicircular arc at the Z^*-plane (Z'' vs Z' plot) due to the grain boundary in all the sintered nanocomposites above 450 °C was clearly observed in the impedance spectrum (see inset of Fig. 4.7). The first semicircle in higher frequency range is the effect of bulk property, whereas the lower frequency ranged semicircle is

the effect of grain boundary property. On the other hand, lowering in semicircular radius of these plots with increasing temperature suggests an evidence of polarization phenomena with distributed relaxation times, and represents an estimation of the R_{gb}. The reduction in radius of the semicircular arc of the complex impedance plots, nevertheless, has been less for unsintered or lower temperature sintered sample (at 450 °C), but more in the higher temperature sintered (at 650, 850, and 1050 °C) nanocomposites. This is a clear indication of the dominant R_{gb} present in the sintered materials. Furthermore, a magnified scale of Cole–Cole plot of sintered material (1050°C) showed a prominent neck at $Z' = 1.37 \times 10^5 \Omega$. The Cole–Cole plots of high-temperature sintered material comprise of two semicircular arcs with their centers lying below the real axis. From the complex impedance Cole–Cole plot, it has been further noted that the centers of the semicircles are located away from the real axis and besides, the centers of the semicircular arcs moved towards the origin. This observation indicates the presence of relaxation species and it also confirms the non-Debye type relaxation process present in the nanocomposites materials. It provides further evidence of polarization phenomena with distribution of relaxation times. The electrical phenomenon that occurred inside the material was analyzed by using the brick-layer model (Raistrick *et al.*, 1987). Hence, from the impedance spectroscopy analysis, it has been confirmed that the grains resistance of the ceramics decreases with the increase in sintering temperature.
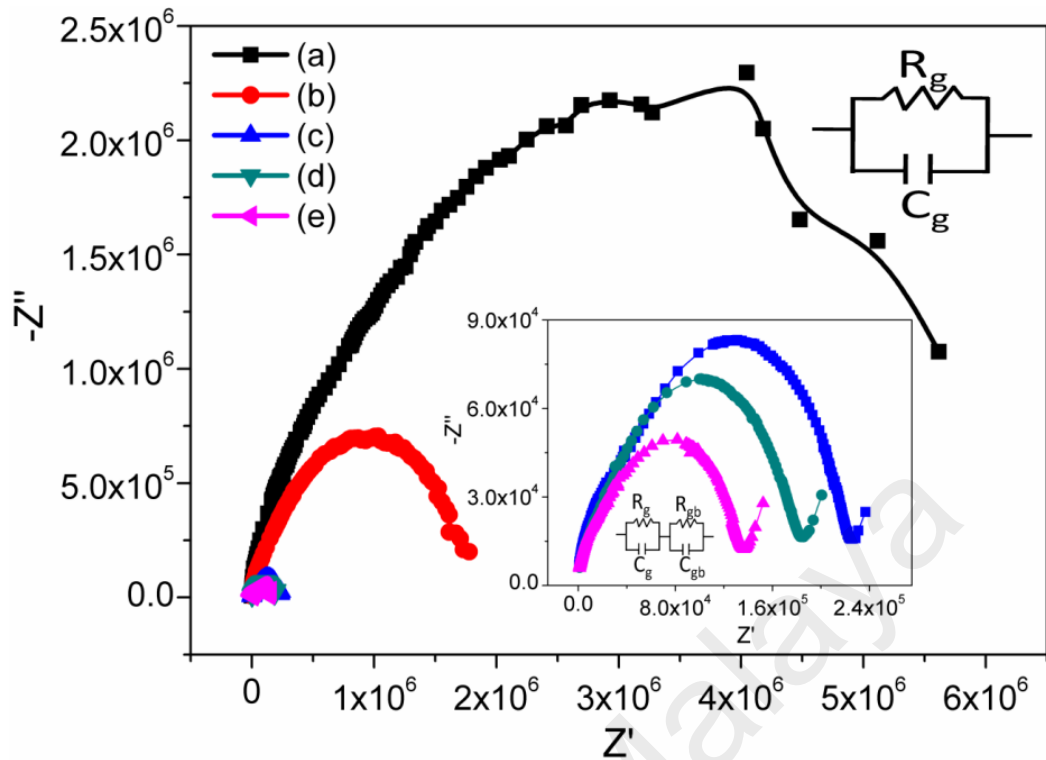
Figure 4.7: Complex impedance Cole–Cole plots of the (a) unsintered compound and sintered at (b) 450 °C, (c) 650 °C, (d) 850 °C, and (e) 1050 °C nanocomposite ceramic materials. Inset image represents a magnified scale of Cole–Cole plot of sintered (at sintered at 650 °C, 850 °C, and 1050 °C) materials with prominent neck at $Z' = 1.37 \times 10^5 \, \Omega$.

The variations of real (Z') and imaginary (Z") parts of impedance with frequency in logarithm scales at room temperature for all the sintered and unsintered samples are depicted in Figures 4.8A and 4.8B, respectively. Figure 4.8A shows that at a low frequency range, Z' displayed a larger value and it decreased significantly with the increase in frequency. Moreover, the effect of polarization in the samples might be responsible for this type of response (Homes *et al.*, 2001). This decreasing trend in Z'-value after 10^3 or 10^4 Hz indicates a possibility of increase in the σ_{ac} with increase in frequency. It was also observed that the impedance value decreased due to the sintering temperature. In higher frequency range, the Z' merged together, which suggests a possible release of space charge and a consequent lowering of the barrier properties in the ceramic composites (Kumar, Singh*, et al.*, 2006; Płcharski & Weiczorek, 1988).

104
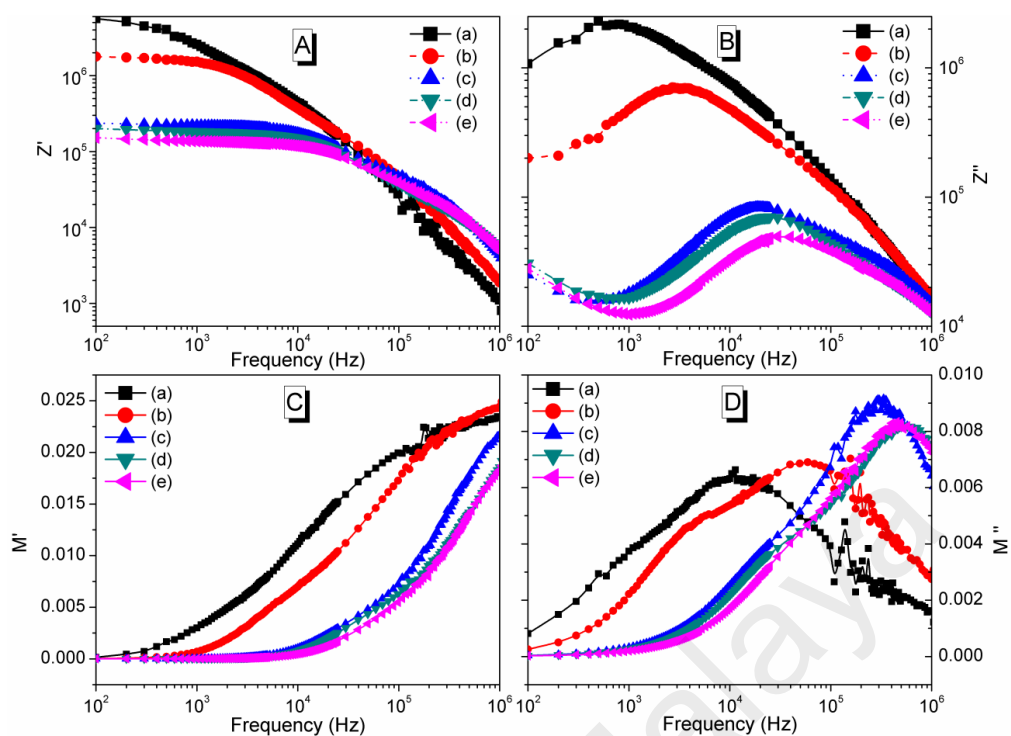
Figure 4.8: Variations in (A) real (Z') impedance(B) imaginary (Z") impedance in log-scale, (C)real (M') modulus(D) imaginary (M") modulus components of the (a) unsintered and sintered at (b) 450 °C, (c) 650 °C, (d) 850 °C, and (e) 1050 °C samples as a function of frequency in logarithmic scale at 25 °C.

Furthermore, the appearance of peak for the Z" with frequency (see Figure 4.8B) suggests the existence of relaxation properties of the material. Due to the increase in sintering temperature, more broadening of the peak was observed. The asymmetric broadening of the peak suggests the presence of electrical processes in the material with spreading relaxation time (Kumar, Choudhary, *et al.*, 2006). This broadening of peak after sintering might be due to some relaxation phenomena caused by hopping of electrons/oxygen ion vacancy/defects among the available localized sites (Kumar, Choudhary, *et al.*, 2006). Further monotonous decrease of Z"-value after maxima with the shift of peaks towards higher frequency side has been observed, and merging all the curves may occur due to the accumulation of space charge of the material.

4.1.2.3 Electrical Modulus Study

In Figures 4.8C and 4.8D, the changes in real (M′) and imaginary (M″) parts of modulus, respectively, as a function of frequency, are depicted. A very low value (nearly zero) of M′ in the low frequency region was observed. The modulus (M′ and M″) value of unsintered or low temperature (450 °C) sintered samples increases with the increase in frequency from the beginning. However, for the higher temperature sintered samples, the M′ or M″ value was almost constant up to 10 kHz. Beyond 10 kHz, the modulus value increased rapidly and reached to maxima. This continuous change in M′ with frequency may occur be due to the short-range mobility of charge carriers. Besides, Figure 4.8D illustrates that the asymmetric modulus (M″) peaks were shifted towards higher frequency. This was attributed to the motions of mobile ion charges (Borsa *et al.*, 1992). The broadening of asymmetry peak shows the spread of relaxation times with different time constant, which further confirms the non-Debye type relaxation phenomenon. Moreover, the peak at low-frequency indicates the long distance ionic movement, whereas the peak at high-frequency suggests the confinement of ions in their potential well. Therefore, from the modulus plot, it has been confirmed that the electrical conduction of these ceramic nanocomposites occur through the hopping mechanism.

In addition, Figure 4.9 depicts the complex modulus Nyquist plot (M″ vs M′) of all the sintered and unsintered samples at 25 °C. The appearance of a single arc in unsintered compound confirms once again the contribution of bulk grains towards the electrical properties in the material. The phenomenon of conductivity relaxation in terms of the variation of M″ as a function of frequency was clearly observed from the complex modulus (M*) response in the sintered composite. The asymmetric nature of semicircular arc is a clear indication of the presence of electrical relaxation phenomenon in all the electroceramics sintered nanocomposites. This complex modulus plot of

sintered samples is also a clear indication of the possibility of two semicircles having the maxima at M′ = 0.003 and 0.017, as observed in Figure 4.9. It strongly suggests a presence of bulk grains and grain boundaries interactions in the sintered materials. The Nyquist plot of the complex modulus in Figure 4.9 also justifies a poly-dispersive nature of the dielectric relaxation at low frequencies. Therefore, it was really difficult to describe the relaxation phenomenon in the entire frequency ranges using the electric modulus response without analyzing the M*-plot.
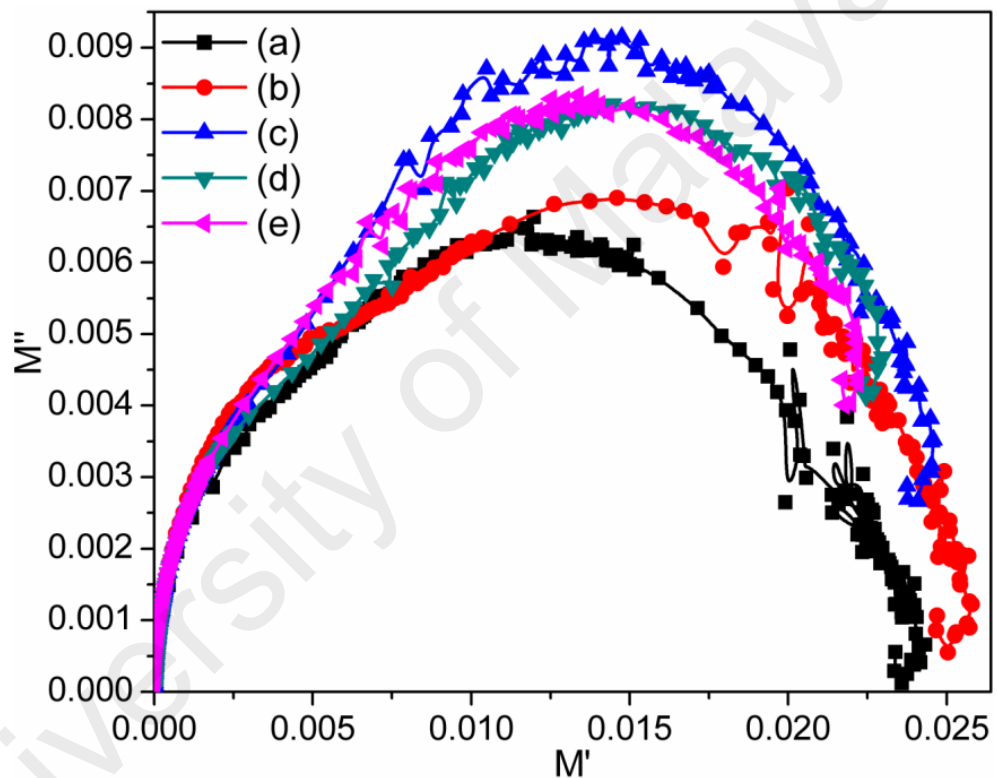
Figure 4.9: Complex modulus Nyquistplot of the (a) unsintered and sintered at (b) 450 °C, (c) 650 °C, (d) 850 °C, and (e) 1050 °C samples.

On top of that, in Figures 4.10A and 4.10B, the scaling behavior of all the sintered and unsintered ceramics is depicted by normalized Z''/Z''_{max} or normalized M''/M''_{max} with normalized f/f_{max} in a logarithm scale at 25 °C; here, f_{max} indicates the frequency corresponding to Z''_{max} or M''_{max}. The merging of both the curves or peaks of all the sintered and unsintered materials is a clear indication of the existence of the dynamic

107

phenomenon in this ceramic composites (Saha & Sinha, 2002). Therefore, the present newly developed materials adhered to the non-Debye phenomenon. Consequently, this scaling of impedance or modulus plot has been proposed as an excellent technique to reveal the relaxation mechanism in the measured frequencies range, as well as the sintering temperature dependent relaxation time. Besides, in Figures 4.10A and 4.10B, it can also be noticed that the maxima of both impedance and modulus responses matched at a single frequency. It suggests similar relaxation time (τ) for both the functions, i.e., $\tau_Z = \tau_M$. In addition, the plots of both the dielectric functions did not completely overlap each other, which suggest the existence of Maxwell-Wagner type relaxation phenomenon in all these newly developed electroceramic nanocomposites.
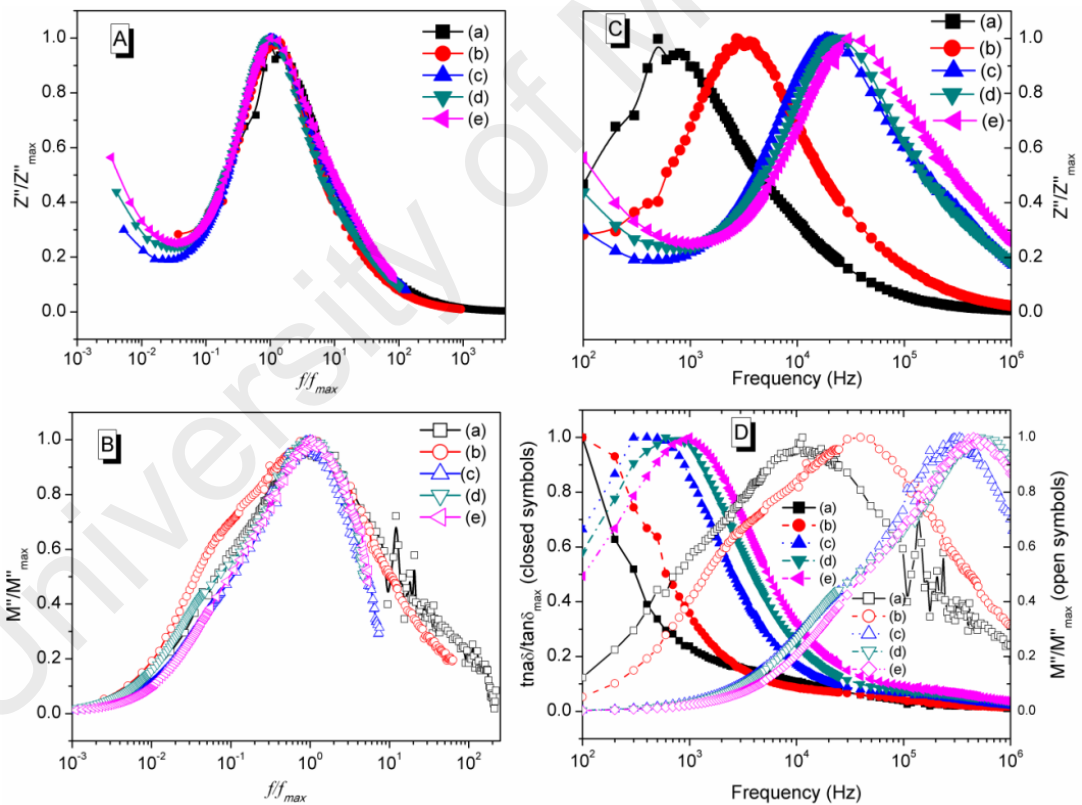
Figure 4.10: Normalized scaling behaviors of imaginary parts of (A)impedance (Z''/Z''_{max}) and (B)modulus M''/M''_{max} with log(f/f_{max}).

Furthermore, a symmetric broadening of the peaks of normalized Z'' as a function frequency for all the sintered and unsintered composites has been observed in Figure 4.10C. The peak was gradually shifted towards high-frequency region after sintering,

which suggests that the relaxation rate is more in sintered samples. The distinct peak frequency of normalized Z'' response of both the samples, thus, might be attributed to the movement of oxygen vacancies, which further suggests the presence of localized movement of oxygen vacancies. From the above analysis, it has been confirmed that the relaxation mechanism depends on sintering temperature, which resembles the non-ideal Debye-type relaxation (Raengthon & Cann, 2012).

Other than that, in order to confirm the short range movement of polaronic particles, this study further analyzed the plots of M''/M''_{max} together with $\tan\delta/\tan\delta_{max}$ as a function of frequency, as depicted in Figure 4.10D. In fact, it has been an effective approach to understand the dynamic nature of the polaronic particles. This response clearly reveals that the peaks of normalized imaginary modulus (i.e., M''/M''_{max}) and normalized $\tan\delta$ (i.e., $\tan\delta/\tan\delta_{max}$) are away from each other. This result confirms a localized or short range characteristic for the polaronic particles (Gerhardt, 1994; Hu W. *et al.*, 2014).

4.1.2.4 Frequency Dependent AC Conductivity (σ_{ac})

Figure 4.11 depicts the variation of alternating current conductivity (σ_{ac}) of all the sintered and unsintered materials as a function of frequency in the range of 100 Hz to 1 MHz at 25 °C. Generally, it is observed that σ_{ac} increases with the increase in frequency. The σ_{ac} of ferrite materials was calculated with Equations 3.14 and 3.15 (Jonscher, 1977; Tiwari *et al.*, 2014). Meanwhile, the exponent, S, was calculated from the slope of $\log(\sigma_{ac})$ versus $\log(f)$ plots. The values of S had been maximum at 0.395 and minimum at 0.194 for those unsintered and sintered samples at 1050 °C, respectively. For sintering temperatures 450, 650, and 850 °C, S was calculated to be 0.359, 0.219, and 0.239, respectively. It indicates that the value of S decreases after sintering. This type of phenomenon, which was only observed in the crystalline-structured oxide materials, suggests that the ionic hopping mechanism is highly

109

responsible for the σ_{ac} in both sintered and unsintered materials (Dyre & Schrøder, 2000; Funke, 1993; George *et al.*, 2006).
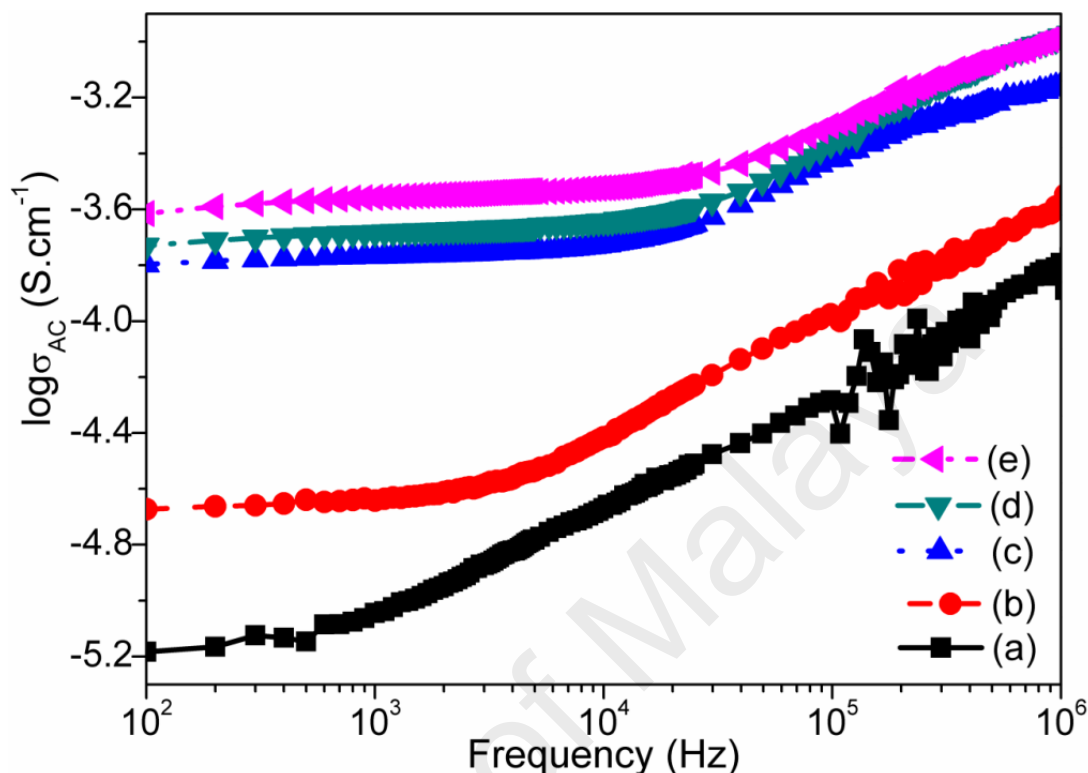
Figure 4.11: Frequency dependent AC conductivity (σ_{ac}) of (a) unsintered compound and sintered at (b) 450 °C, (c) 650 °C, (d) 850 °C, and (e) 1050 °C nanocomposite ceramic materials.

In addition, the non-Debye relaxation mechanism was observed in both unsintered and sintered materials, which confirms that the hopping process among the localized states is indeed responsible for σ_{ac} inside the investigated materials (Ahmed & Bishay, 2001; Ahmed *et al.*, 2001). The resistance of the grain boundaries decreased with the increasing sintering temperature further resulted in an increased σ_{ac} value. This could be due to the effect of inverse spinel ferrite structured Fe_3O_4, which had more influence on grain boundary area. Based on the brickwork layer model (BLM) (Adams *et al.*, 2002), the higher dielectric permittivity of the nanocomposite sintered at 1050 °C compared to unsintered or other sintered materials has been originated from their bigger grains. In

the case of nanocomposite sintered at 1050 °C, more stability of grain boundary resistance at the broad range of frequencies is also responsible for the lowering value of tanδ.

4.2 Characterizations of S1050/PDMS Composite Film

In this section, the structural, morphological, physical, electrical and dielectric characteristics of the S1050/PDMS composite film are discussed.

4.2.1 Structural Characterizations of S1050/PDMS Composite Film

Structural characterizations of S1050/PDMS composite film by XRD, SEM, pore size distribution (PSD), and FTIR analysis are discussed in the following sub sections.

4.2.1.1 XRD Analysis

The XRD-pattern of S1050/PDMS composite thin film is shown in Figure 4.12. It shows a broad semi crystalline peak (black: *) of PDMS (Ataollahi *et al.*, 2015) is found nearly at $2\theta=12°$ along with the crystalline peaks of $Fe_2MgTi_3O_{10}$ (red: 101) and $CaTiO_3$ (blue: 510, 440, 640, 800).
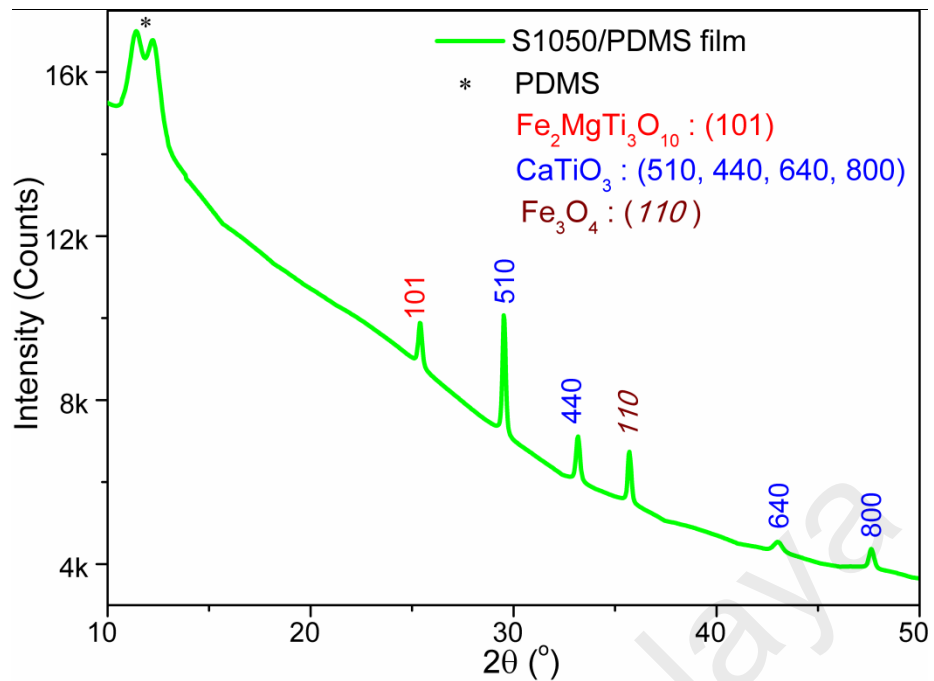
Figure 4.12: XRD (CuKα, λ=1.54056Å) patterns of the S1050/PDMS composite film.

It indicates that the composite is homogeneous. A small peak (brown: *110*) of Fe_2O_3 shifted from $2\theta = 35.83°$ to $35.70°$ indicates the formation of magnetic Fe_3O_4 that was also found in the S1050 as well as S1050/PDMS composite film which may further provoke it in remote sensing applications (Morris *et al.*, 1985). The crystalline peaks corresponding to the three different phases such as armalcolite ($Fe_2MgTi_3O_{10}$), perovskite ($CaTiO_3$), and ferrite (Fe_3O_4) are also resembled with the XRD pattern of S1050 sample, as depicted in Figure 4.2e.

4.2.1.2   SEM Analysis

Figures 4.13a and 4.13b show the SEM micrographs of the eletroceramic S1050 and its flexible nanocomposite S1050/PDMS. The flexible S1050/PDMS composite film shows good particle matrix bonding at the interface in Figure 4.13b. The digital images of the rigid S1050 pellet and flexible S1050/PDMS composite film are also depicted as inset of Figures 4.13a and 4.13b, respectively.
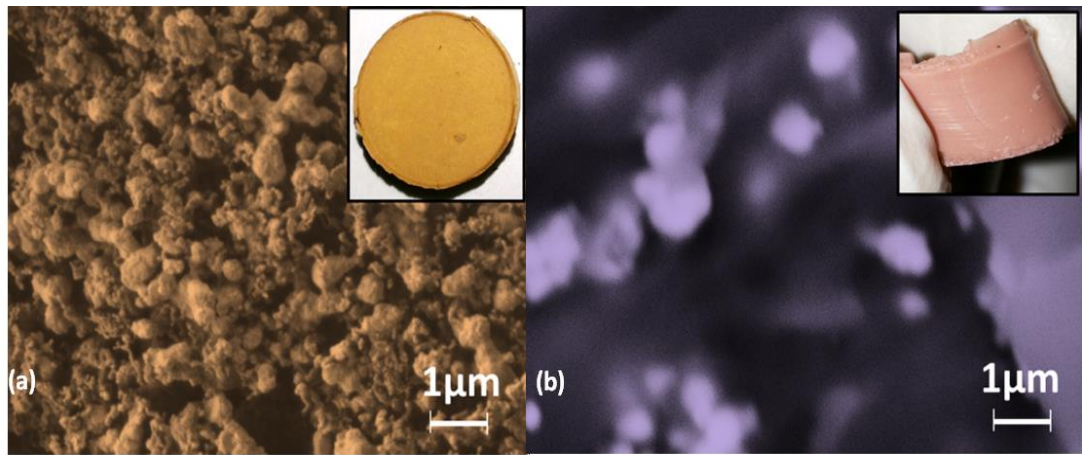
Figure 4.13: FESEM images of the (a) S1050 and (b) S1050/PDMS composite film.

4.2.1.3 Pore Size Distribution (PSD) Analysis

Figures 4.14a–b depict the calculated PSD of the S1050 pellets, and S1050/PDMS film using ImageJ software corresponding to their FESEM images in Figure 4.13a–b, respectively. Mainly three modes of pore size such as nearly 3 μm, 1.75 μm and less than 1.5 μm in the S1050 which were found in S1050 sample also revealed in flexible S1050/PDMS compsite film. It indicates that three different types of claster have been developed by three different phases such as armalcolite, perovskite and ferrite, which was confirmed by XRD study (see Figure 4.12).
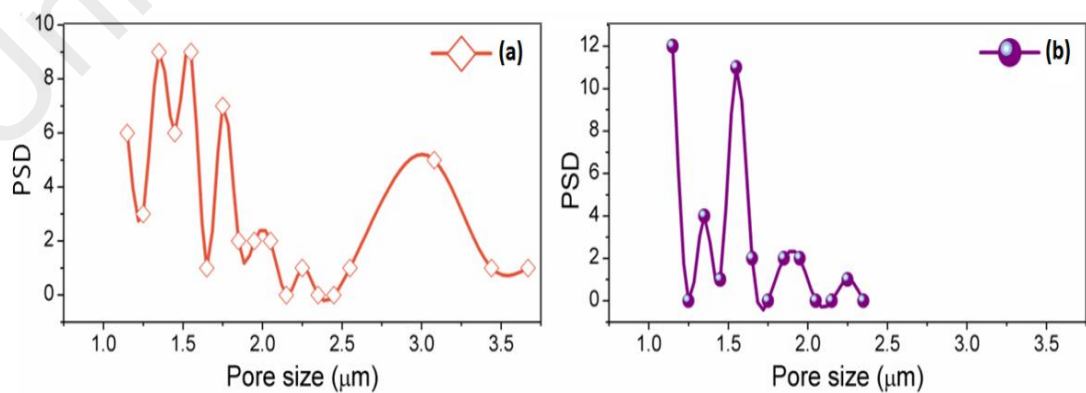
Figure 4.14: PSD of (a) S1050 and (b) S1050/PDMS composite film.

4.2.1.4 FTIR

FTIR spectra depicted in Figure 4.15 indicate the new bond formation after developing the composite. All the FTIR peaks of pristine PDMS elastomer at 602 cm^{-1} related to Si–C stretching, 650-720 cm^{-1} attributed to Si–O–Si stretching, and 842 cm^{-1} corresponding to Si–CH$_3$ stretching were also present in the S1050/PDMS composites in addition to the FTIR peaks of the S1050 ceramic at 470 cm^{-1} corresponding to Ca–O–Ti vibration from titanate and 754 cm^{-1} related to symmetric Ca–O–Ca stretching vibration (Ataollahi *et al.*, 2015; Lozano-Sánchez *et al.*, 2013).
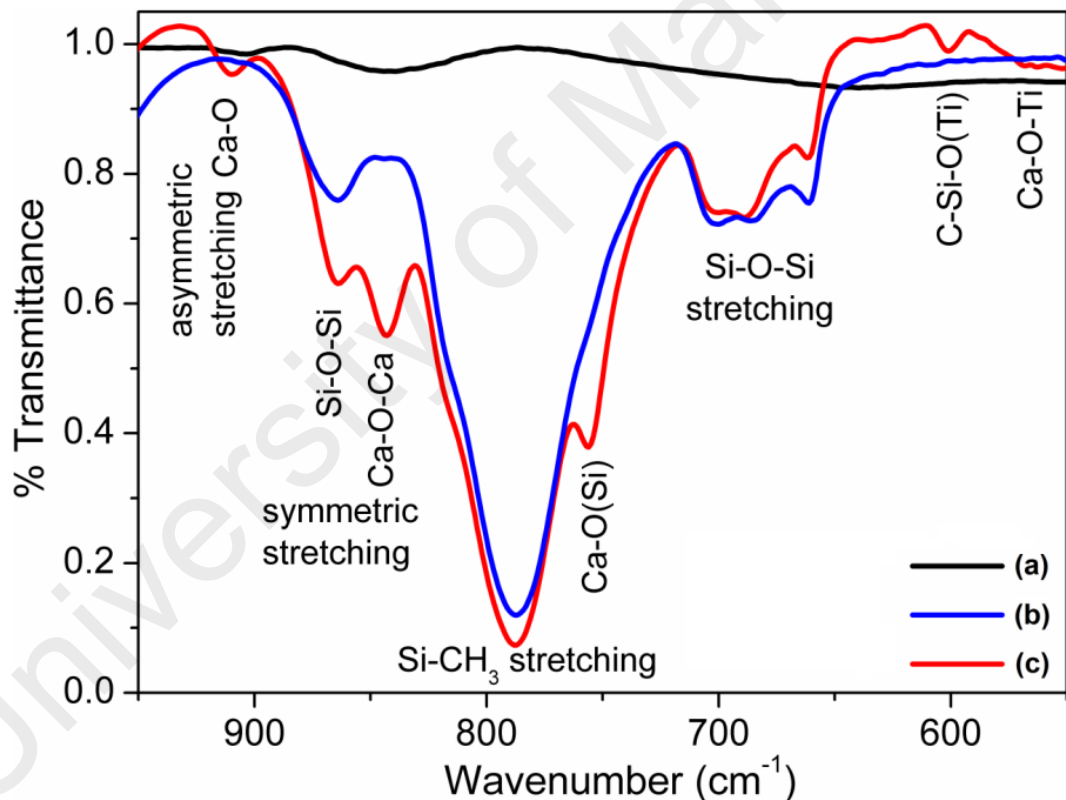
Figure 4.15: FTIR spectra of the (a) ceramic powder sintered at 1050 °C (S1050), (b) pristine polydimethylsiloxane (PDMS) film, and (c) S1050/PDMS composite film.

Interestingly, the three new peaks at 600 cm^{-1} corresponding to C–Si–O from the armalcolite and PDMS, and at 754 and 910 cm^{-1} corresponding to Ca–O(Si) and

asymmetric stretching of Ca–O, respectively from titanate and PDMS reactions have been found in the S1050/PDMS composite.

4.2.2   Physical Characterizations of S1050/PDMS Composite Film

Figure 4.16 depicts the bulk density, open porosity, water absoption and WCA of all the materials. Bulk density was measured to evaluate the open porosity present in the materials. Lower range in density values of these pelletes compared to its comprised commercial raw materials indicates higher amount of porosity. Water absorption indicates the total porosity present in the materials (see Figure 4.16).
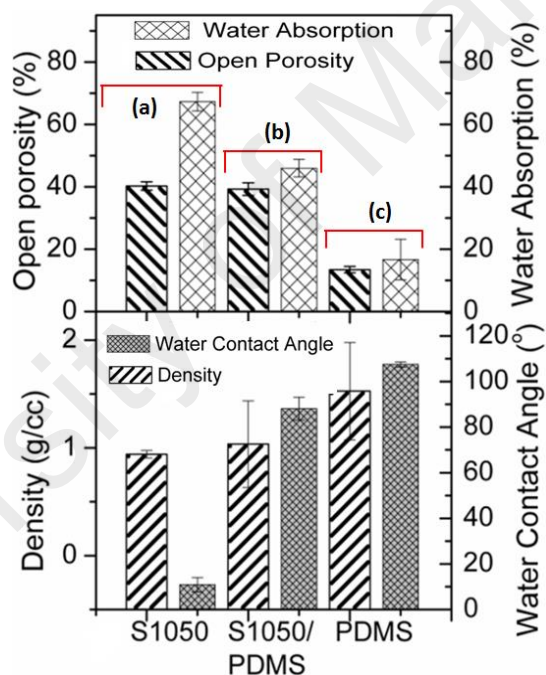
Figure 4.16: Density, open-porosity, water absorption and WCA of (a) S1050 ceramic (b) S1050/PDMS composite film and (c) PDMS samples.

The higher amount of water absorption (~ 67%) in S1050 supports the uniform porosity that was revealed in the FESEM-image (see Figure 4.13a). The open-porosity of all these materials is lower than close-porosity. Lower WCA in the ceramics strictly responsible for changing the PDMS from hydrophobic (WCA =107°, i.e., >> 90°

(Ataollahi *et al.*, 2015)) to hydrophilic (up to WCA=88.1°, i.e., < 90°) for S1050/PDMS composite film. Therefore, this flexible S1050/PDMS composite film can be used as a potential *humidity sensitive film* in many advanced remote contrlled humidity sensors (Ataollahi *et al.*, 2015; Chuang *et al.*, 2010; Tripathy *et al.*, 2014; Yazawa *et al.*, 2012).

4.2.3   Mechanical Characterizations of S1050/PDMS Composite Film

Mechanical characteristics of S1050/PDMS composite film are discussed by using three different analyses, including static analysis and dynamic mechanical analysis as well as atomic force spectroscopy.

4.2.3.1   Static Mechanical Analysis

In order to evaluate the flexibity of the samples, S1050/PDMS composite film (open-symbol, black colour) was compared with pristine PDMS film (close-symbol, red colour). The Young's was measured from the of the selected part of the stress-strain plot of elastomers as depicted in Figure 4.17.
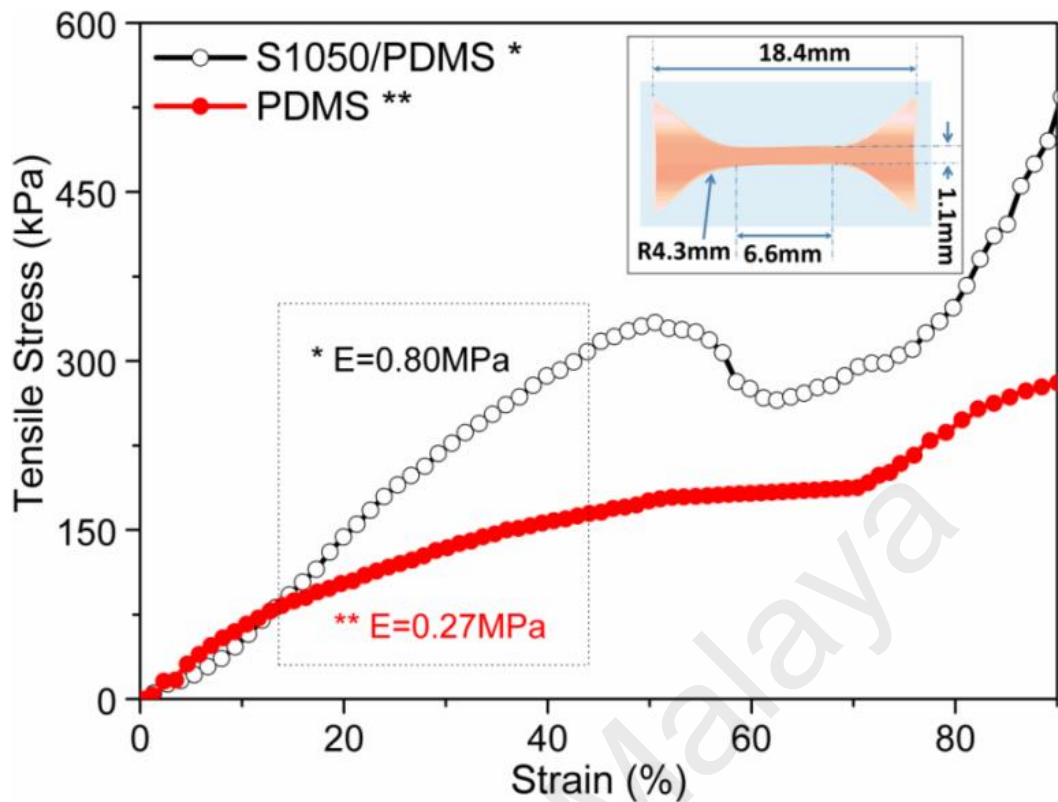
Figure 4.17: Static tensile properties of PDMS (close-symbol, red colour) and S1050/PDMS composite film (open-symbol, black colour). The inset is represented a schematic design of the film specimen according to the standard ASTM D412 method.

The static tensile test was performed up to 90% of the elongation. The modulus of the S1050/PDMS composite film was found to 0.80±0.21 MPa, wich significantly higher than PDMS film (0.27±0.08 MPa). It can be noticed that both the sample showed elongation more than 90%. It indicates that the composite S1050/PDMS composite films are as flexible as pristine PDMS film. Further, the modulus value which is substantially lower than the other PDMS composites indticates the higher flexibility (Ataollahi *et al.*, 2015).

The force spectroscopy and tapping mode AFM study confirms the exact Young's modulus and corresponding topological morphology of the PDMS and S1050/PDMS composite films. A comparison in Young's modulus of the PDMS and S1050/PDMS composite films depicted in Figure 4.18a indicates the close support of the tensile

117

moduli values for both the samples. The AFM topographs of PDMS and S1050/PDMS composite films showed in Figure 4.18b and 4.18c, respectively reveal the smooth surface for PDMS film and rough surface having homogeneously dispersed particulates on the top layer for the S1050/PDMS composite film.
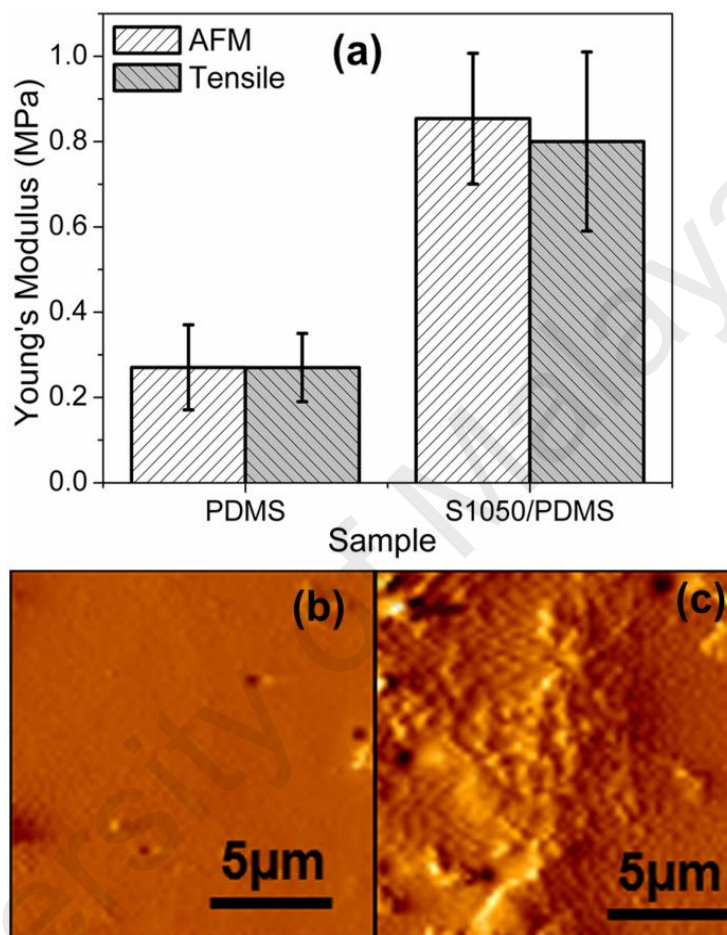
Figure 4.18: (a) A comparisons in Young's modulus measured from tensile study and AFM force spectroscopy. AFM topography of (b) PDMS and (c) S1050/PDMS composite films.

4.2.3.2   Dynamic Mechanical Analysis

Figure 4.19 depicts the dynamic mechanical properties of the as-prepared PDMS and S1050/PDMS composite films in tensile mode. The storage and loss moduli were recorded in a cryozonic condition. The viscoelstic properties in tensile mode of PDMS and S1050/PDMS composite films are shown in Figure 4.19. The Table 4.3 illustrates

the glass transition temperature (T_g), which was determined by the maximum loss in storage modulus (E') and loss modulus (E'') or damping factor ($\tan\delta = E''/ E'$) peaks occurred towards higher temperature after addition of ceramic (S1050) particles in PDMS. The higher T_g value compared to other study indictaes the improved mechanical strength (Bosq *et al.*, 2014; Meng *et al.*, 2014). The higher T_g value was obtained may be owing to the new primary or secondary bonding formations bentween the S1050 and PDMS in the composite film. The higher storage modulus value in S1050/PDMS composite film was obtained owing to addition of stiffer ceramic particles in the PDMS matrix. This result also supports the static tensile test result. The value of the E' in DMA study is higher than the Young's modulus of static tensile mode, which was done at 25 °C, becaue of the using of cryozonic condition for DMA. At cryozonic temperature, the mobility of PDMS polymer chains has been hindered, thus increased the stiffness or modulus of the polymeric materials. The E' decreases significantly with increasing the temperature attributed to the transformation of glassy phase to rubbery phase. The damping factor value indicates the amount of enrgy dissipation related the molecular motion of the polymer chains during test. The lower $\tan\delta$ value in S1050/PDMS composite indicates the minimum loss of energy due to applied cyclic load. The $\tan\delta$ value of the PDMS based composite (S1050/PDMS) in the present study (0.225) is significantly higher than other composites of PDMS reported in elswhere (Bosq *et al.*, 2014). It clearly indicates that the newly developed S1050/PDMS composite has higher flexibility beside having higher strength. It has happened probably due to the formation of chemical bonding between the PDMS chains and the armalcolite ($Fe_2MgTi_3O_{10}$) as well as calcium titanate ($CaTiO_3$) of the S1050 ceramic particles. The probable reaction is presented in the Reaction (4.1). The new chemical band formations were also confirmed by FTIR spectra as depicted in Figure 4.15.

$$(CH_3)_3-Si-O-[-Si(CH_3)_2-O-]_n-Si-(CH_3)_3 \quad (CH_3)_2-Si-O-[-Si(CH_3)_2-O-]_n-Si-(CH_3)_2$$
$$+ \longrightarrow$$
$$Fe_2MgTi_3O_{10}/CaTiO_3/Fe_3O_4 \qquad Fe_2MgTi_3O_{10} \quad / \qquad CaTiO_3 \ / \ Fe_3O_4 \qquad (4.1)$$
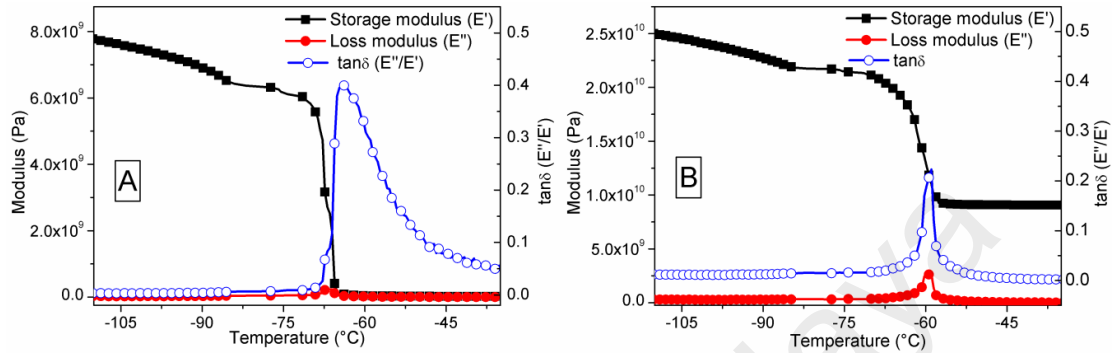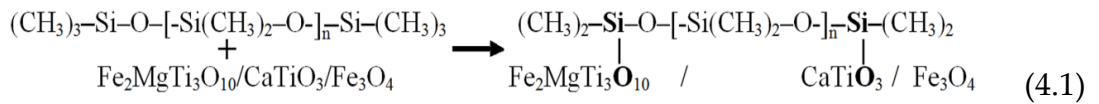
Figure 4.19: Dynamic mechanical properties in tensile mode of (A) PDMS and (B) S1050/PDMS composite film.

Table 4.3: Dynamic mechanical properties of PDMS and S1050/PDMS films.

Material	Maximum E′ (Pa) at 110°C	Temperature (°C) at Maximum loss of E′	Temperature (°C) at E″ Peak	Temperature (°C) at tanδ Peak	tanδ Value (E″/E′)
PDMS	7.7×10^9	-68	-67.5	-63.9	0.404
S1050/PDMS	2.5×10^{10}	-60	-59.2	-58.8	0.225

4.2.4   Electrical and Dielectric Characterizations of S1050/PDMS Composite Film

Figure 4.20 depicts a typical comparisons in ε′ and tanδ between the S1050 ceramic and S1050/PDMS composite film at different log(*f*). Figure 4.20 indicates that the ε′ (i.e., 72–330) of the S1050/PDMS film is considerably lower than the S1050 ceramic but significantly higher than other pure PDMS or PDMS based materials, which show generally less than 10 (Du *et al.*, 2011). The excellent enhancement in ε′ has been obtained owing to the incorporation of giant dielectric material such as S1050 ceramic

particles homogeneously in the PDMS matrix. In addition, the tanδ value of S1050/PDMS film is significantly lower than that of S1050 ceramic, indicates the very low loss in energy dissipation.
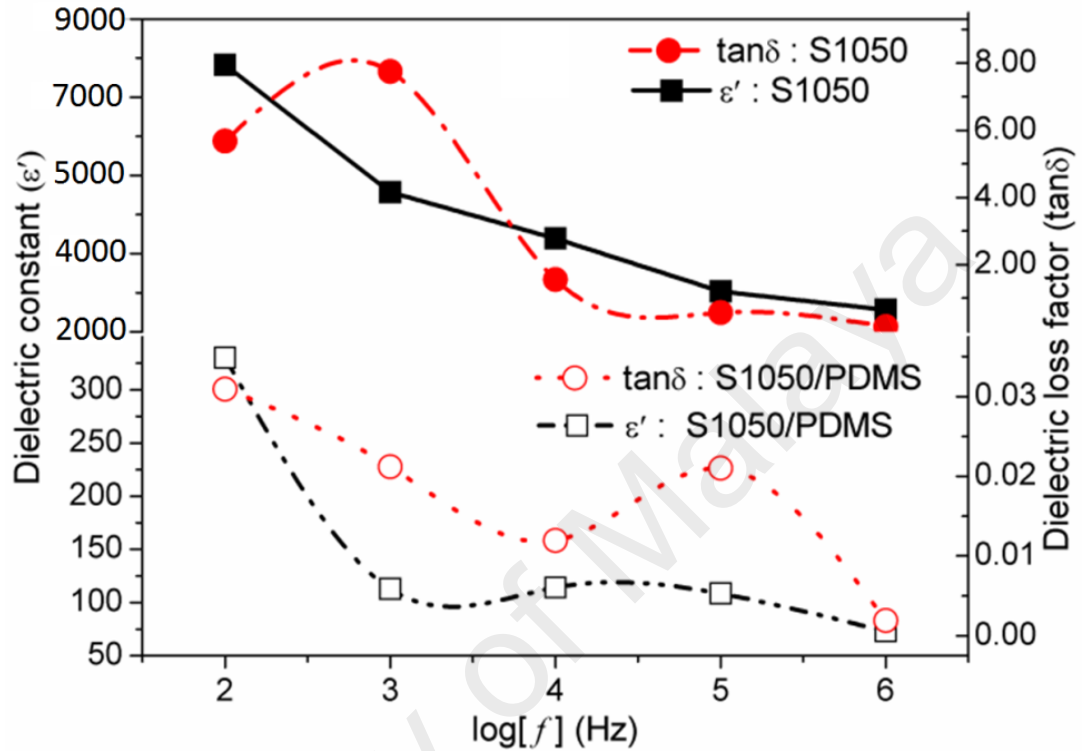
Figure 4.20: A typical comparisons in ε′ and tanδ of S1050 ceramic and S1050/PDMS composite film at the different log(*f*).

The dielectric tangent loss of the S1050/PDMS composite is compared with the S1050 ceramic material in Figure 4.21. It has been found the the dilectric tangent loss factor of the S1050/PDMS composite film (0.02–0.002) is extremely lower than that of S1050 ceramic pellet (5.75–0.15) in the range of 100 Hz to 1 MHz frequency region. A precise observation at a frequency range of 10^5–10^6 Hz, similar to the other study (Thomas *et al.*, 2010), on the change in tanδ value for S1050 ceramic pellet and flexible S1050/PDMS composite film is depicted in the bottom inset of Figure 4.21. It indicates that the PDMS has influenced significantly on the dielectric properties of ceramic and vice-versa. It might be possible owing to the new bonding formation between the silicon

of backbone chains of PDMS with the compositions of S1050 ceramic. The newly developed bonds have been found in FTIR spectra, which is depicted in Figure 4.15. The dielectric loss tangent of the S1050/PDMS composite film also resembled the values of PDMS (Tiercelin *et al.*, 2006). The lower dielctric tangent loss is clear indication of improvement of the quality factor of sensors or electronic devices. Hence, it evidently suggests that the sensing properties of the S1050/PDMS composite film would be potential for sensor device applications. The frequency dependence of the dielectric tangent loss (tanδ) of S1050/PDMS composite at very precise observation is depicted at top inset in Figure 4.21, indicates the two relaxations. The tanδ loss peak at lower frequency region nearly 100 Hz is occurred due to the relaxation attributed to molecular motion in the crystalline regions of PDMS polymer chains as well as grain-grain boundary interfacial polarizations (Singh *et al.*, 2013; Thomas *et al.*, 2010) and the second sharp peak at higher frequency region nearly 10^5 Hz indicates another relaxation associated to the glass transition of PDMS polymer (Thomas *et al.*, 2010).
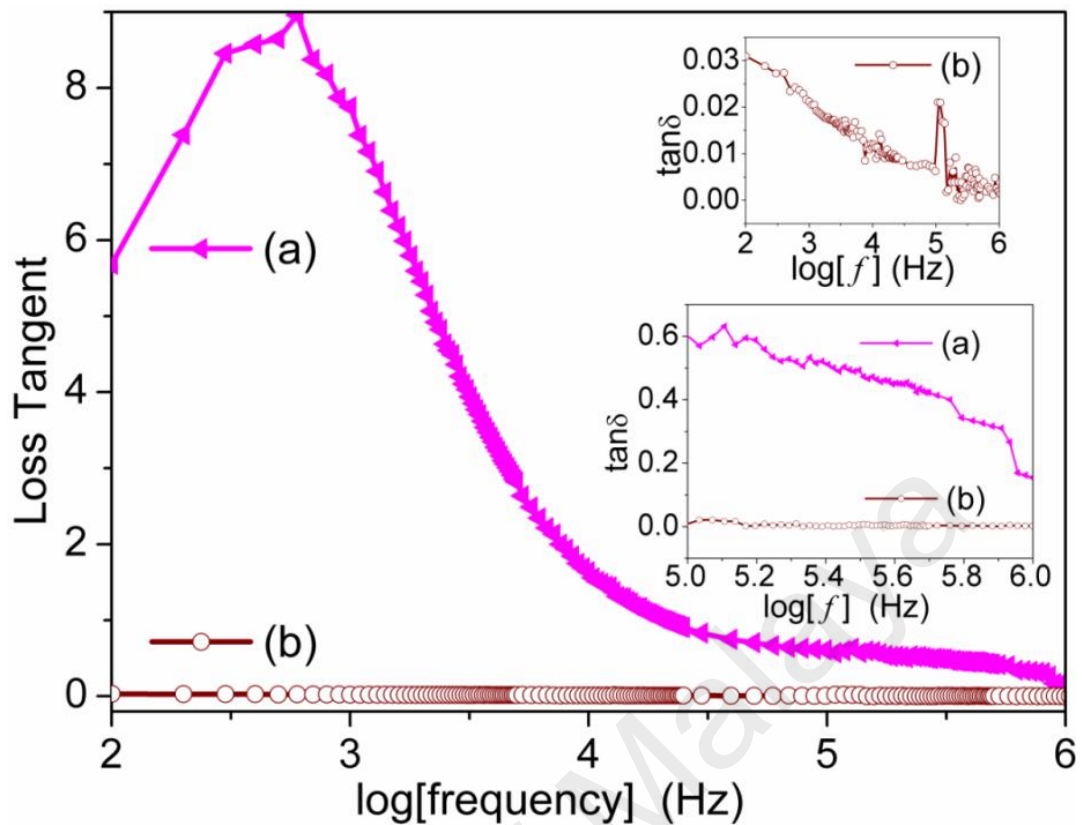
Figure 4.21: Frequency dependence dielectric loss tangent (tanδ) of (a) Sintered pellet at
1050 °C – pink (S1050) and (b) composite film – brown (S1050/PDMS).
The inset represents the precise observation at 10^5 – 10^6 Hz on the tanδ
changes for ceramic pellet of S1050 and flexible film of S1050/PDMS
composite.

A frequency dependent AC conductivity (σ_{ac}) of the S1050 pellet and S1050/PDMS
composite film is depicted in Figure 4.22. The both materials showed a slower and a
faster increment at below and after $\log(f)$ = 4.4 Hz, respectively. It clearly suggests that
an insulator-semiconductor transition zone in electrical conductivity is occurred nearly
at 25×10^3 Hz. This phenomenon in the crystalline oxide based materials is attributed to
the ionic hopping mechanism, which is highly possible in both sintered crystalline
S1050 and its flexible composites film (S1050/PDMS) (Dyre & Schrøder, 2000; George
et al., 2006).
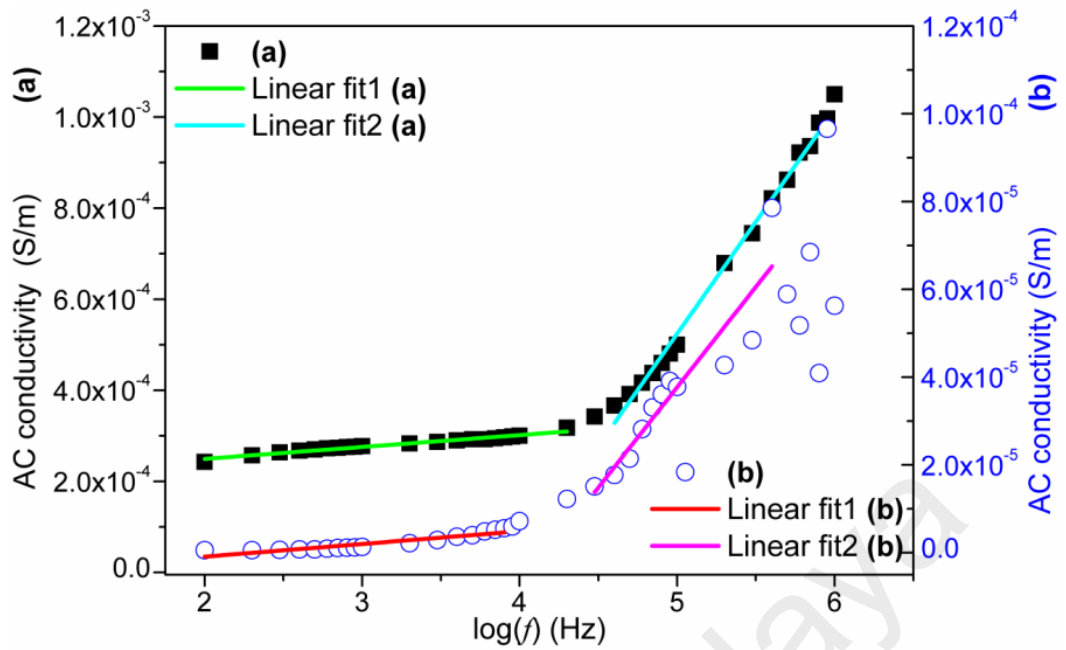
Figure 4.22: Frequency dependence AC conductivity (σ_{ac}) of (a) Sintered pellet at 1050 °C – pink (S1050) and (b) composite film – brown (S1050/PDMS).

The frequency capacitance of the S1050/PDMS nanocomposite is compared with the S1050 ceramic dielctric material in Figure 4.23. Since dielectric constant, which is directly proportional to the capacitance value ($C = \varepsilon'\varepsilon_o A/t$, where C is capacitance, ε' is real dielectric constant, ε_o is the free space permittivity, A is cross-sectional area and t is the thickness of the sample), of the S1050 was significantly highest at all frequencies (see Figure 4.23), its capacitance value would be best in comparison with unsintered or any other sintered material. Therefore, only S1050/PDMS composite was used to develop a flexible composite film with potentially be best in performance.
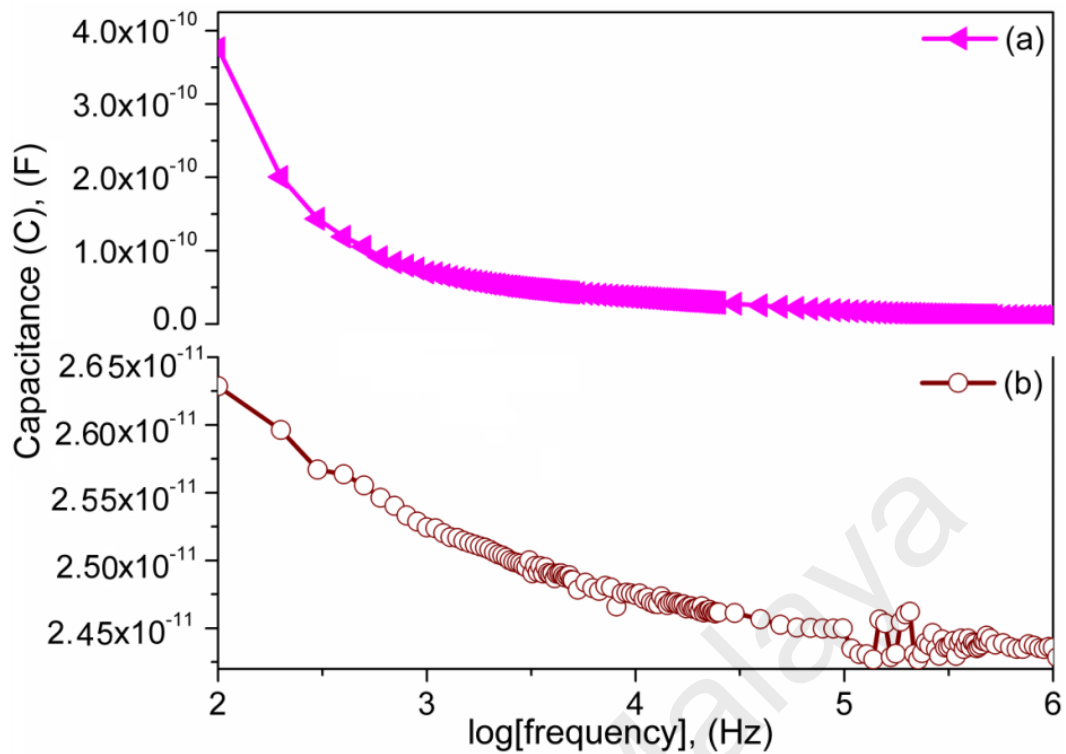
Figure 4.23: Frequency dependence capacitance of (a) Sintered pellet at 1050 °C – pink (S1050) and (b) composite film – brown (S1050/PDMS).

The capacitance values of the S1050 ceramic and S1050/PDMS composite film were in the order of 10^{-10} F and 10^{-11} F, respectively wich are closely resembled with the different nanoparticles and composites (Imran *et al.*, 2013; Wang C.-T. *et al.*, 2005). The capacitance value of the S1050/PDMS composite film is significantly higher than the other titanate fibrous materials (Imran *et al.*, 2013). Therefore, the S1050/PDMS composite film will capable of storing large amounts of electrical energy, which are worthy for several electronic and power devices (Nayak *et al.*, 2013). The capacitance values of both the dilectric materials also followed a decreasing trend with frequency. It is obvious due to the loss of ionic polarizations with increasing of frequency. The grain-grain boundary interfacial polarizations and molecular motion in the crystalline regions of PDMS polymer chains increase the capacitance value of the S1050 ceramic and S1050/PDMS composite film, respectively at lower frequency (100–3000 HZ). At higher frequency range, 10^5–10^6 Hz, the two pikes of capacitive value in S1050/PDMS

125

composite film is attributed to the glass transitions, such as α- or β- transition, of PDMS polymer. The first peak may be related to a breakage of weak secondary bond, such as Van der Waals dipole interactions between the ceramic particles and polymer chain and second peak may be owing to another the stronger secondary bond, such as hydrogen bonds within the PDMS polymer chains (Bai & Jin, 2008).

4.3 *In Vitro* Biocompatibility Study of S1050 and S1050/PDMS Nanocomposite Film

The *in vitro* biocompatibility study was performed on HDF cells to evaluate the biocompatibility and the non-toxicity of the newly developed armalcolite nanocomposite based ceramic composite (S1050), as well as the flexible nanocomposite film with PDMS (S1050/PDMS) material, as potential wound healing drug carrier and skin-compatible humidity sensors. The quantitative analysis of DNA-assay result indicates that the total number of DNA significantly ($p < 0.05$) increased with the increasing time point from day-1 to day-7 (see Figure 4.24) for all the three samples. However, the amount of DNA was insignificant ($p > 0.05$) for a particular time point among the samples. This result clearly indicates that both S1050 and S1050/PDMS film samples possess varied cell proliferation properties.
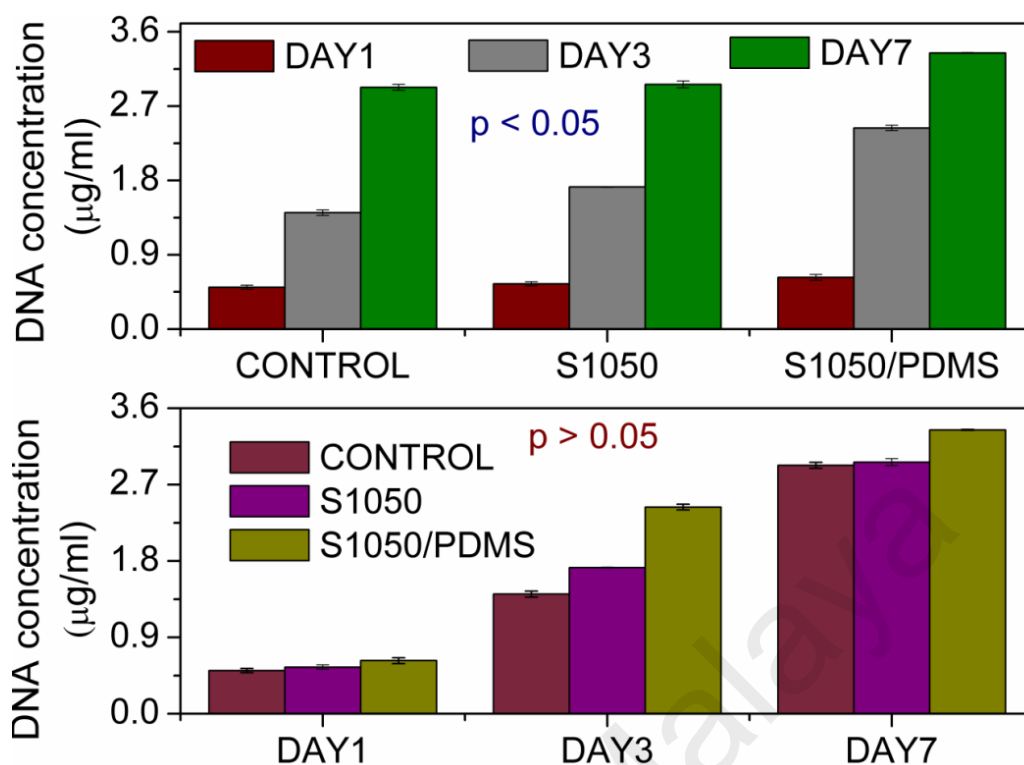
Figure 4.24: DNA-assay of positive control (Thermanox), S1050 and S1050/PDMS at day-1, day-3, and day-7.

The different types of cell proliferation were also confirmed by the confocal microscopic study. The quantitative live–dead cell present in the specimen was observed from the confocal micrographs of the samples (see Figure 4.25). The number of green cells increased with cell culture time points from day-1 to day-7, particularly after day-3. This result supports the DNA-assay. It was also noted that the number of green cells present in S1050 (see 2nd column in Figure 4.25) and S1050/PDMS (see 3rd column in Figure 4.25) samples had been larger than the positive control thermanox (see 1st column in Figure 4.25) even after day-7 study. The more number of green (live) cells present in S1050 than the positive control thermanox confirms the biocompatibility and the non-toxicity characteristics of the newly developed S1050 nanocomposite. Furthermore, the size of green (live) cells was also high in S1050/PDMS film. The number of red (dead) cells, nonetheless, had been less in S1050/PDMS compared to S1050. This could be due to two reasons: (i) the size of the dumbbell shaped cell was

127

found in the S1050/PDMS film due to the polymer matrix because this type of cell growth was also found on the control (special thermanox polymer sheet), and (ii) the number of dead cells was high on the composite film due to the combined biocompatibility effect of both S1050 and PDMS. The HFB cell growth behavior of this electroceramic material also very closely resembles the other bioceramic materials on the same cells found by some recently published works (Manna *et al.*, 2016; Pramanik *et al.*, 2015). Therefore, the biocompatibility study indicates that the newly developed S1050 material has been indeed highly biocompatible and bioactive. Hence, this would be potential for wound healing applications. Since the S1050/PDMS composite displays excellent biocompatibility, humidity sensors based on these materials also could be used at skin-socket interfaces of the artificial stumps.
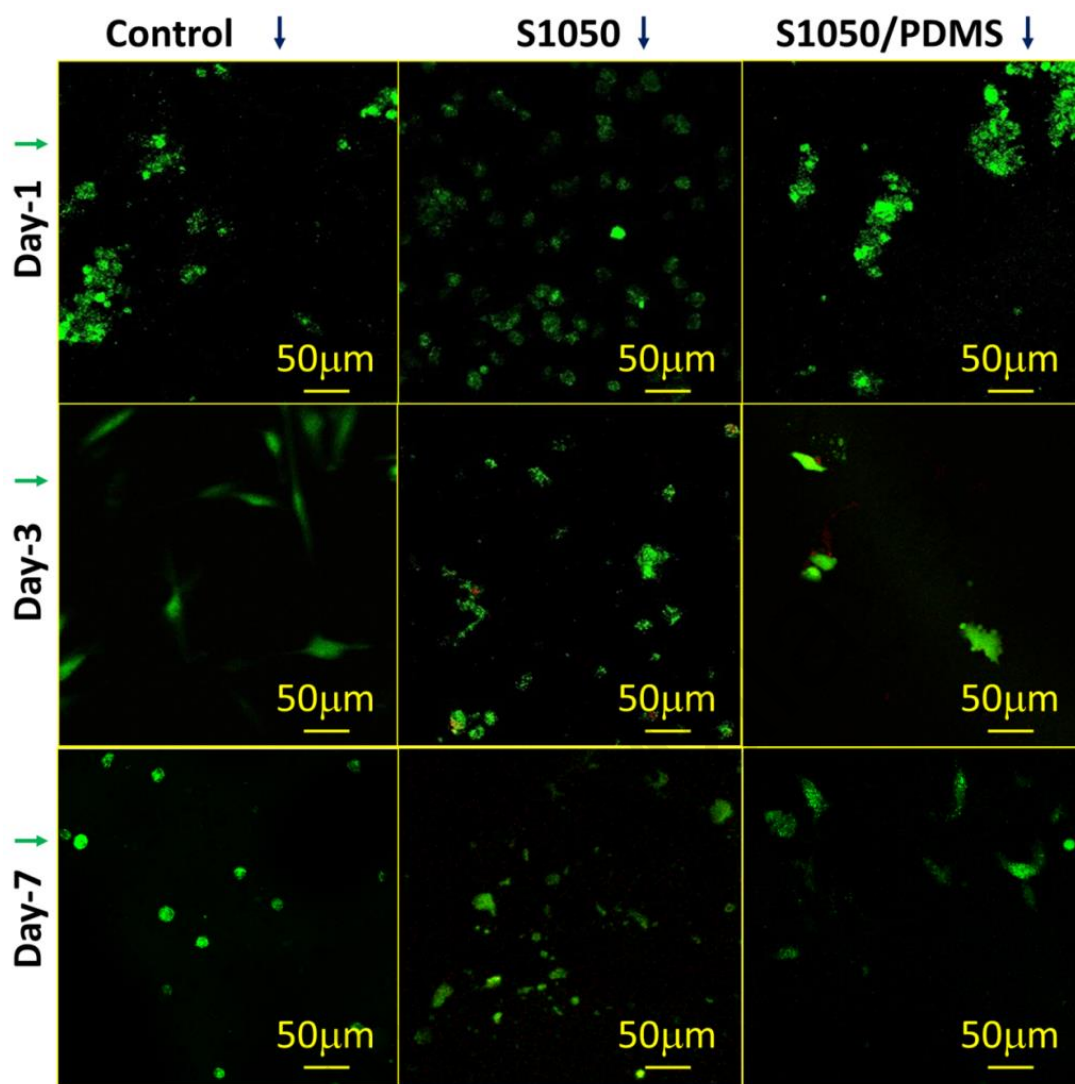
Figure 4.25: Confocal micrographs of positive control thermanox (1st column), S1050 (2nd column) and S1050/PDMS (3rd column) at day-1 (1st row), day-3 (2nd row), and day-7 (3rd row).

4.4 Drug Release Study

In order to investigate the ability of S1050 nanocarrier based PVA hydrogel to effectively deliver the curcumin, *in vitro* release studies were performed. A certain amount of prepared curcumin loaded hydrogel and curcumin loaded S1050 NPs based hydrogel had been diluted in 3 ml of PBS (pH = 7.4) at 37 °C. The standard UV-Vis absorption curve at different known concentrations of curcumin drug is shown in Figure 4.26. Based on the raw drug absorption vs. raw drug concentration curve, the

129

concentrations of the diluted PBS solutions of the two hydrogels (i.e., curcumin loaded hydrogel and curcumin loaded S1050 NPs based hydrogel) were calculated at different releasing time. Furthermore, the percentage of drug release was calculated from the drug released by the two hydrogels using Equation 4.3.

$$\text{Drug release (\%)} = \frac{C_0 - C_t}{C_0} \times 100 \qquad (4.3)$$

where, drug concentration (C_t) in mg/ml present in the solution at a measured time (t) and (C_0) is the initial concentration at zero time (Manna *et al.*, 2016).

Figure 4.27 shows the concentrations of the curcumin loaded hydrogel and curcumin loaded S1050 NPs based hydrogel at different releasing times. It was clearly observed that initial drug loading significantly influenced the release behavior of curcumin from hydrogel. Besides, the release study demonstrated that the percentage of drug released from the curcumin loaded hydrogel was 20% within 60 min, but it was 46% from curcumin loaded S1050 NPs based hydrogel. The drug release study indicates that incorporation of S1050 armalcolite nanocomposite significantly enhanced the release rate (Li *et al.*, 2015; Madhavi *et al.*, 2012). Meanwhile, Figure 4.27 shows that the drug release rate was faster after 20 min and continued up to 60 min. This result may be due to the fact that the nano size particles of S1050 based armalcolite nanocomposite increase the surface area available for drug release (Lou *et al.*, 2014; Madhavi *et al.*, 2012). Furthermore, it is also be possible that since the S1050 armalcolite is an iron-rich material, the Fe^{3+} ion of S1050 forms a complex with curcumin drug at a molecular level, which enhances the absorbance with respect to time and consequently enhances the concentration of released drug (Li *et al.*, 2012). Therefore, the release kinetic response confirmed the better drug release ability of S1050 nanocarrier.
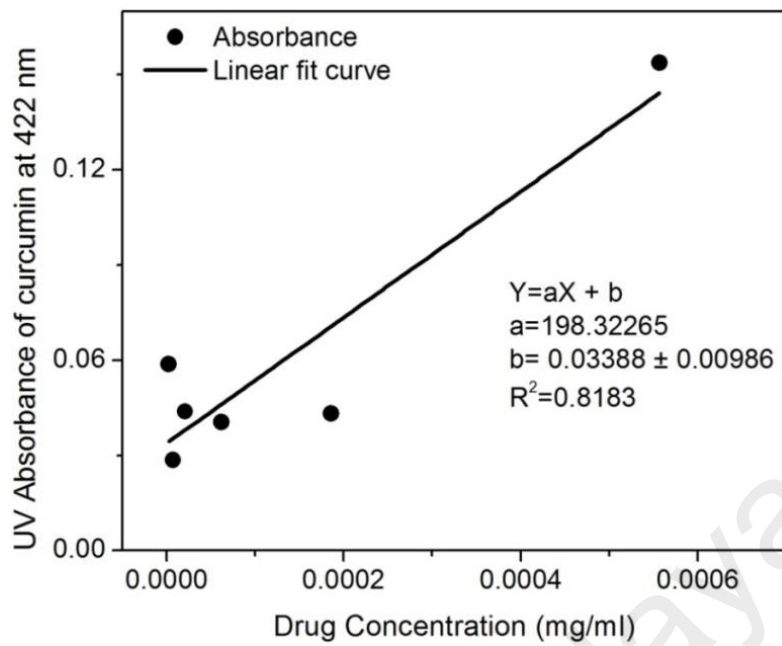
Figure 4.26: Absorbance of raw curcumin drug with PBS solution at their maxima of λ ≈ 422 nm.
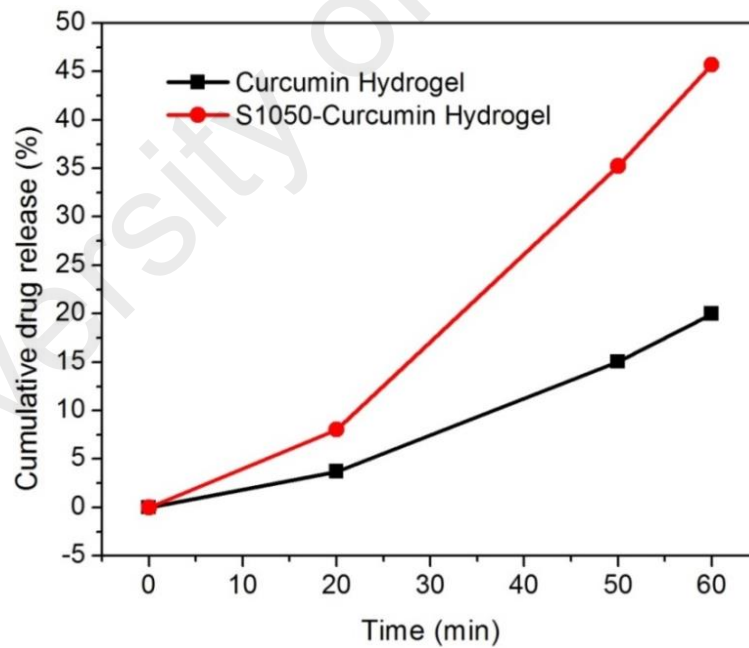
Figure 4.27: *In vitro* drug release profile of curcumin loaded hydrogel and curcumin loaded S1050 NPs based hydrogel up to 60 min.

CHAPTER 5: CMFTO BASED NANOCOMPOSITE FOR HUMIDITY SENSOR AND WOUND HEALING APPLICATIONS

The potential applications of newly developed CMFTO nanocomposite are described in this section. The first part of the section narrated the effective humidity sensing ability of the CMFTO nanocomposite and the second part explained the excellent biocompatibility characteristics by using *in vivo* approach on diabetic rat models.

5.1 CMFTO Nanocomposite as a High Sensitive Capacitive Humidity Sensor

Humidity dependent capacitive responses of CMFTO nanocomposite have been discussed in this section. This section mainly focused the sensitivity, hysteresis, response and recovery time, stability and the water absorption mechanism of CMFTO based humidity sensor.

5.1.1 Humidity Sensing Capacitance Measurements

All the aforementioned physical properties in Chapter 4 favour considering the porous CMFTO electroceramic sintered at 1050 °C to be the best hydrophilic material among the all ceramics developed in the present study. The hydrophilic characteristics of its surface with meso- or submicro- pores should be helpful for improving the water molecule adsorption/desorption process and hence, enhance the sensitivity of humidity sensors. To investigate the effect of frequency on sensing characteristics of the CMFTO electro-ceramic based sensor, its capacitance values have been calculated under different humidity environments with various test frequencies such as 10^2, 10^3, 10^4, 10^5 and 10^6 Hz at 25 °C and the results are depicted in Figure 5.1. It has been observed that higher frequencies lower the capacitance; for example, at 95% RH the highest capacitance value of 9.974×10^{-10} F at 10^2 Hz and lowest capacitance (*C*) of 1.780×10^{-11} F at 10^6 Hz have been observed. It has also been found that when the RH increases

from 33% to 95%, the capacitance value increases monotonically. The plots of the inset image of Figure 5.1 are a better representation of the change in *C*-values as a function of % RH (33%–95%) at different frequencies (10^2–10^6 Hz). This suggests that the capacitance is an effective physical parameter in order to evaluate the sensor response.
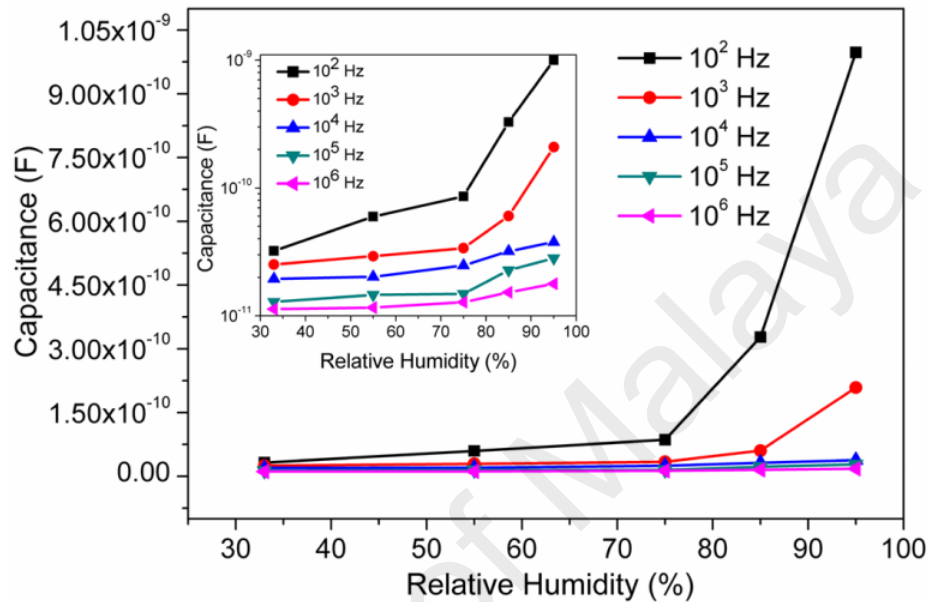
Figure 5.1: The response curves of the capacitance *versus* relative humidity (RH) at different frequencies of CMFTO electroceramic at 25 °C. Inset image represents the variation of capacitance with RH at 25 °C at different frequency in logarithmic scale (log(*C*) *vs.* % RH).

The relations between capacitance and frequency at 25 °C of the present capacitive-type sensor at different RH values are depicted in Figure 5.2. It has been observed that the *C*-value decreases with increasing frequency and the rate of decrease is faster at higher RH. The capacitance value increases significantly with % RH in the lower frequency range (below 10^4 Hz) but in a higher frequency range, the capacitance value is small and hardly changes with humidity. Generally in the ideal capacitive sensor, the *C*-value is independent of applied frequency. However, in low humidity environments, the sensing material absorbs a small amount of water, which could be considered as an ideal situation. Due to the absorption of water molecules, the sensing material possesses

133

a leak conduction (γ) (Wang J. *et al.*, 2005). The capacitance (*C*) of the material with leak conduction can be expressed by a relation as shown in Equation 5.1 (Bi *et al.*, 2013; Wang J. *et al.*, 2005):

$$C = \varepsilon^* C_0 = \left(\varepsilon_r - i \frac{\gamma}{\omega \varepsilon_0} \right) C_0 \qquad (5.1)$$

where ε^*, C_0 and ε_r are the complex dielectric constant, capacitance and relative dielectric constant of an ideal capacitor, respectively; ω is the angular frequency, γ is the conductance and ϵ_0 is the permittivity at free space. From Equation 5.1, it can be noticed that the capacitance of the sensing material is inversely proportional to frequency ω and directly proportional to γ. Hence, the *C*-value decreases with increasing frequency and this relation becomes more prominent under higher RH conditions. In addition, γ is attributed to the physisorption of water molecules on the surface of porous CMFTO electro-ceramic. Here, γ increases with increasing of % RH and as a result, *C*-value increases with rising RH with respect to ω.
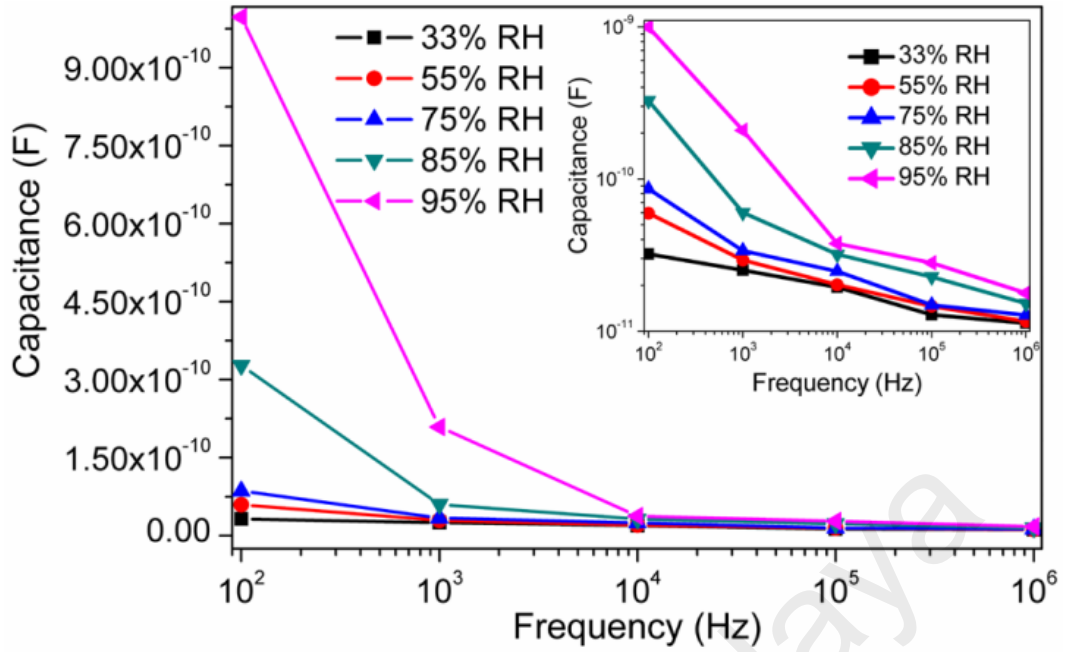
Figure 5.2: The variations of capacitance with frequency at different humidity condition (33%–95% RH) for CMFTO based humidity sensor at 25 °C. Inset image represents the variation of capacitance with frequency at different RH in logarithmic scale (log(*C*) *vs.* log(RH)).

To explain the humidity dependent capacitive characteristics of CMFTO electroceramic, the device sensitivity (S_C) due to change in capacitance has been calculated by using the Equation 5.2 (Wang W. C. *et al.*, 2013):

$$S_c = \frac{C_{RH} - C_{33}}{C_{33}} \times 100 \text{ %} \tag{5.2}$$

Where, C_{33} and C_{RH} stands for the capacitances measured at 33 %RH and at a certain RH level, respectively. Figure 5.3 shows that the applied test frequency has highly influence on the sensitivity of humidity sensors. It has been also observed that the values of *C* (Figure 5.2) and *S* (Figure 5.3) with %RH (in the range 33–95%) increases with decreasing the test frequencies (from 10^6 to 10^2 Hz). The *C*-value increased from 3.2183×10^{-11} F to 9.9741×10^{-10} F, with a '*S*' of ~3000% at the signal frequency of 10^2 Hz, but when the test frequency is 10^5 Hz, the capacitance varied from 1.2832×10^{-11} to 2.8174×10^{-11} F with '*S*' of ~120% across the RH range of 33%–95%, respectively.

135
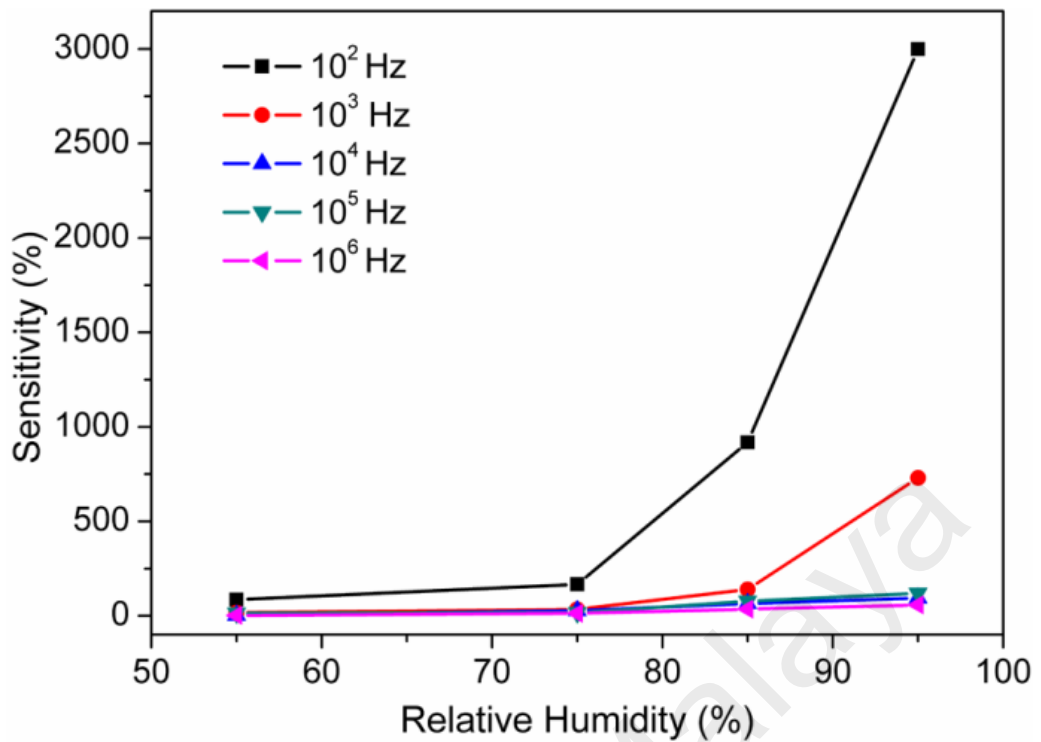
Figure 5.3: The sensitivity (%S) response of CMFTO based capacitive sensor with % RH at different test frequencies at 25 °C.

The sensitivity of the developed sensor is higher than some other ceramic based humidity sensors (for example, ~2900% for Porous $ZnAl_2O_4$ spinel nanorod, ~85% for silica nanoparticles aerogel thin film, ~ 966% for SiC nanowires, ~ 800% for thermally carbonized porous silicon, ~ 1500% for alumina nanowire, 1490% for (PEPC+NiPc+Cu₂O)- and so on based humidity sensors) reported elsewhere (Ahmad *et al.*, 2013; Björkqvist *et al.*, 2004; Cheng *et al.*, 2013; Feng *et al.*, 2012; Wang C.-T. *et al.*, 2005; Wang *et al.*, 2012). Therefore, in the further study the 10^2 Hz is considered as best test frequency for the analysis of sensor characteristics.

The humidity sensing mechanism of the CMFTO electro-ceramic could be explained by adsorption phenomena of water molecules and their effect on the capacitance variation of the system. The mechanism for humidity-dependent electrical characteristics of the oxide-based nanomaterial is not very clear to date. Therefore, a possible physical adsorption mechanism of water molecules for the humidity dependent electrical characteristics of the oxide based electro-ceramic nanomaterials is explained

136

here. The relationship between the capacitance and the RH, can be interpreted by using Equation 5.1. On the other hand, the ionic conductivity increases with increasing RH (Wang *et al.*, 2011), and as a result, the capacitance value increases with RH as a function of frequency. In general, under low RH conditions, the water molecules are primarily physisorbed or chemisorbed onto the available active sites of the oxide based CMFTO electroceramic surfaces through double hydrogen bonding as indicated by the dotted-line in Figure 5.4. Due to the double hydrogen bonding, the water molecules are not able to move freely. Thus, more energy is required for the hopping transfer of protons between adjacent hydroxyl groups. Hence, the CMFTO electroceramic exhibits very high electrical impedance in the double hydrogen bonding regime. The protons in CMFTO ceramic which are hindered by discontinuous mobile layers may generate leak conduction and thus increase the capacitance (Wang *et al.*, 2011). On the other hand, at higher %RH, second or multi physisorbed layers are formed by physisorption of water molecules onto the available active sites of the surface oxygen of the oxide-based CMFTO electroceramic through single hydrogen bonding (Figure 5.4). Owing to the single bonds, the water molecules become mobile and progressively more identical to those in the bulk liquid. With further increase of RH, the multilayer physical adsorption increases and as a result the physisorbed water molecules are ionized and produce a large number of hydronium ions (H_3O^+) as charge carriers due to the application of external electric field. In very high humidity conditions, the amount of water content increases and the physisorbed water layers gradually behave like normal condensed liquid. In this condition, the protons require very low energy for hopping between adjacent water molecules; as a result the ionic conductivity increases. This charge transport mechanism can be explained by a Grotthuss chain reaction ($H_2O + H_3O^+ \rightarrow H_3O^+ + H_2O$) conductivity (Agmon, 1995). In addition to the above discussion, at higher RH, the physisorbed water penetrates into the interlayer of CMFTO electroceramic. As

137

a result, the hydrolysis process becomes more effective with the functional groups of oxide based CMFTO electroceramic. Thus, more ions are generated due to the vigorous hydrolysis reaction, and these ions participate in the ionic conduction, and as a result the impedance value decreases (Gao *et al.*, 2011). In addition to the impedance, due to increase of water molecules, the capacitance value increases, which significantly alters the dielectric constants of the material. For instance, the dielectric constant of CMFTO electroceramic nanomaterial is calculated to be 233 at low RH (33 %RH) and 5617 at high RH (95 %RH).
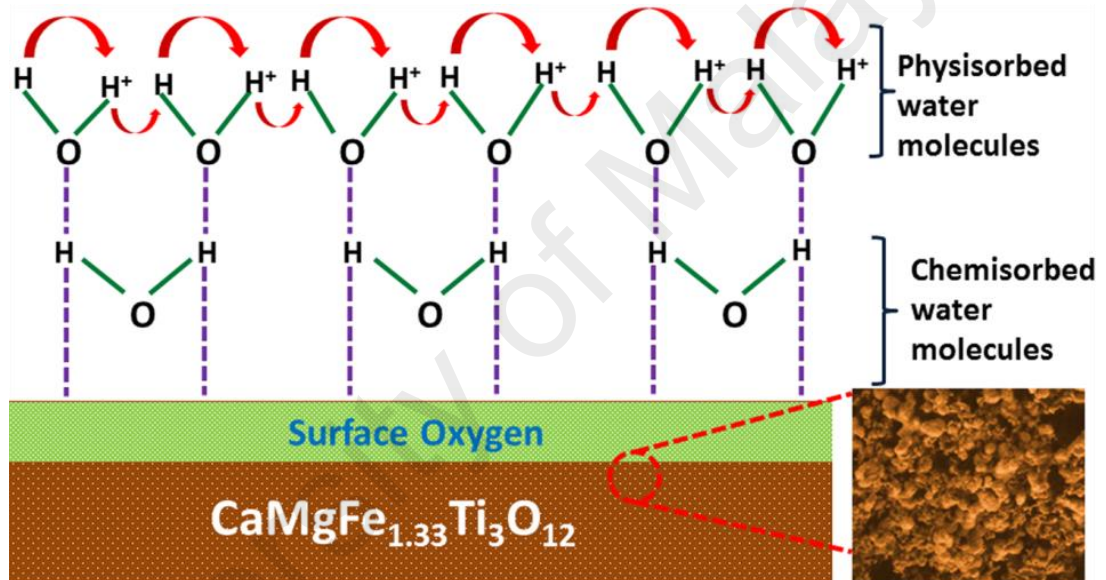
Figure 5.4: Schematic representation of the humidity sensing mechanism of CMFTO electroceramic at different humidity environment.

The nonlinear characteristics on RH dependent capacitive response (Figure 5.1) might be a systematic error in standardization for practical applications of the present humidity sensor. Therefore, to overcome this nonlinearity drawback, an exponential function can be introduced to make the nonlinear response more linear (Wang W. C. *et al.*, 2013). Therefore, in the present study, a transformed logarithmic capacitive-RH response curve was generated and is depicted in Figure 5.5. It has been observed that

two different slope-linear relations revealed in the log*C vs.* RH response curve intersect. This intersection point at 75 %RH is considered as a critical point. It has been analyzed that the data could be well fitted linearly with a slope of 0.0102 and intersect at 10.8148 in negative log*C*-axis in the RH range from 33% to 75%, but in the higher humidity range (75–95 %RH), the slope of the linear fitted curve was found to increase to 0.0532 (see Figure 5.5). Here, the regression (R^2) values of both the fitted curves were very close to 1 (more than 0.97), representing the best fit of the curves to improve linearity. The two different slopes of logC *vs.* RH response plot might be contributed to the change of the adsorption mode of water molecules from a monolayer chemisorption and the multilayer physisorption at low and high RH, respectively (McCafferty & Zettlemoyer, 1971; Seiyama *et al.*, 1983; Traversa, 1995). This linearity and sensitivity consideration of the logarithmic response curve represent a breakthrough for the CMFTO electroceramic as a suitable humidity sensing material.
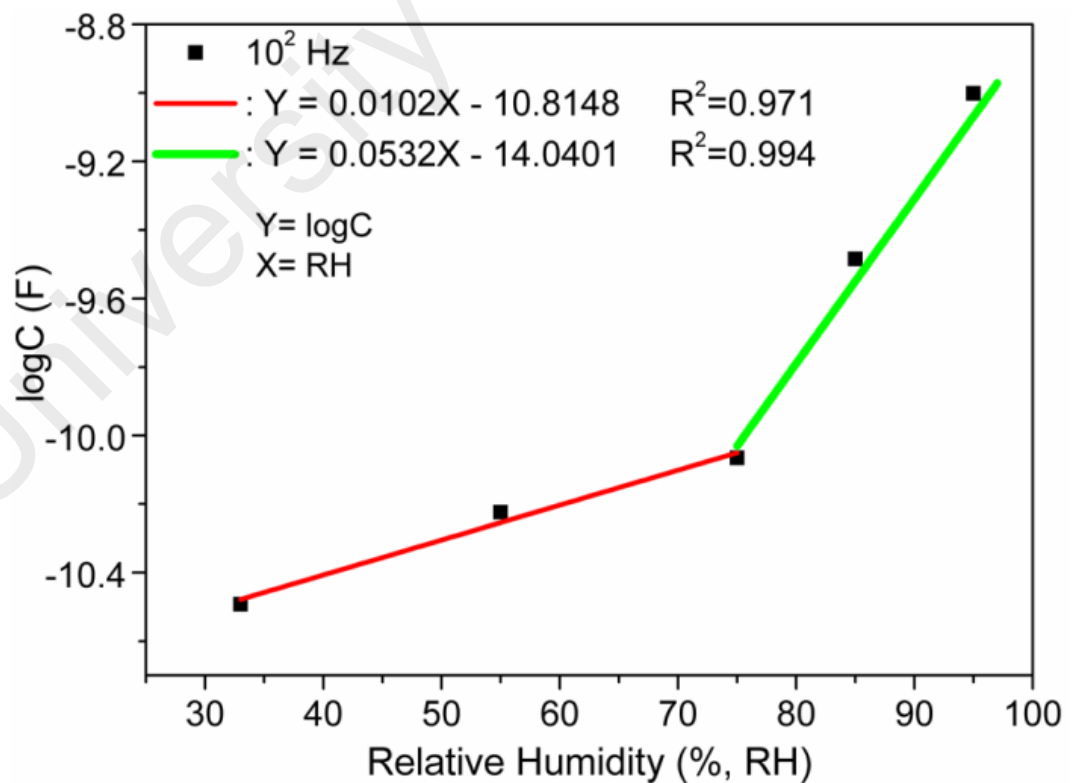
Figure 5.5: The transformed response curves of logarithmic capacitance (logC) *vs.* RH of CMFTO electroceramic based capacitive sensor.

139

The maximum difference in *C*-value between the humidification and desiccation curve is known as hysteresis. High hysteresis values have long been a major drawback in practical humidity sensor applications. The maximum hysteresis rate (E_{max}) of the developed sensor has been calculated by using Equation 5.3 (Wang W. C. *et al.*, 2013):

$$E_{max} = \frac{\Delta m}{Y_{FS}} \times 100\% \tag{5.3}$$

where, Δm stands for the maximum hysteresis and Y_{FS} is the full scale output.

The CMFTO electroceramic based humidity sensor showed a maximum hysteresis of about 3.2 % corresponding to 85 %RH (see Figure 5.6). This result indicates that the hysteresis of the developed CMFTO electroceramic based humidity sensor is relatively lower than that of other different capacitive humidity sensors (i.e., ~4.16% for ZnO/Si-based, ~4.5% for SiC nanowire-based, ~4% for alumina nanowire-based, ~5% for graphene oxide-based, ~12% for (PEPC+NiPc+Cu_2O)-based and so on) developed by other studies (Ahmad *et al.*, 2013; Bi *et al.*, 2013; Feng *et al.*, 2012; Wang *et al.*, 2012; Wang L. L. *et al.*, 2013).
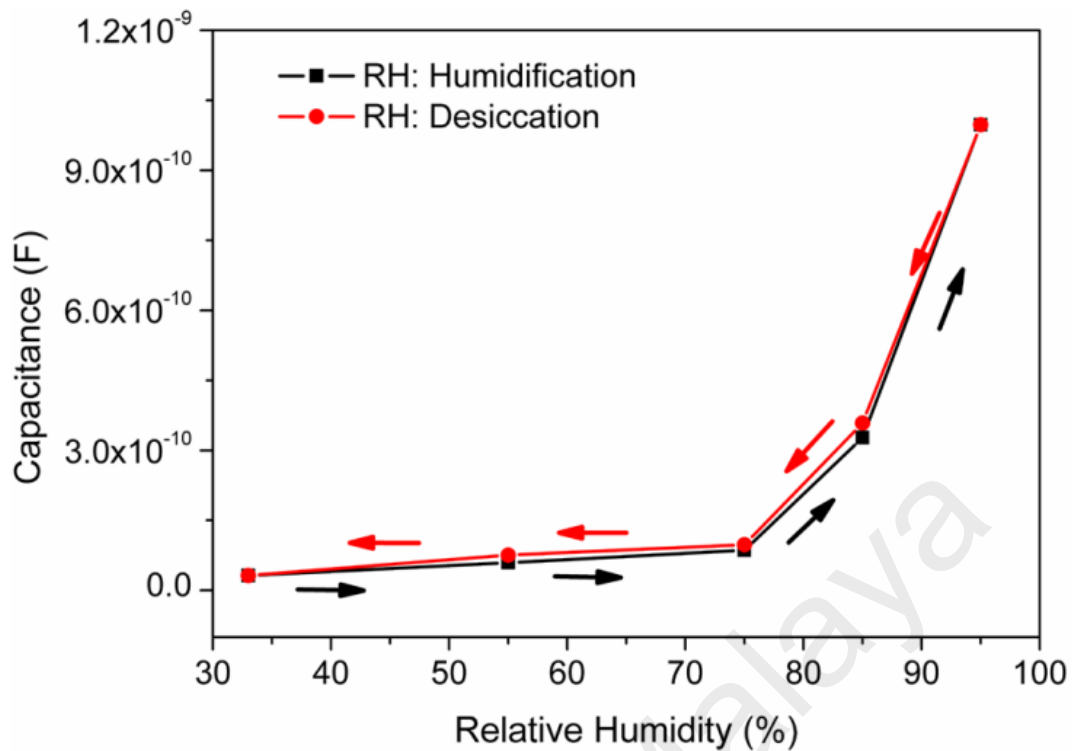
Figure 5.6: The hysteresis property of CMFTO electroceramic-based capacitive humidity sensor at 10^2 Hz under 25 °C.

The lower hysteresis value was obtained owing to the relatively faster adsorption and desorption rate of water molecules on the surface of the CMFTO electroceramic in comparison to the other materials (Bi *et al.*, 2013; Wang W. C. *et al.*, 2013).

The response and recovery times have a significant effect on the performance of humidity sensors. Time taken by a sensor to achieve ~ 90% of the total capacitance change is defined as the response time in case of adsorption or the recovery time in case of desorption of the water vapors. For a good sensor, the response and recovery time of humidity sensors must be very small. The response (see Figure 5.7A) and recovery (see Figure 5.7B) characteristic curves of the CMFTO electroceramic based humidity sensor show a change in capacitance with time in seconds. From the plots, it has been observed that the response and the recovery times of the sensor were 14.5 s and 34.27 s, respectively. The obtained response and recovery times of the CMFTO electroceramic

141

based capacitive humidity sensor are better than those of other conventional capacitive sensors.
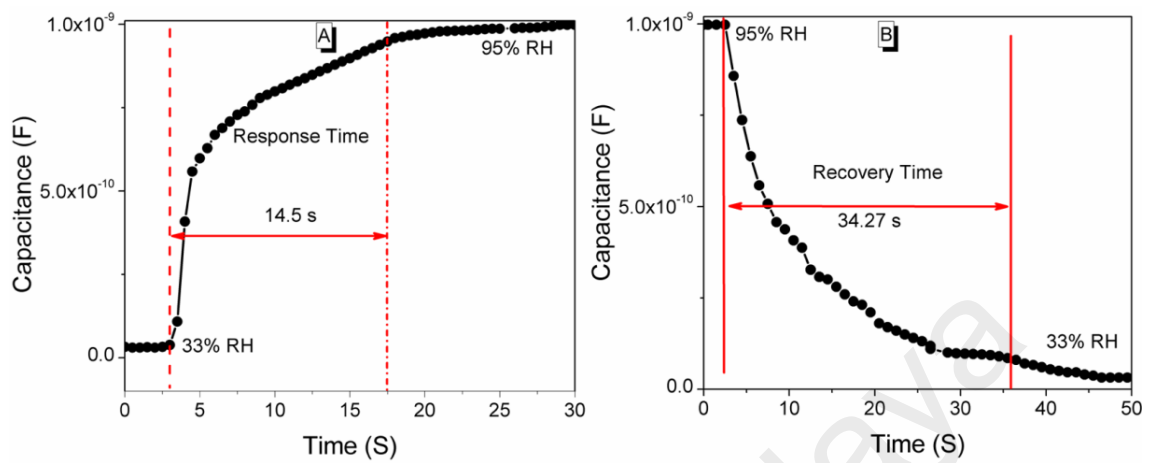
Figure 5.7: Response and recovery times of the CMFTO humidity sensors for humidity levels between 33 %RH and 95 %RH at 10^2 Hz. (A) Response time (14.5 s); (B) Recovery time (34.27 s).

For example, the response time of the present sensor based on CMFTO electroceramic is significantly better than some humidity sensors based on other materials such as silicon nanowires (32 s in 11.3%–93% RH), anodic aluminum oxide (188 s in 30%–95% RH), multi-wall carbon nanotubes (45 s in 11%–86 % RH), macroporous silicon (20 min in 0–100% RH), and so on (Chen W. P. *et al.*, 2009; Chen *et al.*, 2011; Kim *et al.*, 2009; Wang *et al.*, 2010).

Stability is one of the most important parameter for any sensor application. The present CMFTO electroceramic based humidity sensor was tested repeatedly at 10^2 Hz under fixed humidity levels (33%, 55%, 75%, 85% and 95% RH) for a period of 30 days and its humidity sensing parameters were measured repeatedly every 2 days. The characteristics of the present CMFTO sensor depicted in Figure 5.8 exhibit a good stability since there is only slight variation in capacitance as time progresses. Therefore,

the obtained stability characteristics confirm that CMFTO sensor is a good promising material for practical applications.
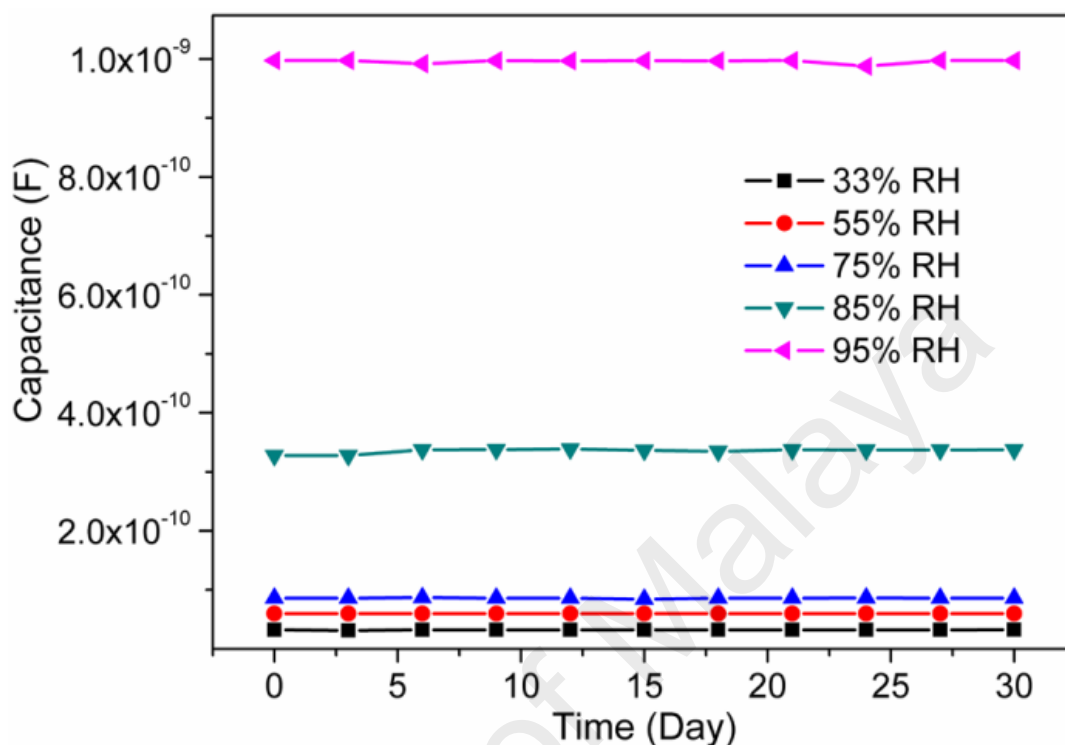
Figure 5.8: Stability analysis of CMFTO electro-ceramic-based humidity sensor measured at a test frequency 10^2 Hz at 25 °C.

Complex impedance spectroscopy is a powerful tool to understand the polarization processes and that take place in a humidity sensor due to absorption of water particles and the conductivity mechanism. The Nyquist/complex impedance plot of the CMFTO-based humidity sensor at different RH (33%–95 %RH) was measured over a frequency range of 10^2 Hz to 10^6 Hz with 1 V AC signal at 25 °C. The variation in impedance spectra suggests different water absorption mechanisms related to electrical conductivity and polarization occur in the CMFTO electro-ceramic. When the RH is low (33%–75 %RH), a half semicircle is observed in the complex impedance plot as depicted in Figure 5.9A. These semicircle characteristics can be explained by the resistance-capacitance parallel electrical circuits as shown in Figure 5.9A (inset).

Therefore, the intrinsic resistance of the sensing electroceramic is responsible for the formation of the semicircle. The curvature of the semicircle decreases with increasing RH and results the decrease in intrinsic impedance, which is mainly due to the interaction between the sensing nanomaterial and water molecules. The polarization processes and conductivity mechanism that take place in a humidity sensor can be expressed by the resistance and capacitance electrical model as well by ionic interface and diffusion phenomena. With increasing RH (85%–95 %RH), a straight line is generated in the low-frequency range and the semicircle becomes small (Figure 5.9B). The ionic as well as electrolytic conductivity are mainly responsible for the formation of a straight line in the complex impedance plot (Song *et al.*, 2009; Su & Wang, 2011). The straight line connected semicircular response curve represents another type of sensing mechanism which can be modelled by a capacitive and resistive equivalent electrical model as depicted in Figure 5.9B (inset) (Song *et al.*, 2009; Su & Wang, 2011). In these equivalent circuits of such complex impedance plots, R_f stands for the resistance of the CMFTO electro-ceramic, which decreases as RH increases, C_f is the capacitance of the CMFTO electro-ceramic and Z_i is the interfacial impedance at the electrodes/CMFTO electro-ceramic (Song *et al.*, 2009; Su & Wang, 2011). At very low RH, the capacitive behavior is mainly attributed to the conductivity of protons and the resistive characteristic is related to H_3O^+ ions. When the RH increases gradually, a huge number of water molecules participate in the physisorbed process on the large specific surface area of the CMFTO electro-ceramic. Thus, proton hopping between the adjacent water molecules occurs easily in CMFTO electro-ceramic. This causes a decrease in the intrinsic resistance of the CMFTO electro-ceramic corresponding to the more depressed semicircles and longer straight lines in Figure 5.9B at higher RH values. As higher the %RH, the line becomes longer and the semicircle becomes smaller. The line represents the Warburg impedance and occurs due to the diffusion of the electroactive species at

144

the electrodes (Qi, Zhang, Yu, *et al.*, 2008). Hence, the complex impedance plots represent a single semicircle appears at lower humidity (33%–75 %RH) (Figure 5.9A) and a straight line appears just after the 75 %RH (Figure 5.9B). The single semicircle and the semicircle with straight line show completely two different sensing mechanisms. It was also clearly observed in Figure 5.5 where two different slopes of log$C$ *vs*. RH plot contributed to the change in adsorption mode of water molecules from a monolayer chemisorption at low RH and a multilayer physisorption at high RH. It is thus indicated that the 75 %RH is a critical point for water absorption mechanism of the present CMFTO and it is clearly confirmed that the two different conduction mechanisms take place at the surfaces of CMFTO electro-ceramic.
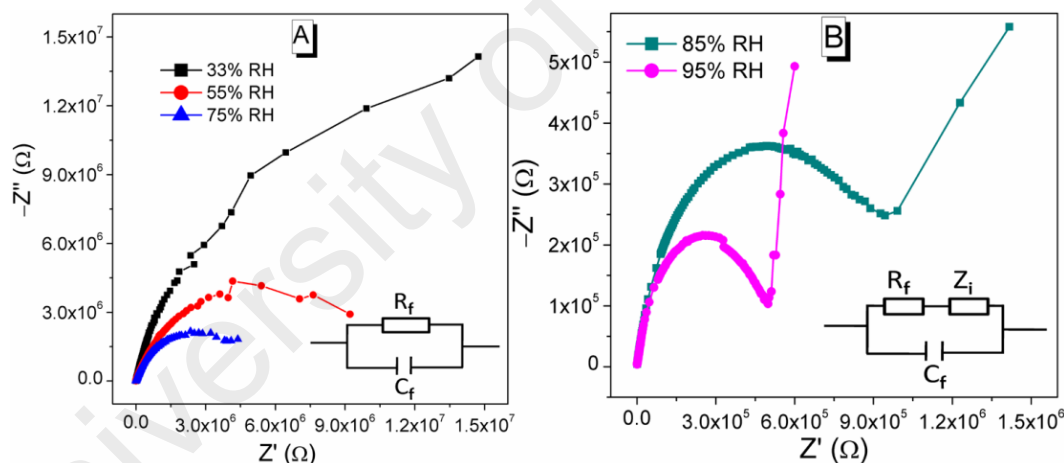
Figure 5.9: Complex impedance plots and equivalent circuits of CMFTO based electro-ceramic under different humidity levels. (A) At lower humidity range (33%–75 %RH); (B) At higher humidity condition (85%–95 %RH), the insets represent the equivalent circuits at lower and higher RH.

5.1.2   Concluding Remark of Capacitive Humidity Sensor

A novel submicroporous Ca,Mg,Fe,Ti-oxides electroceramic based capacitive humidity sensor has been fabricated from some inexpensive oxide nanomaterials using a

solid-state step-sintering process. The presented sintering technique helped to get nanomaterials with the desired morphology, lower density and high porosity. This newly developed Pb-free CMFTO electroceramic has shown improved capacitive humidity sensing properties via physisorption. It has shown two distinct conduction mechanisms by displaying a critical RH at 75 %RH. The capacitance of the sensor of the CMFTO electro-ceramic increased from 3.2183×10^{-11} F to 9.9741×10^{-10} F as the RH changed from 33% to 95% at a testing frequency of 10^2 Hz. It has shown a high sensitivity (3000%), rapid response (14.5 s) and recovery (34.27), which is much lower than the values of other conventional capacitive humidity sensors. The present capacitive sensor showed a very low hysteresis of 3.2%. Therefore, all the above improved sensing characteristics, together with the good linearity and stability of the CMFTO electro-ceramic indicate that it can be used as a potential humidity sensing material for advanced applications.

5.2 Humidity Dependent Impedance Spectroscopic Study of CMFTO Nanocomposite based Impedance Sensor

This section mainly focused on the humidity dependent impedance responses of CMFTO nanocomposite.

5.2.1 Humidity Sensing Impedance Measurements

The complex impedance spectra of the newly developed CMFTO nanoceramic derived sintered electroceramic nanocomposite material based humidity sensor with different humidity conditions i.e., 33%-95% RH are depicted in Figure 5.10(A-E). It was observed that the value of impedance decreased with the increasing humidity. This study describes the mechanism of impedance response with the function of humidity. From the SEM analysis, it was confirmed that at 1050 °C sintering temperature, the

porosity of the sintered nanocomposite was achieved to the desired level, which enhanced the hydrophilic surface characteristics of the developed sensors material. When the porous sintered nanocomposite was placed in a humid environment, the oxygen and water from the surrounding atmosphere could be chemisorbed onto its hydrophilic surface, which played a vital role to alter the sensing characteristics of the sensor. In addition, due to the increase of RH from 33% to 95%, more amounts of water particles had been absorbed on the surface of the composite. It mainly results in a decrease in impedance, such a manner that the dielectric properties can be tailored. In Figure 5.10, it has been further observed that at lower humidity levels, one semicircle is formed and as humidity increases, a line starts to appear. This line is associated to electrode/interface effect. As humidity increases, the semicircle starts to shrink and the line becomes longer. Therefore, it indicates that at higher RH value, the dielectric properties seem to increase.
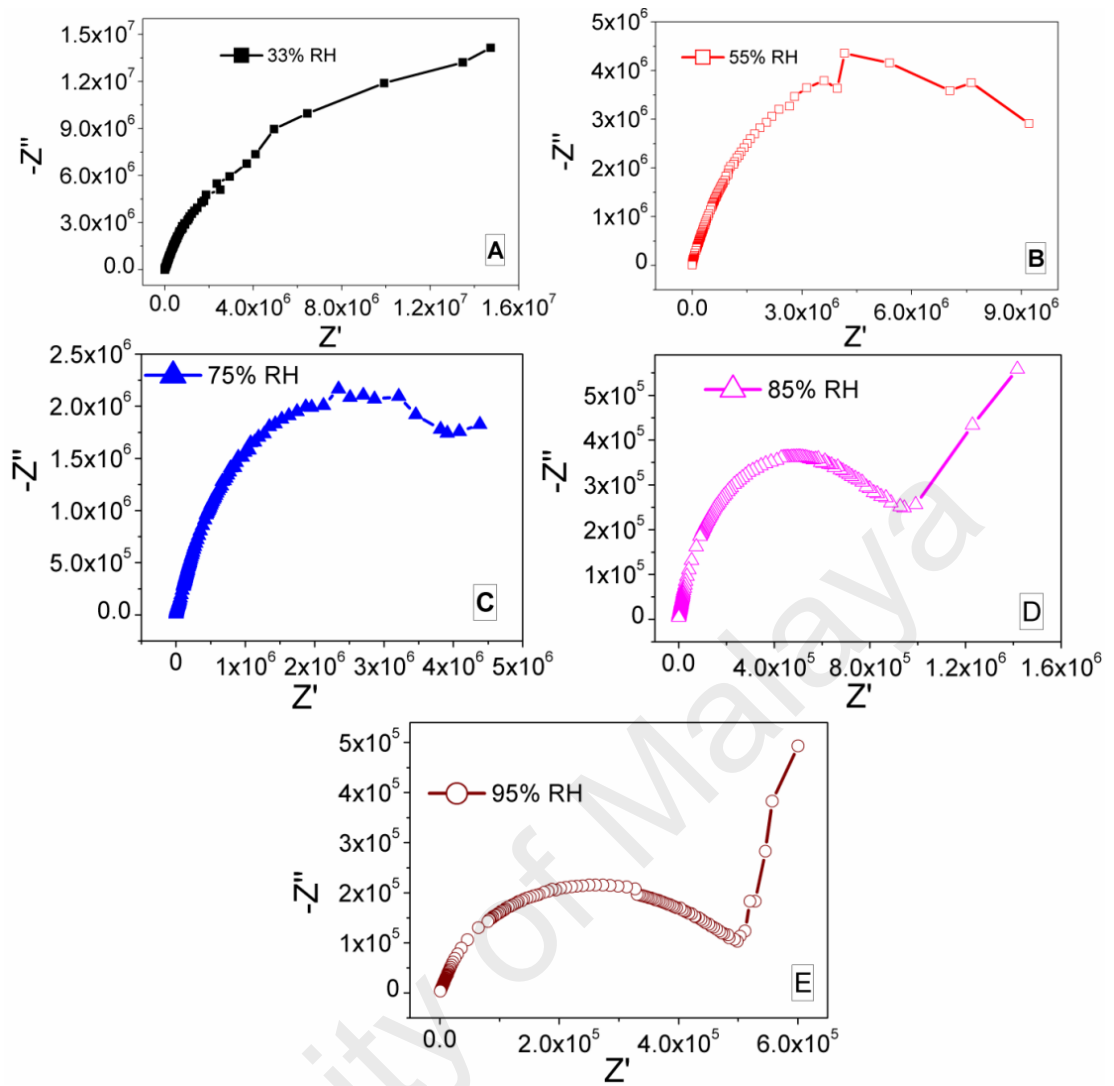
Figure 5.10: Nyquist plots of CMFTO nanocomposite device at: (A) 33 %RH, (B) 55 %RH, (C) 75 %RH, (D) 85 %RH, (E) 97 %RH.

In addition, in order to analyze the effect of humidity on the CMFTO electroceramic nanocomposite device, this study measured the impedance, the capacitance, and the modulus at different humidity conditions at a frequency range of 10^2 Hz – 1 MHz at 25 °C. The RH dependent capacitance effect is depicted in Figure 5.11. It was observed that for all the relative humidity levels, the value of capacitance decreased with the increase in frequency. This decreasing rate, nonetheless, has been faster at low frequencies, but slower at higher frequencies. On the other hand, the capacitance value was found to increase with the increasing humidity. As humidity increased, more

148

number of H^+ ions was available in adsorbed water layers on the surface of the sensor material and hence, the capacitance value became higher (Usman *et al.*, 2014). Impedance also highly depends on the frequency value since it is directly related to energy of charge carriers. At lower humidity condition, due to discontinuity of water particles, higher energy is required for the hopping transfer of protons between the adjacent hydroxyl groups. Thus, this sensors material of sintered electroceramic nanocomposite has exhibited very high electrical impedance. However, at higher humidity condition, the proton requires very low energy for hopping between the adjacent water molecules owing to the continuous water layer. As a result, the ionic conductivity has increased and hence, the electrical impedance has decreased.
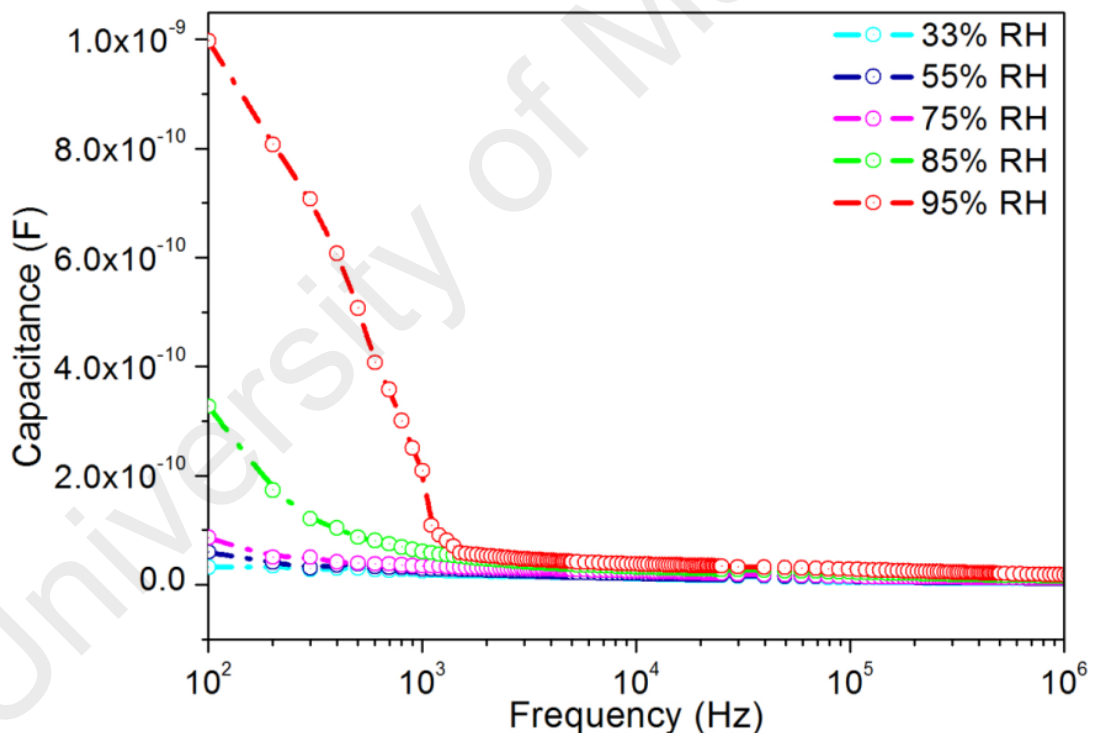
Figure 5.11: Variation of capacitance of CMFTO electroceramic nanocomposite at different relative humidity as a function of frequency in logarithmic scale at 25°C.

Moreover, the frequency dependent impedance (Z') responses of the CMFTO electroceramic nanocomposite at different RH values are depicted in Figure 5.12. It was

149

observed that the value of impedance decreased with the increasing frequency. This decreasing rate had been faster at a lower frequency range of 10^2-10^3 Hz, but became slow and almost constant at higher frequencies of $> 10^4$ Hz. The impedance value decreased when the RH was increased. This is because the number of increased H^+ ions by the increase in concentration of the adsorbed water. These H^+ ions have played a vital role in the conduction mechanism and gradually, helped to increase the mobility of ions.
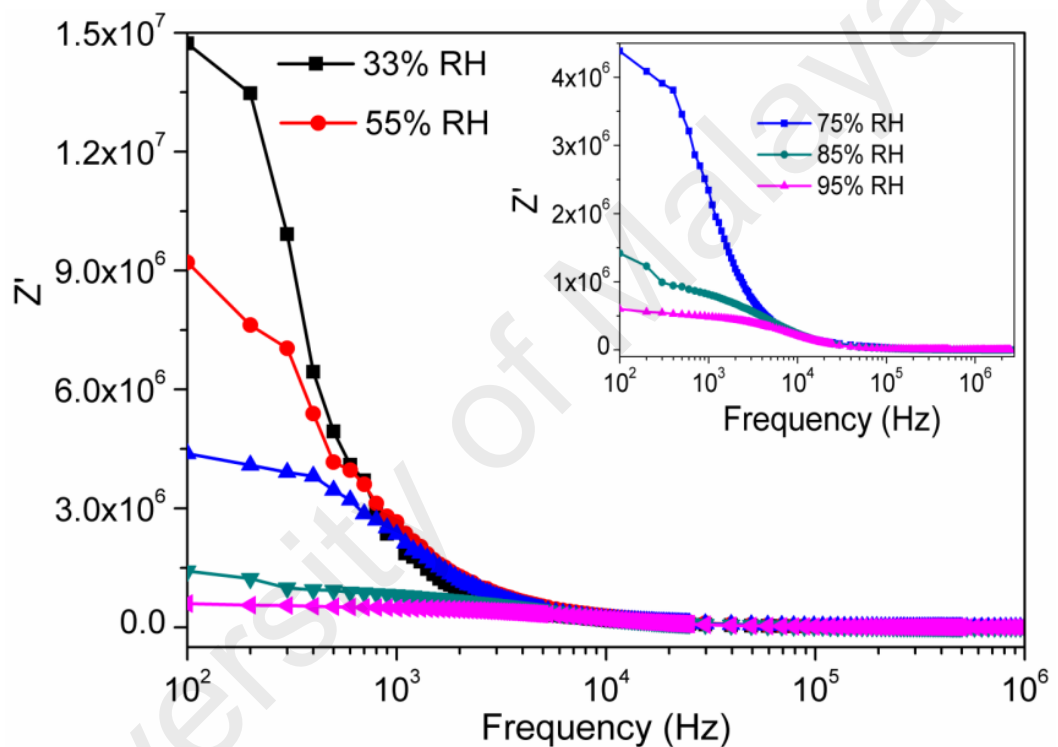
Figure 5.12: Variation of real impedance (Z') of CMFTO electro-ceramic nanocomposite at different relative humidity as a function of frequency in logarithmic scale at 25 °C.

The frequency dependent capacitive reactance of the sintered CMFTO electroceramic nanocomposite has reflected the imaginary part of the impedance (Z"). It is plotted with frequency at different RHs in Figure 5.13. A peak was observed in each curve. The peak frequencies shifted towards right with increasing humidity. This

phenomenon has been attributed to the capacitive property of the sample (Hu & Fu, 2010).
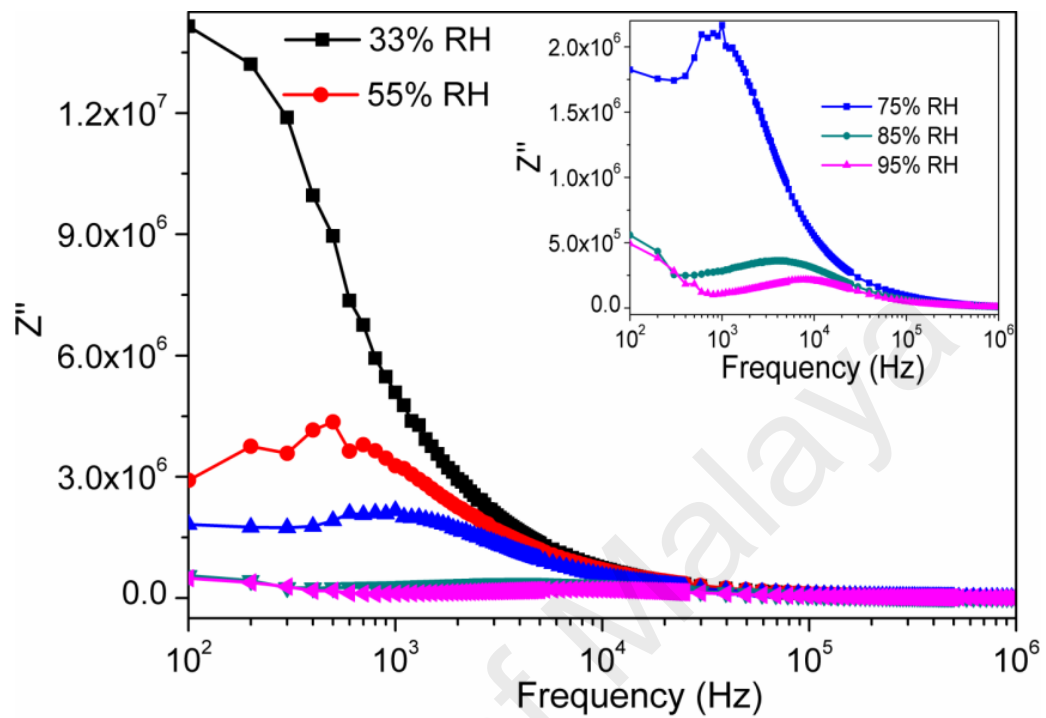
Figure 5.13: Variation of imaginary (Z") impedance of CMFTO electro-ceramic nanocomposite at different relative humidity as a function of frequency in logarithmic scale at 25 °C. Inset image represents a magnified scale of Z" vs log(f) plot of developed ceramic at higher RH (at 75, 85 and 95% RH) with prominent relaxation peak.

Other than that, humidity dependent impedance responses at 10^2 Hz, 10^3, 10^4, 10^5, and 10^6 Hz for sintered CMFTO electroceramic nanocomposite sensors are depicted in Figure 5.14. The impedance of the electroceramic nanocomposite humidity device decreased with increasing RH, as shown in Table 5.1.

Table 5.1: Frequency dependent impedance variation at lowest (33%) and highest (95%) relative humidity condition.

Frequency (Hz)	Impedance (Ω) at 33% RH	Impedance (Ω) at 95% RH
10^2	1.47×10^7	6×10^5
10^3	2.51×10^6	4.8×10^5
10^4	2.02×10^5	1.6×10^5
10^5	1.7×10^4	1.6×10^4
10^6	2.2×10^3	5.43×10^2

Therefore, it indicates that the change in humidity affects the impedance considerably at intermediate and low frequencies. Nonetheless, this change is very small at higher frequencies. Besides, to explain the humidity dependent impedance characteristics of nanocomposite sensor, the device sensitivity (S_Z), due to change in impedance, was calculated by using Equation 5.4 (Imran *et al.*, 2013; Pandey & Tiwari, 2010).

$$S_Z = \frac{\Delta Z}{\Delta \% \, RH} \tag{5.4}$$

where, ΔZ is change in impedance (i.e., Z') at the corresponding change RH, i.e., $\Delta \% RH$. From Equation 5.4, the sensitivity of the device is 0.23 MΩ/Δ%RH (33% – 95% RH), 0.032 MΩ/Δ%RH, 0.68 kΩ/Δ%RH, and 0.027 kΩ/Δ%RH at 10^2 Hz, 10^3 Hz, 10^4 Hz, and 10^6 Hz, respectively. These results confirm that the highest sensitivity has been observed at 10^2 Hz, which was noticeably higher than the other conventional resistive humidity sensor (S_Z of BaTiO$_3$ thin film $\sim$ 0.16 MΩ/Δ%RH, TiO$_2$/Li$_2$O/V$_2$O$_5$ based composite $\sim$ 0.011 MΩ/Δ%RH, Porous ZnAl$_2$O$_4$ spinel nanorods $\sim$ 0.08 MΩ/Δ%RH, LiZnVO$_4$-doped SnO$_2$ $\sim$ 0.0012 MΩ/Δ%RH, ZnO nanorods $\sim$ 0.082 MΩ/Δ%RH and so on, at 100Hz) (Aoki *et al.*, 2008; Cheng *et al.*, 2013; Hu & Fu, 2010; Yuk & Troczynski, 2003; Zhang, Yu, Jiang*, et al.*, 2005). Therefore, 10^2 Hz frequency was adopted as the testing frequency in all the succeeding analyses of the present sensor.
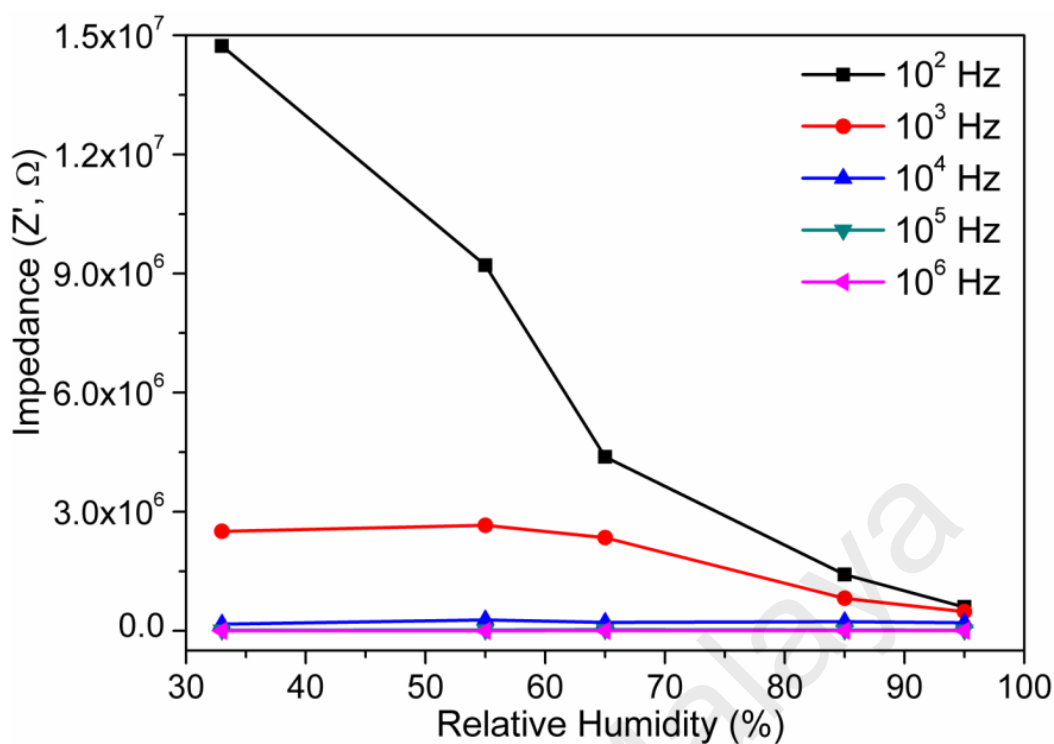
Figure 5.14: Impedance versus RH measured of CMFTO electroceramic nanocomposite at various frequencies at 25 °C.

In estimation of the performance of humidity sensors, the response and the recovery behaviors are the most significant features. The response time was measured as the time needed to reach 90% of the final signal for a given relative humidity. On the other hand, the recovery time was calculated as the time taken for the signal to come to within 10% of the initial value. The response and recovery times were determined by alternately exposing to 33–95% RH. The response and recovery times had been very structure sensitive. Hence, for practical application, they must be as short as possible to function as a good sensor. Besides, in order to determine the response and recovery times, a graph between impedance and time was plotted at AC voltage of 1 V and frequency of 100 Hz. For the present electroceramic nanocomposite based impedance type sensor, the response time is 20 s when RH changed from 33% to 95%, whereas the recovery time is 40 s when RH changed reversely from 95% to 33%, as depicted in Figure 5.15. The newly developed impedance or resistive type humidity sensor has displayed faster

153

response and recovery times than the reported conventional sensors (e.g., response and recovery times of LiZnVO$_4$-doped SnO$_2$ ~60 s and ~100 s, Ba$_{0.5}$Ni$_{0.5}$SnO$_3$ ~3 min and ~4 min, Li-doped mesoporous silica A-SBA-15 ~60 s and ~180 s, LiCl-doped mesoporous silica MCM-41 ~100 s and ~150 s, mesoporous ZnO–SiO$_2$ composite ~50 s and ~100 s respectively, and so on) (Doroftei *et al.*, 2012; Hu & Fu, 2010; Wang *et al.*, 2008; Yuan *et al.*, 2010; Zhang, Wang*, et al.*, 2008).
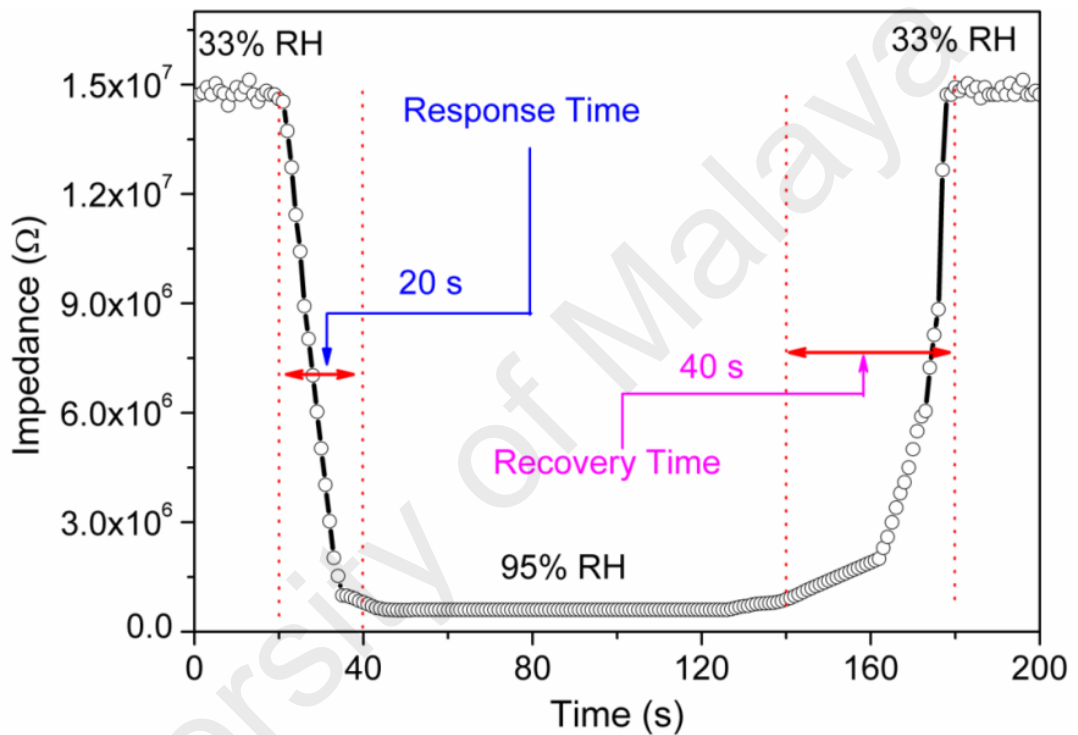
Figure 5.15: Response and recovery curve of CMFTO electro-ceramic nanocomposite measured at 10^2 Hz for humidity levels between 33% RH and 95% RH at 10^2 Hz.

The humidity hysteresis is one of the most important parameters of a humidity sensor. The maximum difference between humidification and desiccation curve is known as hysteresis. The hysteresis response of the present CMFTO electroceramic nanocomposite sensor is shown in Figure 5.16. The maximum hysteresis of ~ 3.4% was observed in the devices at 100 Hz, indicating good reliability of this sensor. The obtained hysteresis value of the developed humidity sensor, however, is lower than the

154

many conventional resistive humidity sensors (LiZnVO$_4$-doped SnO$_2$ ~6%, CdTiO$_3$ ~7%, BaTiO$_3$ nanofibers ~5%, BaTiO$_3$/polystyrene sulfonic sodium ~8%, and so on) (Hu & Fu, 2010) (Imran *et al.*, 2013) (He *et al.*, 2010) (Wang, Xu*, et al.*, 2003).
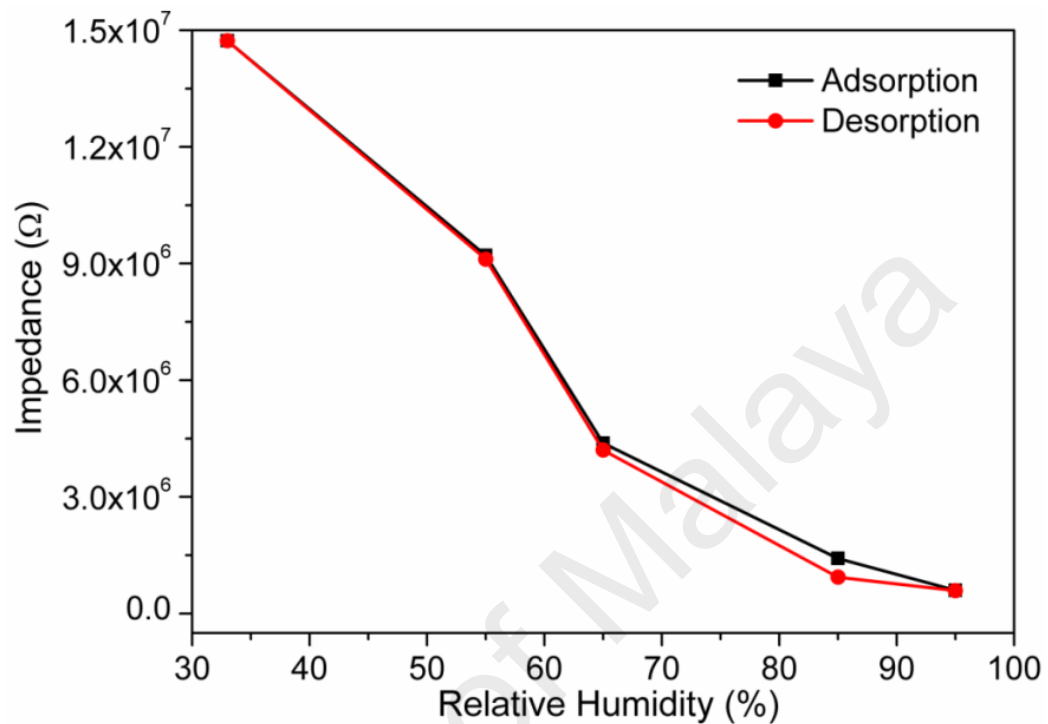
Figure 5.16: Humidity response of the sensor based on sintered CMFTO electroceramic nanocomposite during humidification and desiccation process at 10^2 Hz.

In addition to the aforementioned electrical parameters, stability is another important measuring property in order to evaluate the merit of a humidity sensor. To test the long term stability, the present CMFTO electroceramic nanocomposite based impedance type humidity sensor was kept for 30 days in air at 25 °C, and its impedances were measured repeatedly for every 2 days at different RH values, as depicted in Figure 5.17. The measurements were done at 10^2 Hz with 1V AC power supply at 25 °C. Very little fluctuation or almost no change in the impedance of the device had been observed over 30 days. In fact, the sensor resistance slightly increased in room atmosphere after aging. It evidently confirms that the present resistive sensor has significantly good stability. The increased response of conductivity with RH of the present electroceramic

155

nanocomposite could be explained by the Grotthuss mechanism (Agmon, 1995), which correlates this characteristic with the tunneling of proton from one water molecule to another (Chen & Lu, 2005).
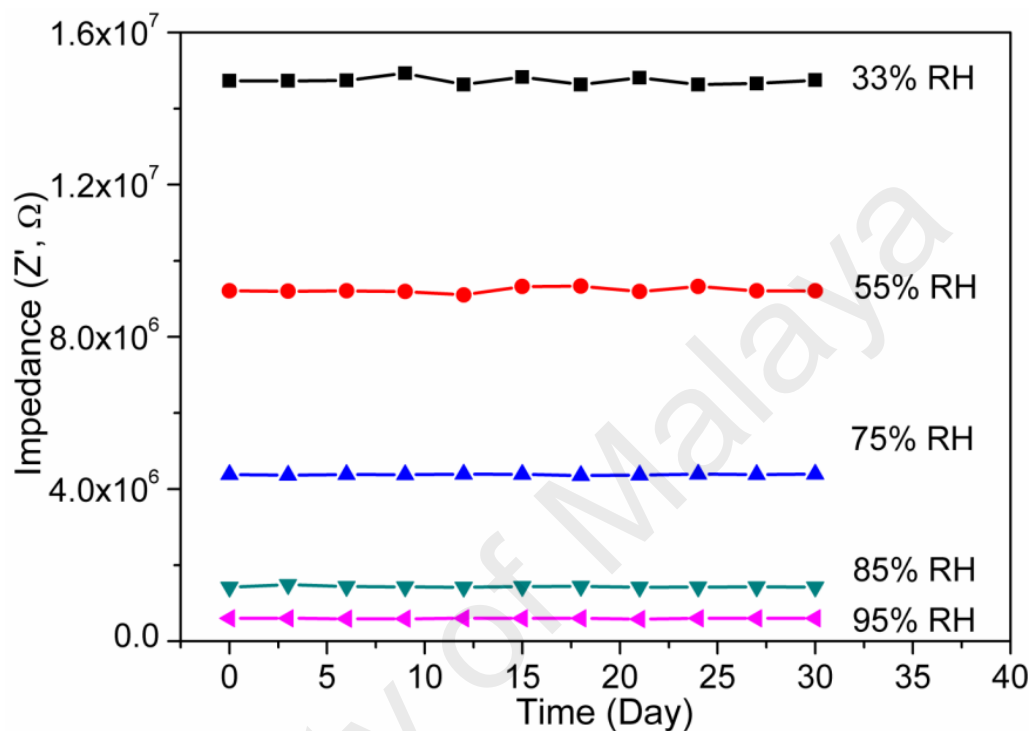
Figure 5.17: Long term stability property of the sensor based on sintered CMFTO electroceramic nanocomposite over 30 days measured at 10^2 Hz and 1V.

At lower RH condition, the water molecules are chemically adsorbed (chemisorption) onto the available active sites of the oxide-based CMFTO electroceramic surface through double hydrogen bonding, as depicted in Figure 5.18. Due to double hydrogen bonding, the water molecules fail to move freely. As a result, the impedance of the nanocomposite increases. With further increase in humidity, the physical adsorption (physisorption) of water molecules is occurred. The water molecules are physisorbed onto the available active sites of the oxide-based CMFTO electroceramic nanocomposite surface via single hydrogen bonding (Figure 5.18). Due to the single bond, the water molecules become mobile and the conductivity increases

156

progressively. With further rise of RH, the multilayer physical adsorption increases and due to the application of external electric field, the physisorbed water molecules are ionized. As a result, a large number of hydronium ions (H_3O^+) might be available for conduction (Nahar, 2000).
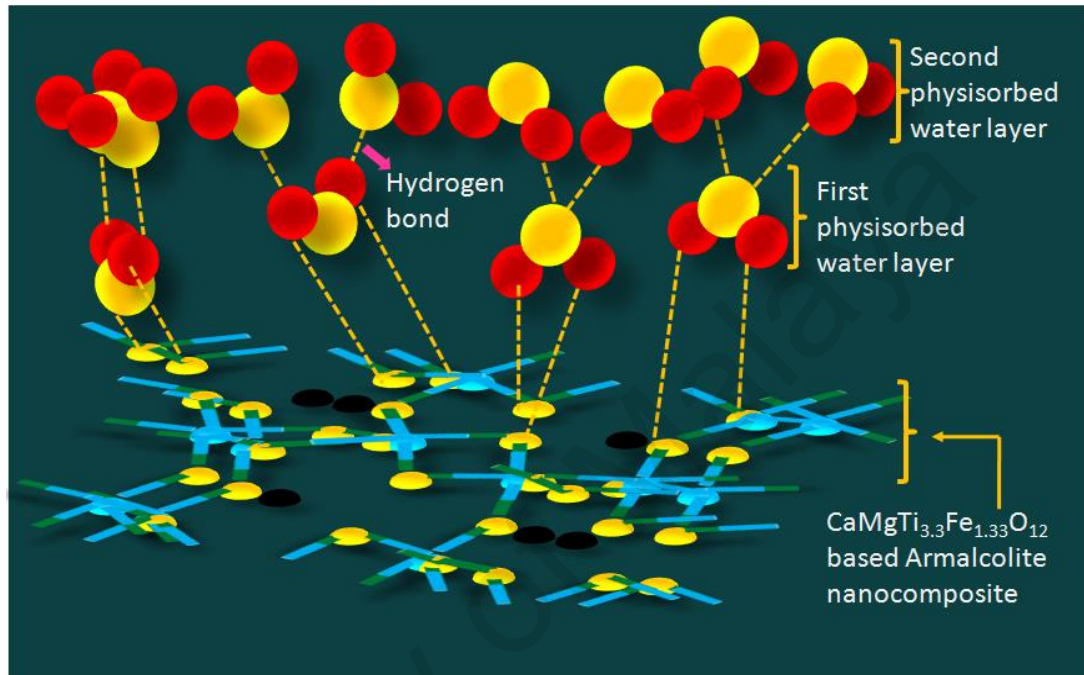
Figure 5.18: Schematic representation of the humidity sensing mechanism of the sensor based on CMFTO nanoceramic derived sintered electroceramic armalcolite nanocomposite at low and high humidity.

The complex electric modulus (M^*) can be expressed by using Equation 3.10 (Gerhardt, 1994). To suppress the electrode polarization and space charge injection phenomena, the complex modulus analysis has been an effective method. The frequency dependent M' and M'' responses at different RHs are shown in Figures 5.19 and 5.20, respectively. In Figure 5.19, when the value of M' changed from low to high, a sigmoidal shape curve was observed. This observation confirms the existence of relaxation phenomenon inside the newly developed nanocomposite at the time of interaction to the water particles. This observed phenomenon can be accompanied by a

loss peak in log(f) vs M″ plot, as shown in Figure 5.20. The existence of relaxation

peaks was further confirmed by the plots depicted in Figure 5.20. Besides, it was

observed that the relaxation peak frequencies shifted towards higher frequencies with

the increase in relative humidity. The shifting of peaks towards higher frequencies

suggests the increase in direct current (DC) conductivity (σ_{dc}) with relative humidity

(Usman *et al.*, 2014). The frequency, where the peak was formed, is known as

relaxation frequency and its corresponding time is known as relaxation time, i.e., $\tau =$

½πf_{max}, where f_{max} is peak frequency. This implies that the relaxation time, τ is inversely

proportional to the peak frequency, f_{max}. Since the relaxation frequency increased with

the increasing RH, the relaxation time decreased with the increase in humidity.
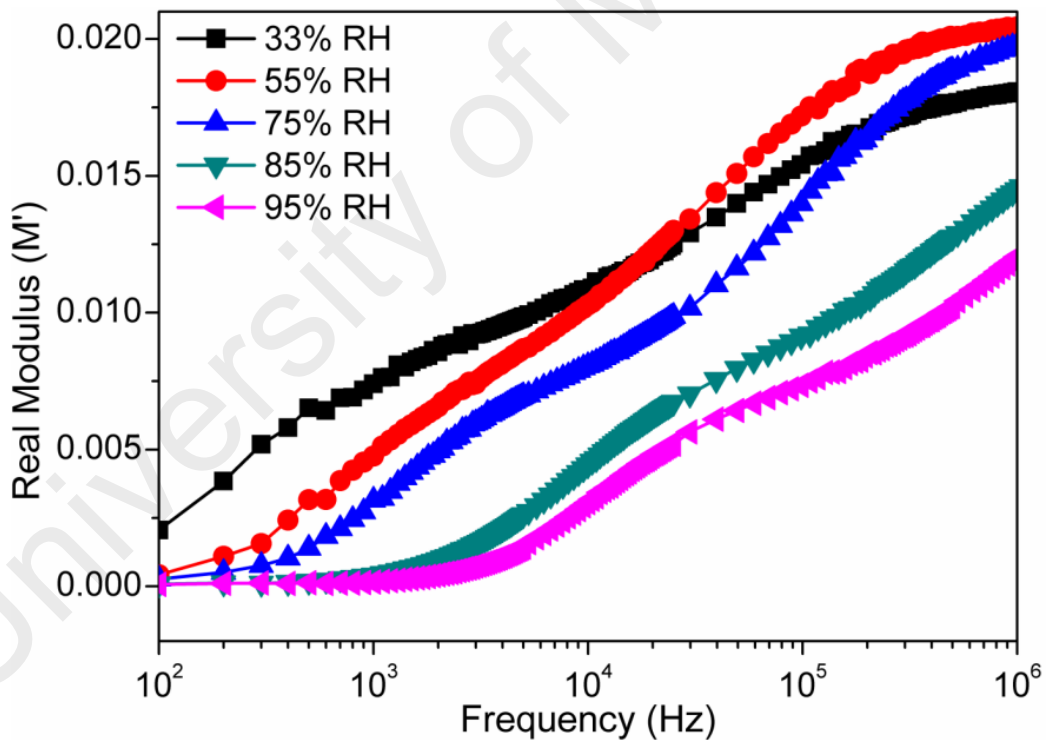
Figure 5.19: The variation of real (M') modulus components of the CMFTO electroceramic nanocomposite at different RH as a function of frequency in logarithmic scale at 25 °C.
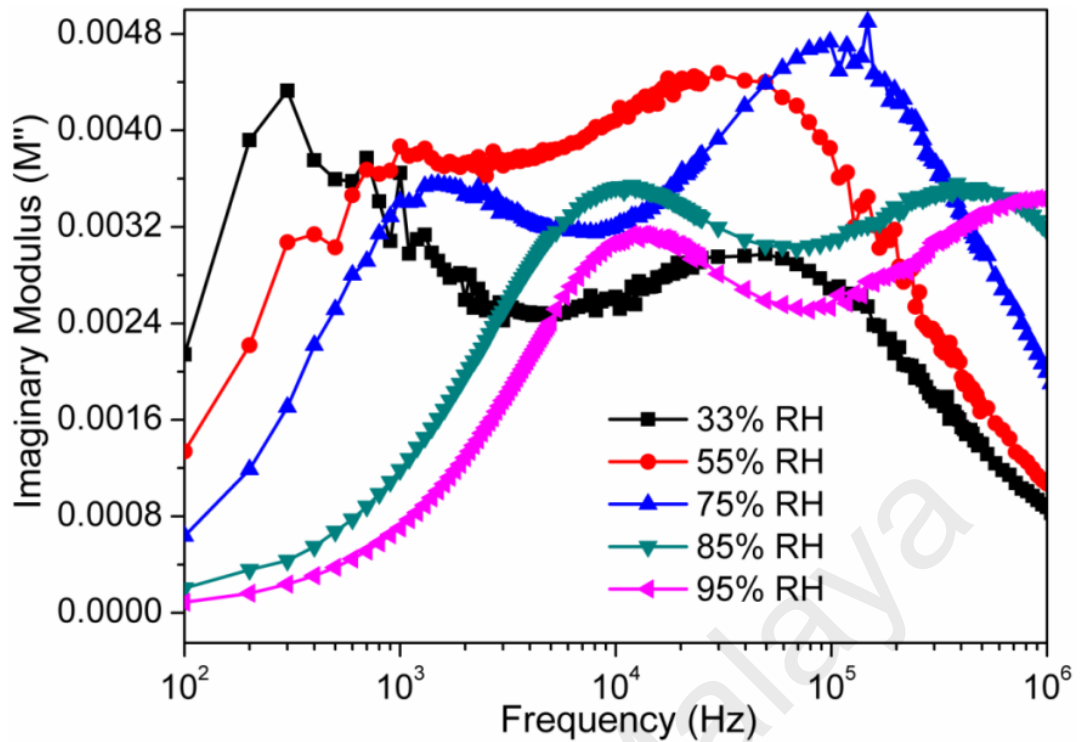
Figure 5.20: Variations in imaginary (M") modulus components of the sensor based on CMFTO electroceramic nanocomposite at different RH as a function of frequency in logarithmic scale at 25 °C.

The complex modulus spectra (M″ vs. M′) of the present CMFTO electroceramic nanocomposite sensor device at different RHs are depicted in Figure 5.21. The modulus data highlighted in the complex modulus plots help to understand the conductivity relaxation phenomenon in terms of the variation of M" as a function of frequency. The asymmetric semicircular arc observed in this complex modulus plot confirms the association of relaxation phenomenon in the present electroceramic nanocomposite sensor system. As the relative humidity increased, the radius of the semicircle decreased. This indicates that the bulk resistance of the present CMFTO nanoceramic derived sintered electroceramic nanocomposites based humidity sensing device has decreased with the increase in relative humidity.
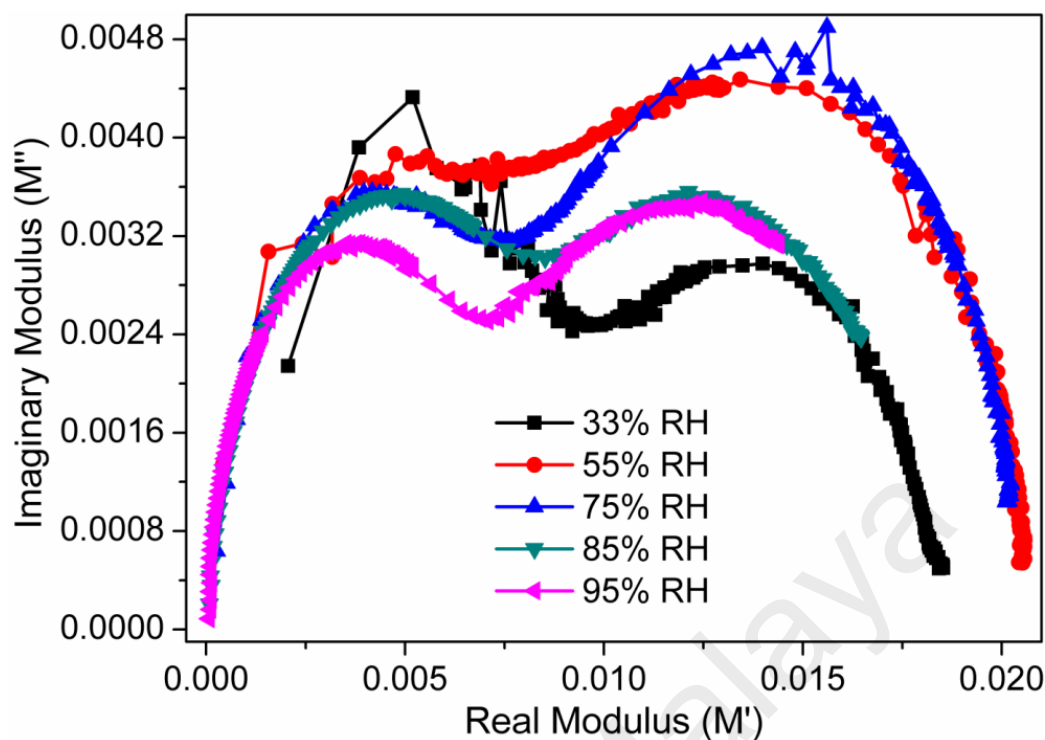
Figure 5.21: Complex modulus responses between real (M') and imaginary (M") at different RH of the sensor based on sintered CMFTO electroceramic nanocomposite at 25 °C.

5.2.2   Conclusion of Impedance humidity Sensor

This study had successfully fabricated impedance type humidity sensor based on CMFTO nanoceramic derived porous sintered electroceramic nanocomposites by using the solid-state step-sintering technique. The structural and morphological analyses had been carried out by using XRD and SEM methods. The desired grain size, high porosity, and good surface-hydrophilicity properties had been obtained for the nanocomposites sintered at 1050 °C. The sintered CMFTO electroceramic exhibited excellent humidity sensing characteristics, including high sensitivity, small hysteresis (3.4%), fast response time (20 s), fast recovery time (40 s), and good stability overlong period. These advanced and improved characteristics had been attributed to the suitable and stable grain size, as well as the porous nature of the nanocomposite. The obtained electrical results confirmed that the newly developed CMFTO nanoceramic derived

sintered electroceramic nanocomposite material based humidity sensor had been better than the many existing conventional metal oxide-based humidity sensors. The best performance of the present sintered electroceramic nanocomposite based humidity sensor had been due to the desired grain size, the highly hydrophilic attribute, and the desired porous nature at the sintering condition at 1050°C. The sensing properties of the present electroceramic based impedance type humidity sensor were further improved by varying the composition and the sintering conditions according to the desired properties for specific application. Therefore, the present novel fabrication technique and the newly developed sintered electroceramic nanocomposite would be very promising for advanced humidity sensor applications.

5.3 Effect of Humidity on the Dielectric Characteristics of the CMFTO (Armalcolite) Nanocomposite based Humidity Sensor

Humidity dependent dielectric characteristics of the CMFTO (armalcolite) nanocomposite based humidity sensor have been described thoroughly in this section.

5.3.1 Frequency Dependent Dielectric Analyses

In order to analyze the frequency dependence of the dielectric type sensor, the dielectric response of armalcolite nanocomposite with respect to RH under the different testing frequencies of 10^2, 10^3, 10^4, 10^5, and 10^6 Hz had been measured at room temperature with 1 Volt AC signal, and the results are plotted in Figure 5.22. The results clearly showed that with the changing of RH from 33% to 95%, the output dielectric constant (ε') increased monotonically with RH. This "giant dielectric response" behavior strongly indicates that the dielectric property could be a good physical quantity for expressing the RH variation.
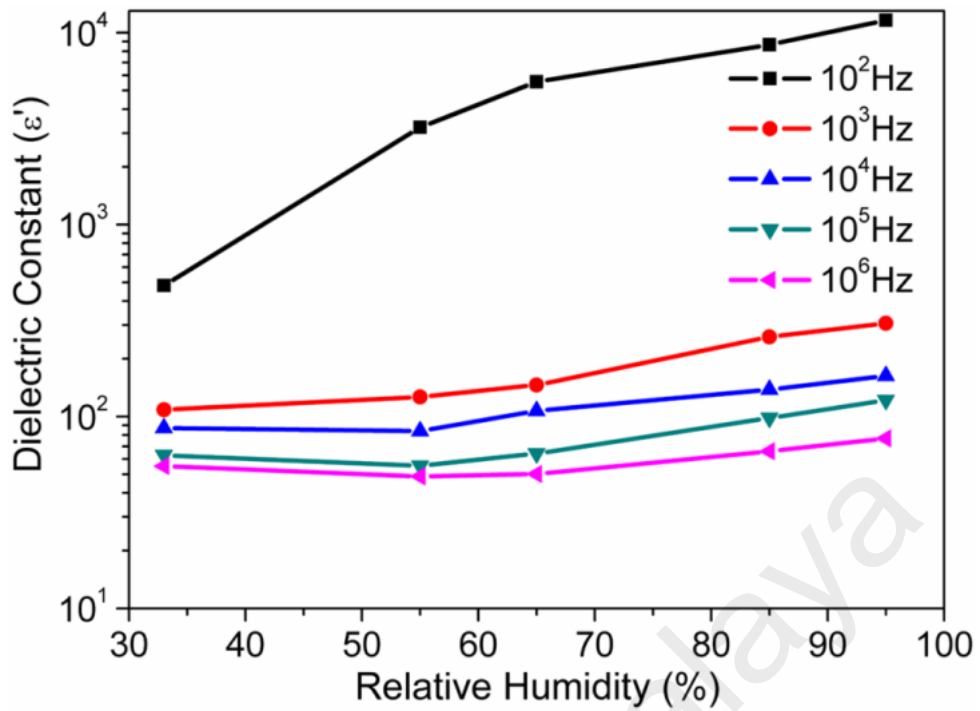
Figure 5.22: Dielectric constant (ε′) versus RH measured of armalcolite nanocomposite at various frequencies at 25 °C.

To analyze the dielectric behavior of armalcolite nanocomposite with RH, the device sensitivity (S_ε), due to dielectric change, was determined with Equation 5.5:

$$S_\varepsilon(\%) = \frac{\epsilon_{RH} - \epsilon_{33}}{\epsilon_{33}} \times 100 \tag{5.5}$$

where, ϵ_{33} and ϵ_{RH} represent the dielectric constants measured at minimum RH = 33% and at a certain RH level, respectively. It is well-known that the signal or testing frequency influences significantly the sensitivity of a humidity sensor. The variations in dielectric constant and the sensitivity increased with the decreasing testing frequency. Over a 33–95 % RH range, at the signal frequency of 100 Hz, the ε′ increased from 482 to 11616 with an S_ε of ~2310%, while at 1 kHz, ε′ increased from 109 to 306 with an S_ε of ~182%, respectively. These results suggest that the 100 Hz is the best testing frequency. Therefore, 100 Hz was selected as the testing frequency for stability,

hysteresis, as well as response and recovery times, for further analyses in the present investigation.

For more distinct analysis, the frequencies of dependent real permittivity or dielectric constant (ε') at different humidity conditions are depicted in Figure 5.23. The results showed that the ε' value increased with the increasing RH, but decreased with the increasing frequency. It was also observed that the ε' increased very rapidly with lowering frequency, but it became small and changed very slowly at higher frequency ranges with RH. This has occurred because at higher relative humidity, the H^+ ions increased in adsorbed water layers on armalcolite nanocomposite surfaces and hence, the ε' increased.
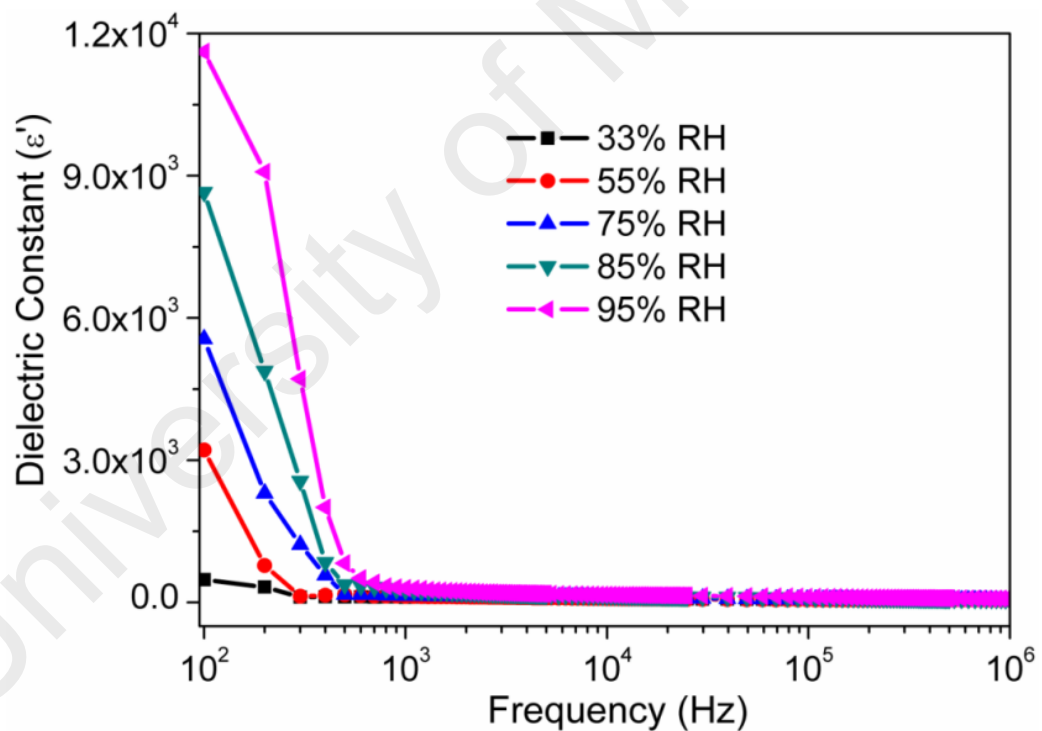
Figure 5.23: Variation of dielectric constant (ε') of armalcolite nanocomposite at different relative humidity as a function of frequency in logarithmic scale at 25 °C.

Other than that, in order to analyze the ionic conductivity at higher humid environment, the frequency dependent imaginary permittivity or dielectric loss (ε'') in the 33%–95% RH was studied and the results are shown in Figure 5.24. Normally, the peak of ε''-curve and step change in ε' represent the relaxation (Wang *et al.*, 2009). The ε'' response reveals that no peak is appeared at lower RH (in the range 33-75% RH). This phenomenon indicates that in lower humidity (33-75% RH) range, only one type of carrier participates in the conduction process, which may be due to the electrons of the internal materials. Moreover, as the RH increased to a higher value, the ε'' decreased faster with frequency. The decreased response of ε'' further confirms the contribution of ionic conduction. At high humidity conditions ($\geq$ 85% RH), a peak was observed on the curve (see Figure 5.24). The present relaxation peaks of armalcolite nanocomposite in Figure 5.24 (low frequency region: 10^2 Hz to 10^3 Hz) are in agreement with those reported by Fu et al., (2007) (Fu *et al.*, 2007). Besides, it was observed that these peaks had been shifted towards higher frequency with increasing RH at higher humidity range. This characteristic could be attributed to the Maxwell–Wagner (M–W) relaxation phenomenon, which is normally called as dielectric polarization. The dielectric polarizations are typically observed when local regions of conduction are in series with blocking capacitive interfaces. These M–W type relaxations suggest the existence of charge carriers and/or their mobility inside the armalcolite nanocomposite (Fu *et al.*, 2007). The aforementioned relaxation phenomenon also explained that at higher humidity conditions, the ions of the armalcolite nanocomposite were dominated completely. Therefore, the ε'' plots confirmed that the sensing principle of armalcolite nanocomposite based sensor depended on the electronic in low RH region and on the ionic conductivity in high RH range.

Figure 5.24: Variation of dielectric loss (ε″) of armalcolite nanocomposite at different relative humidity as a function of frequency in logarithmic scale at 25 °C.

Furthermore, the change in normalized dielectric loss tangent (tanδ/tanδ$_{max}$) with frequency at different RH conditions is depicted in Figure 5.25. This result exemplifies that for all RH values, the normalized dielectric loss tangent displayed a peak, and the peak was shifted towards higher frequency region with increasing RH. Based on the dielectric phenomenon, the tanδ represents the energy change inside the material, which led the molecules to relaxation polarization. Normally, the relaxation inside the material appears due to friction and collision among the molecules by their reorientation induced by an externally applied electric field. The tanδ can also be explained as the combination of the leak conductance loss tangent (tanδ$_c$) and polarization loss tangent (tanδ$_p$) under the consideration of leak conductance of the materials, as explained in Equation 5.6:

$$tan\delta = \tan\delta_p + \tan\delta_c = \frac{(\varepsilon_s-\varepsilon_\infty)\omega\tau}{\varepsilon_s+\varepsilon_\infty\omega^2\tau^2} + \frac{\gamma}{\omega\varepsilon_0}\left[\frac{1}{\varepsilon_\infty+(\varepsilon_s-\varepsilon_\infty)/(1+\omega^2\tau^2)}\right] \qquad (5.6)$$

165

When $\frac{d \tan \delta}{d\omega} = 0$, one obtains $\omega_m \propto \gamma$. It suggests that ω is directly proportional to γ (Wang J. *et al.*, 2005; Zhang, He*, et al.*, 2008). This relation indicates that the value of γ increased with RH and as a result, a larger value of ω was obtained. Therefore, it clearly reveals the reason behind the shifting of tanδ peak towards higher frequency when RH is increased. The more prominent tanδ peak found in the higher RH range implies that the molecule relaxation polarization occur in the higher humidity range. This result, therefore, suggests that only electrons or ions and dipoles have contributed to the conduction in the higher and lower humidity ranges, respectively.
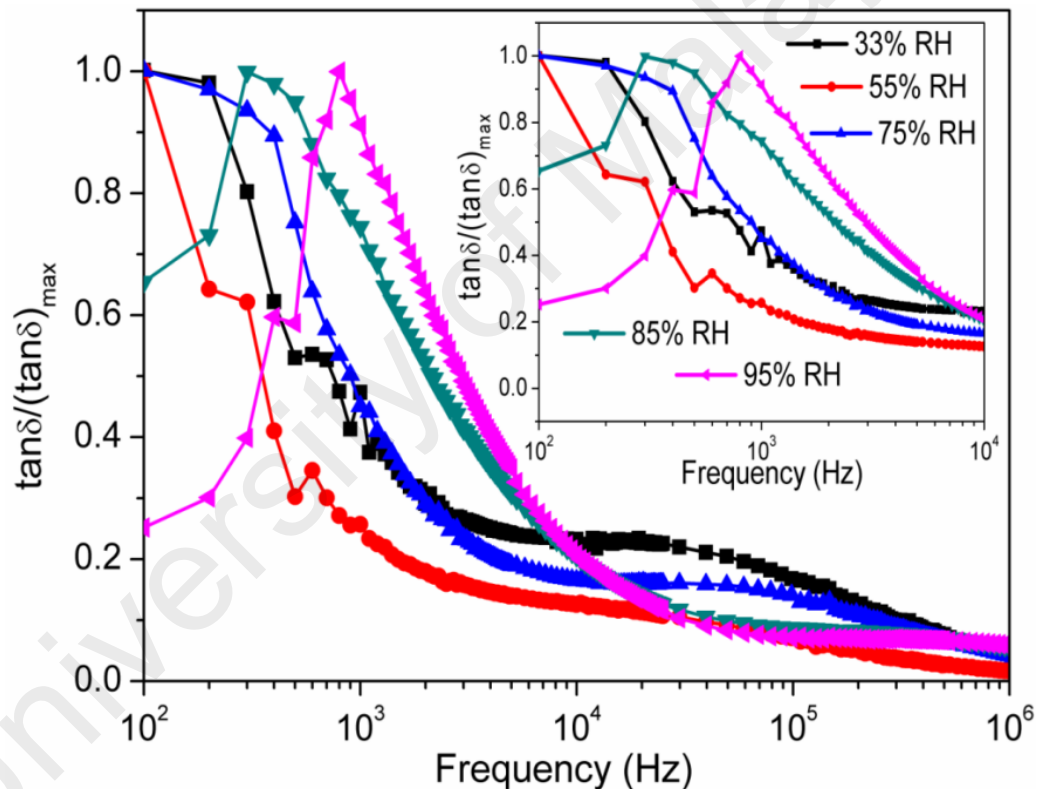
Figure 5.25: Variation of normalized dielectric loss tangent (tanδ/tanδ$_{max}$) of armalcolite nanocomposite at different relative humidity as a function of frequency in logarithmic scale at 25 °C.

Moreover, the effect of humidity highly influenced the electrical conductivity of ceramic composite or porous materials. This analysis is highly essential to develop an effective and reliable humidity sensor. The electrical conduction, due to humidity in

166

ceramic composites and porous materials, mainly occurred via surface mechanism. The humidity-dependent conductivity in the present porous oxide-based ceramic nanocomposites was caused by the transport of protons in water molecules, which were adsorbed on the wide surface and separated the porous oxide surface from the atmosphere. This transport mechanism is widely known as the Grotthuss chain reaction (Agmon, 1995; Garcia-Belmonte *et al.*, 2003). Figure 5.26 shows the typical frequency dependent AC conductivity response at different RH conditions for armalcolite nanocomposite. In Figure 5.26, a nearly constant σ_{ac} response was observed in the intermediate-frequency range at higher humidity condition. This represents the low frequency quasi-direct current (DC) conductivity (σ_{dc}). The value of σ_{ac} increased sharply at higher frequencies, and adhered to the frequency dependent power law (see Equation 3.15). At lower humidity condition (33-75%RH), the σ_{ac} approached towards a constant value above the frequency 10^5 Hz (shown in Figure 5.26). It was also noted that at relatively higher humidity range (>75% RH), the value of σ_{ac} decreased for frequencies lower than 10^3 Hz. Besides, the σ_{ac} response in Figure 5.26 has shown transition characteristics between the two power-law regimes, which is corresponded to two straight lines (asymptotic behavior). This transition response was represented by a characteristic crossover frequency ω_c. Therefore, the σ_{ac} adhered to a different frequency dependent power law pattern, as portrayed in Equation 5.7.

$$\sigma(\omega) \alpha \begin{cases} \omega^p, \omega < \omega_c \\ \omega^n, \omega > \omega_{c,} \end{cases} \tag{5.7}$$

Where, *p* is the low-frequency exponent and *n* is the high-frequency exponent. The value of *p* <0.07, which shows the quasi-σ_{ac} characteristics (*p*=0, for the ideal σ_{ac}). The value of *n* is always larger than 0.44.

Meanwhile, Figure 5.26 illustrates the low-frequency σ_{ac} value, as well as the crossover frequency ω_c, which increased monotonically with the increasing humidity.

This observation confirmed that there was indeed a common origin shared by both low- and high- frequency regimes in the underlying transport mechanism (Garcia-Belmonte *et al.*, 2003). Normally, the surface protonic conduction belongs to this type of conduction pattern. To understand the ionic contribution to conduction under high humidity conditions, it is necessary to follow the power law, Equation 5.7. The '*n*' value was calculated from the slope of $\log(\sigma_{ac})$ vs. $\text{Log}(f)$ curve. The value of *n* varied from 0.44 to 0.58. It indicates that the value of *n* decreased with the increase in humidity. This decreased response of exponent with increased humidity was only observed in the crystalline-structured oxide materials. It also revealed that the polarized ions had been responsible for the AC conduction in the entire frequency range. The MW relaxation phenomenon had already been conformed in dielectric polarization, which offered a strong support to the contribution of ionic conduction for the σ_{ac} at higher humidity range.
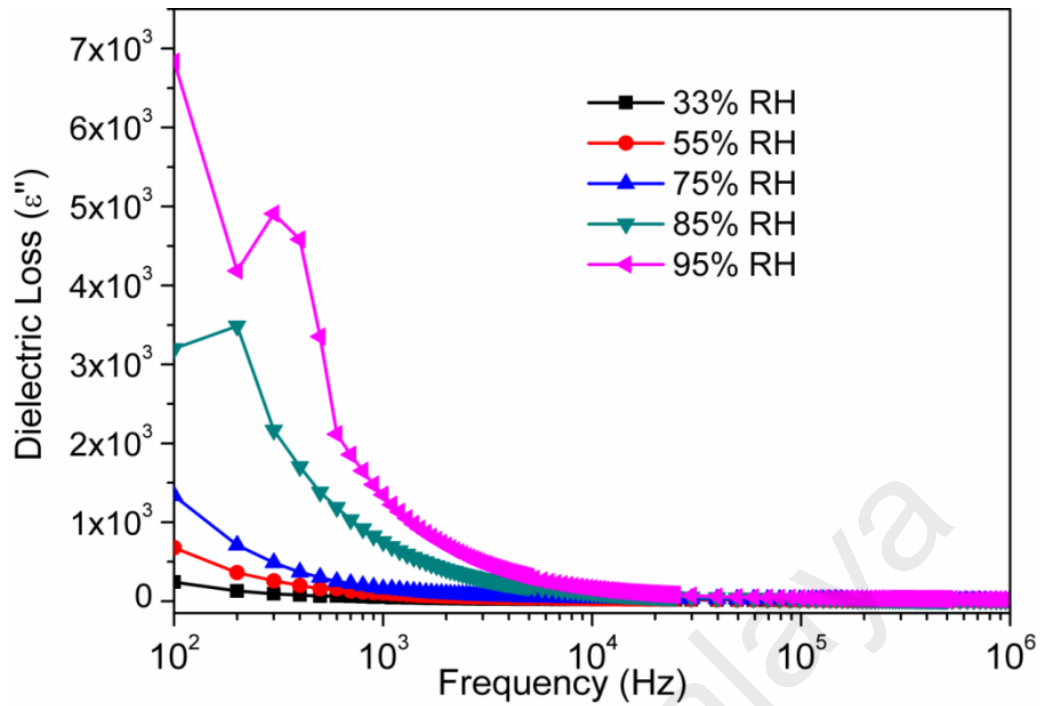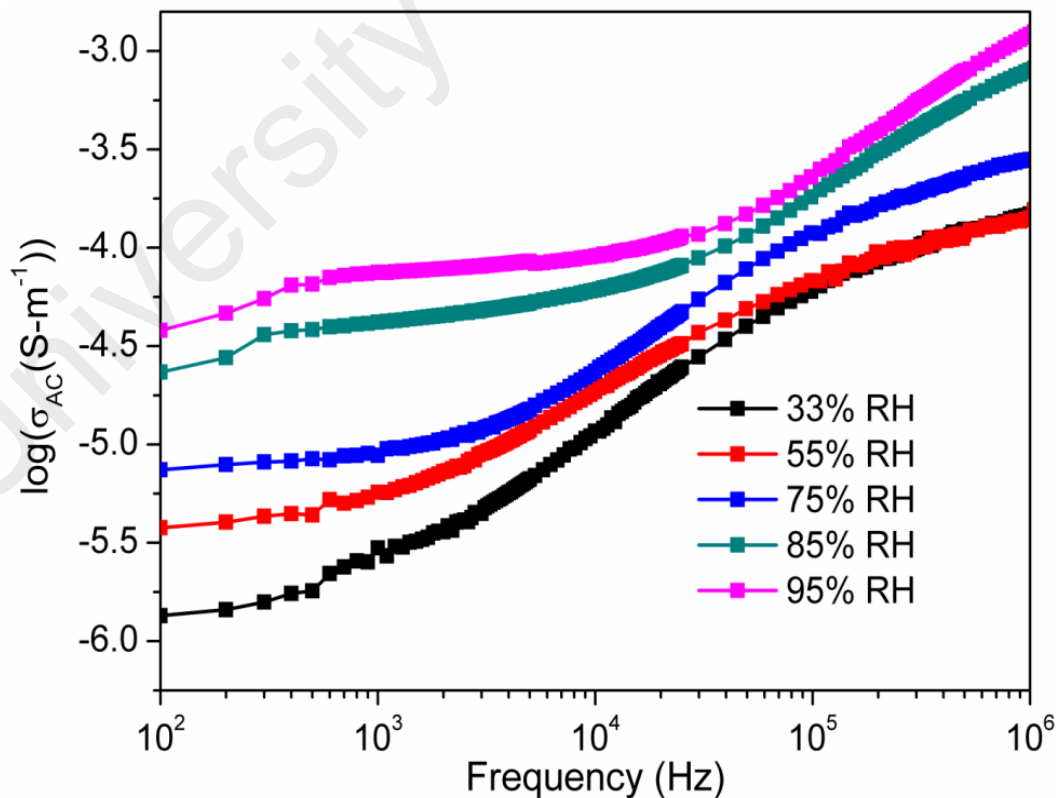

Figure 5.26: Variation of AC Conductivity spectra of armalcolite nanocomposite at different relative humidity as a function of frequency in logarithmic scale (i.e. $\log\sigma_{ac}$ vs. $\text{Log}(f)$) at 25 °C.

In addition, the typical hysteresis between absorption and desorption processes had been less than 3.5% RH in the range of 11–95%RH, as shown in Figure 5.27. Low hysteresis was observed for the armalcolite nanocomposite due to faster response and recovery times. Moreover, the value of dielectric constant on desorption process is slightly higher than that of the absorption process.
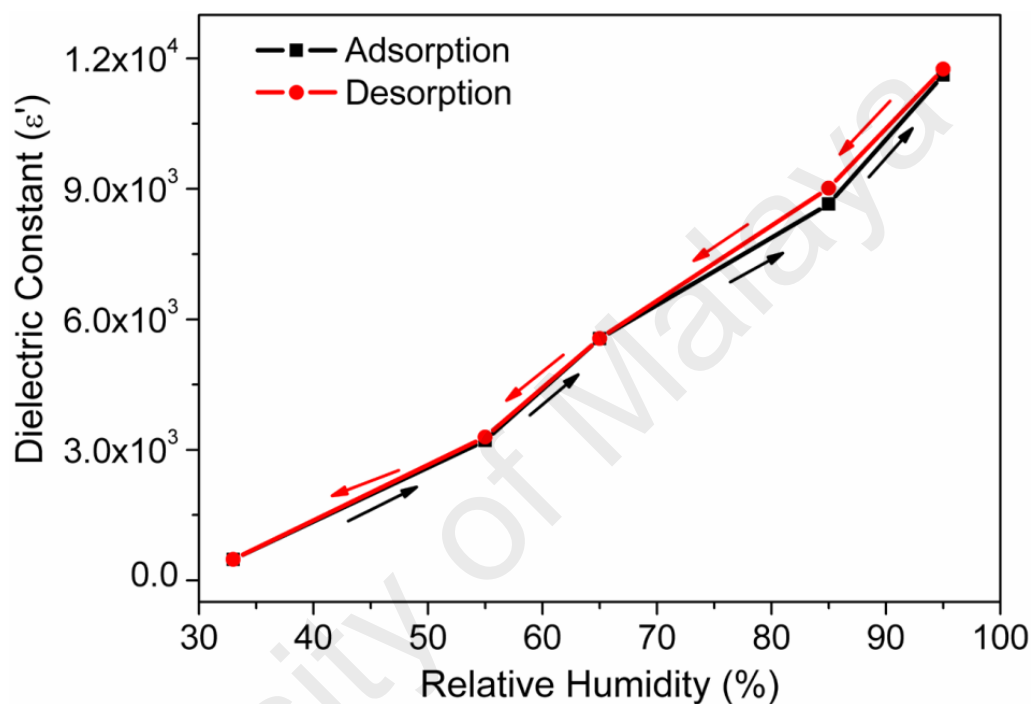
Figure 5.27: Humidity response of the sensor based on armalcolite nanocomposite during humidification and desiccation process at 10^2 Hz.

The response and recovery characteristics of the armalcolite nanocomposite, measured at 25 °C by 1V and 100Hz, are illustrated in Figure 5.28. The response time is defined as the time needed to reach 95% of the final value for a given relative humidity, while the recovery time is defined as the time taken for the signal to come to within 10% of the initial value. Both response and recovery times were determined by alternately exposing to 33–95% RH. The response time of the armalcolite nanocomposite is 18 s, whereas the recovery time is 35 s. Since desorption is an

endothermic process, it takes a longer time to desorb the water vapor; therefore, the recovery time is always greater than the response time (Saha *et al.*, 2005).
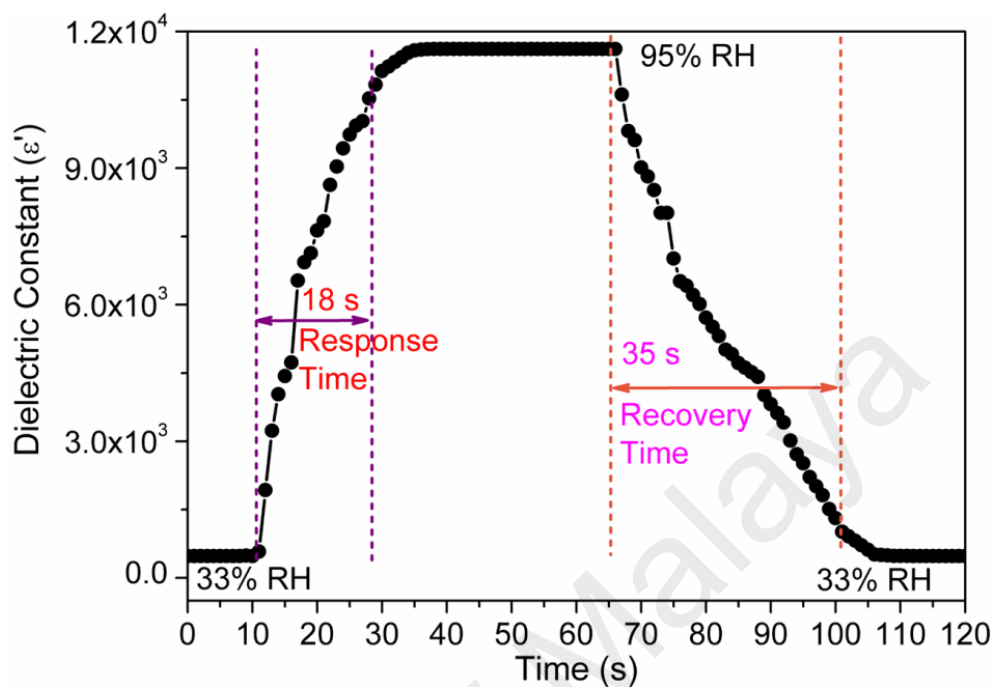
Figure 5.28: Response and recovery curve of armalcolite nanocomposite measured at 10^2 Hz for humidity levels between 33 %RH and 95 %RH at 10^2 Hz. Response time,~18 s. Recovery time,~35 s.

The long-term stability of armalcolite nanocomposite at 33%–95% RH is shown in Figure 5.29. The response of dielectric constant to RH was measured after storage in a natural environment for about 1 month (Figure 5.29). As a result, it was found that a little drift of dielectric constant even after a long time was present. Hence, it evidently has shown that the humidity sensing properties of armalcolite nanocomposite has been indeed very stable over a long time.
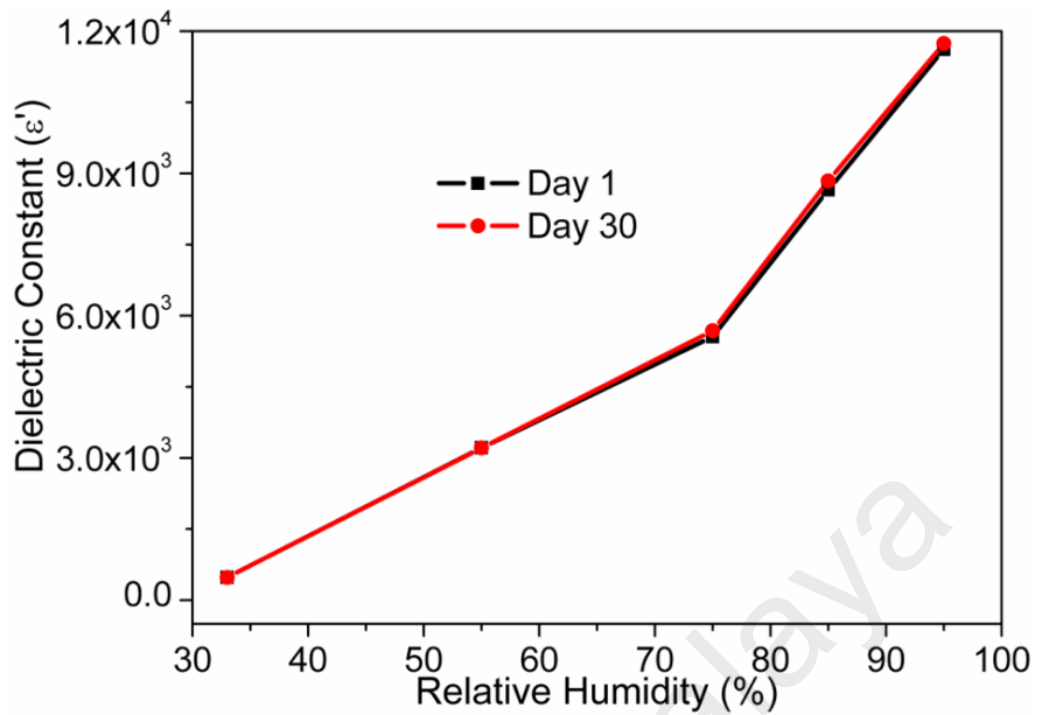
Figure 5.29: Long term stability property of the sensor based on armalcolite nanocomposite over 30 days measured at 10^2 Hz and 1 V.

5.3.2 Conclusion of Dielectric based Humidity Sensor

This study reports a significant response of dielectric constants to humidity in armalcolite nanocomposite. The solid-state step-sintering technique helped in synthesizing the armalcolite nanocomposite with appropriate grain size, low density, and high porosity for humidity sensor application, which marked a scientific breakthrough for versatile applications in different areas where humidity plays an important role. The humidity-sensing mechanism of the sensor is discussed in four terms of electronic properties. This study showed that electrons and ions contributed to the conduction depending on the RH range. The ε'' property showed that the dipoles contributed to the conduction in the whole RH range. Meanwhile, the dielectric response suggested that the frequency and RH significantly influenced the dielectric characteristics of the nanocomposites. In the ε'' analysis, the associated Maxwell–

Wagner relaxation phenomenon confirmed the presence of charge carriers and/or their mobility in the sample. The observed σ_{ac} can be explained by the surface protonic conduction and ionic contribution to conduction at low and high humidity ranges, respectively. Besides, the ε' at 95% relative humidity was about 24 times larger than ε' at 33% relative humidity for armalcolite nanocomposite measured at 10^2 Hz. Furthermore, the armalcolite-based sensor exhibited lower hysteresis (<3.5%), good stability, as well as faster response (18 s) and recovery time (35 s), compared to the conventional humidity sensors based on other electroceramic materials (Cheng *et al.*, 2013; Yuk & Troczynski, 2003). Therefore, the armalcolite-based porous nanocomposite can be a promising sensing material for advanced new humidity sensors.

5.4 Humidity Sensing Response of S1050 and PDMS/S1050 Composite based Humidity Sensor

All designed sensors based on the present novel electroceramic composite comprising armalcolite ($Fe_2MgTi_3O_{10}$), perovskite ($CaTiO_3$), and ferrite (Fe_3O_4) phases have shown excellent performance compared to the other sensors developed by various researchers. However, flexibility of this electroceramic sensor is still a great challenge for many advanced applications. To overcome the challenges of the ceramic sensors, a flexible thin film of the armalcolite/perovskite/ferrite and polydimethylsiloxane (PDMS) nanocomposite has been developed. It is done mainly to improve the flexibility beside good water absorption for flexible humidity sensor applications. This section describes the combined humidity sensitivity and capacitive response of S1050 (armalcolite/perovskite/ferrite) and S1050/PDMS composite thin film sensors.

5.4.1   Humidity Sensing Capacitive and Impedance Measurements

The relationship between capacitance and frequency (10^2-10^6 Hz) at RH range of 33–95 %RH of the S1050 pellet and flexible S1050/PDMS nanocomposite film is depicted in Figure 5.30A and 5.30B, respectively. It shows that capacitance increases with increasing of %RH at low frequencies up to 10^3 Hz. However, at higher frequencies (> 10^3 Hz), the change in capacitance becomes almost independent of the RH and the capacitance value reduced significantly. Both the materials showed similar trends but the capacitance values for the porous ceramics were almost an order of magnitude higher compared to the composite film. The result is quite expected since hydrophobic PDMS polymer is used as matrix material in the S1050/PDMS nanocomposite. The S1050 ceramic played an active role in humidity sensing layer by the hydrophilic characteristics of its porous surface where numerous nanopores helps for improving the water molecules adsorption/desorption process or enhancing the sensitivity of the sensor. The trend in capacitance-change of these materials indicates that the electrical field direction changes slowly at low frequency and there by appearance of the space–charge polarization owing to adsorbed water. Higher %RH implies more adsorbed water, stronger the polarization, and thus the larger dielectric constant, impedance as well as capacitance. When frequency is high, the electrical field direction changes such a faster speed that the polarization of the water cannot catch up with it and hence, the dielectric constant becomes smaller and independent of %RH (Bondarenka *et al.*, 1995; Wang, Wan*, et al.*, 2003). Similar observation was also obtained for the capacitance response with %RH condition at different frequency points (see Figure 5.31A and 5.31B).

173
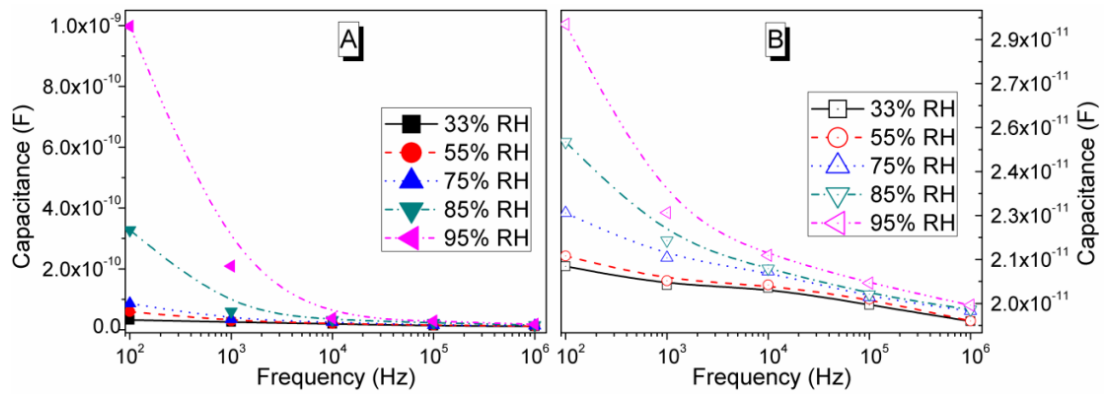
Figure 5.30: Frequency dependent capacitance of (A) Sintered pellet at 1050 °C (S1050)–filled symbols and (B) composite film (S1050/PDMS)–opened symbols at different humidity conditions (33, 55, 75, 85, and 95 %RH) in the frequency range of 10^2–10^6 Hz.
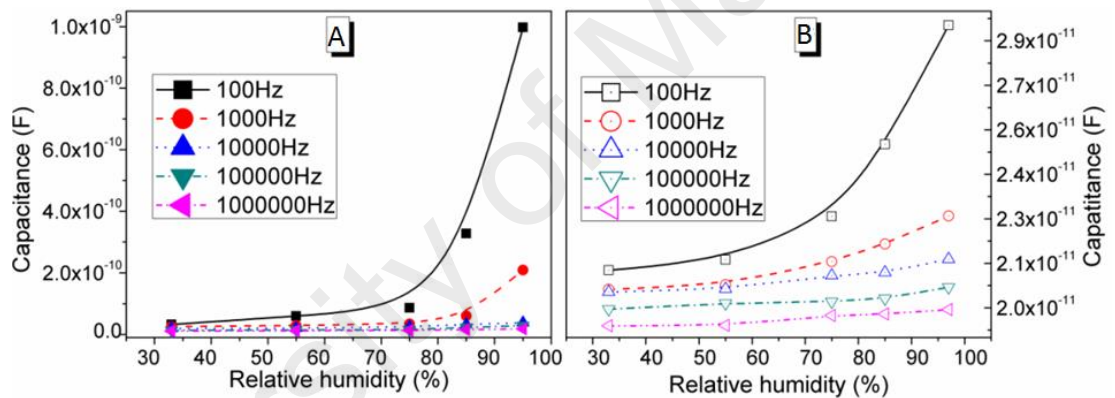
Figure 5.31: The capacitance response with %RH condition at different frequency points (10^2, 10^3, 10^4, 10^5 and 10^6 Hz) for (A) Sintered pellet at 1050 °C (S1050)–filled symbols and (B) composite film (S1050/PDMS)–opened symbols.

To evaluate the humidity dependent capacitive characteristics of the S1050 electroceramic and humidity dependent resistive characteristic of flexible S1050/PDMS nanocomposite film, the device sensitivities (S_C and S_z) are calculated by using Equation 5.2 (Wang W. C. *et al.*, 2013) and Equation 5.4 (Pandey & Tiwari, 2010), respectively.

The value of capacitance increased from 3.2183×10^{-11} F to 9.9741×10^{-10} F, with S_C of 2900% at the signal frequency of 100 Hz. This value is improved in comparison to the other materials (3000% even at 85 Hz) (Björkqvist *et al.*, 2004). It has been found that at test frequency 10^5 Hz, the S_C comes down to 120% as the capacitance varied from 1.2832×10^{-11} to 2.8174×10^{-11} F across the RH range of 33%–95%. On the other hand, for flexible S1050/PDMS nanocomposite film, the S_Z is found to be 306 and 1.212 kΩ/%RH at 10^2 and 10^5 Hz, respectively in the range of 33–97 %RH. The value of S_Z at 10^2 Hz is significantly higher than other resistive type humidity sensors materials (S_Z=160 kΩ/%RH for BaTiO$_3$) (Yuk & Troczynski, 2003). Therefore, the present electroceramic (S1050) and its flexible composite (S1050/PDMS) thin film have shown a best performance at test frequency 10^2 Hz as sensor characteristics.

The response and recovery result of the flexible sensor showed that the response time for humidification (from 33 %RH to 95 %RH) was 10 s and recovery time for desiccation (from 95 %RH to 33 %RH) was 29 s. Therefore, the obtained result, both response time and recovery time of the present flexible humidity sensor is noticeably better than Li-silica SBA-15 based flexible sensor (response time =21 s at 11 %RH to 95 %RH and recovery time=51 s at 95 %RH to 11 %RH) (Geng *et al.*, 2007), Fe-SilicaSBA-15 based sensor (response time =20 s at 11 %RH to 95 %RH and recovery time=50 s at 95 %RH to 11 %RH) (Qi, Zhang, Zheng*, et al.*, 2008) and TiO$_2$ NPs/PPy/PMAPTAC based flexible sensor (response time =30 s at 30 %RH to 90 %RH and recovery time=45 s at 90 %RH to 30 %RH) (Su & Wang, 2008) and so on. The hysteresis of the developed flexible sensor is ~3.37%, which is lower than the conventional sensors such as CdTiO$_3$ based sensor (less than 7) (Imran *et al.*, 2013), Li-silica SBA-15 based flexible sensor (less than 6)(Geng *et al.*, 2007), poly(2-acrylamido-2-methylpropane sulfonate) (less than 8) (Su *et al.*, 2011). The, the newly developed

flexible sensor shows excellent stability over the 30 days time span (see Figure 5.32A and 5.32B).
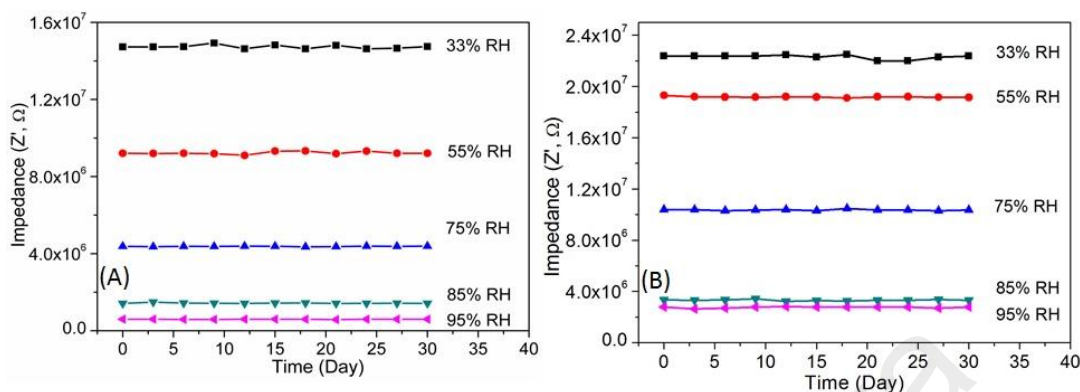
Figure 5.32: Long term stability of (A) S1050 and (B) S1050/PDMS based humidity sensors over 30 days measured at 10^2 Hz and 1V.

5.5   Effect of Curcumin Drug Loaded S1050 Composite on Wound Healing Diabetic Rats

Skin wound healing is a complex physiological process that involves multiple tissues and cell types. The skin wound progresses towards homeostasis through mainly three steps, such as involving inflammation, new tissue formation, and tissue remodeling (Gurtner *et al.*, 2008). However, cutaneous wound healing is a major interest for the public health sector because the skin wounds affect a large number of patients. Skin wounds noticeably affect the patient's life, requiring extended hospitalization time and increase a significant amount of healthcare expenditure. Furthermore, the scientific information about the potential effect of topical agents on skin wound healing is limited. Natural products have consistently been an important source of therapeutic agents, but ceramic oxide-based nanocomposite in therapeutic application is limited. Therefore, in this research work, a novel attempt has been made by using the S1050 ceramic as nanocarrier for curcumin drug in diabetic wound healing application. The ability of S1050 and curcumin to stimulate insulin secretion in the diabetic rats could explain the

176

improvement in FBG and HbAIc levels. Amelioration of hyperglycemia in diabetic rats that received S1050 and curcumin treatment led to the body weight, as well as food and water intake, to achieve the desired level, as observed in normal control rats.

5.5.1 Body Weight Observation

Body weight was measured thrice during the study on the 1st, 7th, and 14th days (just before sacrificing the animals). The average body weight in different experimental rats is shown in Figure 5.33. The initial body weight was equal in all experimental groups. However, on the 7th and 14th days, the body weight significantly increased among normal control rats when compared to the initial body weight. In contrast, on the 7th and 14th days, their body weight significantly ($p<0.05$) decreased in diabetic control with pure hydrogel (DC) rats as compared to the normal control with pure hydrogel (NC) rats. When DC rats were applied with curcumin, it prevents body weight losses compared to DC rats. Interestingly, only S1050 hydrogel applied to DC rats (DC+S1050) demonstrated prevention of body weight losses. Therefore, as expected, the diabetic rats applied with curcumin+S1050 hydrogel to the DC rats (DC+S1050+C) significantly have prevented body weight losses when compared to DC rats.
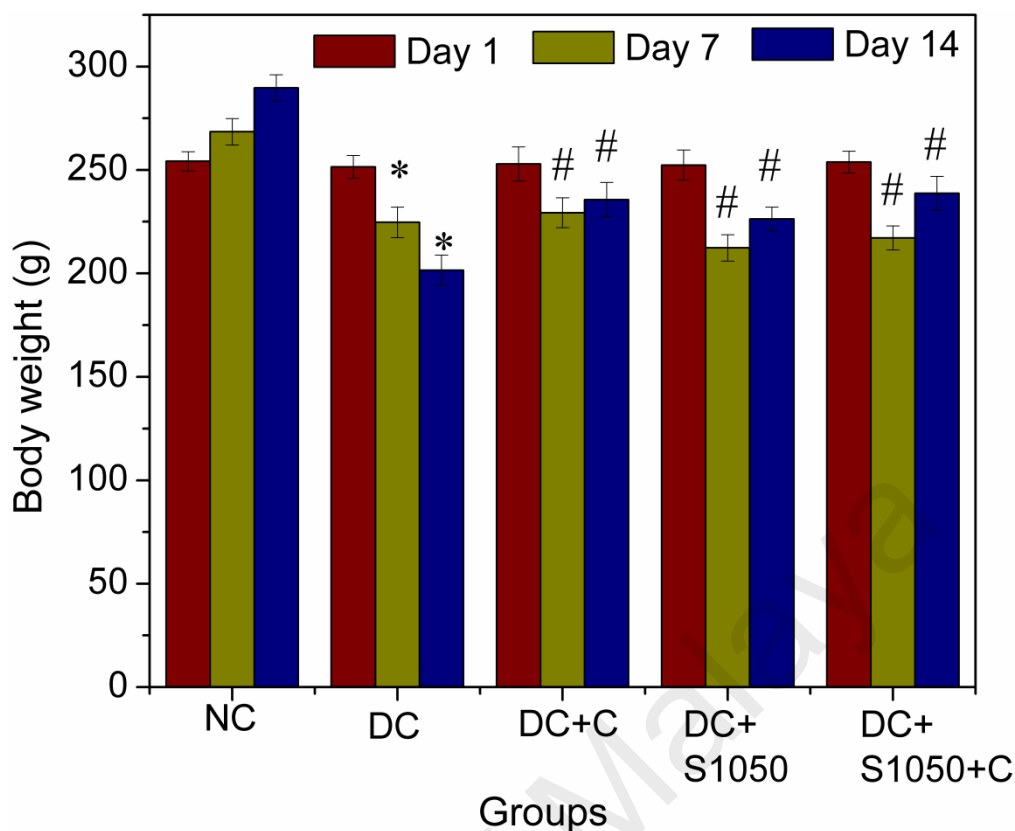
Figure 5.33: Body weight changes in experimental groups. NC: Normal control applied with pure hydrogel, DC: Diabetic control applied with pure hydrogel, DC+C: Diabetic rats applied with Curcumin hydrogel, DC+S1050: Diabetic rats applied with S1050 hydrogel, and DC+S1050+C: Diabetic rats applied with S1050+Curcumin hydrogel. Values represent mean ± S.E.M. of six rats. *$p<0.05$ compared to NC, #$p<0.05$ compared to DC.

5.5.2   Food Intake Observation of Normal & Diabetic Rats

Figure 5.34 shows the food intake by the experimental rats. The DC rats showed significantly ($p<0.05$) higher food intake compared to the NC rats. However, food intake was significantly ($p<0.05$) decreased in DC rats when curcumin hydrogel was applied compared to only DC rats. Furthermore, the DC rats applied with S1050 hydrogel (DC+S1050) showed significantly ($p<0.05$) lower food intake compared to DC and DC+C rats. The body weight and food intake results indicated that the S1050 nanocarrier had no any side effect. Therefore, the drug loaded carrier (curcumin+S1050)

hydrogel applied upon DC rats (DC+S1050+C) have shown significantly ($p<0.05$) lower food intake compared to DC rats.
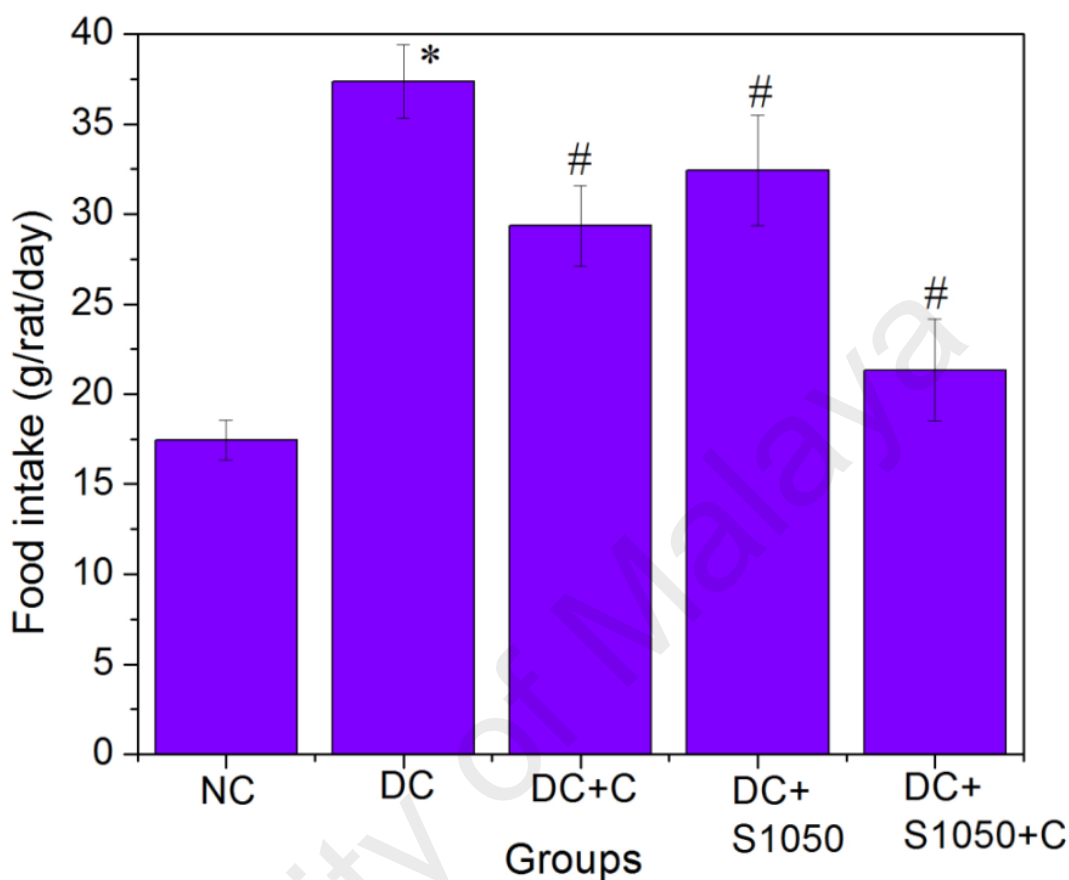
Figure 5.34: Food intake in different experimental groups. NC, DC, DC+C, DC+S1050, and DC+S1050+C. Values represent mean ± S.E.M. of six rats. *$p<0.05$ compared to NC, #$p<0.05$ compared to DC.

5.5.3   Water Intake Observation between Normal and Diabetic Rats

The water intake of all the different groups of experimental rats is depicted in Figure 5.35. Significantly ($p<0.05$), higher water intake was observed in the DC rats in comparison to the NC rats. However, water intake was significantly ($p<0.05$) decreased in DC+C rats, compared to DC rats. Furthermore, the water intake in DC+S1050 was significantly ($p<0.05$) lower than that of DC. Interestingly, the DC+S1050+C rats showed significantly ($p<0.05$) lower water intake when compared with any other group

of DC rats, including DC+S1050, DC+C, or DC. Therefore, the above three studies fairly indicate that S1050 has very good curcumin drug loading and drug releasing capacities.
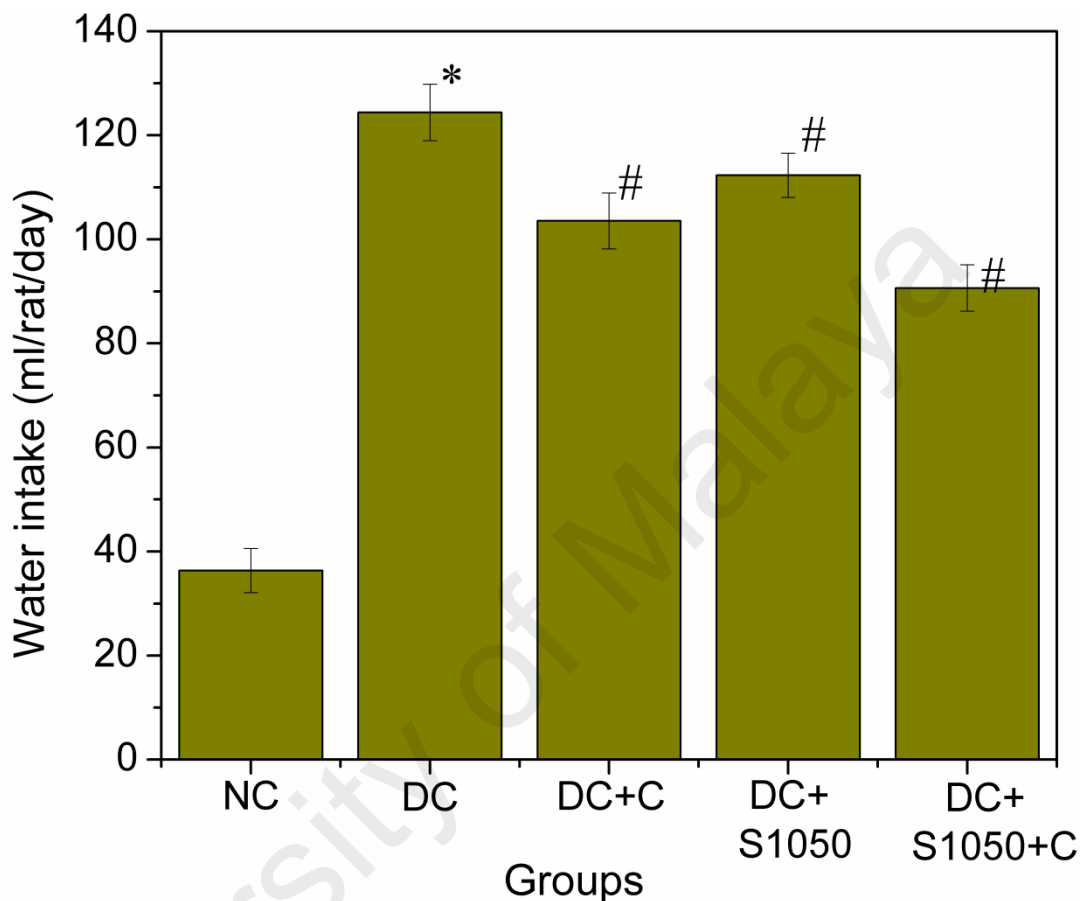
Figure 5.35: Water intake in different experimental groups. NC, DC, DC+C, DC+S1050, and DC+S1050+C. Values represent mean ± S.E.M. of six rats. *p<0.05 compared to NC, #p<0.05 compared to DC.

5.5.4 Effects of Nano Carrier, Drug, and Drug-Carrier Nanocomposite on Fasting Blood Glucose Levels of Diabetic Rats

Figure 5.36 represents the fasting blood glucose (FBG) levels of all the groups of experimental rats. Following treatment with different hydrogels, the blood glucose level of diabetic-induced rats was found to increase from an initial normal range of 4.8–5.0 mmol/L before diabetic induction to as high as 22.0 mmol/L 72 h after induction. In DC

rats, fasting blood glucose levels at the 1st, 7th, and 14th days were significantly (p<0.05) higher compared to NC rats. However, in DC+C rats, the FBG level was increased from 1st to 14th days gradually. From 7th to 14th days, the FBG levels of the other diabetic group rats (DC +C, DC+S1050, and DC+S1050+C) were significantly (p<0.05) lower compared to those of the DC rats. Similarly, DC+S1050 rats showed significantly lower FBG on the 14th day compared to the initial FBG. Furthermore, the diabetic rats applied with curcumin+S1050 hydrogel (DC+S1050+C) showed very low FBG levels on the 7th and 14th days compared to the 1st day and all three days, in which the FGB levels were significantly lower than those of DC rats. Therefore, this result indicates that due to very good curcumin drug loading and drug releasing capacities of S1050, the curcumin+S1050 hydrogel has shown best healing properties in diabetes.
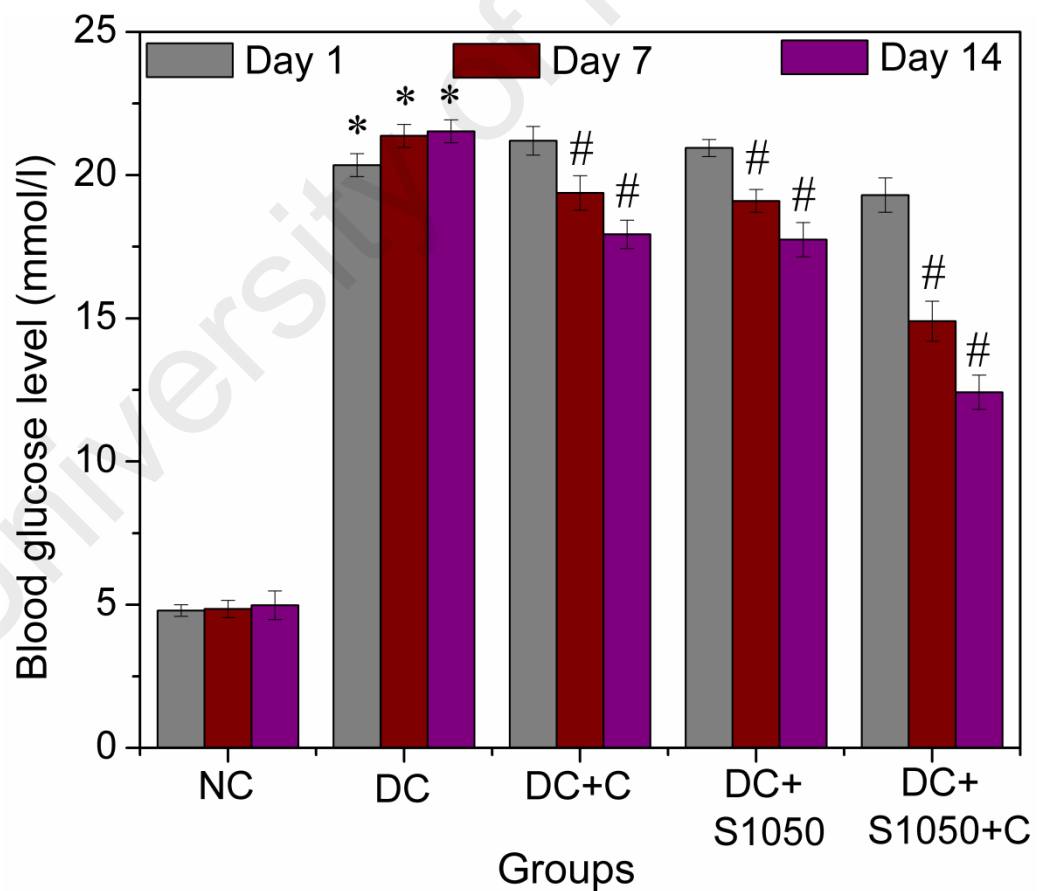
Figure 5.36: Fasting blood glucose level in different experimental groups. NC, DC, DC+C, DC+S1050, And DC+S1050+C. Values represent mean ± S.E.M. of six rats. *p<0.05 compared to NC, #p<0.05 compared to DC.

5.5.5 Effects on Insulin

The serum insulin levels in experimental rats for the 14-day treatment have been plotted in Figure 5.37. Diabetic rats treated with curcumin, S1050 or their composite (S1050-Curcumin) hydrogels exhibited remarkably better effect. It showed that the serum insulin levels of DC rats were significantly ($p < 0.05$) lower as compared with NC rats. The diabetic rats applied with curcumin hydrogel (DC+C) showed significantly higher ($p < 0.05$) serum insulin levels than the diabetic rats applied with pure hydrogel (DC). Thus, there was a very highly significant improvement in insulin levels of diabetic rats treated with curcumin, S1050, and S1050-Curcumin hydrogels when compared with pure hydrogel treated diabetic group. The S1050-Curcumin hydrogel was more effective than curcumin and S1050 hydrogel alone; as it exhibited remarkable glycemic control in the diabetic group. This result is in agreement with that obtained by Seo et al., (2008), who revealed that curcumin improved homeostasis model assessment of insulin resistance and elevated the plasma insulin level in diabetic rats (Seo *et al.*, 2008). Moreover, Gupta et al., (2012) showed that curcumin revealed an anti-hyperglycemic effect and improved insulin sensitivity (Gupta *et al.*, 2012). Other than that, Best et al., (2007) reported that curcumin induced electrical activity in rat pancreatic β-cells by activating volume-regulated anion channel, in which this effect led to depolarization of cell membrane potential, generation of electrical activity, and enhanced insulin release (Best *et al.*, 2007).
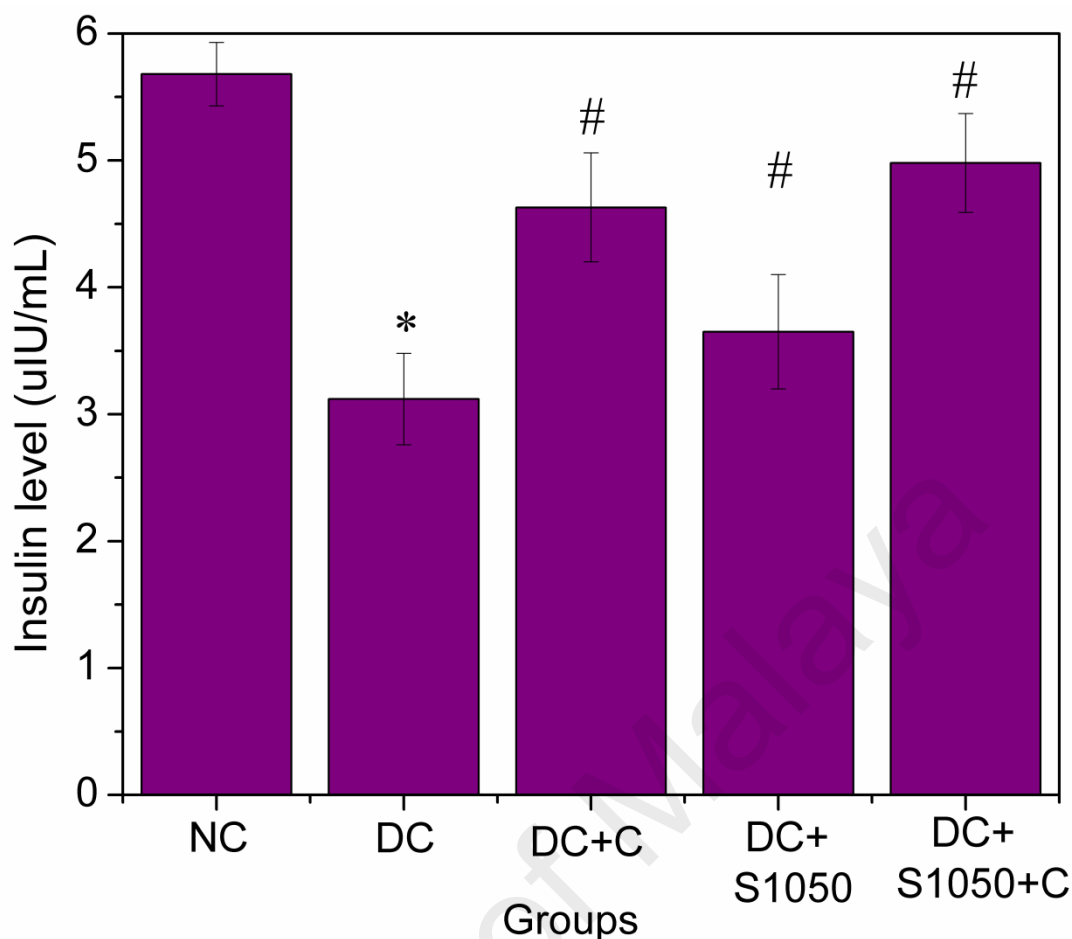
Figure 5.37: Insulin level in different experimental groups after 14 days treatment. NC, DC, DC+C, DC+S1050, and DC+S1050+C. Values represent mean ± S.E.M. of six rats. *p<0.05 compared to NC, #p<0.05 compared to DC.

5.5.6   Effects on HbA1c

Figure 5.38 shows that the HbA1c levels were significantly (p < 0.05) higher in DC rats as compared to NC rats. Moreover, diabetic rats treated with curcumin hydrogel resulted in significantly (p < 0.05) lower HbA1c levels as compared to diabetic control rats. Similarly, diabetic rats treated with S1050 hydrogel showed lower HbA1c levels when compared with diabetic rats. Also, curcumin+S1050 hydrogel applied diabetic rats resulted in lower HbA1c levels when compared with diabetic rats.
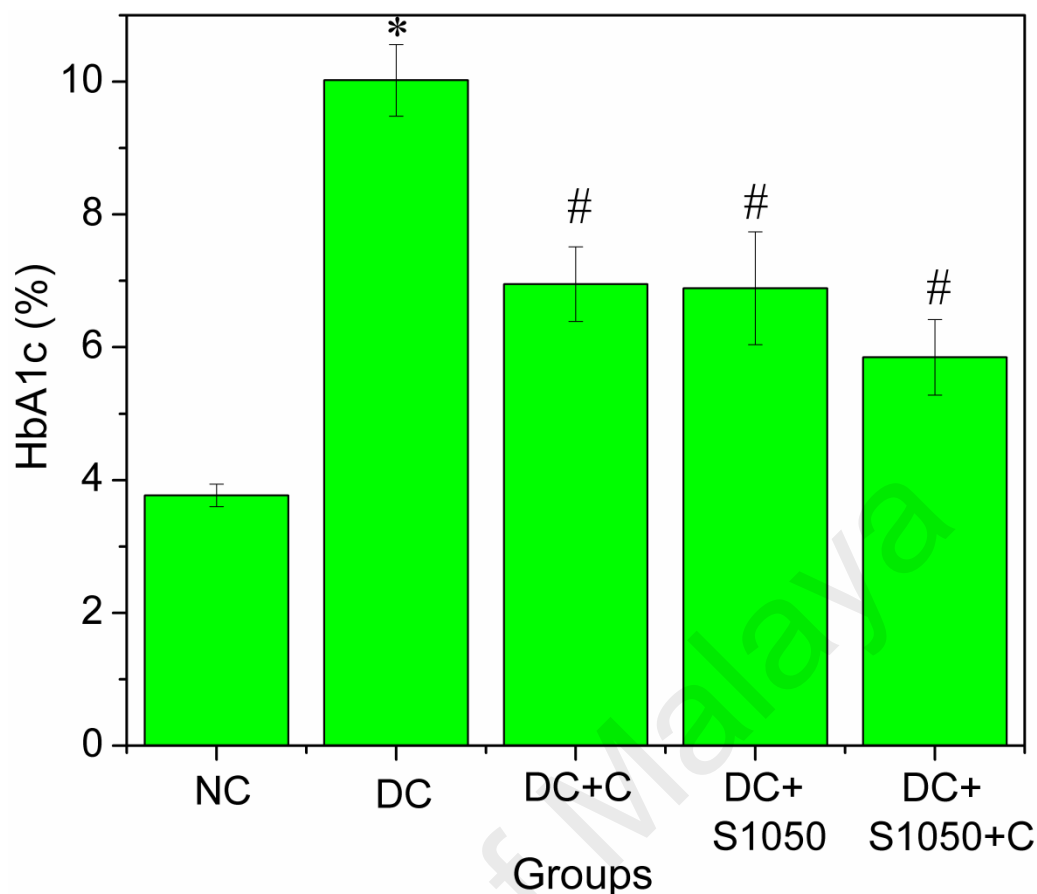
Figure 5.38: HbA1c level in different experimental groups after 14 days treatment. NC, DC, DC+C, DC+S1050, and DC+S1050+C. Values represent mean ± S.E.M. of six rats. *$p<0.05$ compared to NC, #$p<0.05$ compared to DC.

5.5.7 Effect of Nanocarrier and Drug Based Nanocarrier Hydrogel on Wound Size and Wound Contraction in Diabetic-Treated Rats

The rate of wound healing was monitored for 14 days of treatment. The percentage of the healing and the wound closure are shown in Table 5.2 and Figure 5.39, respectively. It shows that the wound area of each group is reduced significantly within the experimented time (14 days). The overall progress of the wound healing in NC rats was very fast. However, in DC rats, the progress of wound healing was slower than that in NC rats. In fact, the DC rats treated with curcumin hydrogel (DC+C) resulted in significantly ($p<0.05$) accelerated wound closure compared to DC rats. Furthermore, S1050 hydrogel applied upon diabetic rats (DC+S1050) showed significant ($p<0.05$)

184

wound healing improvement compared to DC rats. Moreover, curcumin+S1050 hydrogel applied upon DC rats (DC+S1050+C) showed significant (p<0.05) acceleration of wound healing when compared with DC rats and the data are shown in Figure 5.40. In addition, the results showed that the total closure rate of wounds applied with Curcumin, S1050 nanocarrier, and S1050-curcumin drug based hydrogels had been faster than the wounds dressed with only hydrogel. The upward trend in wound healing by using curcumin and S1050-curcumin hydrogels resulted in more than 89% and 95% closure rates, respectively. This result supported the drug carrying efficiency of the S1050 nanocarrier in recovering wounds. From the excellent wound healing response of S1050-curcumin based hydrogel, it has been hypothesized that the composite of S1050 nanocarrier and nano-curcumin with hydrogel might significantly elevate the rate of wound healing due to the synergy of these two components. Moreover, topical administration of S1050-curcumin hydrogel has been expected to increase curcumin bioavailability, as released in injury site, yet resulting in the improvement of wound healing (Li *et al.*, 2012).
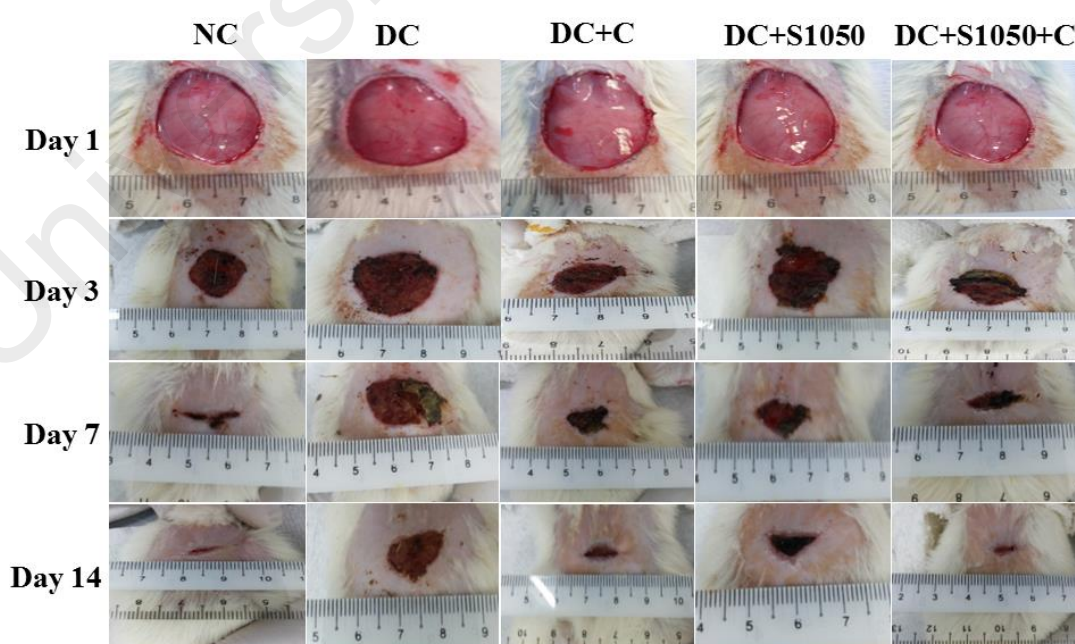
Figure 5.39: Representative photographs of diabetic rat wounds treated for Day 1, Day 3, Day 7 and Day 14 with the hydrogels NC, DC, DC+S1050, DC+C and DC+S1050+C.

Table 5.2: Contraction rates of skin wound on different days of the experimental rats.

Experimental Groups	3rd day (%)	7th day (%)	14th day (%)
NC	56.30±0.47	85.00±0.43	98.12±0.09
DC	22.56±0.41*	38.35±0.64*	58.52±0.16*
DC+C	51.16±0.20	73.46±0.33	89.00±0.11#
DC+S1050	34.00±0.37	64.81±0.46	81.06±0.19#
DC+S1050+C	50.64±0.17#	79.24±0.19#	95.42±0.06#

Note: Values were expressed as mean ± S.E.M. for six rats in each group. * Significantly different from normal control (NC) ($p < 0.05$). # Significantly different from diabetic control (DC) ($p < 0.05$).
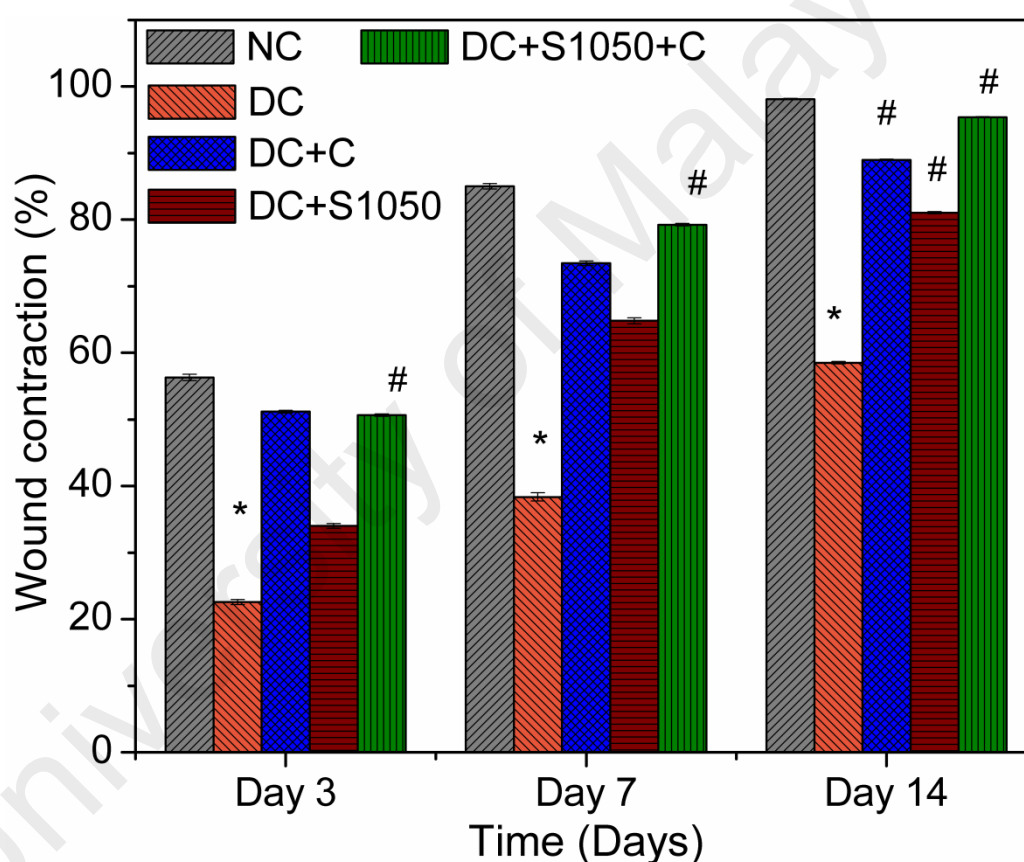
Figure 5.40: Effect of topical treatments on percentage of wound contraction at day 3, 7 and 14, n = 6; in five groups. Data are reported as means ± S.E.M. of six animals per group.

5.5.8 Histology of Wounds after Treatment

In this section, two main biological characterization such H&E staning and immunohitochemistry (IHC) have been discussed to understand the histopathological

186

changes in the wound tissues. For the clear understanding on cell proliferation, three proteins, EGF-2, MMP-2, and FGF had been used in the IHC study.

5.5.8.1   Effects on Histopathological (H&E) Changes

The effects of pure PVA hydrogel, curcumin hydrogel, S1050 hydrogel, and S1050-curcumin hydrogel on wound healing were examined by employing the histological study. Hematoxylin and eosin stained sections (H&E staining) were employed to examine the epithelial regeneration and formation of granulation tissue. The histopathological changes from the *in vivo* wound healing experiments on the 14th day treatment are depicted in Figure 5.41. In control group, the histopathological analysis of wound showed better epithelialization and more effective reorganization of the dermis (D). Moreover, the histopathological analysis for the wounds of DC rats showed less epithelialization and reorganization of the dermis (D). Meanwhile, diabetic rats treated with curcumin hydrogel (DC+C) showed moderate epithelialization and reorganization of the dermis (D) compared to DC rats. Similarly, S1050 hydrogel applied upon diabetic rats (DC+S1050) showed mild epithelialization and reorganization of the dermis (D) compared to DC rats. For curcumin+S1050 hydrogel applied upon diabetic rats, better epithelialization and more effective reorganization of the dermis (D) was observed compared to DC rats. Furthermore, when compared between the treated groups, the curcumin+S1050 hydrogel treated rats group have shown the best efficient result because of the complete remodeling of epidermis (E), which indicates the regression of the wounds.
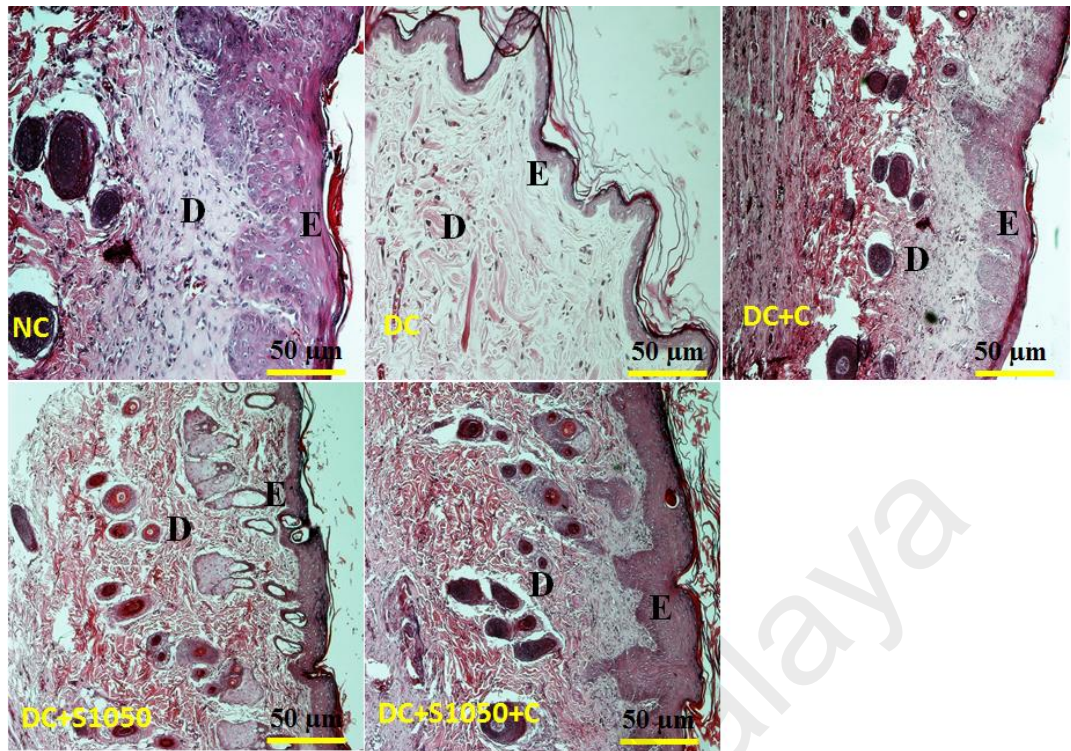
Figure 5.41: Histopathologic (H&E) changes in experimental groups of wound tissue after 14 days for NC, DC, DC+C, DC+S1050, and DC+S1050+C. D – dermis; E – epidermis.

5.5.8.2 Effects on Fibroblast Growth Factor (FGF-2) Expression

FGF-2, which is a basic fibroblast growth factor, encompasses a pivotal role during wound healing (Liu *et al.*, 2007). The FGF-2 exerts a strong effect upon fibroblasts, and its participation is linked to multiple fibrotic disorders (Inoue *et al.*, 2002; Strutz *et al.*, 2000). This observation suggests that under physiological conditions, FGF-2 may play a key regulatory role during wound resolution and may have encouraged fibroblast proliferation to repair damaged tissue. In order to reform the damaged granular tissues, rapid wound healing is essential. FGF-2 ensures massive deposition of collagen (Tsuboi & Rifkin, 1990). The FGF-2 also plays a vital role in enhancing vascularization of disrupted vessels and functions with extracellular matrix, necessary for chronic wound recovery (Flaumenhaft *et al.*, 1989). Based on the above study, an immunohistochemical experiment was conducted to analyze the FGF-2 expression in

this experimental model. Figure 5.42 represents the immunohistochemistry of FGF-2 at wound after 14 days of treatment. The immunoreactivity expression of FGF-2 was higher in epidermis (E) and dermis (D) in control rats. However, the DC rats showed lesser FGF-2 expression in epidermis and dermis when compared to NC rats. The moderate distribution of FGF-2 expression in wound tissue was observed in curcumin applied diabetic rats (DC+C) when compared with DC rats. Moreover, mild expression of FGF-2 had been noted in dermis and epidermis of wound tissue in S1050 hydrogel applied rats when compared with diabetic rats. On top of that, the diabetic rats treated with curcumin+S1050 hydrogel (DC+S1050+C) showed better expression of FGF-2 in both dermis and epidermis compared to DC rats.
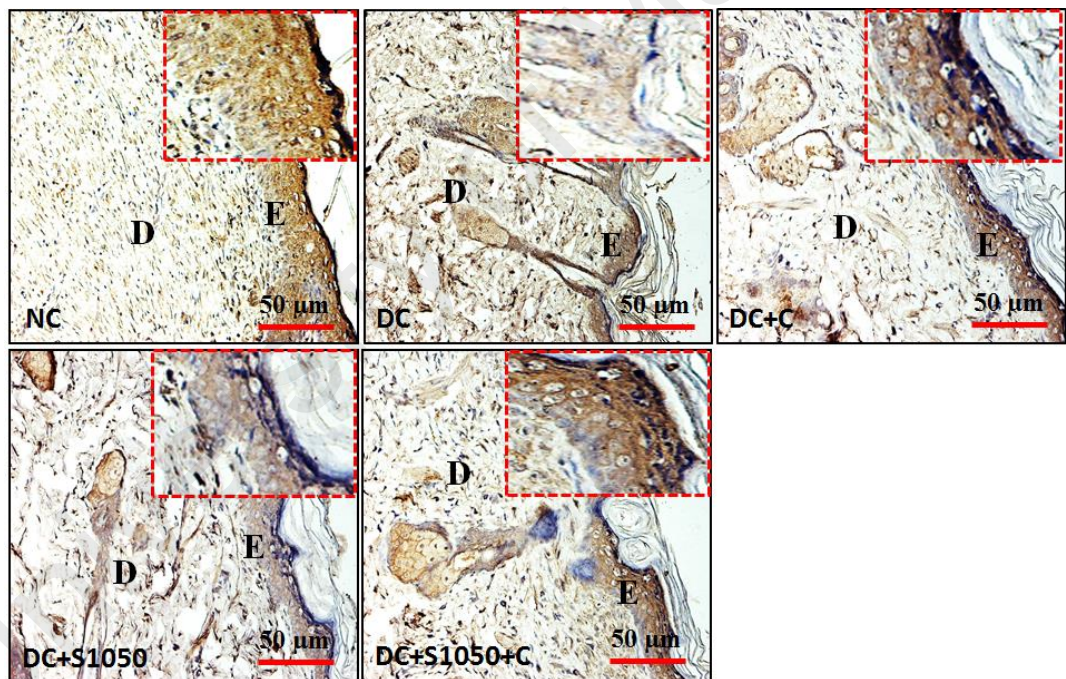
Figure 5.42: FGF-2 expression levels in different experimental groups: NC, DC, DC+C, DC+S1050, and DC+S1050+C. D – dermis; E – epidermis. Inset image represents a magnified scale of EGF-2 expression at epidermis.

5.5.8.3   Effects on Matrix Metalloproteinase (MMP-2) Expression

Matrix metalloproteinases (MMPs), an endopeptidase family of 24 mammalian members, degrade a variety of substrates, including extracellular matrix (ECM) proteins, proteinases and their inhibitors, chemotactic molecules, and cell surface receptors (Chang & Werb, 2001; Matrisian, 1992; Sternlicht & Werb, 2001). They participate in both physiological and pathological events associated with cell motility, development, inflammation, and wound healing (Björklund & Koivunen, 2005). Wound healing is a multifactorial process that involves with the migration, proliferation, and differentiation into several cell populations with subsequent formation of extracellular matrix. MMPs may influence cell migration through extracellular matrix degradation or by altering cellular adhesive properties. MMPs may also stimulate proliferation and/or antiapoptosis by altering the extracellular matrix microenvironment. They further modulate the activity of growth factors and receptors. In accordance with these studies, the immunohistochemical technique had been used to observe the expression of MMP-2 in this experimental model.

The results of immunohistochemistry of MMP-2 on five experimental groups at wound after 14 days of treatment are presented in Figure 5.43. The MMP-2 expression in epidermis (E) and dermis (D) of NC rats wound was lower. The MMP-2 expression in epidermis and dermis of DC rats had been higher compared to the NC rats. The moderate distribution of MMP-2 expression in wound tissue was observed in curcumin applied diabetic rats (DC+C) when compared with diabetic rats. Moreover, mild expression of MMP-2 in dermis and epidermis of wound tissue had been noted in S1050 hydrogel treated rats when compared with diabetic rats. Also, diabetic rats treated with curcumin+S1050 hydrogel showed very less expression of MMP-2 in dermis and epidermis when compared with diabetic rats.
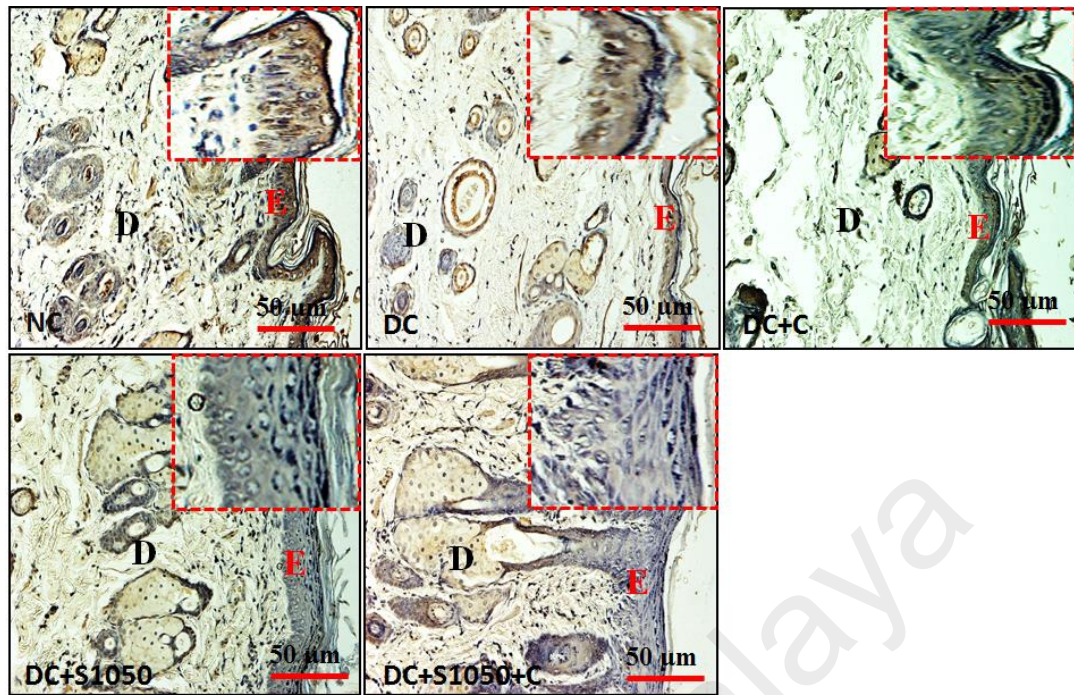
Figure 5.43: MMP-2 expression levels in different experimental groups for NC, DC, DC+C, DC+S1050, and DC+S1050+C. D – dermis; E – epidermis. Inset image represents a magnified scale of MMP-2 expression at epidermis.

5.5.8.4   Effects on Epidermal Growth Factor (EGF) Expression

The EGF consists of pleiotropic membrane-spanning cell surface receptors with intracellular tyrosine kinase activities that are triggered by homo- or hetero-dimerization when engaged by growth factors. In physiological condition, EGF binds with heparan sulfate proteoglycans on cellular surface of dermal wound tissues. After binding, they regulate dermal wound healing in a controlled and therapeutic way (Johnson & Wang, 2013; Tolino *et al.*, 2011). From this study, it has been confirmed that EGF is an effective marker to observe the expression of wound tissues.

The healing effect of EGF on open wounds was studied in five different groups of rats. Figure 5.44 represents the immunohistochemistry of EGF at wound after 14 days of treatment. The results showed that the immunoreactivity expression of EGF was higher in epidermis (E) and dermis (D) of NC rats. The EGF expression was lesser in

epidermis and dermis of DC rats in comparison to NC rats. Besides, the EGF expression was moderate in both curcumin-based (DC+C) and S1050-based (DC+S1050) diabetic rats compared to DC rats. However, the EGF expression in dermis (D) and epidermis (E) had been high in diabetic rats applied with curcumin+S1050 hydrogel (DC+S1050+C) compared with DC rats, indicating enhanced proliferation of keratinocyte for rapid wound closure.
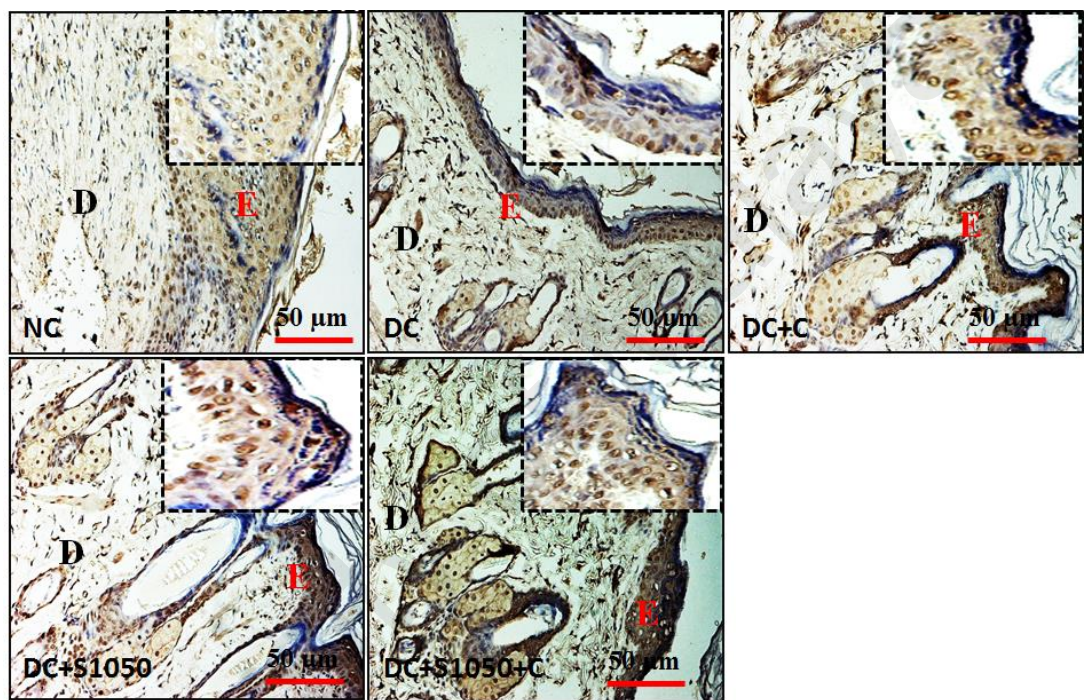
Figure 5.44: EGF expression levels in different experimental groups for NC, DC, DC+C, DC+S1050, and DC+S1050+C. D – dermis; E – epidermis. Inset image represents a magnified scale of EGF expression at epidermis.

5.5.9 Superoxide Dismutase, Glutathion Peroxidase, Catalase Activities and Malondialdehyde Levels in Wound Tissue

In this section, activities of the four antioxidatory parameters, such as SOD, GPx, CAT and MDA in the wound tissue had been observed. Figures 5.45(a), (b), and (c) show the dermal superoxide dismutase (SOD), glutathion peroxidase (GPx), and catalase (CAT) activity in different experimental rats. Dermal SOD, GPx, and CAT activities significantly ($p < 0.05$) decreased in DC rats when compared to NC rats.

However, diabetic rats treated with curcumin hydrogel (DC+C) showed higher SOD, GPx, and CAT activities in dermal tissue compared to DC rats. Similarly, S1050 hydrogel applied upon diabetic rats (DC+S1050) showed significantly ($p<0.05$) higher SOD, GPx, and CAT activities compared with DC rats. Moreover, diabetic rats treated with curcumin+S1050 hydrogel (DC+S1050+C) resulted in significantly ($p<0.05$) higher dermal SOD, GPx, and CAT activities compared to diabetic rats.

In addition, the detected malondialdehyde (MDA) value in tissue homogenates led to achieve close levels of MDA in wound of rats treated by curcumin, S1050, and curcumin-S1050 based hydrogels of diabetic rats when compared to the NC and DC groups. As marker of lipid peroxidation in tissue, the least MDA level indicated the most lipid peroxidation inhibition activity. This result declared that the wound of rats treated with curcumin-S1050 hydrogel (DC+S1050+C) showed the lowest lipid peroxidation activity among the groups in this test (Figure 5.45 (d)). Moreover, it was noticed that the MDA value had been significantly low for the rats treated with curcumin-S1050 hydrogel (DC+S1050+C). Meanwhile, in dermal tissue of diabetic rats, LPO that produced MDA was significantly higher compared to normal control rats. The activity of LPO that produced MDA enzyme in diabetic rats due to curcumin hydrogel (DC+C) had been significantly ($p < 0.05$) lower than the diabetic rats treated with pure hydrogel (DC). Besides, in S1050 hydrogel treated diabetic rats (DC+S1050), the level of MDA also decreased significantly ($p < 0.05$). Moreover, in curcumin+S1050 hydrogel treated diabetic rats (DC+S1050+C), the MDA was found to decrease significantly ($p < 0.05$) when compared to DC rats. Therefore, this result indicates the rapid reduction of the formation of reactive oxygen species, which has been responsible for oxidative stress.
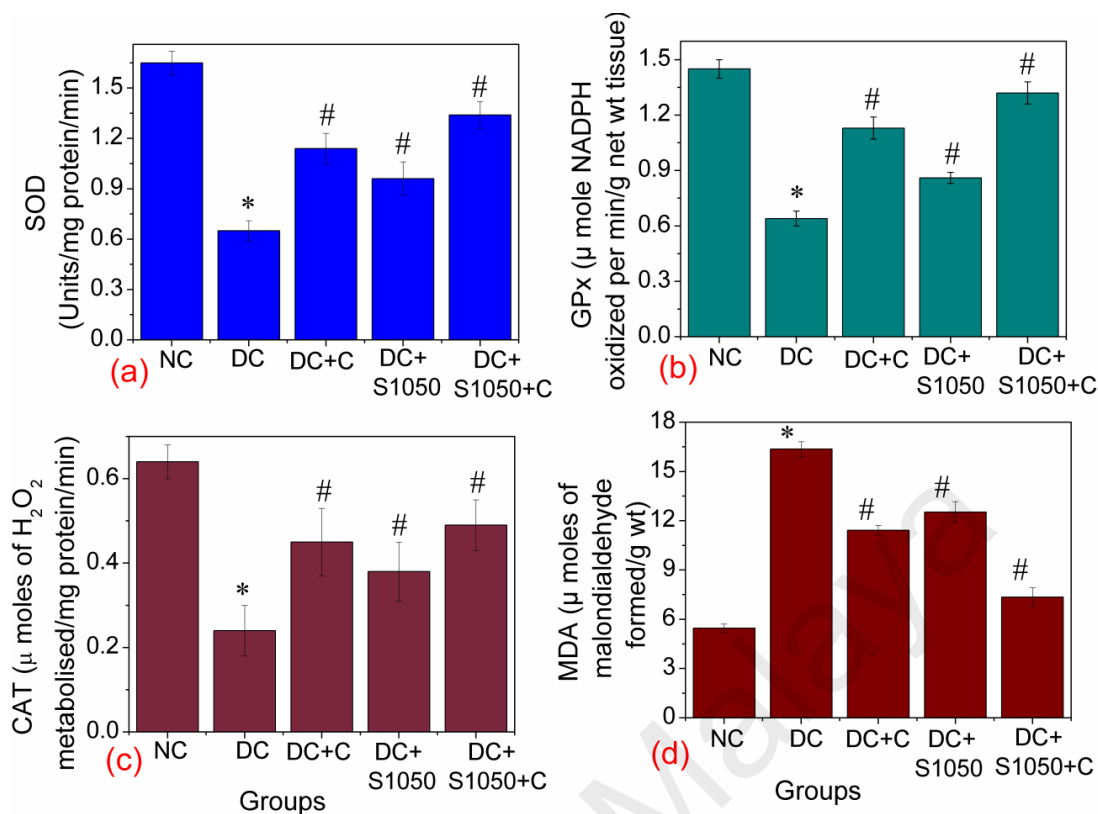
Figure 5.45: SOD, GPx, CAT and MDA levels in wound tissue, superoxide dismutase (SOD), Glutathion peroxidase (GPx), catalase (CAT) activities and Malondialdehyde (MDA) levels in tissue homogenates of day-14 dermal wounds of different experimental groups. NC, DC, DC+C, DC+S1050, and DC+S1050+C. Values represent mean ± S.E.M. of six rats. *p<0.05 compared to NC, #p<0.05 compared to DC.

CHAPTER 6: CONCLUSIONS AND FUTURE DIRECTIONS

From the outcome of the peer reviewed literature survey on oxide-based composites, the first aim was to develop a novel Ca-Mg-Fe-Ti-oxide (CMFTO) based armalcolite/perovskite/ferrite structured nanocomposite with desired morphology and high porosity. The amount of Ca, Mg, Fe, and Ti oxides contents were also chosen in such a way that the ceramic nanocomposite would have better properties for humidity sensor and biomedical applications. Once the parameters for the ceramic nanocomposite had been established, the commercial PDMS polymer was functionalized to improve the interfacial bonding between polymer and flexibility in the composites. The intention for functionalization of the PDMS polymer was not only to generate high strength flexible composites, but also to be used in memory devices, sensors, and other advanced applications. The armalcolite and its PDMS composite were developed to obtain high strength, high flexibility, and highly sensitive humidity sensor to be used in drug delivery and other advanced biomedical applications. Finally, the newly developed armalcolite nanocomposite and its PDMS-based flexible thin film had proved that their efficiency as highly sensitive humidity sensor materials and the ceramics powder sintered at 1050ºC sintering condition displayed better biocompatibility, as well as drug-carrying ability for wound healing applications.

Chapter 6 depicts some important concluding remarks on the development of armalcolite nanocomposite in three separate sections. Section 6.1 describes the syntheses and the characterizations of armalcolite/perovskite/ferrite (S1050) electroceramic nanocomposite and its composite film with PDMS. Next, section 6.2 describes their humidity dependent electrical responses. Lastly, section 6.3 explains their biocompatibility (using *in vitro* study) and the potential application of the S1050

electroceramic-based hydrogels in wound healing (*in vivo* study on diabetic rat model) study.

6.1 Developments of Armalcolite Nanocomposite and PDMS based Flexible Nanocomposite Film

The armalcolite, perovskite, and ferrite-phased ceramics were obtained by solid-state step-sintering technique, which was determined by TGA. The complete chemical reactions after ball-milling at 25 °C and calcining or sintering up to 1050 °C of the used ceramic oxide powders first time had been unveiled in the present study. Different phases of the sintered material were distinctly determined via XRD technique. The significant amount of smaller sized new perovskite $CaTiO_3$ phased NPs had been found to be formed by *in situ* solid-state step-sintering via lattice diffusion mechanism in the temperature range of 800–1050 °C. Besides, the most homogeneous uniform structure of porous sintered ceramic materials was found at 1050 °C. The present sintering technique helped to achieve the desired morphology, lower density, and highly porous nanomaterials. Furthermore, owing to the higher water absorption, lower WCA, and optimum density, the S1050 was selected for making the composite film with PDMS elastomer. The flexibility of the S1050/PDMS composite film had been clearly noticed from the suppressed tensile modulus and improved elongation compared to other PDMS composites (Ataollahi *et al.*, 2015). Besides, both the samples showed more than 90% tensile elongation. The improved viscoelastic property, such as lower damping factor of the S1050/PDMS composite (tanδ=0.225) compared to the pristine PDMS film (tanδ=0.404), indicated higher mechanical strength. The dielectric loss tangent of the newly developed S1050/PDMS (0.02 and 0.002 at 100 Hz and 1 MHz, respectively) and S1050 ceramics (5.75 and 0.155 at 100 Hz and 1 MHz, respectively) had been noticeably lower than that of the other ceramics or composites of silicone rubber, as reported by Tiercelin et al., (2006) (Tiercelin *et al.*, 2006). Thus, it can promisingly

196

improve the quality factor of sensors or electronic devices. The dielectric constant of the newly developed S1050 electroceramic and S1050/PDMS nanocomposites was also significantly higher than the other recently developed nanocomposites by Nayak et al., (2013) (Nayak *et al.*, 2013). This flexible 'giant dielectric' material would be an ideal replacement of CCTO-based brittle materials (Thomas *et al.*, 2010). The improved capacitance values of S1050 ceramic and S1050/PDMS film, therefore, can promisingly be used for capacitive type humidity sensors (Islam *et al.*, 2015). In the present study, armalcolite-based capacitive, resistive, and dielectric humidity sensors had been fabricated successfully.

6.2   Humidity Dependent Electrical Responses of Armalcolite Nanocomposite and its Flexible Film

The RH dependent capacitive, resistive, and dielectric responses of the armalcolite electroceramic had been carried out at 25 °C with the RH changing from 33% to 95%. Besides, the capacitance of the sensor increased from 3.2183×10^{-11} F to 9.9741×10^{-10} F with the changing of RH from 33% to 95% at the testing frequency of 10^2 Hz, and a high sensitivity of 3000% was obtained. The response and recovery times of capacitive humidity sensor were 14.5 s and 34.27 s, respectively, which had been extremely lower than the other conventional capacitive humidity sensors. The impedance sensor further showed improved sensitivity of 0.23 MΩ/Δ%RH. The response and recovery times were 20 s and 40 s, respectively for resistive sensor. The dielectric sensor, nonetheless, showed rather high sensitivity ~ 2310%. The response and recovery times in the dielectric sensor were 18 s & 35 s, respectively. All the three capacitive, resistive, and dielectric sensors showed extremely low values for hysteresis loss.

The pellet and film-based humidity sensors absorbed more water molecules at higher %RH. Besides, it was highly responsible to generate strong polarization in the present

197

electroceramic and its thin film. It finally improved the dielectric constant, impedance, as well as capacitance. Since the particle sizes of the ceramics comprising of $Fe_2MgTi_3O_{10}$, $CaTiO_3$, and Fe_3O_4 phases were in nanoscale; the thin film can be designed less than 1 μm, which is extremely needed for miniaturization of advanced electronic devices. Therefore, the capacitance values of the newly developed ceramic, as well as S1050/PDMS flexible composite film with 'giant dielectric' constant, are extremely promising. Hence, the S1050/PDMS composite film or membrane with higher strength, flexibility, and hydrophilicity, as well as improved dielectric properties, could be suitable potential material in capacitive- and resistive- type sensors for remote and humidity sensing applications.

6.3 Potential Application of Biocompatible Armalcolite Electroceramics in Diabetic Wound Healing

In order to evaluate the biocompatibility of the S1050 and S1050/PDMS composite film-based sensors with direct contact to dermal surface, an *in vitro* study was employed using human dermis fibroblast cells. The biocompatibility study confirmed that the newly developed S1050 material is highly biocompatible and is potential for wound healing application. In this study, for the first time, the armalcolite-based electroceramic S1050 had been used as nanocarrier. The S1050 loaded with curcumin drug showed higher therapeutic property for wound healing. This study had demonstrated better tissue formation, reepithelialisation, and reorganization of the granular tissue in diabetic rats treated with S1050 carrier with curcumin. Elevated blood glucose levels were observed after 72 h in all the rats induced with diabetes during the entire experimental period of 14 days. This finding is in accordance with other reported studies. There was a possibility that S1050 and curcumin could stimulate together the uptake of glucose. This could lead to an increase in insulin release by enhancing the influx of glucose into the

198

cells. Furthermore, the ability of S1050 and curcumin to stimulate insulin secretion in diabetic rats could explain the improvement noted in FBG and HbAIc levels. Other than that, the amelioration of hyperglycemia in diabetic rats with S1050 and curcumin treatment could then lead to the body weight, as well as food and water intakes, to approach the level observed in non-diabetic rats.

One of the leading causes of impaired wound healing is diabetes mellitus. In diabetic rats, a minor skin wound often leads to chronic, non-healing ulcers, and ultimately results in gangrene, or even amputation. Reactive oxygen species (ROS) and oxidative stress arise from inflammatory cells, which are strongly implicated in the pathogenesis of several diseases, including chronic ulcers (Abd-El-Aleem *et al.*, 2000; Moseley *et al.*, 2004; Rojkind *et al.*, 2002). Rasik and Shukla et al., reported that the decrease in antioxidants and the increase in oxidative stress delay healing in excision cutaneous wounds in diabetic, aged, and immunocompromised animals (Rasik & Shukla, 2000). They further showed that skin levels of catalase, glutathione, vitamin C, and vitamin E in streptozotocin-induced diabetic rats were lower when compared to those nondiabetics. In this study, the immunohistochemical technique was used to observe the expressions of FGF2, MMP2, and EGF in the experimental model. The results indicated that FGF2, MMP2, and EGF expressions had been very high in wounds of diabetic rats. On the other hand, diabetic rats treated with curcumin or S1050 resulted in a significant decrease in MMP2 expression, but it significantly increased the FGF2 and EGF expressions, as observed in dermal tissue. In the present study, the skin levels of lipid peroxidation (LPO) significantly increased in the diabetic skin adjacent to the wounds compared to the control skin of normal (NC) rats. High glucose can also increase the LPO that causes oxidative stress level. The level of oxidative stress inversely correlates with activity levels of anti-oxidative enzymes, i.e., SOD, CAT, and GPx. In the present study, the levels of SOD, CAT, and GPx antioxidant enzymes were seen to be

significantly decreased in diabetic rats treated with pure hydrogel group rather than the rest of the diabetic treated groups. Meanwhile, in DC rats treated with curcumin, S1050 or S1050+curcumin hydrogels, the SOD, CAT, and GPx levels in dermal tissue were increased. This indicated that curcumin or S1050 may have antioxidant properties that can help to scavenge the free radicals in diabetic wound.

In summary, a novel PVA-based hydrogel incorporated with curcumin and S1050 NPs was prepared in view of a potential wound dressing with enhanced healing efficacy. On the other hand, the curcumin drug loaded S1050 nanocarrier that was immobilized on large PVA particles had been proven to enhance the proliferation of wound tissue. From the perspective of substrate, the present study elucidated a possible mechanism for cell proliferation. Moreover, the present work clearly demonstrates that a simple topical application of S1050-curcumin hydrogel can accelerate the healing of full-thickness dermal wounds in a rat model. S1050 nanocomposite would have properties of anti-inflammatory, antioxidation, and non-antiangiogenesis for contributing to the repair of cutaneous wounds. The results of the present work unfold a new horizon for the application of S1050 in the field of wound therapy.

6.4   Future Directions

This section outlines some future directions of this dissertation, as well as some suggestions for betterment. The present investigation has opened a wide range of research scopes. A number of suggestions and applications related to future directions of this investigation are briefly remarked below.

I.   The developed armalcolite nanocomposite displayed high dielectric property ($\varepsilon' \sim 8000$). The ε' value may be more enhanced by incorporating copper oxide, $BaTiO_3$, or BST in the armalcolite nanocomposite. Thereafter, it can be used as an excellent and promising material in energy storage, as well as for supercapacitive application in the future energy technology.

II.   The flexibility of armalcolite nanocomposite can, as in I be improved by adding other polymers or elastomers, such as polyvinylidene fluoride (PVDF), PVA, polyaniline, nanocomposite, to solve the demand of flexible electronic devices in the modern industrial research and development.

III. Due to the good and flexible properties of armalcolite/PDMS nanocomposite, it may be used as a good pressure-sensing material.

IV.   Since the armalcolite nanocomposite has a porous structure, this material would be an ideal candidate for drug carrier. The armalcolite nanocomposite is a biocompatible material and it has already shown its wound healing ability with curcumin nano drugs on a diabetic wound rat model. Therefore, the wound healing study with other nanomedicines could also be carried out for better performances.

REFERENCES

Abd-El-Aleem SA, Ferguson MW, Appleton I, Kairsingh S, Jude EB, Jones K, McCollum CN & Ireland GW (2000). Expression of nitric oxide synthase isoforms and arginase in normal human skin and chronic venous leg ulcers. *The Journal of pathology,* 191(4): 434-442.

Adam SH, Giribabu N, Rao PV, Sayem AS, Arya A, Panichayupakaranant P, Korla PK & Salleh N (2016). Rhinacanthin C ameliorates hyperglycaemia, hyperlipidemia and pancreatic destruction in streptozotocin-nicotinamide induced adult male diabetic rats. *European Journal of Pharmacology,* 771: 173-190.

Adams TB, Sinclair DC & West AR (2002). Giant barrier layer capacitance effects in $CaCu_3Ti_4O_{12}$ ceramics. *Advanced Materials,* 14(18): 1321-1323.

Aezinia F, Wang Y & Bahreyni B (2012). Three dimensional touchless tracking of objects using integrated capacitive sensors. *IEEE Transactions on Consumer Electronics,* 58(3): 886-890.

Agarwal S & Sharma G (2002). Humidity sensing properties of $(Ba,Sr)TiO_3$ thin films grown by hydrothermal–electrochemical method. *Sensors and Actuators B: Chemical,* 85(3): 205-211.

Agmon N (1995). The grotthuss mechanism. *Chemical Physics Letters,* 244(5): 456-462.

Ahmad Z, Prasad A & Prasad K (2009) A comparative approach to predicting effective dielectric, piezoelectric and elastic properties of PZT/PVDF composites. *Physica B: Condensed Matter,* 404(20): 3637-3644.

Ahmad Z, Zafar Q, Sulaiman K, Akram R & Karimov KS (2013). A humidity sensing organic-inorganic composite for environmental monitoring. *Sensors,* 13(3): 3615-3624.

Ahmed M & Bishay ST (2001). Conductivity improvement of Li-Co-Yb ferrite. *Journal of Physics D: Applied Physics,* 34(9): 1339.

Ahmed M, Bishay ST & Abdelatif G (2001). Effect of ytterbium on the electrical properties of Li–Co ferrite. *Journal of Physics and Chemistry of Solids,* 62(6): 1039-1046.

Ajji Z, Othman I & Rosiak J (2005). Production of hydrogel wound dressings using gamma radiation. *Nuclear Instruments and Methods in Physics Research Section B: Beam Interactions with Materials and Atoms,* 229(3): 375-380.

Albiero M, Menegazzo L, Boscaro E, Agostini C, Avogaro A & Fadini G (2011). Defective recruitment, survival and proliferation of bone marrow-derived progenitor cells at sites of delayed diabetic wound healing in mice. *Diabetologia,* 54(4): 945-953.

Ali R, Khan MA, Mahmood A, Chughtai AH, Sultan A, Shahid M, Ishaq M & Warsi MF (2014). Structural, magnetic and dielectric behavior of $Mg_{1-x}Ca_xNi_yFe_{2-y}O_4$

nano-ferrites synthesized by the micro-emulsion method. *Ceramics International,* 40(3): 3841-3846.

Allahverdiyev AM, Abamor ES, Bagirova M & Rafailovich M (2011). Antimicrobial effects of TiO_2 and Ag_2O nanoparticles against drug-resistant bacteria and leishmania parasites. *Future Microbiology,* 6(8): 933-940.

Anbia M & Fard SM (2011). Humidity sensing properties of La^{3+} and K^+ co-doped $Ti_{0.9}Sn_{0.1}O_2$ thin films. *Journal of Rare Earths,* 29(7): 668-672.

Anbia M & Fard SM (2012). A humidity sensor based on KCl-doped nanoporous $Ti_{0.9}Sn_{0.1}O_2$ thin films prepared by the sol–gel method. *Scientia Iranica,* 19(3): 546-550.

Ang B, Yaacob I & Wong Y (2014). Phase and surface area studies of maghemite nanoparticles dispersed in silica gel. *Materials Research Innovations,* 18(S6): 32-35.

Aoki H, Azuma Y, Asaka T, Higuchi M, Asaga K & Katayama K (2008). Improvement of response characteristics of TiO_2 humidity sensors by simultaneous addition of Li_2O and V_2O_5. *Ceramics International,* 34(4): 819-822.

Ardakani HA, Alizadeh M, Amini R & Ghazanfari MR (2012). Dielectric properties of $CaCu_3Ti_4O_{12}$ improved by chromium/lanthanum co-doping. *Ceramics International,* 38(5): 4217-4220.

Aruna S, Muthuraman M & Patil K (1998). Synthesis and properties of Ni-YSZ cermet: anode material for solid oxide fuel cells. *Solid State Ionics,* 111(1): 45-51.

Ataollahi F, Pramanik S, Moradi A, Dalilottojari A, Pingguan-Murphy B, Wan Abas WAB & Abu Osman NA (2015). Endothelial cell responses in terms of adhesion, proliferation, and morphology to stiffness of polydimethylsiloxane elastomer substrates. *Journal of Biomedical Materials Research - Part A,* 103(7): 2203–2213.

Augustine R, Malik HN, Singhal DK, Mukherjee A, Malakar D, Kalarikkal N & Thomas S (2014). Electrospun polycaprolactone/ZnO nanocomposite membranes as biomaterials with antibacterial and cell adhesion properties. *Journal of Polymer Research,* 21(3): 1-17.

Babu S & Govindan A (2014). Dielectric Properties of $CaCu_3Ti_4O_{12}$ (CCTO) Prepared by Modified Solid State Reaction Method. *International Review of Applied Engineering Research,* 4(3): 275-280.

Bai Y, Cheng Z-Y, Bharti V, Xu H & Zhang Q (2000). High-dielectric-constant ceramic-powder polymer composites. *Applied Physics Letters,* 76(25): 3804-3806.

Bai Y & Jin L (2008). Characterization of frequency-dependent glass transition temperature by Vogel–Fulcher relationship. *Journal of Physics D: Applied Physics,* 41(15): 152008.

Bamzai K, Kour G, Kaur B & Kulkarni S (2014). Preparation, and Structural and Magnetic Properties of Ca Substituted Magnesium Ferrite with Composition $MgCa_xFe_{2-x}O_4$ (= 0.00, 0.01, 0.03, 0.05, 0.07). *Journal of Materials,* 2014.

Barui AK, Veeriah V, Mukherjee S, Manna J, Patel AK, Patra S, Pal K, Murali S, Rana RK, Chatterjee S & Patra CR (2012). Zinc oxide nanoflowers make new blood vessels. *Nanoscale,* 4(24): 7861-7869.

Batra A, Aggarwal M, Edwards ME & Bhalla A (2008). Present status of polymer: Ceramic composites for pyroelectric infrared detectors. *Ferroelectrics,* 366(1): 84-121.

Bauskar D, Kale B & Patil P (2012). Synthesis and humidity sensing properties of $ZnSnO_3$ cubic crystallites. *Sensors and Actuators B: Chemical,* 161(1): 396-400.

Bell AJ (2008). Ferroelectrics: The role of ceramic science and engineering. *Journal of the European Ceramic Society,* 28(7): 1307-1317.

Best L, Elliott AC & Brown PD (2007). Curcumin induces electrical activity in rat pancreatic β-cells by activating the volume-regulated anion channel. *Biochemical Pharmacology,* 73(11): 1768-1775.

Bhuvanesh NS & Gopalakrishnan J (1997). Solid-state chemistry of early transition-metal oxides containing d^0 and d^1 cations. *Journal of Materials Chemistry,* 7(12): 2297-2306.

Bi H, Yin K, Xie X, Ji J, Wan S, Sun L, Terrones M & Dresselhaus MS (2013). Ultrahigh humidity sensitivity of graphene oxide. *Scientific Reports,* 3: 2714-2720.

Björklund M & Koivunen E (2005). Gelatinase-mediated migration and invasion of cancer cells. *Biochimica et Biophysica Acta (BBA)-Reviews on Cancer,* 1755(1): 37-69.

Björkqvist M, Salonen J, Paski J & Laine E (2004). Characterization of thermally carbonized porous silicon humidity sensor. *Sensors and Actuators A: Physical,* 112(2): 244-247.

Bondarenka V, Grebinskij S, Mickevičius S, Volkov V & Zacharova G (1995). Thin films of poly-vanadium-molybdenum acid as starting materials for humidity sensors. *Sensors and Actuators B: Chemical,* 28(3): 227-231.

Bonfig K, Denker M & Kuipers U (1988). Das Direkte Digitale Messverfahren (DDM) als Grundlage einfacher und dennoch genauer und störsicherer Sensoren. In *Sensor,* 4: 223-228.

Boonlakhorn J & Thongbai P (2015). Mg-doped $CaCu_3Ti_4O_{12}$ nanocrystalline powders prepared by a modified sol–gel method: Preparation, characterization, and their giant dielectric response. *Japanese Journal of Applied Physics,* 54(6S1): 06FJ06.

Borsa F, Torgeson D, Martin SW & Patel HK (1992). Relaxation and fluctuations in glassy fast-ion conductors: Wide-frequency-range NMR and conductivity measurements. *Physical Review B,* 46(2): 795-800.

Bosq N, Guigo N, Persello J & Sbirrazzuoli N (2014). Melt and glass crystallization of PDMS and PDMS silica nanocomposites. *Physical Chemistry Chemical Physics,* 16(17): 7830-7840.

Brize V, Gruener G, Wolfman J, Fatyeyeva K, Tabellout M, Gervais M & Gervais F (2006). Grain size effects on the dielectric constant of $CaCu_3Ti_4O_{12}$ ceramics. *Materials Science and Engineering B,* 129: 135–138.

Buege JA & Aust SD (1978). Microsomal lipid peroxidation. *Methods Enzymol,* 52: 302-310.

Bueno PR, Ribeiro WC, Ramírez MA, Varela JA & Longo E (2007). Separation of dielectric and space charge polarizations in $CaCu_3Ti_4O_{12}/CaTiO_3$ composite polycrystalline systems. *Applied Physics Letters,* 90(14): 142912.

Burczak K, Fujisato T, Hatada M & Ikada Y (1994). Protein permeation through poly (vinyl alcohol) hydrogel membranes. *Biomaterials,* 15(3): 231-238.

Carrow JK & Gaharwar AK (2015). Bioinspired polymeric nanocomposites for regenerative medicine. *Macromolecular Chemistry and Physics,* 216(3): 248-264.

Castel E, Michau D & Maglione M (2009). Flexible relaxor materials: $Ba_2Pr_xNd_{1-x}FeNb_4O_{15}$ tetragonal tungsten bronze solid solution. *Journal of Physics: Condensed Matter,* 21(45): 452201.

Chandratreya S, Fulrath RM & Pask JA (1981). Reaction mechanisms in the formation of PZT solid solutions. *Journal of the American Ceramic Society,* 64(7): 422-425.

Chang C & Werb Z (2001). The many faces of metalloproteases: cell growth, invasion, angiogenesis and metastasis. *Trends in Cell Biology,* 11(11): S37-S43.

Chang D & Tseng T (1990). Humidity-sensitivity characteristics of $CaTiO_3$ porous ceramics. *Journal of Materials Science Letters,* 9(8): 943-944.

Chattopadhyay S & Raines RT (2014). Review collagen-based biomaterials for wound healing. *Biopolymers,* 101(8): 821-833.

Chawla KK (2012). *Composite materials: science and engineering*: Springer Science & Business Media, Birmingham, USA.

Chen S, Chang S & Lin I (2000). The influence of grain boundary internal stress on permeability: temperature curve for Mn–Zn ferrites. *Journal of Magnetism and Magnetic Materials,* 209(1): 193-196.

Chen WP, Zhao ZG, Liu XW, Zhang ZX & Suo CG (2009). A capacitive humidity sensor based on multi-wall carbon nanotubes (MWCNTs). *Sensors,* 9(9): 7431-7444.

Chen X, Lei B, Wang Y & Zhao N (2009). Morphological control and in vitro bioactivity of nanoscale bioactive glasses. *Journal of Non-Crystalline Solids,* 355(13): 791-796.

Chen X, Zhang J, Wang Z, Yan Q & Hui S (2011). Humidity sensing behavior of silicon nanowires with hexamethyldisilazane modification. *Sensors and Actuators B: Chemical,* 156(2): 631-636.

Chen Z & Lu C (2005). Humidity sensors: a review of materials and mechanisms. *Sensor Letters,* 3(4): 274-295.

Cheng B, Ouyang Z, Tian B, Xiao Y & Lei S (2013). Porous $ZnAl_2O_4$ spinel nanorods: High sensitivity humidity sensors. *Ceramics International,* 39(7): 7379-7386.

Cheng B, Tian B, Xie C, Xiao Y & Lei S (2011). Highly sensitive humidity sensor based on amorphous Al_2O_3 nanotubes. *Journal of Materials Chemistry,* 21(6): 1907-1912.

Cheng KC, Lin CM, Wang SF, Lin ST & Yang CF (2007). Dielectric properties of epoxy resin–barium titanate composites at high frequency. *Materials Letters,* 61(3): 757-760.

Cheng S & Wu Z (2010). Microfluidic stretchable RF electronics. *Lab on a Chip,* 10(23): 3227-3234.

Chimene D, Alge DL & Gaharwar AK (2015). Two-Dimensional Nanomaterials for Biomedical Applications: Emerging Trends and Future Prospects. *Advanced Materials,* 27(45): 7261-7284.

Chopra S, Tripathi A, Goel T & Mendiratta R (2003). Characterization of sol-gel synthesized lead calcium titanate (PCT) thin films for pyro-sensors. *Materials Science and Engineering: B,* 100(2): 180-185.

Chu J, Peng X, Feng P, Sheng Y & Zhang J (2013). Study of humidity sensors based on nanostructured carbon films produced by physical vapor deposition. *Sensors and Actuators B: Chemical,* 178: 508-513.

Chuang SH, Gao RH, Wang DY, Liu HP, Chen LM & Chiang MY (2010). Synthesis and Characterization of Ilmenite-Type Cobalt Titanate Powder. *Journal of the Chinese Chemical Society,* 57(4B): 932-937.

Colilla M, Martínez-Carmona M, Sánchez-Salcedo S, Ruiz-González ML, González-Calbet JM & Vallet-Regí M (2014). A novel zwitterionic bioceramic with dual antibacterial capability. *Journal of Materials Chemistry B,* 2(34): 5639-5651.

Day RM (2005). Bioactive glass stimulates the secretion of angiogenic growth factors and angiogenesis in vitro. *Tissue Engineering,* 11(5-6): 768-777.

206

DeJean G, Bairavasubramanian R, Thompson D, Ponchak G, Tentzeris M & Papapolymerou J (2005). Liquid crystal polymer (LCP): a new organic material for the development of multilayer dual-frequency/dual-polarization flexible antenna arrays. *Antennas and Wireless Propagation Letters, IEEE* 4: 22-26.

Desmouliere A, Redard M, Darby I & Gabbiani G (1995). Apoptosis mediates the decrease in cellularity during the transition between granulation tissue and scar. *The American Journal of Pathology,* 146(1): 56.

Devan R & Chougule B (2007). Effect of composition on coupled electric, magnetic, and dielectric properties of two phase particulate magnetoelectric composite. *Journal of Applied Physics,* 101(1): 014109.

Dias C, Igreja R, Marat-Mendes R, Inacio P, Marat-Mendes J & Das-Gupta D (2004). Recent advances in ceramic-polymer composite electrets. *IEEE Transactions on Dielectrics and Electrical Insulation,* 11(1): 35-40.

Dixit A, Maurya D, Singh DP, Agrawal DC & Mohapatra YN (2007). Dielectric Properties of Sol-gel-derived Calcium Copper Titanate and Calcium Barium Copper Titanate Thin Films. *Defence Science Journal,* 57(1): 55-60.

Doroftei C, Popa P & Iacomi F (2012). Study of the influence of nickel ions substitutes in barium stannates used as humidity resistive sensors. *Sensors and Actuators A: Physical,* 173(1): 24-29.

Du P, Lin X & Zhang X (2011). *Dielectric constants of PDMS nanocomposites using conducting polymer nanowires.* 16th International Solid-State Sensors, Actuators and Microsystems Conference, Beijing, China, 05 Jun - 09 Jun 2011.

Dyre JC & Schrøder TB (2000). Universality of ac conduction in disordered solids. *Reviews of Modern Physics,* 72(3): 873.

Ederer C & Spaldin NA (2004). Magnetoelectrics: A new route to magnetic ferroelectrics. *Nature Materials,* 3(12): 849-851.

Ehrlich HP & Rajaratnam JB (1990). Cell locomotion forces versus cell contraction forces for collagen lattice contraction: an in vitro model of wound contraction. *Tissue and Cell,* 22(4): 407-417.

El-Mohdy HA (2013). Radiation synthesis of nanosilver/poly vinyl alcohol/cellulose acetate/gelatin hydrogels for wound dressing. *Journal of Polymer Research,* 20(6): 1-12.

Erol-Taygun M, Zheng K & Boccaccini AR (2013). Nanoscale bioactive glasses in medical applications. *International Journal of Applied Glass Science,* 4(2): 136-148.

Estella J, de Vicente P, Echeverría JC & Garrido JJ (2010). A fibre-optic humidity sensor based on a porous silica xerogel film as the sensing element. *Sensors and Actuators B: Chemical,* 149(1): 122-128.

207

Faia P, Furtado C & Ferreira A (2004). Humidity sensing properties of a thick-film titania prepared by a slow spinning process. *Sensors and Actuators B: Chemical,* 101(1): 183-190.

Feng ZS, Chen XJ, Chen JJ & Hu J (2012). A novel humidity sensor based on alumina nanowire films. *Journal of Physics D: Applied Physics,* 45(22): 225305.

Flaumenhaft R, Moscatelli D, Saksela O & Rifkin DB (1989). Role of extracellular matrix in the action of basic fibroblast growth factor: Matrix as a source of growth factor for long-term stimulation of plasminogen activator production and DNA synthesis. *Journal of Cellular Physiology,* 140(1): 75-81.

Friedman AJ, Han G, Navati MS, Chacko M, Gunther L, Alfieri A & Friedman JM (2008). Sustained release nitric oxide releasing nanoparticles: characterization of a novel delivery platform based on nitrite containing hydrogel/glass composites. *Nitric Oxide,* 19(1): 12-20.

Fu D & Itoh M (2011). Ferroelectricity in Silver Perovskite Oxides. *Ferroelectrics-Material Aspects*, Mickael Lallart (Ed.), InTech, Rijeka, Croatia.

Fu M, Chen G, Dissado L, Fothergill JC & Zou C (2007). *The effect of gamma irradiation on space charge behaviour and dielectric spectroscopy of low-density polyethylene.* IEEE International Conference on Solid Dielectrics proceedings, Winchester, United Kingdom, 08 Jul - 13 Jul 2007.

Funke K (1993). Jump relaxation in solid electrolytes. *Progress in Solid State Chemistry,* 22(2): 111-195.

Gao W, Singh N, Song L, Liu Z, Reddy ALM, Ci L, Vajtai R, Zhang Q, Wei B, & Ajayan PM (2011). Direct laser writing of micro-supercapacitors on hydrated graphite oxide films. *Nature Nanotechnology,* 6(8): 496-500.

Garcia-Belmonte G, Kytin V, Dittrich T & Bisquert J (2003). Effect of humidity on the ac conductivity of nanoporous TiO_2. *Journal of Applied Physics,* 94(8): 5261-5264.

Geng W, Wang R, Li X, Zou Y, Zhang T, Tu J, He Y & Li N (2007). Humidity sensitive property of Li-doped mesoporous silica SBA-15. *Sensors and Actuators B: Chemical,* 127(2): 323-329.

George M, Nair SS, John AM, Joy P & Anantharaman M (2006). Structural, magnetic and electrical properties of the sol-gel prepared $Li_{0.5}Fe_{2.5}O_4$ fine particles. *Journal of Physics D: Applied Physics,* 39(5): 900.

George S & Sebastian MT (2009). Three-phase polymer–ceramic–metal composite for embedded capacitor applications. *Composites Science and Technology,* 69(7): 1298-1302.

Gerhardt R (1994), Impedance and dielectric spectroscopy revisited: distinguishing localized relaxation from long-range conductivity. *Journal of Physics and Chemistry of Solids,* 55(12): 1491-1506.

Gerlach G & Sager K (1994). A piezoresistive humidity sensor. *Sensors and Actuators A: Physical,* 43(1): 181-184.

Ghannam A, Viallon C, Bourrier D & Parra T (2009). *Dielectric microwave characterization of the SU-8 thick resin used in an above IC process.* European Microwave Conference, Rome, Italy, 29 Sep - 01 Oct 2009.

Ghobril C & Grinstaff M (2015). The chemistry and engineering of polymeric hydrogel adhesives for wound closure: a tutorial. *Chemical Society Reviews,* 44(7): 1820-1835.

Gonzalez JS, Maiolo AS, Ponce AG & Alvarez VA. (2011). *Composites based on poly (vinyl alcohol) hydrogels for wound dressing.* Paper presented at the XVIII The Argentine Congress of Bioengineering and Clinical Engineering Conference VII, SABI, Argentina, 28 Sep - 30 Sep 2011.

Goswami S & Sen A (2010). Low temperature sintering of CCTO using P_2O_5 as a sintering aid. *Ceramics International,* 36(5): 1629-1631.

Gottrup F (2001). Experimental wound healing research, The use of models. *European Wound Management Association, J* 1(2): 5-7.

Goyal R, Jadhav P & Tiwari A (2011). Preparation and properties of new polyphenylene sulfide/AlN composites for electronic packaging. *Journal of Electronic Materials,* 40(6): 1377-1383.

Greenspan L (1977). Humidity fixed points of binary saturated aqueous solutions. *Journal of Research of the National Bureau of Standards,* 81(1): 89-96.

Guerrero C, Roldan J, Ferrater C, Garcia-Cuenca M, Sanchez F & Varela M (2001). Growth and characterization of epitaxial ferroelectric $PbZr_xTi_{1-x}O_3$ thin film capacitors with $SrRuO_3$ electrodes for non-volatile memory applications. *Solid-State Electronics,* 45(8): 1433-1440.

Gupta SC, Patchva S, Koh W & Aggarwal BB (2012). Discovery of curcumin, a component of golden spice, and its miraculous biological activities. *Clinical and Experimental Pharmacology and Physiology,* 39(3): 283-299.

Gurtner GC, Werner S, Barrandon Y & Longaker MT (2008). Wound repair and regeneration. *Nature,* 453(7193): 314-321.

Haertling GH & LAND CE (1971). Hot-Pressed (Pb,La)(Zr,Ti)O_3 Ferroelectric Ceramics for Electrooptic Applications. *Journal of the American Ceramic Society,* 54(1): 1-11.

Hassan CM, Stewart JE & Peppas NA (2000). Diffusional characteristics of freeze/thawed poly (vinyl alcohol) hydrogels: applications to protein controlled release from multilaminate devices. *European Journal of Pharmaceutics and Biopharmaceutics,* 49(2): 161-165.

Hayob JL & Essene EJ (1995). Armalcolite in crustal paragneiss xenoliths, central Mexico. *American Mineralogist,* 80(7): 810-822.

He Y, Zhang T, Zheng W, Wang R, Liu X, Xia Y & Zhao J (2010). Humidity sensing properties of $BaTiO_3$ nanofiber prepared via electrospinning. *Sensors and Actuators B: Chemical,* 146(1): 98-102.

Hebestreit N, Hofmann J, Rammelt U & Plieth W (2003). Physical and electrochemical characterization of nanocomposites formed from polythiophene and titaniumdioxide. *Electrochimica Acta,* 48(13): 1779-1788.

Herzer G, Vazquez M, Knobel M, Zhukov A, Reininger T, Davies H, Grössinger R & Ll JS (2005). Round table discussion: Present and future applications of nanocrystalline magnetic materials. *Journal of Magnetism and Magnetic Materials,* 294(2): 252-266.

Homes C, Vogt T, Shapiro S, Wakimoto S & Ramirez A (2001). Optical response of high-dielectric-constant perovskite-related oxide. *Science,* 293(5530): 673-676.

Hu MS, Maan ZN, Wu JC, Rennert RC, Hong WX, Lai TS, Cheung AT, Walmsley GG, Chung MT, McArdle A & Longaker MT (2014). Tissue engineering and regenerative repair in wound healing. *Annals of Biomedical Engineering,* 42(7): 1494-1507.

Hu S, Chen H, Fu G & Meng F (2008). Humidity sensitive properties of K^+-doped SnO_2–$LiZnVO_4$. *Sensors and Actuators B: Chemical,* 134(2): 769-772.

Hu S & Fu G (2010). Humidity-sensitive properties based on liquid state $LiZnVO_4$-doped SnO_2. *Sensors and Actuators A: Physical,* 163(2): 481-485.

Hu W, Li L, Li G, Liu Y & Withers RL (2014). Atomic-scale control of TiO_6 octahedra through solution chemistry towards giant dielectric response. *Scientific Reports,* 4: 6582.

Hu Y, Jeng TS & Liu JS (2012). Effect of the MgO substitution for CuO on the properties of $CaCu_3Ti_4O_{12}$ ceramics. *Ceramics International,* 38(4): 3459-3464.

Huang Z, Zheng X, Yan D, Yin G, Liao X, Kang Y, Yao Y, Huang D & Hao B (2008). Toxicological effect of ZnO nanoparticles based on bacteria. *Langmuir,* 24(8): 4140-4144.

Ibrahim S, Mohd Yasin SM, Nee NM, Ahmad R & Johan MR (2012). Conductivity and dielectric behaviour of PEO-based solid nanocomposite polymer electrolytes. *Solid State Communication,* 152(5): 426-434.

Im DH, Jeon CJ & Kim ES (2012). $MgTiO_3$/polystyrene composites with low dielectric loss. *Ceramics International,* 38: S191-S195.

Imran Z, Batool SS, Jamil H, Usman M, Israr-Qadir M, Shah SH, Jamil-Rana S, Rafiq MA, Hasan MM, & Willander M (2013). Excellent humidity sensing properties of cadmium titanate nanofibers. *Ceramics International,* 39(1): 457-462

Ingle A, Rai M, Gade A & Bawaskar M (2009). Fusarium solani: a novel biological agent for the extracellular synthesis of silver nanoparticles. *Journal of Nanoparticle Research,* 11(8): 2079-2085.

Inoue Y, King Jr TE, Barker E, Daniloff E & Newman LS (2002). Basic fibroblast growth factor and its receptors in idiopathic pulmonary fibrosis and lymphangioleiomyomatosis. *American Journal of Respiratory and Critical Care Medicine,* 166(5): 765-773.

Islam T, Nimal A, Mittal U & Sharma M (2015). A micro interdigitated thin film metal oxide capacitive sensor for measuring moisture in the range of 175–625ppm. *Sensors and Actuators B: Chemical,* 221: 357-364.

Izquierdo-Barba I, Colilla M & Vallet-Regí M (2016). Zwitterionic ceramics for biomedical applications. *Acta Biomaterialia,* 40: 201–211.

Jain J, Arora S, Rajwade JM, Omray P, Khandelwal S & Paknikar KM (2009). Silver nanoparticles in therapeutics: development of an antimicrobial gel formulation for topical use. *Molecular Pharmaceutics,* 6(5): 1388-1401.

Janardhanan C, Thomas D, Subodh G, Harshan S, Philip J & Sebastian MT (2012). Microwave dielectric properties of flexible butyl rubber–strontium cerium titanate composites. *Journal of Applied Polymer Science,* 124(4): 3426-3433.

Jayakumar R, Prabaharan M, Kumar PS, Nair S & Tamura H (2011). Biomaterials based on chitin and chitosan in wound dressing applications. *Biotechnology Advances,* 29(3): 322-337.

Johnson D, Ghate B & Wang F (1985). Advances in Ceramics, vol. 15. *American Ceramic Society,* Columbus, Ohio, USA.

Johnson NR & Wang Y (2013). Controlled delivery of heparin-binding EGF-like growth factor yields fast and comprehensive wound healing. *Journal of Controlled Release,* 166(2): 124-129.

Jonscher AK (1977). Theuniversal'dielectric response. *Nature,* 267: 673-679.

Kalashnikova I, Das S & Seal S (2015). Nanomaterials for wound healing: scope and advancement. *Nanomedicine,* 10(16): 2593-2612.

Kar KK & Pramanik S (2014). Hydroxyapatite poly (etheretherketone) nanocomposites and method of manufacturing same. *US Patent,* February, 18, 2014: US8652373 B2.

Kawai H (1969). The piezoelectricity of poly (vinylidene fluoride). *Japanese Journal of Applied Physics,* 8(7): 975.

Kerativitayanan P, Carrow JK & Gaharwar AK (2015). Nanomaterials for engineering stem cell responses. *Advanced healthcare Materials,* 4(11): 1600-1627.

Khan A, Pommier A, Neumann GA & Mosegaard K (2013). The lunar moho and the internal structure of the Moon: A geophysical perspective. *Tectonophysics,* 609(0): 331-352.

Khatri P, Behera B & Choudhary RNP (2009). Structural and impedance properties of $Ca_3Nb_2O_8$ ceramics. *Journal of Physics and Chemistry of Solids,* 70(2): 385-389.

Kim Y, Jung B, Lee H, Kim H, Lee K & Park H (2009). Capacitive humidity sensor design based on anodic aluminum oxide. *Sensors and Actuators B: Chemical,* 141(2): 441-446.

Knobel M, Vazquez M & Kraus L (2003). Giant magnetoimpedance. *Handbook of Magnetic Materials,* 15: 497-563.

Koh A, Carpenter AW, Slomberg DL & Schoenfisch MH (2013). Nitric oxide-releasing silica nanoparticle-doped polyurethane electrospun fibers. *ACS Applied Mmaterials & Interfaces,* 5(16): 7956-7964.

Kokabi M, Sirousazar M & Hassan ZM (2007). PVA–clay nanocomposite hydrogels for wound dressing. *European Polymer Journal,* 43(3): 773-781.

Kulwicki BM (1991). Humidity sensors. *Journal of the American Ceramic Society,* 74(4): 697-708.

Kumar A, Choudhary R, Singh B & Thakur AK (2006). Effect of strontium concentration on electrical conduction properties of Sr-modified $BaSnO_3$. *Ceramics International,* 32(1): 73-83.

Kumar A, Singh B, Choudhary R & Thakur AK (2006). Characterization of electrical properties of Pb-modified $BaSnO_3$ using impedance spectroscopy. *Materials Chemistry and Physics,* 99(1): 150-159.

Kumar B, Vijayakumar M, Govindarajan R & Pushpangadan P (2007). Ethnopharmacological approaches to wound healing—exploring medicinal plants of India. *Journal of Ethnopharmacology,* 114(2): 103-113.

Kumar S & Kumar P (2010). Study of structural, dielectric and pyroelectric properties of modified PT system. *Physica B: Condensed Matter,* 405(13): 2869-2873.

Kwon S, Huang C-C, Patterson EA, Cann DP, Alberta EF, Kwon S & Hackenberger WS (2008). The effect of Cr_2O_3, Nb_2O_5 and ZrO_2 doping on the dielectric properties of $CaCu_3Ti_4O_{12}$. *Materials Letters,* 62(4): 633-636.

Lam K & Chan H (2005). Piezoelectric and pyroelectric properties of 65PMN-35PT/P (VDF-TrFE) 0–3 composites. *Composites Science and Technology,* 65(7): 1107-1111.

Leu A & Leach JK (2008). Proangiogenic potential of a collagen/bioactive glass substrate. *Pharmaceutical Research,* 25(5): 1222-1229.

Li C, Fu R, Yu C, Li Z, Guan H, Hu D, Zhao D & Lu L (2013). Silver nanoparticle/chitosan oligosaccharide/poly (vinyl alcohol) nanofibers as wound dressings: a preclinical study. *International Journal of Nanomedicine,* 8: 4131.

Li J, Chen T, Deng F, Wan J, Tang Y, Yuan P & Zhang L (2015). Synthesis, characterization, and *in vitro* evaluation of curcumin-loaded albumin nanoparticles surface-functionalized with glycyrrhetinic acid. *International Journal of Nanomedicine,* 10: 5475.

Li JY, Xu TW, Li ST, Jin HY & Li W (2010). Structure and electrical response of $CaCu_3Ti_4O_{12}$ ceramics: effect of heat treatments at the high vacuum. *Journal of Alloys and Compounds,* 506(1): L1-L4.

Li X, Chen S, Zhang B, Li M, Diao K, Zhang Z, Li J, Xu Y, Wang X, & Chen H (2012). In situ injectable nano-composite hydrogel composed of curcumin, N, O-carboxymethyl chitosan and oxidized alginate for wound healing application. *International Journal of Pharmaceutics,* 437(1): 110-119.

Li Y, Neoh K & Kang E (2004). Poly (vinyl alcohol) hydrogel fixation on poly (ethylene terephthalate) surface for biomedical application. *Polymer,* 45(26): 8779-8789.

Lim WH, Yap YK, Chong WY & Ahmad H (2014). All-optical graphene oxide humidity sensors. *Sensors,* 14(12): 24329-24337.

Liu M, Sun J & Chen Q (2009). Influences of heating temperature on mechanical properties of polydimethylsiloxane. *Sensors and Actuators A: Physical,* 151(1): 42-45.

Liu SY, Chua L, Tan KC & Valavan S (2010). Novel ferroelectric capacitor for non-volatile memory storage and biomedical tactile sensor applications. *Thin Solid Films,* 518(24): e152-e155.

Liu Y, Cai S, Shu XZ, Shelby J & Prestwich GD (2007). Release of basic fibroblast growth factor from a crosslinked glycosaminoglycan hydrogel promotes wound healing. *Wound Repair and Regeneration,* 15(2): 245-251.

Lou J, Hu W, Tian R, Zhang H, Jia Y, Zhang J & Zhang L (2014). Optimization and evaluation of a thermoresponsive ophthalmic in situ gel containing curcumin-loaded albumin nanoparticles. *International Journal of Nanomedicine,* 9: 2517.

Lozano-Sánchez L, Lee S-W, Sekino T & Rodríguez-González V (2013). Practical microwave-induced hydrothermal synthesis of rectangular prism-like $CaTiO_3$. *CrystEngComm,* 15(13): 2359-2362.

Lunkenheimer P, Fichtl R, Ebbinghaus S & Loidl A (2004). Nonintrinsic origin of the colossal dielectric constants in $CaCu_3Ti_4O_{12}$. *Physical review B,* 70(17): 172102.

Ma H, Lin K, Liu L, Yang B, Rong Y, Chen J, Deng J, Kawaguchi S, Kato K & Xing X (2015). Structure and electrical properties of tetragonal tungsten bronze $Ba_2CeFeNb_4O_{15}$. *RSC Advances,* 5(94): 76957-76962.

Madhavi M, Madhavi K & Jithan A (2012). Preparation and in vitro/in vivo characterization of curcumin microspheres intended to treat colon cancer. *Journal of Pharmacy And Bioallied Sciences,* 4(2): 164.

Maehly AC & Chance B (1954). The assay of catalases and peroxidases. *Methods Biochem Anal,* 1: 357-424.

Magnéli A (1949). The crystal structure of tetragonal potassium tungsten bronze. *Arkiv for Kemi,* 1(3): 213-221.

Manna A, Pramanik S, Tripathy A, Radzi Z, Moradi A, Pingguan-Murphy B & Osman NAA (2016). Design and development of an in situ synthesized layered double hydroxide structure of Fe-induced hydroxyapatite for drug carriers. *RSC Advances,* 6(30): 25549-25561.

Mardare A, Mardare C & Joanni E (2005). Bottom electrode crystallization of PZT thin films for ferroelectric capacitors. *Journal of the European Ceramic Society,* 25(5): 735-741.

Masiello P, Broca C, Gross R, Roye M, Manteghetti M, Hillaire-Buys D, Novelli M & Ribes G (1998). Experimental NIDDM: development of a new model in adult rats administered streptozotocin and nicotinamide. *Diabetes,* 47(2): 224-229.

Matko V (2011). Next generation AT-cut quartz crystal sensing devices. *Sensors,* 11(5): 4474-4482.

Matko V & Donlagic D (1996). Sensor for high-air-humidity measurement. *Instrumentation and Measurement, IEEE Transactions,* 45(2): 561-563.

Matko V & Milanović M (2014). Temperature-compensated capacitance–frequency converter with high resolution. *Sensors and Actuators A: Physical,* 220: 262-269.

Matrisian LM (1992). The matrix-degrading metalloproteinases. *Bioessays,* 14(7): 455-463.

Matsuo Y & Sasaki H (1965). Formation of Lead Zirconate-Lead Titanate Solid Solutions. *Journal of the American Ceramic Society,* 48(6): 289-291.

Matsuyama H, Teramoto M & Urano H (1997). Analysis of solute diffusion in poly (vinyl alcohol) hydrogel membrane. *Journal of Membrane Science,* 126(1): 151-160.

Maxwell JC (1973). Electricity and Magnetism. *Oxford University Press,* New York.

Mbairi FD & Hesselbom H (2005). *High frequency design and characterization of SU-8 based conductor backed coplanar waveguide transmission lines.* International Symposium on Advanced Packaging Materials: Processes, Properties and Interfaces, Irvine, CA, USA, 16 Mar - 18 Mar 2005.

McCafferty E & Zettlemoyer A (1971). Adsorption of water vapour on α-Fe_2O_3. *Discussions of the Faraday Society,* 52: 239-254.

214

Medvedev AY (1996). Synthetic armalcolite and pseudobrookite. *Mineralogical Magazine,* 60: 347-354.

Mehendale F & Martin P (2001). The cellular and molecular events of wound healing. *In: Falanga V (ed) Cutaneous Wound Healing,* 1st edn. London: Martin Dunitz. pp 15–37.

Meng Y, Chu J, Xue J, Liu C, Wang Z & Zhang L (2014). Design and synthesis of non-crystallizable, low-t g polysiloxane elastomers with functional epoxy groups through anionic copolymerization and subsequent epoxidation. *RSC Advances,* 4(59): 31249-31260

Minamikawa T, Yonezawa Y, Heya A, Fujimori Y, Nakamura T, Masuda A & Matsumura H (2001). Preparation of SiN x passivation films for PZT ferroelectric capacitors at low substrate temperatures by catalytic CVD. *Thin Solid Films,* 395(1): 284-287.

Misra HP & Fridovich I (1972). The role of superoxide anion in the autoxidation of epinephrine and a simple assay for superoxide dismutase. *Journal of Biological Chemistry,* 247(10): 3170-3175.

Moradi A, Pramanik S, Ataollahi F, Khalil AA, Kamarul T & Pingguan-Murphy B (2016). A comparison study of different physical treatments on cartilage matrix derived porous scaffolds for tissue engineering applications. *Science and Technology of Advanced Materials,* 15(6): 65001-65012.

Morris RV, Lauer HV, Lawson CA, Gibson EK, Nace GA & Stewart C (1985). Spectral and other physicochemical properties of submicron powders of hematite (α-Fe_2O_3), maghemite (γ-Fe_2O_3), magnetite (Fe_3O_4), goethite (α-FeOOH), and lepidocrocite (γ-FeOOH). *Journal of Geophysical Research: Solid Earth, (1978–2012)* 90(B4): 3126-3144.

Moseley R, Hilton JR, Waddington RJ, Harding KG, Stephens P & Thomas DW (2004). Comparison of oxidative stress biomarker profiles between acute and chronic wound environments. *Wound Repair and Regeneration,* 12(4): 419-429.

Moura LI, Dias AM, Carvalho E & de Sousa HC (2013). Recent advances on the development of wound dressings for diabetic foot ulcer treatment—A review. *Acta Biomaterialia,* 9(7): 7093-7114.

Mu C, Zhang H, He Y & Liu P (2010). Influence of temperature on dielectric properties of Fe-doped $CaCu_3Ti_4O_{12}$ ceramics. *Physica B: Condensed Matter,* 405(1): 386-389.

Mühlebach A, Müller B, Pharisa C, Hofmann M, Seiferling B & Guerry D (1997). New water-soluble photo crosslinkable polymers based on modified poly (vinyl alcohol). *Journal of Polymer Science Part A: Polymer Chemistry,* 35(16): 3603-3611.

Murugendrappa M & Prasad MA (2006). Dielectric spectroscopy of polypyrrole–γ–Fe_2O_3 composites. *Materials Rresearch Bulletin,* 41(7): 1364-1369.

Nahar R (2000). Study of the performance degradation of thin film aluminum oxide sensor at high humidity. *Sensors and Actuators B: Chemical,* 63(1): 49-54.

Nayak B & Pereira LMP (2006). Catharanthus roseus flower extract has wound-healing activity in Sprague Dawley rats. *BMC Complementary and Alternative Medicine,* 6(1): 41.

Nayak S, Sahoo B, Chaki TK & Khastgir D (2013). Development of polyurethane–titania nanocomposites as dielectric and piezoelectric material. *RSC Advances,* 3(8): 2620-2631.

Neufuss K & Rudajevová A (2002). Thermal properties of the plasma-sprayed $MgTiO_3$–$CaTiO_3$ and $CaTiO_3$. *Ceramics International,* 28(1): 93-97.

Nikolaou S, Ponchak GE, Papapolymerou J & Tentzeris MM (2006). Conformal double exponentially tapered slot antenna (DETSA) on LCP for UWB applications. *IEEE Transactions on Antennas and Propagation,* 54(6): 1663-1669.

Nitta T, Terada Z & Hayakawa S (1980). Humidity-Sensitive Electrical Conduction of $MgCr_2O_4$-TiO_2 Porous Ceramics. *Journal of the American Ceramic Society,* 63(5-6): 295-300.

Noda M, Hashimoto K, Kubo R, Tanaka H, Mukaigawa T, Xu H & Okuyama M (1999). A new type of dielectric bolometer mode of detector pixel using ferroelectric thin film capacitors for infrared image sensor. *Sensors and Actuators A: Physical,* 77(1): 39-44.

Pandey N & Tiwari K (2010). Morphological and relative humidity sensing properties of pure ZnO nanomaterial. *Sensors & Transducers,* 122(11): 9.

Park HM. (2003). *Comparing group means: t-tests and one-way ANOVA using Stata, SAS, R, and SPSS:* University Information Technology Services (UITS) Centre for Statistical and Mathematical Computing, Indiana University, Bloomington, Indiana.

Park S-E & Shrout TR (1997). Characteristics of relaxor-based piezoelectric single crystals for ultrasonic transducers. *IEEE Transactions on Ultrasonics, Ferroelectrics, and Frequency Control,* 44(5): 1140-1147.

Parthibavarman M, Hariharan V & Sekar C (2011). High-sensitivity humidity sensor based on SnO_2 nanoparticles synthesized by microwave irradiation method. *Materials Science and Engineering,* C 31(5): 840-844.

Pascal-Delannoy F, Sorli B & Boyer A (2000). Quartz crystal microbalance (QCM) used as humidity sensor. *Sensors and Actuators A: Physical,* 84(3): 285-291.

Patel I, Siores E & Shah T (2010). Utilisation of smart polymers and ceramic based piezoelectric materials for scavenging wasted energy. *Sensors and Actuators A: Physical,* 159(2): 213-218.

Patterson EA, Kwon S, Huang C-C & Cann DP (2005). Effects of ZrO_2 additions on the dielectric properties of $CaCu_3Ti_4O_{12}$. *Applied Physics Letters,* 87 (18): 2911.

Pauzi NAS, Muhammad AA, Fakurazi S, Arulselvan P & Ahmad Z (2013). Preliminary study of the optimization of protocol for development of type 2 diabetic model in rats. *Indian Journal of Science and Technology,* 6(7): 4960-4965.

Peng X, Chu J, Yang B & Feng PX (2012). Mn-doped zinc oxide nanopowders for humidity sensors. *Sensors and Actuators B: Chemical,* 174: 258-262.

Peppas NA & Merrill EW (1976). Differential scanning calorimetry of crystallized PVA hydrogels. *Journal of Aapplied Polymer Science,* 20(6): 1457-1465.

Petchsuk A, Supmak W & Thanaboonsombut A (2009). A series of 0-3 composites of lead zirconate titanate and ferroelectric nylon77: Preparation and electrical properties. *Journal of Applied Polymer Science,* 114(2): 1048-1054.

Pimple B, Kadam P & Patil M (2012). Ulcer healing properties of different extracts of Origanum majorana in streptozotocin-nicotinamide induced diabetic rats. *Asian Pacific Journal of Tropical Disease,* 2(4): 312-318.

Płcharski J & Weiczorek W (1988). PEO based composite solid electrolyte containing nasicon. *Solid State Ionics,* 28: 979-982.

Pokhrel S & Nagaraja K (2003). Electrical and humidity sensing properties of Chromium (III) oxide–tungsten (VI) oxide composites. *Sensors and Actuators B: Chemical,* 92(1): 144-150.

Ponrasu T & Suguna L (2012). Efficacy of Annona squamosa on wound healing in streptozotocin-induced diabetic rats. *International Wound Journal,* 9(6): 613-623.

Prakash BS & Varma K (2006). Microstructural and dielectric properties of donor doped $(La^{3+})CaCu_3Ti_4O_{12}$ ceramics. *Journal of Materials Science: Materials in Electronics,* 17(11): 899-907.

Prakash BS, Varma K, Michau D & Maglione M (2008). Deposition and dielectric properties of $CaCu_3Ti_4O_{12}$ thin films deposited on $Pt/Ti/SiO_2/Si$ substrates using radio frequency magnetron sputtering. *Thin Solid Films,* 516(10): 2874-2880.

Pramanik S, Ataollahi F, Pingguan-Murphy B, Oshkour AA & Abu Osman NA (2015). In Vitro Study of Surface Modified Poly(ethylene glycol)-Impregnated Sintered Bovine Bone Scaffolds on Human Fibroblast Cells. *Scientific Reports,* 5: 9806.

Pramanik S, Hanif ASM, Pingguan-Murphy B & Abu Osman NA (2012). Morphological change of heat treated bovine bone: a comparative study. *Materials,* 6(1): 65-75.

Pramanik S, Pingguan-Murphy B & Abu Osman NA (2013). Developments of immobilized surface modified piezoelectric crystal biosensors for advanced applications. *International Journal of Electrochemical Science,* 8: 8863-8892.

Pramanik S, Pingguan-Murphy B, Cho J & Abu Osman NA (2014). Design and development of potential tissue engineering scaffolds from structurally different longitudinal parts of a bovine-femur. *Scientific Reports,* 4*:* 5843-5843.

Prasad K, Bhagat S, Priyanka, AmarNath K, Chandra KP & Kulkarni AR (2010). Electrical properties of $BaY_{0.5}Nb_{0.5}O_3$ ceramic: Impedance spectroscopy analysis. *Physica B: Condensed Matter,* 405(17): 3564-3571.

Pullar RC, Penn SJ, Wang X, Reaney IM & Alford NM (2009). Dielectric loss caused by oxygen vacancies in titania ceramics. *Journal of the European Ceramic Society,* 29(3): 419-424.

Qi Q, Zhang T, Wang S & Zheng X (2009). Humidity sensing properties of KCl-doped ZnO nanofibers with super-rapid response and recovery. *Sensors and Actuators B: Chemical,* 137(2): 649-655.

Qi Q, Zhang T, Yu Q, Wang R, Zeng Y, Liu L & Yang H (2008). Properties of humidity sensing ZnO nanorods-base sensor fabricated by screen-printing. *Sensors and Actuators B: Chemical,* 133(2): 638-643.

Qi Q, Zhang T, Zeng Y & Yang H (2009). Humidity Sensing Properties of KCl-doped Cu–Zn/CuO–ZnO Nanoparticles. *Sensors and Actuators B: Chemical,* 137(1): 21-26.

Qi Q, Zhang T, Zheng X & Wan L (2008). Preparation and humidity sensing properties of Fe-doped mesoporous silica SBA-15. *Sensors and Actuators B: Chemical,* 135(1): 255-261.

Qiu Y & Park K (2001). Environment-sensitive hydrogels for drug delivery. *Advanced Drug Delivery Reviews,* 53(3): 321-339.

Radwan FA, Ahmed MA & Abdelatif G (2003). Screening effect of Ti^{4+} ions on the electrical conductivity and thermoelectric power of Mg ferrite. *Journal of Physics and Chemistry of Solids,* 64(12): 2465-2477.

Raengthon N & Cann DP (2012). Dielectric relaxation in $BaTiO_3–Bi(Zn_{1/2}Ti_{1/2})O_3$ ceramics. *Journal of the American Ceramic Society,* 95(5): 1604-1612.

Raevski I, Prosandeev S, Bogatin A, Malitskaya M & Jastrabik L (2003). High dielectric permittivity in $AFe_{1/2}B_{1/2}O_3$ nonferroelectric perovskite ceramics (A= Ba, Sr, Ca; B= Nb, Ta, Sb). *Journal of Applied Physics,* 93(7): 4130-4136.

Raghupathi KR, Koodali RT & Manna AC (2011). Size-dependent bacterial growth inhibition and mechanism of antibacterial activity of zinc oxide nanoparticles. *Langmuir,* 27(7): 4020-4028.

Rai AK, Mandal K, Kumar D & Parkash O (2009). Dielectric properties of lanthanum-doped $CaCu_3Ti_4O_{12}$ synthesized by semi-wet route. *Journal of Physics and Chemistry of Solids,* 70(5): 834-839.

Rai AK, Mandal K, Kumar D & Parkash O (2010). Dielectric properties of $CaCu_3Ti_{4-x}Co_xO_{12}$ (x= 0.10, 0.20, and 0.30) synthesized by semi-wet route. *Materials Chemistry and Physics,* 122(1): 217-223.

Rai AK, Singh NK, Acharya SK, Singh L & Mandal K (2012). Effect of tantalum substitutions on microstructures and dielectric properties of calcium copper titanate ($CaCu_3Ti_4O_{12}$) ceramic. *Materials Science and Engineering: B,* 177(14): 1213-1218.

Rai AK, Singh NK, Lee S-K, Mandal K, Kumar D & Parkash O (2011). Dielectric properties of iron doped calcium copper titanate, $CaCu_{2.9}Fe_{0.1}Ti_4O_{12}$. *Journal of Alloys and Compounds,* 509(36): 8901-8906.

Raistrick I, Franceschetti D & Macdonald JR (1987). Impedance spectroscopy. *Wiley, New York* 71(5): 101-104.

Ramajo L, Castro M & Reboredo M (2010). Dielectric response of Ag/BaTiO$_3$/epoxy nanocomposites. *Journal of Materials Science,* 45(1): 106-111.

Ramajo LA, Reboredo MM & Castro MS (2007). Characterisation of epoxy/BaTiO$_3$ composites processed by dipping for integral capacitor films (ICF). *Journal of Materials Science,* 42(10): 3685-3691.

Rao Y, Ogitani S, Kohl P & Wong C (2000). *High dielectric constant polymer-ceramic composite for embedded capacitor application.* IEEE International Symposium on Advanced Packaging Materials: Processes, Properties and Interfaces, 8 Aug. 2000.

Rao Y, Wong C, Qu J & Marinis T. (2000). *Effective dielectric constant prediction of polymer-ceramic composite based on self-consistent theory.* Proceedings at 50th Electronic Components & Technology Conference, IEEE, Las Vegas, Nevada, USA, May 21-24, 2000.

Rasik AM & Shukla A (2000). Antioxidant status in delayed healing type of wounds. *International Journal of Experimental Pathology,* 81(4): 257-263.

Rayber G (2001). Epidemiology of foot ulcers and amputations in the diabetic foot. Bowker JH, Pfeifer, MA. *The diabetic foot. 6th Ed. St louis, Missouri. Mosby Inc*: 13-32.

Rieger KA, Birch NP & Schiffman JD (2013). Designing electrospun nanofiber mats to promote wound healing–a review. *Journal of Materials Chemistry B,* 1(36): 4531-4541.

Risbud MV, Hardikar AA, Bhat SV & Bhonde RR (2000). pH-sensitive freeze-dried chitosan–polyvinyl pyrrolidone hydrogels as controlled release system for antibiotic delivery. *Journal of Controlled Release,* 68(1): 23-30.

Rittersma Z (2002). Recent achievements in miniaturised humidity sensors—a review of transduction techniques. *Sensors and Actuators A: Physical,*96(2): 196-210.

Robson MC, Steed DL & Franz MG (2001). Wound healing: biologic features and approaches to maximize healing trajectories. *Current Problems in Surgery,* 38(2): A1-140.

Rojkind M, Dominguez-Rosales J-A, Nieto N & Greenwel P (2002). Role of hydrogen peroxide and oxidative stress in healing responses. *Cellular and Molecular Life Sciences CMLS,* 59(11): 1872-1891.

Rosiak JM (1994). Radiation formation of hydrogels for drug delivery. *Journal of Controlled Release,* 31(1): 9-19.

Rotruck J, Pope A, Ganther H, Swanson A, Hafeman DG & Hoekstra W (1973). Selenium: biochemical role as a component of glutathione peroxidase. *Science,* 179(4073): 588-590.

Rozman M & Drofenik M (1998). Sintering of nanosized MnZn ferrite powders. *Journal of the American Ceramic Society,* 81(7): 1757-1764.

Safari A, Panda RK & Janas VF (2011). *Ferroelectric Ceramics: Processing. Properties and Applications.* Rutgers University, Piscataway New Jersey, 8855.

Sager K, Gerlach G & Schroth A (1994). A humidity sensor of a new type. *Sensors and Actuators B: Chemical,* 18(1): 85-88.

Saha D, Giri R, Mistry KK & Sengupta K (2005). Magnesium chromate–TiO_2 spinel tape cast thick film as humidity sensor. *Sensors and Actuators B: Chemical,* 107(1): 323-331.

Saha S & Sinha T (2002), Low-temperature scaling behavior of $BaFe_{0.5}Nb_{0.5}O_3$. *Physical Review B,* 65(13): 134103.

Said M, Velayutham TS, Gan WC & Abd Majid WH (2015). The structural and electrical properties of $Sr_xBa_{(1-x)}Nb_2O_6$ (SBN) ceramic with varied composition. *Ceramics International,* 41(5, Part B): 7119-7124.

Sberveglieri G, Rinchetti G, Groppelli S & Faglia G (1994). Capacitive humidity sensor with controlled performances, based on porous Al_2O_3 thin film growm on SiO_2-Si substrate. *Sensors and Actuators B: Chemical,* 19(1): 551-553.

Seabra AB & de Oliveira MG (2004). Poly (vinyl alcohol) and poly (vinyl pyrrolidone) blended films for local nitric oxide release. *Biomaterials,* 25(17): 3773-3782.

Sebastian MT & Jantunen H (2010). Polymer–ceramic composites of 0–3 connectivity for circuits in electronics: a review. *International Journal of Applied Ceramic Technology,* 7(4): 415-434.

Seiyama T, Yamazoe N & Arai H (1983). Ceramic humidity sensors. *Sensors and Actuators,* 4: 85-96.

Seo KI, Choi MS, Jung UJ, Kim HJ, Yeo J, Jeon SM & Lee MK (2008). Effect of curcumin supplementation on blood glucose, plasma insulin, and glucose

220

homeostasis related enzyme activities in diabetic db/db mice. *Molecular Nutrition & Food Research,* 52(9): 995-1004.

Shah J, Kotnala R, Singh B & Kishan H (2007). Microstructure-dependent humidity sensitivity of porous $MgFe_2O_4$–CeO_2 ceramic. *Sensors and Actuators B: Chemical,* 128(1): 306-311.

Shalumon K, Anulekha K, Nair SV, Nair S, Chennazhi K & Jayakumar R (2011). Sodium alginate/poly (vinyl alcohol)/nano ZnO composite nanofibers for antibacterial wound dressings. *International Journal of Biological Macromolecules,* 49(3): 247-254.

Shanmugasundaram T, Radhakrishnan M, Gopikrishnan V, Pazhanimurugan R & Balagurunathan R (2013). A study of the bactericidal, anti-biofouling, cytotoxic and antioxidant properties of actinobacterially synthesised silver nanoparticles. *Colloids and Surfaces B: Biointerfaces,* 111: 680-687.

Shen Z, Wang X, Luo B & Li L (2015). $BaTiO_3$–$BiYbO_3$ perovskite materials for energy storage applications. *Journal of Materials Chemistry A,* 3(35): 18146-18153.

Shin JH, Metzger SK & Schoenfisch MH (2007). Synthesis of nitric oxide-releasing silica nanoparticles. *Journal of the American Chemical Society,* 129(15): 4612-4619.

Si S, Li S, Ming Z & Jin L (2010). Humidity sensors based on ZnO Colloidal nanocrystal clusters. *Chemical Physics Letters,* 493(4): 288-291.

Simpson DM & Ross R (1972). The neutrophilic leukocyte in wound repair: a study with antineutrophil serum. *Journal of Clinical Investigation,* 51(8): 2009.

Sinclair DC & West AR (1989). Impedance and modulus spectroscopy of semiconducting $BaTiO_3$ showing positive temperature coefficient of resistance. *Journal of Applied Physics,* 66(8): 3850-3856.

Singer AJ & Dagum AB (2008). Current management of acute cutaneous wounds. *New England Journal of Medicine,* 359(10): 1037-1046.

Singh L, Rai U, Mandal K & Rai AK (2013). Effect of processing routes on microstructure, electrical and dielectric behavior of Mg-doped $CaCu_3Ti_4O_{12}$ electro-ceramic. *Applied Physics A,* 112(4): 891-900.

Singh N, Armstrong DG & Lipsky BA (2005). Preventing foot ulcers in patients with diabetes. *Jama,* 293(2): 217-228.

Sivakumar N, Narayanasamy A, Greneche J-M, Murugaraj R & Lee Y (2010). Electrical and magnetic behaviour of nanostructured $MgFe_2O_4$ spinel ferrite. *Journal of Alloys and Compounds,* 504(2): 395-402.

So JH, Thelen J, Qusba A, Hayes GJ, Lazzi G & Dickey MD (2009). Reversibly deformable and mechanically tunable fluidic antennas. *Advanced Functional Materials,* 19(22): 3632-3637.

Song X, Qi Q, Zhang T & Wang C (2009). A humidity sensor based on KCl-doped SnO$_2$ nanofibers. *Sensors and Actuators B: Chemical,* 138(1): 368-373.

Steed DL, Attinger C, Colaizzi T, Crossland M, Franz M, Harkless L, Johnson A, Moosa H, Robson M, *Serena T, Sheehan P* (2006). Guidelines for the treatment of diabetic ulcers. *Wound Repair and Regeneration,* 14(6): 680-692.

Sternlicht MD & Werb Z (2001). How matrix metalloproteinases regulate cell behavior. *Annual Review of Cell and Developmental Biology,* 17: 463.

Strutz F, Zeisberg M, Hemmerlein B, Sattler B, Hummel K, Becker V & Müller GA (2000). Basic fibroblast growth factor expression is increased in human renal fibrogenesis and may mediate autocrine fibroblast proliferation. *Kidney International,* 57(4): 1521-1538.

Su M & Wang J (2011). Preparation and humidity sensitivity of multi-layered zirconia thin films by sol–gel method. *Sensor Letters,* 9(2): 670-674.

Su PG, Li WC, Tseng JY & Ho CJ (2011). Fully transparent and flexible humidity sensors fabricated by layer-by-layer self-assembly of thin film of poly (2-acrylamido-2-methylpropane sulfonate) and its salt complex. *Sensors and Actuators B: Chemical,* 153(1): 29-36.

Su PG & Wang CP (2008). Flexible humidity sensor based on TiO$_2$ nanoparticles-polypyrrole-poly-[3-(methacrylamino) propyl] trimethyl ammonium chloride composite materials. *Sensors and Actuators B: Chemical,* 129(2): 538-543.

Subodh G, Deepu V, Mohanan P & Sebastian M (2009). Polystyrene/Sr$_2$Ce$_2$Ti$_5$O$_{15}$ composites with low dielectric loss for microwave substrate applications. *Polymer Engineering & Science,* 49(6): 1218-1224.

Subramanian M, Li D, Duan N, Reisner B & Sleight A (2000). High dielectric constant in ACu$_3$Ti$_4$O$_{12}$ and ACu$_3$Ti$_3$FeO$_{12}$ phases. *Journal of Solid State Chemistry,* 151(2): 323-325.

Sudheesh Kumar P, Lakshmanan V-K, Anilkumar T, Ramya C, Reshmi P, Unnikrishnan A, Nair SV & Jayakumar R (2012). Flexible and microporous chitosan hydrogel/nano ZnO composite bandages for wound dressing: in vitro and in vivo evaluation. *ACS Applied Materials & Interfaces,* 4(5): 2618-2629.

Takezoe H, Robert K-i-C, WC, Merton C, Bernard I, Edward J, Subhash M & Patrick V (2001). Ferroelectric, antiferroelectric, and ferrielectric liquid crystals: Applications. *Encyclopedia of Materials, Science and Technology*, 3063-3074.

Tanase T, Kobayashi Y, Miwa T & Konno M (2005). Fabrication and dielectric properties of barium strontium titanate nano-particles/amorphous lead zirconate titanate composite thin film. *Thin Solid Films,* 485(1): 22-26.

Taya M (2005). *Electronic composites: modeling, characterization, processing, and MEMS applications*: University of Washington, Cambridge University Press, WA, USA.

Taylor JA, Reczek ST & Rosen A (1995). Soft ferrite processing. *American Ceramic Society Bulletin,* 74(4): 91-94.

Tejuca LG & Fierro J. (2000). *Properties and Applications of Perovskite-type Oxides*: CRC Press, New York.

Teoh SL, Latiff AA & Das S (2009). The effect of topical extract of Momordica charantia (bitter gourd) on wound healing in nondiabetic rats and in rats with diabetes induced by streptozotocin. *Clinical and Experimental Dermatology,* 34(7): 815-822.

Thacker C, Liang Y, Peng Q & Hess P (2009). The stability and major element partitioning of ilmenite and armalcolite during lunar cumulate mantle overturn. *Geochimica et Cosmochimica Acta,* 73(3): 820-836.

Thamjaree W, Nhuapeng W, Chaipanich A & Tunkasiri T (2005). Fabrication of combined 0–3 and 1–3 connectivities PZT/epoxy resin composites. *Applied Physics A,* 81(7): 1419-1422.

Thomas P, Varughese K, Dwarakanath K & Varma K (2010). Dielectric properties of Poly (vinylidene fluoride)/$CaCu_3Ti_4O_{12}$ composites. *Composites Science and Technology,* 70(3): 539-545.

Thomas S, Deepu V, Uma S, Mohanan P, Philip J & Sebastian M (2009). Preparation, characterization and properties of $Sm_2Si_2O_7$ loaded polymer composites for microelectronic applications. *Materials Science and Engineering: B,* 163(2): 67-75.

Thostenson E & Chou T-W (1999). Microwave processing: fundamentals and applications. *Composites Part A: Applied Science and Manufacturing,* 30(9): 1055-1071.

Tiercelin N, Coquet P, Sauleau R, Senez V & Fujita H (2006). Polydimethylsiloxane membranes for millimeter-wave planar ultra flexible antennas. *Journal of Micromechanics and Microengineering,* 16(11): 2389.

Tiwari SK, Choudhary RNP & Mahapatra SP (2014). Effect of multiwalled carbon nanotube and temperature on dielectric and impedance spectroscopy of chlorobutyl elastomer nanocomposites. *Journal of Elastomers and Plastics,* 47(6): 549-572.

Tolino MA, Block ER & Klarlund JK (2011). Brief treatment with heparin-binding EGF-like growth factor, but not with EGF, is sufficient to accelerate epithelial wound healing. *Biochimica et Biophysica Acta (BBA)-General Subjects,* 1810(9): 875-878.

Tomasek JJ, Gabbiani G, Hinz B, Chaponnier C & Brown RA (2002). Myofibroblasts and mechano-regulation of connective tissue remodelling. *Nature Reviews Molecular Cell Biology,* 3(5): 349-363.

Traversa E (1995). Ceramic sensors for humidity detection: the state-of-the-art and future developments. *Sensors and Actuators B: Chemical,* 23(2): 135-156.

Tripathy A, Pramanik S, Cho J, Santhosh J & Abu Osman NA (2014). Role of Morphological Structure, Doping, and Coating of Different Materials in the Sensing Characteristics of Humidity Sensors. *Sensors,* 14(9), 16343-16422.

Tripathy A, Pramanik S, Manna A, Azrin Shah NF, Shasmin HN, Radzi Z & Abu Osman NA (2016). Synthesis and Characterizations of Novel Ca-Mg-Ti-Fe-Oxides Based Ceramic Nanocrystals and Flexible Film of Polydimethylsiloxane Composite with Improved Mechanical and Dielectric Properties for Sensors. *Sensors,* 16(3), 292.

Tsuboi R & Rifkin DB (1990). Recombinant basic fibroblast growth factor stimulates wound healing in healing-impaired db/db mice. *The Journal of Experimental Medicine,* 172(1): 245-251.

Tu J, Wang R, Geng W, Lai X, Zhang T, Li N, Yue N & Li X (2009). Humidity sensitive property of Li-doped 3D periodic mesoporous silica SBA-16. *Sensors and Actuators B: Chemical,* 136(2): 392-398.

Usman M, Rasool K, Batool S, Imran Z, Ahmad M, Jamil H, Rafiq M & Hasan M (2014). Humidity Effect on Transport Properties of Titanium Dioxide Nanoparticles. *Journal of Materials Science & Technology,* 30(8): 748-752.

Vaiana CA, Leonard MK, Drummy LF, Singh KM, Bubulya A, Vaia RA, Naik RR & Kadakia MP (2011). Epidermal growth factor: layered silicate nanocomposites for tissue regeneration. *Biomacromolecules,* 12(9): 3139-3146.

Vangchangyia S, Yamwong T, Swatsitang E, Thongbai P & Maensiri S (2013). Selectivity of doping ions to effectively improve dielectric and non-ohmic properties of $CaCu_3Ti_4O_{12}$ ceramics. *Ceramics International,* 39(7): 8133-8139.

Veale CR (1972). *Fine powders: preparation, properties and uses*: Applied Science Publishers, London.

Verwey E (1939). Electronic conduction of magnetite (Fe_3O_4) and its transition point at low temperatures. *Nature,* 144(3642): 327-328.

Vicentini DS, Smania A & Laranjeira MC (2010). Chitosan/poly (vinyl alcohol) films containing ZnO nanoparticles and plasticizers. *Materials Science and Engineering: C,* 30(4): 503-508.

Wagner KW (1973). The distribution of relaxation times in typical dielectrics. *Annals of Physics,* 40: 817–819.

Wang C-T, Wu C-L, Chen I-C & Huang Y-H (2005). Humidity sensors based on silica nanoparticle aerogel thin films. *Sensors and Actuators B: Chemical,* 107(1): 402-410.

Wang DY, Li K & Chan HLW (2004). High frequency 1-3 composite transducer fabricated using sol–gel derived lead-free BNBT fibers. *Sensors and Actuators A: Physical,* 114(1): 1-6.

Wang HY, Wang YQ, Hu QF & Li XJ (2012). Capacitive humidity sensing properties of SiC nanowires grown on silicon nanoporous pillar array. *Sensors and Actuators B: Chemical,* 166: 451-456.

Wang J, Wan H & Lin Q (2003). Properties of a nanocrystalline barium titanate on silicon humidity sensor. *Measurement Science and Technology,* 14(2): 172.

Wang J, Wang X-h & Wang X-d (2005). Study on dielectric properties of humidity sensing nanometer materials. *Sensors and Actuators B: Chemical,* 108(1): 445-449.

Wang J, Xu BK, Ruan SP & Wang SP (2003). Preparation and electrical properties of humidity sensing films of $BaTiO_3$/polystrene sulfonic sodium. *Materials Chemistry and Physics,* 78(3): 746-750.

Wang L, Li D, Wang R, He Y, Qi Q, Wang Y & Zhang T (2008). Study on humidity sensing property based on Li-doped mesoporous silica MCM-41. *Sensors and Actuators B: Chemical,* 133(2): 622-627.

Wang LL, Wang HY, Wang WC, Li K, Wang XC & Li XJ (2013). Capacitive humidity sensing properties of ZnO cauliflowers grown on silicon nanoporous pillar array. *Sensors and Actuators B: Chemical,* 177: 740-744.

Wang R, He Y, Zhang T, Wang Z, Zheng X, Niu L & Wu F (2009). DC and AC analysis of humidity sensitive properties based on K^+ doped nanocrystalline $LaCo_{0.3}Fe_{0.7}O_3$. *Sensors and Actuators B: Chemical,* 136(2): 536-540.

Wang R, Wang D, Zhang Y & Zheng X (2014). Humidity sensing properties of $Bi_{0.5}(Na_{0.85}K_{0.15})_{0.5}Ti_{0.97}Zr_{0.03}O_3$ microspheres: Effect of A and B sites co-substitution. *Sensors and Actuators B: Chemical,* 190: 305-310.

Wang WC, Tian YT, Li K, Lu EY, Gong DS & Li XJ (2013). Capacitive humidity-sensing properties of Zn_2SiO_4 film grown on silicon nanoporous pillar array. *Applied Surface Science,* 273: 372-376.

Wang Y, Park S, Yeow JT, Langner A & Müller F (2010). A capacitive humidity sensor based on ordered macroporous silicon with thin film surface coating. *Sensors and Actuators B: Chemical,* 149(1): 136-142.

Wang Z, Chen X, Ni L & Liu X (2007). Dielectric abnormities of complex perovskite $Ba(Fe_{1/2}Nb_{1/2})O_3$ ceramics over broad temperature and frequency range. *Applied Physics Letters,* 90(2): 2904.

Wang Z, Shi L, Wu F, Yuan S, Zhao Y & Zhang M (2011). The sol–gel template synthesis of porous TiO_2 for a high performance humidity sensor. *Nanotechnology,* 22(27): 275502.

Wei D, Zhou Y, Jia D & Wang Y (2007). Structure of calcium titanate/titania bioceramic composite coatings on titanium alloy and apatite deposition on their surfaces in a simulated body fluid. *Surface and Coatings Technology,* 201(21): 8715-8722.

Whitmire RE, Wilson DS, Singh A, Levenston ME, Murthy N & García AJ (2012). Self-assembling nanoparticles for intra-articular delivery of anti-inflammatory proteins. *Biomaterials,* 33(30): 7665-7675.

Wiederhold PR. (1997). *Water vapor measurement: methods and instrumentation.* Vol. 1: CRC Press, New York.

Wieman TJ (1998). Clinical efficacy of becaplermin (rhPDGF-BB) gel. *The American Journal of Surgery,* 176(2): 74S-79S.

Winter GD (1962). Formation of the scab and the rate of epithelization of superficial wounds in the skin of the young domestic pig. *Nature,* 193: 293-294.

Witte MB & Barbul A (1997). General principles of wound healing. *Surgical Clinics of North America,* 77(3): 509-528.

Wlaschek M, Peus D, Achterberg V, Meyer-Ingold W & Scharffetter-Kochanek K (1997). Protease inhibitors protect growth factor activity in chronic wounds. *British Journal of Dermatology,* 137(4): 646-663.

Wolny WW (2005). Application driven industrial development of piezoceramics. *Journal of the European Ceramic Society,* 25(12): 1971-1976.

Wu J, Nan C-W, Lin Y & Deng Y (2002). Giant dielectric permittivity observed in Li and Ti doped NiO. *Physical Review Letters,* 89(21): 217601.

Wu JY, Li CW, Tsai CH, Chou CW, Chen DR & Wang GJ (2014). Synthesis of antibacterial TiO_2/PLGA composite biofilms. *Nanomedicine: Nanotechnology, Biology and Medicine,* 10(5): e1097-e1107.

Yazawa Y, Yamaguchi A & Takeda H (2012). Lunar Minerals and Their Resource Utilization with Particular Reference to Solar Power Satellites and Potential Roles for Humic Substances for Lunar Agriculture *Moon, Springer,* 5: 105-138.

You L, Cao Y, Sun Y, Sun P, Zhang T, Du Y & Lu G (2012). Humidity sensing properties of nanocrystalline $ZnWO_4$ with porous structures. *Sensors and Actuators B: Chemical,* 161(1): 799-804.

Yu B, Leung KM, Guo Q, Lau WM & Yang J (2011). Synthesis of Ag–TiO_2 composite nano thin film for antimicrobial application. *Nanotechnology,* 22(11): 115603.

Yuan Q, Geng W, Li N, Tu J, Wang R, Zhang T & Li X (2009). Study on humidity sensitive property of K_2CO_3-SBA-15 composites. *Applied Surface Science,* 256(1): 280-283.

Yuan Q, Li N, Tu J, Li X, Wang R, Zhang T & Shao C (2010). Preparation and humidity sensitive property of mesoporous ZnO–SiO$_2$ composite. *Sensors and Actuators B: Chemical,* 149(2): 413-419.

Yuk J & Troczynski T (2003). Sol–gel BaTiO$_3$ thin film for humidity sensors. *Sensors and Actuators B: Chemical,* 94(3): 290-293.

Zabicky J, Frage N, Kimmel G, Hazan N, El-fahel H, Goncharov E, Manor E & Shneck R (1997). Metastable magnesium titanate phases synthesized in nanometric systems. *Philosophical Magazine Part B,* 76(4): 605-614.

Zhang J, Postovit L-M, Wang D, Gardiner RB, Harris R, Abdul MM & Thomas AA (2009). In situ loading of basic fibroblast growth factor within porous silica nanoparticles for a prolonged release. *Nanoscale Research Letters,* 4(11): 1297-1302.

Zhang Q, Cao W, Zhao J & Cross L (1994). Piezoelectric performance of piezoceramic-polymer composites with 2-2 connectivity-a combined theoretical and experimental study. *IEEE Transactions on Ultrasonics, Ferroelectrics, and Frequency Control,* 41(4): 556-564.

Zhang T, He Y, Wang R, Geng W, Wang L, Niu L & Li X (2008). Analysis of dc and ac properties of humidity sensor based on polypyrrole materials. *Sensors and Actuators B: Chemical,* 131(2): 687-691.

Zhang T, Wang R, Geng W, Li X, Qi Q, He Y & Wang S (2008). Study on humidity sensing properties based on composite materials of Li-doped mesoporous silica A-SBA-15. *Sensors and Actuators B: Chemical,* 128(2): 482-487.

Zhang W, Wang R, Zhang Q & Li J (2012). Humidity sensitive properties of K-doped mesoporous silica SBA-15. *Journal of Physics and Chemistry of Solids,* 73(4): 517-522.

Zhang Y, Yu K, Jiang D, Zhu Z, Geng H & Luo L (2005). Zinc oxide nanorod and nanowire for humidity sensor. *Applied Surface Science,* 242(1): 212-217.

Zhang Y, Yu K, Ouyang S, Luo L, Hu H, Zhang Q & Zhu Z (2005). Detection of humidity based on quartz crystal microbalance coated with ZnO nanostructure films. *Physica B: Condensed Matter,* 368(1): 94-99.

Zhang Y, Zheng X & Zhang T (2011). Characterization and humidity sensing properties of Bi$_{0.5}$Na$_{0.5}$TiO$_3$–Bi$_{0.5}$K$_{0.5}$TiO$_3$ powder synthesized by metal-organic decomposition. *Sensors and Actuators B: Chemical,* 156(2): 887-892.

Zhang Y, Zheng X, Zhang T, Gong L, Dai S & Chen Y (2010). Humidity sensing properties of the sensor based on Bi$_{0.5}$K$_{0.5}$TiO$_3$ powder. *Sensors and Actuators B: Chemical,* 147(1): 180-184.

Zhao M, Josephson L, Tang Y & Weissleder R (2003). Magnetic sensors for protease assays. *Angewandte Chemie International Edition,* 42(12): 1375-1378.

227

Zhou Z, Pang S, Liu Z, Xu H & Cui G (2015). Interface engineering for high-performance perovskite hybrid solar cells. *Journal of Materials Chemistry A*, 38 (3), 19205-19217.

Zhu B, Wang Z, Zhang Y, Yu Z, Shi J & Xiong R (2009). Low temperature fabrication of the giant dielectric material $CaCu_3Ti_4O_{12}$ by oxalate coprecipitation method. *Materials Chemistry and Physics,* 113(2–3): 746-748.

LIST OF PUBLICATIONS

1. **Ashis Tripathy**, Sumit Pramanik, Ayan Manna, Hanie Nadia Shasmin, Zamri Radzi and Noor Azuan Abu Osman (2016). Uniformly Porous Nanocrystalline $CaMgFe_{1.33}Ti_3O_{12}$ Ceramic derived Electro-ceramic Nanocomposite for Impedance Type Humidity Sensor. *Sensors*, 16(12), 2029. (**Q1, ISI-cited publication**).

2. **Ashis Tripathy**, Sumit Pramanik, Ayan Manna, Satyanarayan Bhuyan, Nabila Farhana Azrin Shah, Zamri Radzi and Noor Azuan Abu Osman. (2016). Design and Development for Capacitive Humidity Sensor Applications of Lead-Free Ca, Mg, Fe, Ti-Oxides-Based Electro-Ceramics with Improved Sensing Properties via Physisorption. *Sensors*, 16(7), 1135. (**Q1, ISI-cited publication**).

3. **Ashis Tripathy**, Sumit Pramanik, Ayan Manna, Nabila Farhana Azrin Shah, Shasmin HN, Zamri Radzi and Noor Azuan Abu Osman (2016). Synthesis and Characterizations of Novel Ca-Mg-Ti-Fe-Oxides Based Ceramic Nanocrystals and Flexible Film of Polydimethylsiloxane Composite with Improved Mechanical and Dielectric Properties for Sensors. *Sensors,* 16(3), 292. (**Q1, ISI-cited publication**).

4. **Ashis Tripathy**, Sumit Pramanik, Jongman Cho, Jayasree Santosh & Noor Azuan Abu Osman (2014). Role of morphological structure, doping, and coating of different materials in the sensing characteristics of humidity sensors. *Sensors*, 14(9), 16343-16422. (**Q1, ISI-cited publication**).